Dislocations in complex intermetallic phases – Deformation mechanisms determination by nano-mechanical testing

Von der Fakultät für Georessourcen und Materialtechnik der

Rheinisch-Westfälischen Technischen Hochschule Aachen

zur Erlangung des akademischen Grades eines

Doktors der Ingenieurwissenschaften

genehmigte Dissertation

vorgelegt von

Martina Sophia Dominique Freund, M.Sc. RWTH

Berichter: **Univ.-Prof. Dr. Sandra Korte-Kerzel**
Prof. Dr. rer. nat. Gerhard Dehm

Tag der mündlichen Prüfung: 25.11.2024

Diese Dissertation ist auf den Internetseiten der Universitätsbibliothek online verfügbar

Declaration on Publications

This thesis includes the following articles that have been published in international peer-reviewed journals:

Publication 1 (Chapter 5)

M. Freund, D. Andre, P.L. Sun, C.F. Kusch, S. Sandlöbes-Haut, H. Springer, S. Korte-Kerzel, Plasticity of the C15-$CaAl_2$ Laves phase at room temperature. Materials & Design, 2023. **225**: p. 111504.

Publication 2 (Chapter 6)

M. Freund, D. Andre, C. Zehnder, H. Rempel, D. Greber, M. Zubair, S. Sandlöbes-Haut, J.S.K.-L. Gibson, S. Korte-Kerzel., Plastic deformation of the $CaMg_2$ C14-Laves phase from 50-250° C. Materialia, 2021. **20**: p. 101237.

Publication 3 (Chapter 7)

M. Freund, X. Zhuocheng, P.L. Sun, J. Spille, H. Wang, C. Thomas, M. Feuerbacher, M. Lipinska-Chwalek. J. Mayer, S. Korte-Kerzel, Influence of chemical composition on the room temperature plasticity of C15 Ca-Al-Mg Laves phases, Acta Materialia

Publication 4 (Chapter 8)

D. Andre, M. Freund, U. Rehman, W. Delis, M. Felten, J. Nowak, C. Tian, M. Zubair, L. Tanure, L. Abdellaoui, H. Springer, J.P. Best, D. Zander, G. Dehm, S. Sandlöbes-Haut a, S. Korte-Kerzel, Metallographic preparation methods for the Mg based system Mg-Al-Ca and its Laves phases, Materials Characterization, 192, 112187

Publication 5 (Chapter 9)

Anwesha Kanjilal, Ali Ahmadian, Martina Freund, Pei-Ling Sun, Sandra Korte-Kerzel, Gerhard Dehm, James P. Best, Temperature-driven nanoscale brittle-to-ductile transition of the *C*15 $CaAl_2$ Laves phase, Materials & Design, 2024. 224

Publication 6 (Chapter 10)

W. Luo, L. Tanure, M. Felten, J. Nowak, W. Delis, M. Freund, N. Ayeb, D. Zander, C.Thomas, M. Feuerbacher, S. Sandlöbes-Haut, S. Korte-Kerzel, H. Springer, Metallurgical synthesis methods for Mg-Al-Ca scientific model materials

D 82 (Diss. RWTH Aachen University, 2024)

Danksagung

Eine Danksagung ist eine Gelegenheit, allen Personen zu danken, die zur Entstehung der Arbeit beigetragen haben. Hierbei möchte ich allen dankendanken, die mich während meines Werdens und bei dem Entstehen dieser Arbeit unterstützt und bereichert haben. Auf die ich mich verlassen konnte und die mir diesen Schritt ermöglicht haben.

Zunächst gilt mein besonderer Dank meiner Betreuerin Prof. Dr. Sandra Korte-Kerzel, durch die ich die Möglichkeit als Teil des Sonderforschungsbereiches 1394 gehabt habe, meine Dissertation zu erstellen. Dabei ging die Unterstützung weit über diesen Aspekt hinaus. Besonders die Möglichkeit mit Problemen, Ergebnissen oder doch kleinen Brettern vor dem Kopf einfach vorbeikommen zu dürfen und so gemeinsam Lösungen zu finden oder gar weitere Denkanstöße zu bekommen, hat die Zusammenarbeit besonders gemacht. Dankbar bin ich des Weiteren für die Begleitung zu Tagungen, Vorbereitungen auf Konferenzen, Korrekturen von Veröffentlichungen und abschließende immer konstruktiver Kommentare.

Darüber hinaus möchte ich mich bei allen Co-Autoren der bisher aus der wissenschaftlichen Arbeit entstandenen Publikationen bedanken, durch deren Beiträge, Unterstützung bei der Erstellung und dem Einreichungsprozess diese Publikationen erst möglich wurden. Ein besonderer Dank gilt hierbei Doreen Andre, die mir bei den anfänglichen Veröffentlichungen immer zur Seite gestanden hat und mir den Einstieg damit erleichterte. Auch Christoffer Zehnder möchte ich hier nicht außen vorlassen, durch den ich einen sehr lehrreichen Einstieg in das Forschungswesen erlangt habe.

Ein weiterer Dank gilt dem ganzen Team des IMMs, was mir über die ganzen Jahre die ich hier mitwirken durfte, immer zur Seite gestanden hat. Angefangen bei hunderten Stunden von Probenpräparationen mit Herrn David Beckers, was in der HiWi Zeit mit Aluminium zu Stahl führte und dann während meiner Promotion viele Nerven bei der Präparation der Laves Phasen gekostet hat. Dank Dir David haben die Proben es auch irgendwann geschafft das REM von innen zu sehen! Auch dem Team der Werkstatt möchte ich von Herzen danken, die immer motiviert und hilfsbereit waren, oder auch nur für das Winken, wenn ich wieder einmal zu den Mikroskopen gegangen bin. Herrn Thomas Burlet und Max Wollenweber danke ich noch einmal für die drei Wochen unermüdlicher Geduld bei den Hochtemperaturversuchen, bei dem wenigstens immer einer von uns noch gute Laune und Motivation aufbringen konnte, um die Experimente abschließen zu können. Auch hierbei muss Herrn Nico Poschmann und Herrn Detlef Fuchs für die schnellen Anpassungen gedankt werden.

Auch die vielen schönen Laufrunden, die ich mit Herrn Matthias Loeck am Anfang der Promotionszeit hatte, habe ich immer sehr geschätzt und war froh trotz Corona jemanden zu haben mit dem ich sozial interagieren konnte und dabei noch sportlich aktiv zu sein.

Besonders zu schätzen gelernt habe ich meinen Kollegen Wassili Delis, der über die SFB Zeit, die ganzen kleinen und größeren Seminare, die Meetings, Konferenzen und Kaffeetrinken zu einem richtigen Freund geworden ist, ohne den ich die ersten Jahre wahrscheinlich weniger motiviert zur Arbeit gekommen wäre. Durch Dich, Wassili, hatte ich immer was zu lachen und konnte auch in den nicht so leichten Phasen immer wieder was Positives sehen. Von Herzen danke! Auch meinen Bürokollegen und damit das Lehre-Kompetenzzentrum möchte ich nicht unerwähnt lassen. Max, es hat mir immer viel Spaß gemacht deine Bürokollegin und zeitweise Sportpartnerin zu sein. Danke auch für die immer konstante Unterstützung, bei wirklich jedem anliegen. Die unzähligen Mittagspausen, und ich wünschte ehrlich es wären mehr gewesen, mit dir Christina werde ich am meisten vermissen. Ich bin glücklich, dass wir uns dann doch noch irgendwann gefunden haben, sodass wir miteinander gut arbeiten und noch besser Pause machen konnten. Auch dir Tobi danke ich für die schönen Gespräche und wenn Ihr beiden noch einmal einen Taschenhalter fürs Phantasialand braucht, ich bin aller Zeit bereit.

Die tatkräftige Unterstützung von Arndt Ziemons, Miriam Wulfes, Marion Maaß und Sergej Laiko und ihre oft schnelle Mithilfe in diversen Belangen, ob EDV-technischer, metallographischer oder sonstiger Hinsicht, ermöglichte es mir einem optimalen Forschungsalltag nachgehen zu können.

Dankbar bin ich auch für die gute Zusammenarbeit und den kollegialen Austausch im Rahmen des SFBs, der durch die Mitarbeit in diesem möglich wurde.

Zu guter Letzt gilt mein besonderer Dank meiner Familie und meinen Freunden.

Content

Declaration on Publications 2

Danksagung 3

Content 5

List of figures 6

List of tables 9

List of abbreviations 10

Abstract 12

Kurzfassung 14

1 Motivation 17

  Research Questions: 19

2 Literature review 21

  2.1 Laves phases 22

    2.1.1 Laves phase structure 22

    2.1.2 Stability of the Laves phase structure 30

  2.2 Dislocation behaviour 33

    2.2.1 Thermal influence on plasticity 38

    2.2.2 Stacking faults 41

    2.2.3 Plasticity of Laves phases 43

    2.2.4 Stacking faults in Laves phases: Synchro-shear mechanism 48

    2.2.5 Chemistry influence on plasticity 49

  2.3 Mg-Al-Ca System 51

3. Research findings of this study 53

4 Conclusion 69

5. Outlook and Future Work 75

References 76

5. Publication 1 84

6. Publication 2 86

7. Publication 3 88

8. Publication 4 90

9. Publication 5 91

10. Publication 6 92

List of figures

Figure 1: Schematic illustration of this thesis aims and workflow with its research questions. 20

Figure 2: Visualisation of the structure of the three Laves phases prototypes with a single unit cell and aligned to demonstrate the structural similarity, whereas the bigger red atoms correspond to the A atom and the smaller green atoms to the B atom. a) *C*15 Prototype, b) *C*14 Prototype and c) *C*36 prototype, visualised by using VESTA [3]. 22

Figure 3: Coordination polyhedra described by Frank and Kasper a) CN12 b) CN 14 c) CN15 and d) CN16 adopted and **reproduced with permission of Springer Nature** from [46, 47]. 23

Figure 4: Laves phase prototypes a) *C*36, b) *C*15 and c) *C*14, with coloured atoms according to coordination polyhedra CN12 in red (4f), pink (6h) and purple (6g) and CN16 in grey, using VESTA [3]. 25

Figure 5: Structural arrangement of the layers of the Laves phase, showing a) the basic Kagomé layer built up with small B-atoms in purple and a systematic triangular A-atom net indicated by the blue atoms, in b) the triple layer and c) the reversed triple layer, whereby the different sized circles symbolise the A (larger) and B (smaller) atoms, and the color-coding shows the height of the atoms. Adopted and **reproduced with permission of the International Union of Crystallography** from [18, 44]. 27

Figure 6: Different modified layers from Komura et al. [17] to explain the different types of stackings for the Laves phase, whereas the capital Roman letters (A, B, C) show the arrangement of the triangular net, the small Roman letters (a, b, c) show the triangular net for the B-Atoms and the Greek letters (α, β, γ) show the B atoms arranged in the Kagomé net. b) possible stacking sequence, with their arrangement given with coordination parameter Z. The figure is **reproduced with permission of the International Union of Crystallography.** ...27

Figure 7: A thermodynamic interpretation of the size-ratio limits for laves phase formation (Enthalpy of formation vs $rArB$ for binary Laves phases.) adopted from [5] **reproduced with permission of Springer Nature**. 30

Figure 8: Difference between the structural energy of $MgCu_2$, $MgZn_2$, and $MgNi_2$, across the investigated range for $CaAl_{2-x}Mg_x$ and $CaAl_{2-x}Li_x$ calculated by Amerioun et al. [55, 56]. **Reprinted with permission from Laves-Phase Structural Changes in the System $CaAl_{2-x}Mg_x$. Copyright 2003 American Chemical Society.** 31

Figure 9: a) Schematic sketch of the alignment of the two half crystals with the same in-plan distance b spacing and lattice distance d, aligned shifted by b/2 to each other. b) Shows the misalignment φ due to the additional plane in crystal A with the additional in-plane displacement u. Based on [67] **reproduced with permission of Elsevier**. 34

Figure 10: Total misfit energy U_T arises from the misalignment of atoms in a crystal lattice due to dislocations, with the total misfit energy being the sum of these contributions. It quantifies the overall energy cost of dislocation presence. The misalignment potential U_X measures the energy needed to overcome the atomic misalignments associated with dislocations and represents the barrier for dislocation movement through the lattice. The in-plane potential U_i denotes the energy barrier within the crystal plane, reflecting the resistance of the lattice to dislocation motion. Adopted from [9]. 36

Figure 11: Schematic illustration of the resulting energies when a dislocation moves along x, here α, taken from [9, 11]. 37

Figure 12: Schematic illustration of the kink-pair mechanism. Based on [2] and **reproduced with permission of Springer Nature.** 38

Figure 14: SF process in the fcc lattice, a) shows the dislocation dissociation of $b1$ → $b2 + b3$, b) with light blue the hcp stacking is implied. Adopted from [82]. and **reproduced with permission of Springer Nature**...42

Figure 15: Difference between a) intrinsic and b) extrinsic stacking fault or double SF, taken from [1], **reproduced with permission of Elsevier**. 43

Figure 16: Illustration of the synchro-shear mechanism. In a) the rigid Kagomé layer builds out B atoms, in green, is displaced, and in these holes, the location of the A atoms is implied by red lined circles. b) shows the dissociation of the dislocation for cubic and hexagonal Laves phase. c) and d) showing the triple layer t (c)) and t´(d)), which is placed between the single Kagomé layer building this quadruple stacking. Adopted from [90] **reproduced with permission of Elsevier**. 49

Figure 17: Resulting intermetallic phases in the Mg-Al-Ca system. a) cubic *C*15 $CaAl_2$, b) hexagonal *C*14 $CaMg_2$, c) (di-)hexagonal *C*36 $Ca(Al;Mg)_2$ Laves phase and d) β-$Mg_{17}Al_{12}$ phase, illustrated using VESTA [3]. 51

Figure 18: Alignment of the investigated Laves phases in the ternary Mg-Al-Ca diagram. The overall bulk composition is listed in Table 7 below, presented in the diagram as stars with different colour codes: dark green star belongs to the *C*14_S, the light green to *C*14_NS, the dark blue to the *C*15_S, the purple to the *C*15_NS1 and the red star to the *C*15_NS2. 53

Figure 19: Temperature dependent a) hardness and b) indentation modulus of the C14_S sample of the investigated areas, stays on one level irrespective of temperature and orientation. The load-depth curves at c) 100 °C and d) 250 °C show decreasing serrations with increasing temperature [6]..55

Figure 20: Resulting slip lines shown with the belonging temperature, for all indented orientations [6]. 55

Figure 21: Relative activation frequencies against the investigated temperatures for the *C*14 $CaMg_2$ Laves phase. Room temperature results were taken from [8] and up to 50 °C from [6]. 56

Figure 22: Investigated orientations for the C14_NS sample, with corresponding measured hardness and indentation modulus. 58

Figure 23: Activation frequencies of the *C*14_S (dark green) and *C*14_NS (light green) Laves phase for the investigated plane orientations. 58

Figure 24: a) – e) illustrate the compressed micropillars for each orientation, whereas the alignment of these could be taken from Figure 21, with the simulation of the slip planes. f) showing the engineering stress-engineering strain curve from the compressed micropillars.59

Figure 25: a) alignment of the planes taken for the slip line analysis, displaced in the cubic *C*15 lattice. b) relative activation frequency of the activated slip planes for all three samples. The black line shows the amount of possible slip systems in a related to each other [10]............61

Figure 26: Orientation dependent morphology of resulting slip lines for the cubic $CaAl_2$ Laves phase: a) *C*15_S, b) *C*15_NS1, c) *C*15_NS2 visualised in its IPF map, whereas the colour code gives the different morphologies of surface traces for this orientations: green for edges, blue for lines, pink for curves, black for cracks, yellow for only few surface features and red for nothing, modified from [10, 13]. 62

Figure 27: Atomistic simulations for the energy barrier of specific slip systems and its change with the compositions, for a) {111} synchro-shear motion, b) {111} full slip path, c) {112} full slip path and d) {114} full slip path and e) {115} full slip path [10]. 63

Figure 28: a) SE-image of an nanoindentation imprint including a schematic sketch (dotted orange area), from where the TEM lamella was cut out. letters a and b show the orientation of the membrane and how it was analysed in the further investigations. the slip traces in the vicinity of the indent were furthermore correlated with different planes along with the unit cell using vesta [3]. b) STEM image of the lamella. c) BF-TEM image taken at [112] zone axis. The blue rectangle highlights the area with a high dislocation density, whereas the red rectangle indicates the area where dislocation Burgers vector analysis was performed and the yellow rectangle corresponds to the area where the stacking faults were found [13]. 64

Figure 29: a) *C*15_NS1 TEM bright field image in 312 zone axis, showing slip bands on 141 and 141 in light green, 151 in pink and 112. b) *C*15_NS2 in [101] zone axis revealing slip bands on $1\ 11\ 1$ in blue. 131 in green, 161 in orange as well as 121 in white. Adopted and modified from [10]. 65

Figure 30: a) and b) TEM bright field images taken in 111 zone axis. a) with g=(202) two-beam condition at different magnifications, and under b) g=(022) two-beam condition in an indented *C*15_NS1 Laves phase. Different coloured lines mark the orientations of the slip plane. The green rectangle shows a quite wavy segment. The zigzag shape of the slip plane indicates the occurrence of multiple cross-slips of dislocations. 65

Figure 31: Atomistic configurations and energy profiles along minimum energy paths (MEPs) for the motion of the screw $a2$[110] dislocation on (a) (001), (b) (111) triple-kagomé interlayer, (c) (112), (d) (113), (e) (114) and (f) (115) planes were calculated using the nudged elastic band (NEB) method. Only atoms belonging to the dislocation core, as identified by LaCA, are shown here. The orange and magenta symbols indicate the position of the dislocation line in the initial (reaction coordinate RC:0) and final (RC:1) atomistic configurations, while the cyan symbols represent the position of the dislocation line at the intermediate minima. Dashed lines indicate the glide planes between each local minimum. Performed by Dr. Zhuocheng Xie. ..66

Figure 32: Resulting plane activation in *C*15_PT sample. Showing in yellow the relative activation frequency of the {100}, in red {110}, in rose {111} and in green {11n} planes. 67

Figure 33: Hardness and indentation modulus evolution over the tested temperature in sample *C*15_PT. 68

Figure 34: normalised shear stress against homologous T, showing the values for *C*14 $CaMg_2$ with red triangles, for *C*15 $CaAl_2$ with blue circles [7] and *C*15 $CuMg_2$ with green rectangles, gained from nanomechanical experiments. All values are plotted in Pauflers DMM, which he designed for *C*14 $MgZn_2$ in light grey using macroscopic experiments [12], whereas the ideal strength was taken accordingly to Kelly et al. [16]. 73

Figure 35: Stacking of a) hexagonal $\{1010\}$ plane and b) cubic {112} plane. 74

List of tables

Table 1: Laves phase structures characterised by using the Frank-Kasper polyhedra taken from [48]: 24

Table 2: Stacking sequence of Laves phase prototypes [49]. 28

Table 3: Different ways to describe the stacking of the three Laves phase prototypes according to Pearson [4], Jagodzinski [14, 15], Komura [17], and Frank and Kasper [18]. 29

Table 4: Review of *C*15 plasticity, with their corresponding temperature and the "*" labelled, also have CRSS. 44

Table 5: Review of *C*14 plasticity with its corresponding temperature and where "*"-labelled also the CRSS for that specific slip system, mostly also the indentation modulus. 45

Table 6: Calculated CRSS/G values for some given Laves phases, using equation (10) for the calculations, for a specific temperature and slip system. 46

Table 7: Compositions of investigated stoichiometric (S) and off stoichiometric (NS) samples (same colour scheme as Figure 17) and the Prototype (PT). 54

Table 8: Micropillar compression test results from *C*14_S at 150 °C and 250 °C, given the CRSS for the found slip system with their Schmid Factor for Area 1, Area 2 and Area 3. 57

Table 9: Calculated CRSS for the resulting slip systems of *C*14_NS for all analysed orientations, given with their Schmid Factor and engineering stresses. 59

Table 10: Hardness and indentation modulus for the stoichiometric and off stoichiometric cubic $CaAl_2$ Laves phases. 60

List of abbreviations

Al	aluminium
b	Burgers vector
BDTT	brittle to ductile transition temperature
Ca	calcium
CMA	complex metallic alloys
CRSS	critical resolved shear stress
d	lattice spacing
d/b ratio	d/b ratio
δ	atom deviation from initial position
ΔG	energy barrier
DMM	deformation mechanism map
E	young’s modulus
EBSD	electron backscatter diffraction
ε	strain
FIB	focused ion beam
fcc	face centred cubic
g	line element
G	shear modulus
hcp	hexagonal close packed
HT	high temperature
k	Boltzmann constancy
MEP	minimum energy path
Mg	magnesium
NEB	nudge elastic band
ρ_m	mobile dislocation density
RT	room temperature
SE	secondary electrons

SEM	scanning electron microscopy
SF	stacking fault
SFE	stacking fault energy
SRS	strain rate sensitivity
T	temperature
TCP	topological closed packed
TEM	transmission electron microscopy
T_H	homologous temperature
U_i	In-plane potential
U_T	total misfit energy
U_X	misalignment potential
VE	valence electrons
VEC	valence electron configuration
ν	Poisson ratio
ν_A	Debye frequency
$\dot{\gamma}$	shear strain rate
w	width

Abstract

Laves phases represent a class of intermetallic compounds with unique structures and properties. Exploring these phases can lead to the discovery of novel materials with desirable characteristics for various applications, such as in the aerospace, automotive, and electronics industries. Interesting are these for multi-component alloy systems like the Mg-Al-Ca, to strengthen the main magnesium (Mg) matrix. By studying their formation and properties, researchers can optimise alloy compositions for specific purposes, such as enhancing corrosion resistance, improving mechanical properties, or reducing material costs. Especially to be able to investigate this system and the interaction of the main matrix with the Laves phases, the properties of Laves phases must be unravelled to get more knowledge in terms of plasticity and mechanical properties, to have further the ability to understand the interaction. Investigating different compositions of Laves phases contributes to our understanding of phase stability and the influence of chemistry on the mechanical properties. This knowledge is crucial for predicting the behaviour of materials under different conditions. The overarching goal of this thesis is to get more insights into the dislocation behaviour of the formed Laves phases of the Mg-Al-Ca system, namely the hexagonal *C*14 $CaMg_2$ and the cubic *C*15 $CaAl_2$ Laves phase. Therefore, this thesis was subdivided into sub-goals: i) which slip systems can be activated, ii) the influence of the temperature and the local chemistry on the dislocation behaviour, and iii) the attempt to answer the question if the findings of mechanical properties and dislocation behaviour and their changes with temperature and local chemistry can be transferred to similar stacked phases and furthermore be generalisable for Laves phases at all.

The possible slip systems were analysed by a correlative investigation of the surface traces around indentation marks. Therefore, the grain orientations (using electron backscatter diffraction (EBSD)) were taken and aligned with secondary electron (SE) images of forming slip traces around an indentation mark. Transmission electron microscopy (TEM) analyses have identified new slip planes {112}, {113}, {114}, {115}, {116}, and {1 1 11}, summarized as the {11n} planes, with a Burgers vector $\vec{b}$ of 1/2<110>. Statistical analysis showed the highest activation on {11n} planes in the cubic *C*15 Laves phase, with dislocation motion on {111} planes being up to three times lower. Micropillar compression tests revealed that the critical resolved shear stress (CRSS) of {111} and {112} planes are similar. However, the {11n} planes have three times more independent slip systems than {111} planes. Dislocation cross-slip was detected between {111} and {112} planes, and frequently between {114} and {115} planes. Atomistic simulations confirmed the new slip systems, showing low energy barriers and cross-slip ability. Temperature influenced the dislocation structure, with dissociated dislocations

observed after reaching the BDTT. The local chemistry had negligible influence on slip systems in $Ca_{33}Al_{67}$, $Ca_{33}Al_{61}Mg_{6}$, and $Ca_{36}Al_{53}Mg_{11}$, all showing main plasticity on {11n} planes. However, the addition of Mg and Ca decreased hardness and indentation modulus, indicating softening behaviour with the deviation from the stoichiometric compound. Atomistic simulations showed a decreasing energy barrier with increasing Mg and Ca to the $CaAl_2$ Laves phase, and increased anisotropy related to stiffness and surface morphology. The hexagonal *C*14 $MgCa_2$ Laves phase was investigated in the range of 50 – 250 °C revealing at lower temperatures dislocation pinning which decreases with an increase in temperature, facilitating dislocation motion. Contrary to this observation, the visible surface traces were strongly influenced by the orientation and temperature, and at 250°C none were visible. Over the investigated orientations the pyramidal planes were the most detected followed by the 1st order prismatic and then the 2nd order prismatic with the basal plane. However, the mechanical properties like hardness and indentation modulus remained at one level throughout the investigated temperatures. With the combination of the study of the *C*15 Laves phase prototype, namely the $MgCu_2$, which presented the same trend for the influence of the temperature regarding mechanical properties as the *C*15 $CaAl_2$ phase the question of a generalisation can be assumed. By comparing both mechanical properties and their resulting plasticity (here just for room temperature (RT)) and coming up to similar results, although the radius ratio r_A/r_B deviates around 0.13, the first steps in terms of generalisation can be made. Moreover, isostructural similar planes can be found in the *C*14 and *C*15 Laves phase, for example the Laves phase typical triple layer, the basal plane and {111} plane, and prismatic 1st order with the newly found {112} planes. The last two planes have the calculated lowest CRSS at RT for the $CaMg_2$ and $CaAl_2$ Laves phase. With the high amount of Laves phases which are listed up to now, the structurally equivalent planes can be useful to take predictions how changes can influence mechanical properties and plastic behaviour based on already known research. Aiming to have mechanism- and plasticity maps to facilitate sample synthesis and only specific samples have been measured.

The findings acquired during the analysis provided important insights into the dislocation behaviour of Laves phases, especially the new found slip planes for the cubic Laves phase and the ability for dislocations to cross-slip, showing that the introducible plasticity introduced is greater than expected. The influence of the local chemistry seems to have a critical composition to influence the mechanical properties, like the hardness or already the reported brittle ductile transition temperature (BDTT).

Kurzfassung

Laves Phasen stellen eine Klasse von intermetallischen Verbindungen mit einzigartigen Strukturen und Eigenschaften dar. Die Erforschung dieser Phasen kann zur Entdeckung neuartiger Werkstoffe mit wünschenswerten Eigenschaften für verschiedene Anwendungen führen, z. B. in der Luft- und Raumfahrt-, Automobil- und Elektronikindustrie. Interessant sind diese für Mehrkomponenten-Legierungssysteme wie Mg-Al-Ca, um die Mg-Hauptmatrix zu verstärken. Durch die Untersuchung ihrer Bildung und ihrer Eigenschaften können die Forscher die Legierungszusammensetzungen für bestimmte Zwecke optimieren, z. B. zur Erhöhung der Korrosionsbeständigkeit, zur Verbesserung der mechanischen Eigenschaften oder zur Senkung der Materialkosten. Um dieses System und die Wechselwirkung der Hauptmatrix mit den Laves Phasen untersuchen zu können, müssen die Eigenschaften der Laves Phasen entschlüsselt werden, um mehr Erkenntnisse über die Plastizität und die mechanischen Eigenschaften zu gewinnen. Die Untersuchung von Laves Phasen trägt zu unserem Verständnis der Phasenstabilität und des Einflusses der Chemie bei. Dieses Wissen ist entscheidend für die Vorhersage des Verhaltens von Materialien unter verschiedenen Bedingungen. Das übergeordnete Ziel dieser Arbeit ist es, mehr Einblicke in das Versetzungsverhalten der gebildeten Laves Phasen des Mg-Al-Ca-Systems, der hexagonalen *C*14 $CaMg_2$ und kubischen *C*15 $CaAl_2$ Laves Phase, zu erhalten. Daher wurde dieses in Unterziele unterteilt: i) welche Gleitsysteme aktiviert werden können, ii) der Einfluss der Temperatur und der lokalen Chemie auf das Versetzungsverhalten und iii) der Versuch, die Frage zu beantworten, ob die Erkenntnisse über die mechanischen Eigenschaften und das Versetzungsverhalten sowie deren Änderungen mit der Temperatur und der lokalen Chemie auf ähnlich geschichtete Laves Phasen Typen übertragen und des Weiteren für Laves Phasen verallgemeinert werden können.

Die möglichen Gleitsysteme wurden durch eine korrelative Untersuchung der Oberflächenspuren um die Eindringstellen analysiert. Dazu wurden die Kornorientierungen (mit Hilfe der Elektronenrückstreuungsbeugung (EBSD)) aufgenommen und mit Sekundärelektronenbildern (SE) von sich bildenden Gleitebenen um eine Eindringstelle abgeglichen. Transmissions-Elektronenmikroskopie (TEM)-Analysen haben neue Gleitebenen {112}, {113}, {114}, {115}, {116} und {1 1 11} identifiziert, die als {11n} Ebenen zusammengefasst werden, mit einem Burgers-Vektor $\vec{b}$ von $^1/_2$<110>. Die statistische Analyse zeigte die höchste Aktivierung auf {11n} Ebenen in der kubischen *C*15 Laves Phase, wobei die Versetzungsbewegung auf {111} Ebenen bis zu dreimal geringer ist. Mikrosäulendruckversuche ergaben, dass die kritische Schubspannung der {111} und {112} Ebenen ähnlich sind und beide bei der gleichen angewandten Spannung

aktiviert werden können. Allerdings haben die {11n} Ebenen dreimal mehr unabhängige Gleitsysteme als die {111} Ebenen. Zwischen den {111} und {112} Ebenen und häufig auch zwischen den {114} und {115} Ebenen wurde ein Quergleiten der Versetzungen festgestellt. Atomistische Simulationen bestätigten die neuen Gleitsysteme und zeigten niedrige Energiebarrieren und die Fähigkeit zum Quergleiten. Die Temperatur beeinflusste die Versetzungsstruktur, wobei nach Erreichen der spröde-duktilitäts-Übergangstemperatur Versetzungsspalten beobachtet wurde. Der Einfluss der lokalen Chemie war jedoch für die statistische Auswertung der Gleitsysteme vernachlässigbar, wobei sich bei $Ca_{33}Al_{67}$, $Ca_{33}Al_{61}Mg_6$ und $Ca_{36}Al_{53}Mg_{11}$ die Hauptplastizität auf den {11n} Ebenen zeigte, die mechanischen Eigenschaften jedoch durch eine Verringerung der Härte und des Indentationsmoduls beeinflusst wurden. Atomistische Simulationen ergaben, dass die Energiebarriere zur $CaAl_2$ Laves Phase mit zunehmendem Mg und Ca abnimmt. Außerdem wird die Anisotropie in Bezug auf die Steifigkeit und die Oberflächenmorphologie ausgeprägter. Die hexagonale *C*14 $MgCa_2$ Laves Phase wurde im Temperaturbereich von 50 - 250°C untersucht und zeigte bei niedrigeren Temperaturen „Versetzungspinning". Durch die steigende Temperatur nimmt dies aufgrund der erleichterten Versetzungsbewegung ab. Im Gegensatz zu dieser Beobachtung nahmen die sichtbaren Oberflächenspuren in Abhängigkeit von der Orientierung ab und waren bei 250 °C nicht mehr sichtbar. Insgesamt wurden die pyramidalen Ebenen am häufigsten festgestellt, gefolgt von den prismatischen Ebenen erster Ordnung und den prismatischen Ebenen zweiter Ordnung mit der Basalebene. Die mechanischen Eigenschaften wie Härte und Eindringmodul blieben jedoch über die untersuchte Temperatur hinweg auf einem Niveau. In Kombination mit der Untersuchung des Prototyps der *C*15 Laves Phase, der $MgCu_2$-Phase, die den gleichen Trend für den Einfluss der Temperatur auf die mechanischen Eigenschaften zeigt wie die *C*15 $CaAl_2$ Phase, kann die Frage nach einer Verallgemeinerung vorsichtig beantwortet werden. Beim Vergleich beider Phasen weicht das Radienverhältnis r_A/r_B um 0.13 ab und zeigt bei beiden den gleichen Trend. Darüber hinaus lassen sich sowohl in der *C*14 als auch in der *C*15 Laves Phase isostrukturell ähnliche Ebenen finden, z. B. die typische „Triple" Ebenen, im hexagonalen die Basalebene und in kubischen die {111} Ebene, sowie die prismatischen Ebenen erster Ordnung mit den neu gefundenen {112} Ebenen. Diese Ebenen haben die niedrigsten berechneten kritischen Schubspannungen bei Raumtemperatur für die $CaMg_2$ und $CaAl_2$ Laves Phase. Da bis jetzt die Anzahl aller bekannten Laves Phasen sehr hoch ist, wäre es sicherlich nützlich, strukturell äquivalente Ebenen zwischen den Prototypen zu finden, um Änderung der mechanischen Eigenschaften und des plastischen Verhaltens grob abgeschätzt zu können. Ziel wäre die Erstellung eines Mechanismus-Diagramms, was resultierende Plastizität vorhersagen kann, umso hinsichtlich der Probenherstellung gezielte Entscheidungen treffen zu könnten. Die bei der Analyse gewonnenen Erkenntnisse lieferten wichtige Einblicke in das

Versetzungsverhalten der Laves Phasen, insbesondere die neuen Gleitebenen und die Fähigkeit der Versetzungen durch Quergleitprozesse gleiten zu könne zeigt, dass die tatsächliche Plastizität größer ist als erwartet. Der Einfluss der lokalen Chemie scheint eine kritische Zusammensetzung überschreiten zu müssen, um die mechanischen Eigenschaften zu beeinflussen, wie beispielsweise bei der Härte oder in früheren Studien beim spröd-duktil-Übergangstemperatur sichtbar wurde.

1 Motivation

Laves phases belong to one of the most important and abundant suborders of the intermetallic phases and are characterised by their well-ordered structure of two to three different metallic and/or non-metallic components, forming a multi-component system [19, 20]. The resulting compound is a combination of “A” atoms, which have a comparatively high atomic radius, with smaller “B” atoms, leading to an ideal atom ratio of $r_A/r_B \approx 1.225$ resulting in a densely packed AB_2 structure, which can crystallise in three different structure types: the cubic *C*15, the hexagonal *C*14 and the di-hexagonal *C*36 Laves phase [19-26]. Due to this combination, the mechanical and physical properties are changing regarding the pure, not combined component. Especially, by using a transition metal as one component, the forming structure provides high melting points, with good creep resistance as well as high strength and fracture toughness, and is therefore a reasonably good candidate for high temperature applications [20, 27, 28]. The physical properties of these combined structures offer the possibility of hydrogen storage. Additionally, the extended phase width of Laves phases leads to a manipulation of the equilibrium pressure of hydrogen storage [29, 30]. In addition to that, iron based Laves phases show good properties in terms of magnetic and electronic conductivity [31, 32]. Moreover, their superconductivity makes these structures quite interesting for superconductors, showing ranges from 0.07 K to 10 K for the $MgCu_2$-type Laves phase [12, 33, 34]. Besides the mechanical and physical properties, Laves phases have shown to influence the corrosion properties of a multiple phase material, depending on the size of the prototype, their morphologies and interconnectivity to improve or reduce the corrosion resistance [35-37].

These properties result due to their special structure, which goes hand in hand with the difficulty in terms of the investigation of plasticity, especially their room temperature behaviour. A few years ago, it was still challenging to introduce plasticity in these highly dense packed structures. By using nanomechanical experimental settings dislocations can be mobilised and the plasticity can be measured. This allows us to perform the experiments that are needed to investigate the upcoming Laves phases of the Mg-Al-Ca system. Figure 1 represents the whole workflow of the analysed Laves phases and the key findings. In this research, the main focus lies on the investigation of the dislocation structure, in the cubic *C*15 $CaAl_2$ and the hexagonal *C*14 $CaMg_2$ Laves phases. With changes in temperature and strain rates the behaviour of the dislocation will be changed as well, which could be measured due to changes in activation of different slip planes, the occurrence of slip planes, resistance against dislocation motion, visible by the observation of serrations in the not stoichiometric Laves phases. Furthermore, the mechanical and plastic properties of the off-stoichiometric Laves phases, to learn how a deviation from the perfect composition will manipulate them and if which defects will occur. Especially, the question if a defect formation can lead to a specific structure is of main interest. At the end, the question remains, if the mechanical properties, plastic behaviour and the formation of defect structures of Laves phases are predictable by the analysis of different compositions and structure types. Due to the clear definition of the different phases with clearly defined homogeneity regions, the movement of the dislocations along certain planes and directions should follow the same principle. The resistance to this dislocation movement should also result from the structure itself and should therefore be generalisable. It would be appropriate to plot the homologue temperature, as Paufler et al [12] have done for their deformation mechanism diagrams, due to the high and different melting temperatures resulting from these phases. To confirm this, it would be useful to analyse Laves phases with very different radius ratios to plot the resulting influence. Furthermore, the influence of different third elements can be plotted. This would make it possible to select specific material systems according to certain mechanical properties and the resulting plasticity.

Research Questions:

1. Which slip systems can be activated in the Laves phase structure?
2. How can the dislocation structure in the complex intermetallic phase and the mechanical properties be influenced by local chemistry, stoichiometry and with elevated temperature?
3. Can we derive general insights into the dislocation behaviour and the mechanical properties of Laves phases from the gained knowledge? And furthermore, predict the influence of temperature, strain rate and deviating stoichiometry

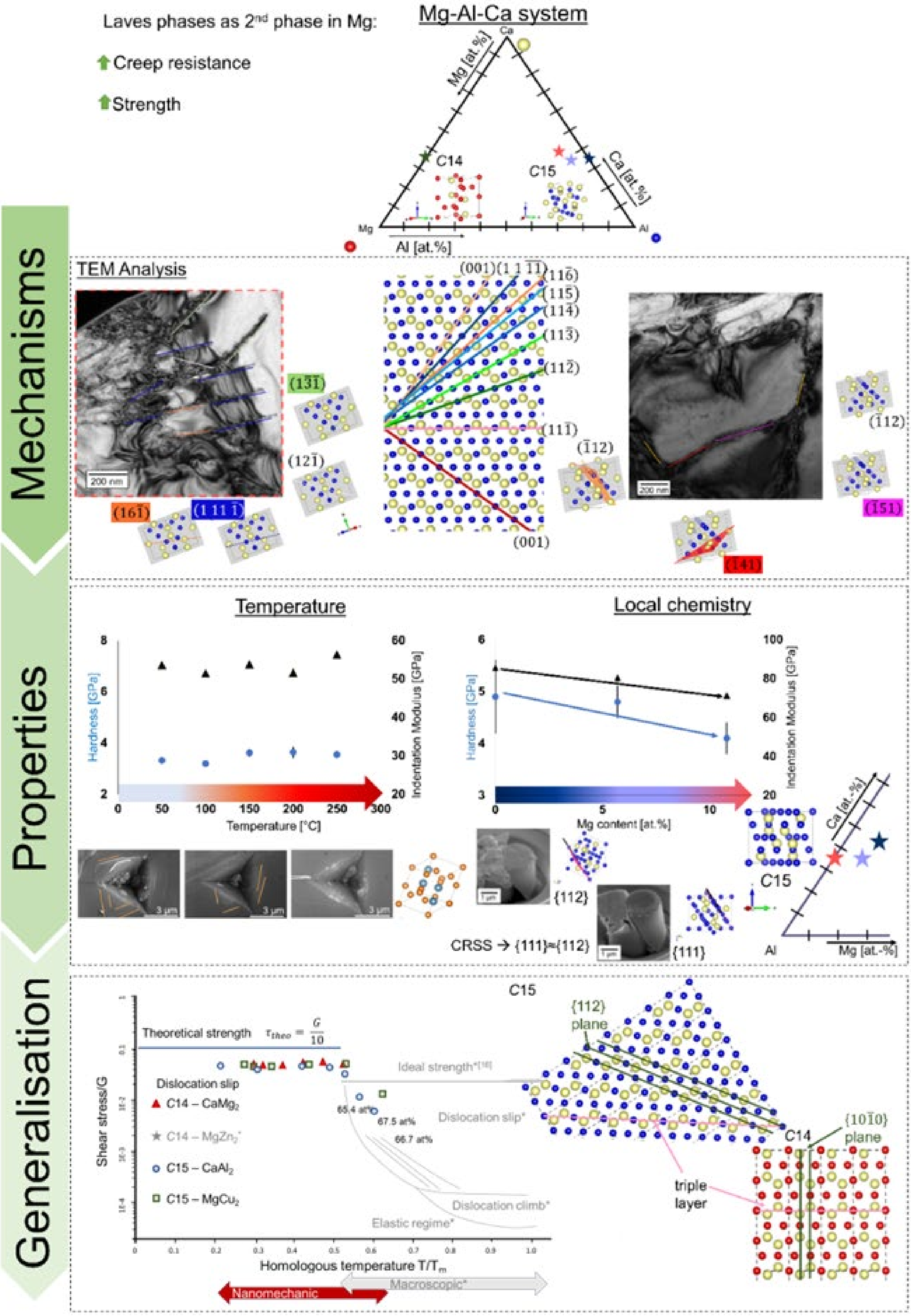

Figure 1: Schematic illustration of this thesis aims and workflow with its research questions.

2 Literature review

In general, the most complex structure is characterised by the complex metallic alloy (CMA), first reported by Paulinger in 1923, showing his investigations of $NaCd_2$. 32 years later he was able to find a cubic $Fd\bar{3}m$ like symmetry with 1152 atoms (AB_2= 384:768). Typical for this kind of material are the large unit cells with a high number of atoms which can be arranged in more than one kind of cluster in a single unit cell and therefore exhibit low symmetry and inherent disorders/misalignment. These structures are mainly built out of more than two elements and are often ternary compounds, like Al-Cu-Fe or Al-Pd-Fe. A way more trivial intermetallic structure is given by Laves phases. Today, 1400 different types of resulting Laves phases (397 binary and 928 ternary) are known, thus representing the most common intermetallic compound with 3%. The *C*15, *C*14, and *C*36 structures comprise 223 binary and 523 ternary, 154 binary and 265 ternary, and 20 binary and 43 ternary phases respectively. [26, 46]. These phases were also initially described by Laves and Witte in 1936. Contrary to the firstly described phases these unit cells are comparably small and exhibit fewer atoms (12-24 atoms per unit cell). Overall, the packing density can be calculated to be 0.71. Here the atomic arrangement is quite structured and densely packed and thus belongs to the group of the topological closed packed (TCP) phases and can therefore be distinguished from the CMAs.

2.1 Laves phases

Laves phases are defined due to their typical AB_2 structure [19, 20, 38, 39]. This describes a structure composed of at least two different metals, at a ratio of 1:2 (A:B), exhibiting different atom radii, whereby the A atom has a greater atomic radius in relation to the B atom. More than 1400 different Laves phase-combinations are listed for this kind of intermetallic configuration [20, 40, 41]. In general, they can be subdivided into three prototypes, which were characterised by Friauf, Laves, and Witte and Schulze who categorised them as Laves phases [25, 26, 38, 39]. Moreover, the complexity of the resulting structure was analysed in more detail by Komura et al. [42, 43]. These structure types are shown in Figure 2 with corresponding prototypes namely the *C*15 Laves phase – $MgCu_2$, *C*14 Laves phase – $MgZn_2$, and *C*36 Laves phase – $MgNi_2$.

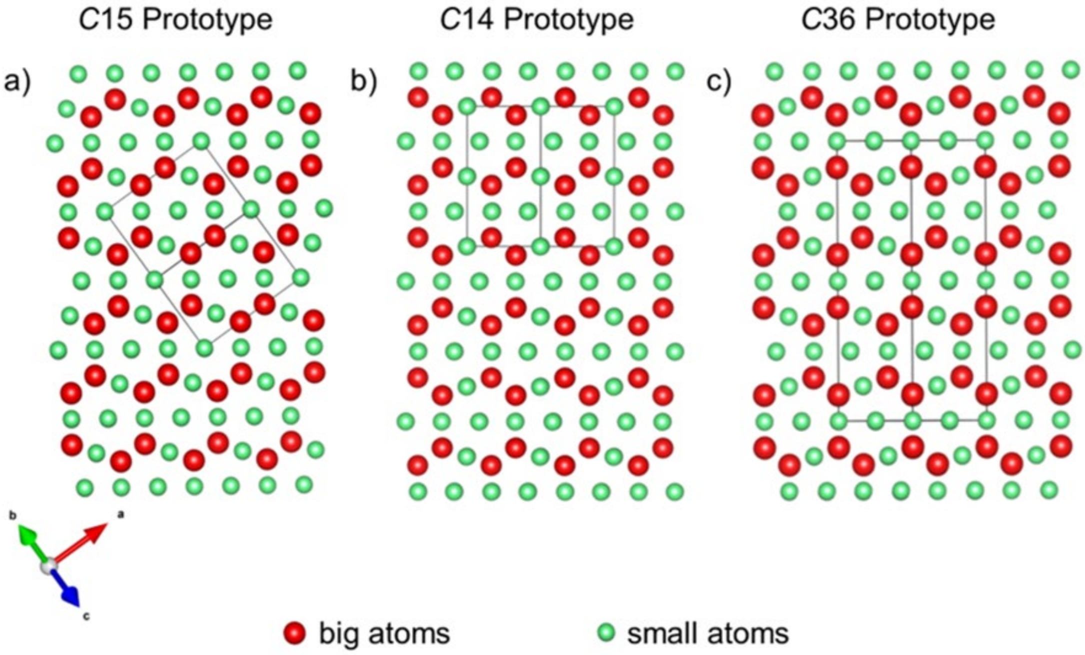

Figure 2: Visualisation of the structure of the three Laves phases prototypes with a single unit cell and aligned to demonstrate the structural similarity, whereas the bigger red atoms correspond to the A atom and the smaller green atoms to the B atom. a) *C*15 Prototype, b) *C*14 Prototype and c) *C*36 prototype, visualised by using VESTA [3].

2.1.1 Laves phase structure

In general, the structure of the Laves phases is more complex than conventional phases and needs a way more detailed description than simply using the Wyckoff symbols. A common way to describe these is by taking different layer sequences. Here the three different prototypes are only distinguished by the different stacking of the layers.

Initially, Frank and Kasper unravelled these structures. They classified these as tetragonal dense packed and topological closed packed structures and were able to define the Laves phase structure by a geometrical analysis and describe them by using polyhedra, which exhibit only triangular faces [18, 44, 45]. One of the distinguishing features of Laves phases is their characteristic icosahedral symmetry. In these structures, clusters of atoms are arranged in a symmetrical manner resembling the shape of an icosahedron, a polyhedron with 20 equilateral triangular faces (CN12). This arrangement of atoms contributes to the high symmetry observed in Laves phases. With this observation, they introduced a systematic way of classifying inter-metallic compounds based on the coordination polyhedra formed by the constituent atoms. They observed that the coordination polyhedra in Laves phases are formed by two types of atoms, typically with different atomic sizes. The larger A atoms occupy the vertices of the polyhedra, while the smaller B atoms occupy the centres of the faces. For the different number of atoms, these polyhedra can be characterised using the coordination numbers (CN) and neighbours, resulting in four different polyhedra (with the CN: 12, 14, 15, and 16), which can fulfil the conditions to maximise the packing efficiency while maintaining the long-range order, like displaced in Figure 3.

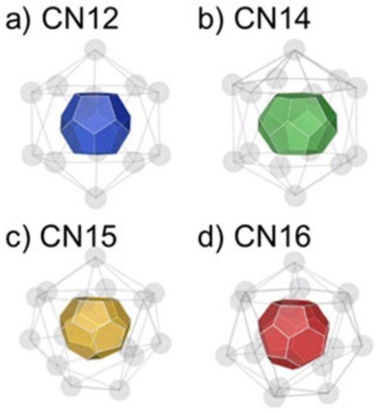

	CN12	CN14	CN15	CN16
Five vertex	12	12	12	12
Six vertex	0	2	3	4
Edges	30	36	39	42
Faces	20	24	26	28

Figure 3: Coordination polyhedra described by Frank and Kasper a) CN12 b) CN 14 c) CN15 and d) CN16 adopted and **reproduced with permission of Springer Nature** from [46, 47].

The formulated conditions for these geometric structures are [24]:

1. built up of flat layers and corrugated intermediate layers.

2. their gaps are exclusively tetrahedral.

3. the coordination polyhedra are triangulated, i.e. surrounded by triangular surfaces.

The configurations of the coordination polyhedra are illustrated in Figure 3. In total, all these polyhedra reveal 12 corners (CN12) with 5 vertices, whereas the CN12 does not include any other vertices. They have shown that besides the 5-fold corner, the 6-fold corner fulfil the condition of only having tetrahedral gaps as well. The following polyhedron types contain, in addition to the 12 corners with 5 vertices, one or more of higher coordinates, resulting in two 6-fold corners for the CN14 type to four 6-fold corners for the CN16 type. A CN13 polyhedron is not realisable because the concept of coordination number is based on the idea of nearest neighbours and in most cases, atoms tend to arrange themselves in a manner that maximizes their proximity to each other while minimizing space between them. Achieving a coordination number of 13 would likely involve a relatively unstable and strained configuration of atoms, making it less favourable from a thermodynamic perspective. This type of classification allows them to describe these Laves phase structures by using the CN16 Frank-Kasper polyhedron (also called Friauf-polyhedron) and CN12 polyhedron. Meaning the larger A atoms (visualised as the red atom in Figure 3) are positioned in the middle of the CN16 polyhedron and the smaller B atoms in the middle of the CN12 icosahedra. Considering the polyhedra to describe the stacking of the Laves phases, only the CN12 and CN16 are needed and listed in Table 1.

Table 1: Laves phase structures characterised by using the Frank-Kasper polyhedra taken from [48]:

Structure type	Atoms	CN12	CN16
*C*14: *hP*12- $MgZn_2$	12	8	4
*C*15: *cF*24- $MgCu_2$	24	16	8
*C*36: *hP*24- $MgNi_2$	24	16	8

This results in structures, where one A atom is surrounded by 4 A atoms and 12 B atoms whereas one B atom is surrounded by 6 A and B atoms. For all three prototypes, this stacking is shown in Figure 4, whereas the colour coding shows the larger A atoms in grey (CN16 prototype) and the smaller B atoms in red which are located on the 4f side, in pink on the 6h side, and in purple on the 6g side. With this visualisation the forming gaps based on the different stacking are observable.

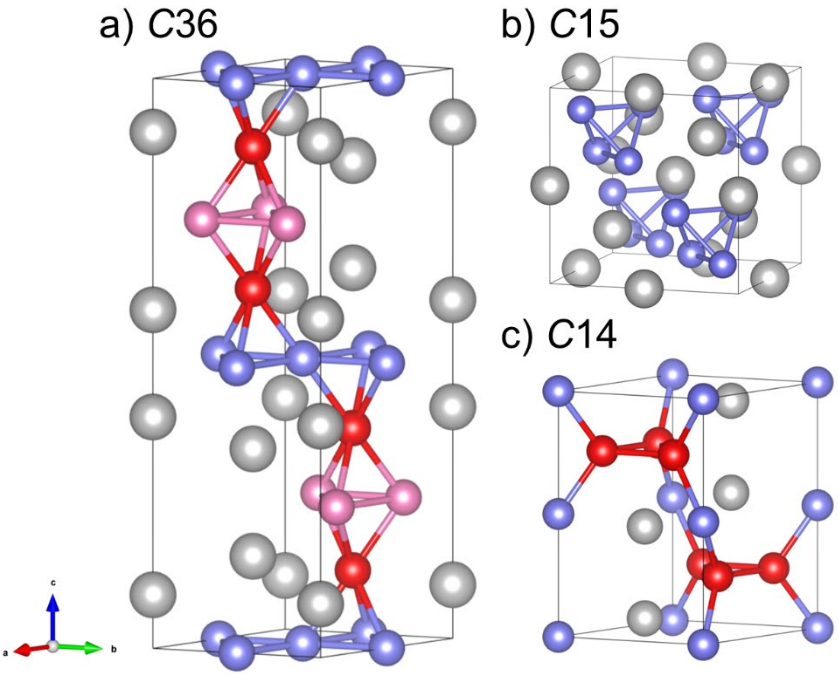

Figure 4: Laves phase prototypes a) *C*36, b) *C*15 and c) *C*14, with coloured atoms according to coordination polyhedra CN12 in red (4f), pink (6h) and purple (6g) and CN16 in grey, using VESTA [3].

The classification of all three Laves phase structure types, due to its layer stacking, is based on the variation of two different building blocks, which can be layered depending on the prototype. These AB_2 structures are built by stacking layers of atoms in a specific sequence. For the description of the stacking sequence, Frank and Kasper used the symbols Δ and ∇ to describe the orientations of the triangular stacking forming from the B atoms in its triangular net (Schläfli symbol '3^{6}') due to the different arrangements. In the case of AB_2 structures, this triangular layer is typically arranged in an alternating fashion built out of 3 layers, starting with a layer consisting of A atoms followed by a layer of B atoms and concluded with an additional layer of A atoms (displayed in Figure 5 b) and c) by using red circles for A atoms and green circles for B atoms).

However, the typical Laves phase layer is described as a quadruple layer, consisting of three different A-B-A layers forming the triangular net enclosed by two Kagomé layers (Schläfli symbol '3.6.3.6'). This Kagomé layer consists of B atoms, which are located at the corners of the six and three-cornered network (shown in green in Figure 5), arranged in a way that one hexagonal cell is surrounded by six triangular cells which in turn are surrounded by three hexagonal cells, like shown in Figure 5.

Take a closer look at this arrangement: the layering starts with the B atom Kagomé net at a height of 0, followed by the stacking of the triangular layer at a height of 3/8 with the bigger A atoms (shown in Figure 5 a)) lying in a triangular ordered way (3^6 net) in the middle of the hexagonal cells of the B atom Kagomé layer, followed by an additional 3^6 net layer of B atoms at the height of 1/2 shown in Figure 5 b) as red atoms and an additional 3^6 net at the height of 5/8 (Figure 5 b) as light red atoms) lying in the middle of the triangles, one layer in the upward tapering triangles and the other layer in the downward tapering triangles. This kind of layer can also exist in a reversed version shown in Figure 5 c). The typical quadruple layering starts with one of the three different Kagomé layers and follows with a triangle layer of A atoms, which are placed in the forming holes of the B atoms, and the next triangular layer of B atoms is arranged in the remaining fap of both structures. At last, it is capped with the A atom triangular layer, as shown in Figure 6. With some modifications, shown in Figure 6, the necessary layers to describe the stacking of the different Laves phase are given, and b) how the layers will be arranged. At last, the different stacking of these layers determines the resulting Laves phase structure.

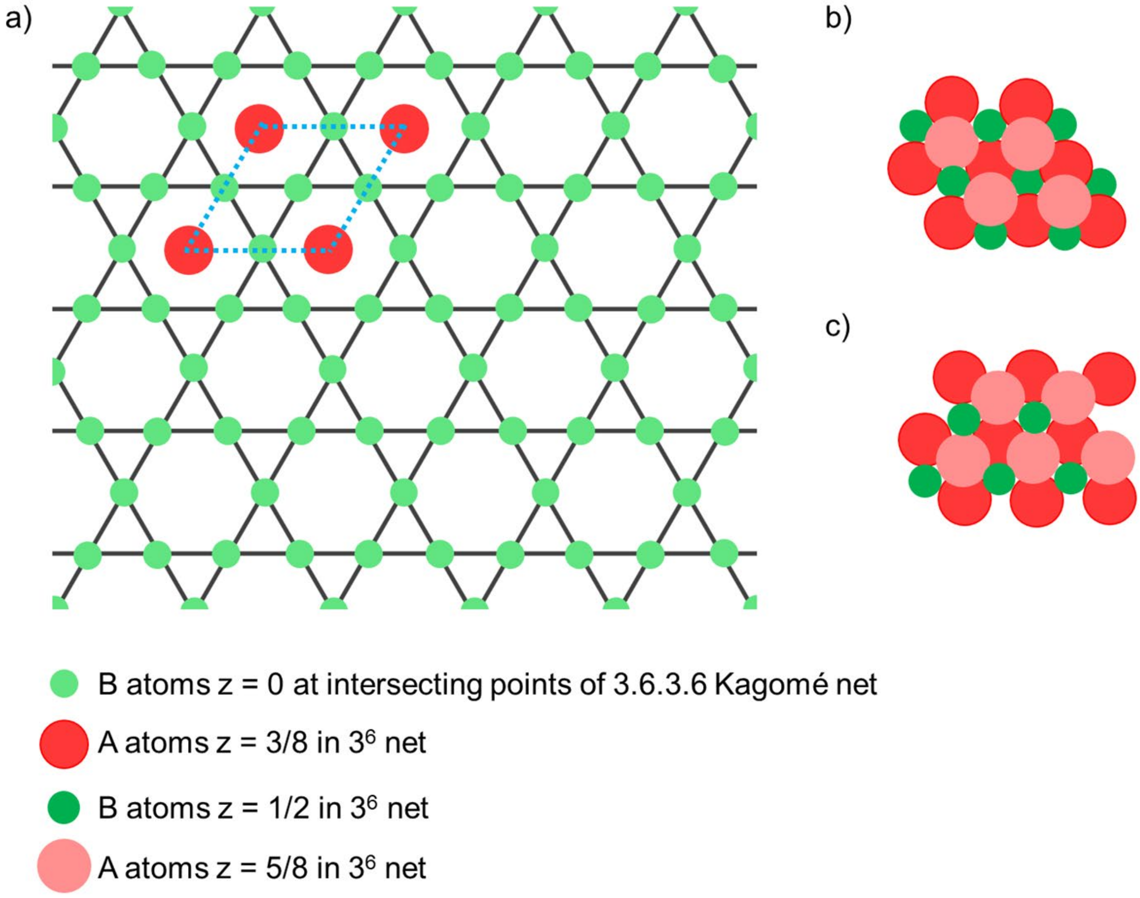

Figure 5: Structural arrangement of the layers of the Laves phase, showing a) the basic Kagomé layer built up with small B-atoms in purple and a systematic triangular A-atom net indicated by the blue atoms, in b) the triple layer and c) the reversed triple layer, whereby the different sized circles symbolise the A (larger) and B (smaller) atoms, and the color-coding shows the height of the atoms. Adopted and **reproduced with permission of the International Union of Crystallography** from [18, 44].

The layering visualised in Figure 6 is a modification of Komura et al.’s [17] description of the Laves phases’ stacking. For the explanation of the different Laves phases, six different kinds of quadruple layers were used: A, B, and C correspond to Frank and Kasper’s Δ, while A’, B’, and C’ belong to ∇. The different atom positions for the stacking of the layers are shown by A, B, and C, while the remaining layers show the mirrored atom positions. The layers exhibit always one Kagomé layer and three triangle layers. In his approach, Komura [17, 42, 43] shows the different layers that make it possible to describe the different TCPs, starting with the atom position 1/2 (B atoms triple layer), followed by 3/8 (A atoms), 0 (B atoms Kagomé) and finally -3/8 (A atoms). The modification starts with the Kagomé layer followed by the triple ones and giving each atom position fixed labels. The Kagomés are labelled using Greek letters (α, β, γ), while the larger atoms are donated by capital Roman letters (A, B, C) and the smaller ones with small Roman letters (a, b, c), like Komura already did, the A and A´ layering, just differ in terms of the location of the B atoms in the triangular layer (Table 2).

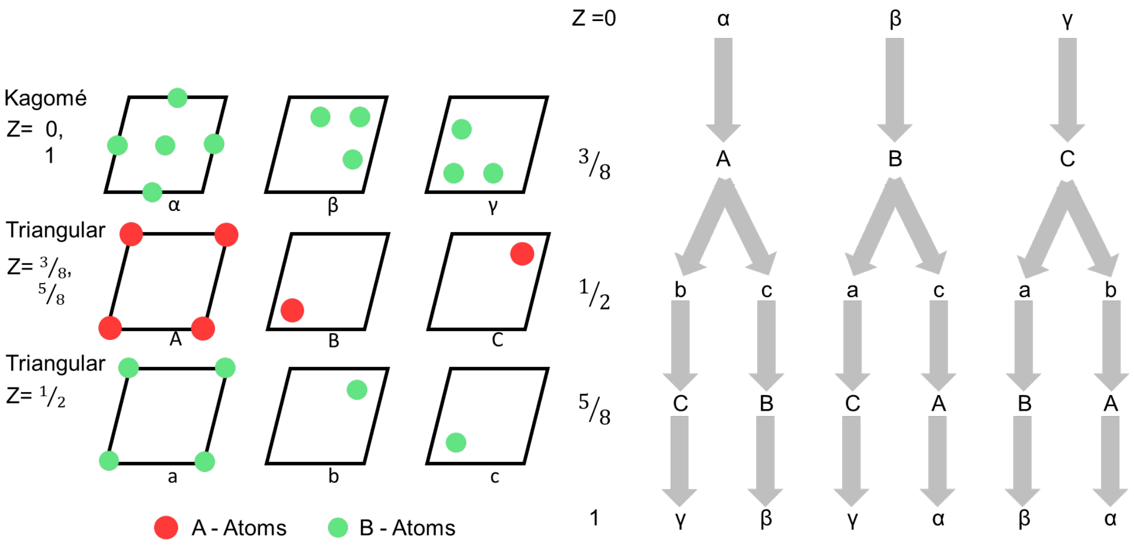

Figure 6: Different modified layers from Komura et al. [17] to explain the different types of stackings for the Laves phase, whereas the capital Roman letters (A, B, C) show the arrangement of the triangular net, the small Roman letters (a, b, c) show the triangular net for the B-Atoms and the Greek letters (α, β, γ) show the B atoms arranged in the Kagomé net. b) possible stacking sequence, with their arrangement given with coordination parameter Z. The figure is **reproduced with permission of the International Union of Crystallography.**

Using the modification shown in Figure 6, the different layers can be finalised by different layering shown in Figure 6 b) resulting in the stackings presented in Table 2.

Table 2: Stacking sequence of Laves phase prototypes [49].

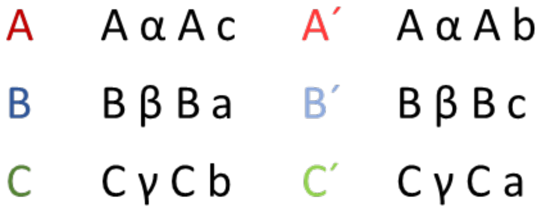

A	A α A c	A´	A α A b
B	B β B a	B´	B β B c
C	C γ C b	C´	C γ C a

The three prototypes can then be explained using these layers, as shown in Table 3. The *C*14 Laves phase consists of only two quadruple layers AB`, while the $MgCu_2$ *C*15 Laves phase consists of three quadruple layers ABC, and the $MgNi_2$ *C*36 Laves phase consists of four quadruple layers AB´A´C.

Over the past few years, there have been various descriptions of the different Laves phase stacking methods, the most popular of which are listed in in Table 3:

Table 3: Different ways to describe the stacking of the three Laves phase prototypes according to Pearson [4], Jagodzinski [14, 15], Komura [17], and Frank and Kasper [18].

Structure Prototype		Space Group	Stacking sequence resulting from Figure 6	Kagomé	Ramsdell symbols	Jagodzinski Wyckoff symbols	Komura	Frank Kasper
C14	$MgZn_2$	$P63/mmc$	…BβBaCγCa…	…βγ…	2H	…hh…	XY´	△▽
C15	$MgCu_2$	$Fd\bar{3}m$	…CγCbAαAcBβBa…	…αβγ…	3C	…ccc…	XYZ	△
C36	$MgNi_2$	$P6222$	…AαAcBβBcAαAbCγCb…	...αβαγ…	4H	…chch…	XY`Z`Y`	△▽▽△

2.1.2 Stability of the Laves phase structure

The stability of the forming Laves phases depends on various factors, such as the atomic size ratio of A and B atoms or the electron concentration, influencing the geometry of the forming phase, like the symmetry, space filling, and number of neighbours [50, 51]. Studies investigating the stability as a function of the ideal radii ratio of A and B atoms have shown that the phase width can differ from the ideal radius ratio of 1.225. In general, Laves phases can be found in a radius ratio of 1.05 – 1.70, whereas it is important to state, that the atomic radii of both atoms forming the Laves phase, will mostly deviate from the metallic diameter, which results from the accommodation if the atoms fit the ideal space filling for the lattice [4, 50, 52, 53]. By deviating from the ideal ratio, the structure reveals additional elastic strains and therefore reduces the bonding energy. Thoma's geometric analysis [54] revealed that the cubic system can reach wider phase widths between radii ratio from 1.10 to 1.35, whereas for the hexagonal systems, it is defined to lay between 1.12 and 1.26. Only 22% of the known *C*14 phases and 27% of the known *C*15 phases exhibit a solubility range. The measured solubility range is higher for a deviation from the ideal radius ratio to smaller atomic ratios, revealing additionally that for large ratios an excess of B atoms will be easier to build into the lattice. Figure 7 shows the results from a study of the relationship between the radius ratio and the formation enthalpy which revealed the most stable phase to be at R_a/R_b =1.225, which was correlated with the highest negative formation enthalpy depending on the bonding character, and can be explained due to the not necessary modifications of the atoms, by compression or expansion to fulfil the Laves phase criteria [5].

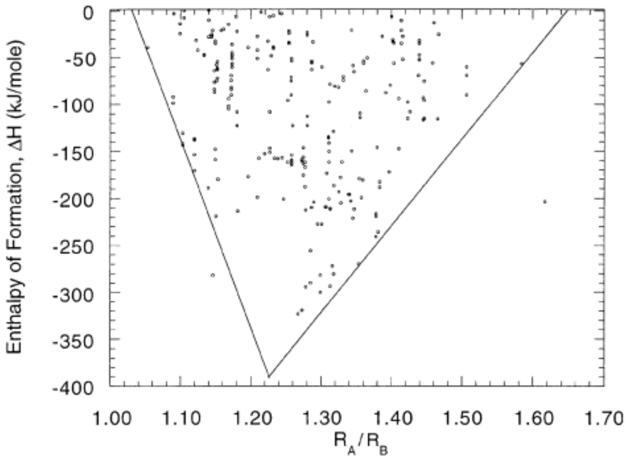

Figure 7: A thermodynamic interpretation of the size-ratio limits for laves phase formation (Enthalpy of formation vs r_A/r_B for binary Laves phases.) adopted from [5] **reproduced with permission of Springer Nature**.

The second main factor is the valence electron configuration (VEC) which is defined for Laves phases as the average number of valence electrons (VE) per atom 'e/a' [18, 44, 57, 58]. These dependencies were often investigated using pseudo ternary Laves phases, which describe a stable binary Laves phase in a ternary region. The first studies indicated the importance of this parameter to predict the forming structure type, especially between the cubic *C*15 and the hexagonal *C*14 phase, which were done by Laves and Witte, investigating pseudo ternary $MgCu_{2-x}Zn_x$ systems, where the structure types change from *C*15 → *C*36 → *C*14 with increasing x and electron concentration [59]. To investigate the electronic density of state (DOS), a band calculation, done by Nesper et al. [60], showed the influence of the number of VE of the observed element and structural disorder on the stability of Laves phases, taking the Hückel tight binding band-structure analysis of the covalent bonds. Instead of the cubic phase, the hexagonal stacking sequence along the Kagomé layer shows two possible electron configurations: the trigonal bipyramid B5 and the tetrahedral B4, have been compared and reveal more free electrons [61]. His investigations were done on the Ca-Al-Li system. With increasing Al content in $CaAl_{2-x}Li_x$, the hexagonal $CaLi_2$ phase is formed, followed by the formation of the $Ca(Li,Al)_2$ phase, which is 50% hexagonal and 50% cubic stacking, and finally, the cubic $CaAl_2$ phase is formed. For this transformation the VE change from 4 to 8 as visible in Figure 6. Additionally, Amerioun et al. [55, 56] also investigated the stability of pseudo-binary Laves phases, which are capable of forming all three Laves phase types by the substitution of atoms, as described for the Mg-Al-Ca system and the Ca-Al-Li system [55, 56, 60], showing the effect of changing VEC, and the response of the structure on the change of compositions, visible in Figure 8.

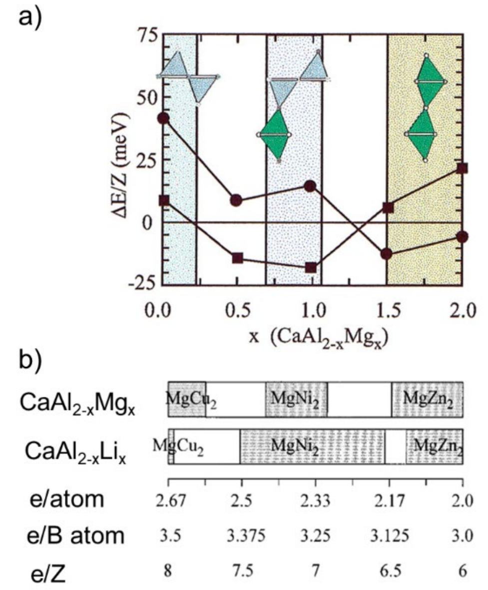

Figure 8: Difference between the structural energy of $MgCu_2$, $MgZn_2$, and $MgNi_2$, across the investigated range for $CaAl_{2-x}Mg_x$ and $CaAl_{2-x}Li_x$ calculated by Amerioun et al. [55, 56]. **Reprinted with permission from Laves-Phase Structural Changes in the System $CaAl_{2-x}Mg_x$. Copyright 2003 American Chemical Society.**

Further investigations by Amerioun et al. [55] for the $CaAl_{2-x}Mg_x$ system show that the phase stability correlates with the VEC. As the $CaAl_{2-x}Li_x$ system, the highest e/a ratio corresponds to the cubic *C*15 and the lowest one to the hexagonal *C*14 phase. Differences are in the phase widths, especially for the *C*36 phase, revealing a higher spectrum for the $CaAl_{2-x}Li_x$ phase.

A study on Nb-Cr_2 based alloys clearly shows that the e/a ratio affected the *C*14/*C*15 stability [58]. Furthermore, Zhu et al. [62] have found that no stable state for the *C*36 phase was detected on their pseudo-binary systems with transition metals. However, the occurrence of *C*36 in the two-phase regime (between the change from *C*14 → *C*15) could not be excluded due to its similarity to the hexagonal phase. The system $Nb(Cr,Co)_2$ changed with increasing Co from *C*15 → *C*14 → *C*15, out of which the *C*14 state was the most stabilised and the other pseudo-binary $Nb(Cr,Fe)_2$ by the substitution of Cr with Fe only revealed the *C*15 → *C*14 transition.

Finally, temperature is also a key parameter for the stability of the forming phase. In systems containing *C*14 and *C*15 Laves phases, Sauthoff et al. [63] stated that, beside the VEC and the radius ratio, the temperature determined the stable phase, whereas for ratios below the ideal *C*14 stabilised at higher temperatures, and *C*15 only at lower temperatures. The transition between these two phases is not clearly defined but takes place more gradually. The *C*36 phase, which is a combination of *C*14 and *C*15, can thus be found at intermediate temperatures [64, 65]. The transformation is believed to occur via shear which is controlled by temperature dependent dislocation mobility. Often this transition from metastable *C*14 to stable *C*15 during annealing must undergo a diffusion process for the shearing to take place [65].

2.2 Dislocation behaviour

Plasticity in materials is achieved by the movement of dislocations within the crystal lattice. Especially, for the material investigated in this thesis, the intermetallic phases, the intrinsic resistance against lattice motion is relatively high compared to face-centred cubic (fcc) alloys. Caused by their comparable large unit cells and their topological closed packed structure resulting in a higher macroscopic brittleness at temperatures below the BDTT.

Dislocations are structural line defects in the crystal structure where the regular arrangement of atoms is disrupted along a line and can be classified based on their line element (g) and Burgers vector (b). When external stress is applied, dislocations can move, allowing the material to undergo plastic deformation without breaking. This dislocation motion is crucial for the material's ability to change shape permanently, and the force that makes this motion possible is defined as lattice resistance. The first fundamentals about the dislocation motion were presented by Peierls in 1930 in his work ‘The size of a dislocation’ [66].

In his work Peierls formulate the needed stress to move an edge dislocation in a simple cubic system at 0 K. The now following explanation will combine the initial statement from Peierls [66] and the modified Peierls analysis from Clegg et al. [11] which allows a clearer visualisation of the process. Therefore, the concept was simplified by considering a simple cubic structure, one edge dislocation, and two half crystals with the same in-plane distance b.

By taking two crystal halfs, half A and B, whereas half A revealed one additional slip plane inserted vertically (the total difference of both planes is 1b), shown in Figure 9 in pink, placing both symmetrically to each other, meaning half A has an overlap of b/2 on each side (Figure 9). The distance between the atoms of crystal half A and B should be b/4, whereas the deviation from this value is reached where the half plane is inserted (most distortion, which faded with the distance from it). This results in deviating atom positions, whereas for A the atoms are arranged horizontally along x with:

$$x_A = n \cdot b \tag{1}$$

$$x_B = n \cdot b \pm \frac{b}{2} \tag{2}$$

shown in Figure 9.

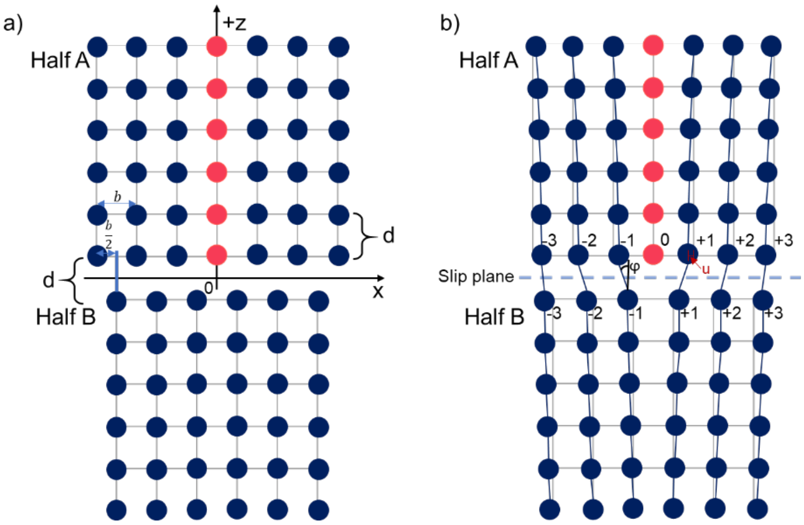

Figure 9: a) Schematic sketch of the alignment of the two half crystals with the same in-plan distance b spacing and lattice distance d, aligned shifted by b/2 to each other. b) Shows the misalignment φ due to the additional plane in crystal A with the additional in-plane displacement u. Based on [67] **reproduced with permission of Elsevier**.

To be able to determine the needed stress, first the displacement of the atoms due to the shortening and lengthening of the interatomic bonds in the crystal half itself and across the slip plane (connecting the atoms of half A and half B) distorted by the additional slip plane in half A, must be clarified. The displacement is visible in Figure 9 b), where the atoms of crystal half A tend inwards and these of crystal B backwards. These can be described taking the resulting misalignment angle φ and the corresponding distance u, which can be added to the atomic distance d (Figure 9 b)). With the arctan function the displacement can be calculated:

$$u_a = -k \cdot \tan^{-1}\left(\frac{x_a}{\omega}\right) \tag{3}$$

$$u_b = k \cdot \tan^{-1}\left(\frac{x_b}{\omega}\right) \tag{4}$$

k Constante

ω Dislocation half-width

With the defined distortion the associated energies can be formulated: The in-plane displacement, resulting due to the shortening and lengthening of the interatomic bonds within each crystal half, which also is equal to the stored elastic energy per volume under uniaxial deformation, and can be express by taking this (5) combined with Hook's law (6) resulting in (7):

$$U_{el} = \frac{1}{2} \cdot \sigma \cdot \varepsilon \tag{5}$$

$$\sigma = E \cdot \varepsilon \tag{6}$$

$$U_{el} = \frac{1}{2} \cdot E \cdot \varepsilon^2 \tag{7}$$

The Young’s Modulus, can be facilitated due to the fact of only applying stress in one directions, coming up to:

$$U_i = \frac{1}{2} \frac{E}{(1 - \nu^2)} \varepsilon^2 (b \cdot d) \tag{8}$$

E	Young’s Modulus
G	Shear Modulus
ν	Poisson Ratio
ε	Strain
δ	Atom deviation from initial position
b	Burgers vector
d	Lattice spacing

The strain ε can be expressed by the deviation from the original distance between two atoms δ, resulting in:

$$\varepsilon = \frac{\delta}{d} \tag{9}$$

However, the relationship between the E, G and ν can be taken as:

$$G = E \cdot \big(2 \cdot (1 + \nu)\big) \tag{10}$$

where some facilitations were made by assuming here a simple uniaxial deformation in x direction.

$$U_i = \frac{1 + \nu}{(1 - \nu^2)} \cdot G \cdot \frac{d}{b} \cdot \delta^2 \tag{11}$$

The second energy results due to the distortion across the slip plane, connecting half A and half B, the misalignment displacement, which were previously described by Frenkel [68], who investigated the critical stress to plastically extend or shear a crystalline body before it tends to yield, with the assumption of two planes in an elastic equilibrium, coming up with the definition of the theoretical shear stress τ_{theo}:

$$\tau_{theo} = \frac{G \cdot b}{2\pi \cdot d} \sin\left(\frac{2\pi x}{b}\right) \tag{12}$$

Transferring this approach to the energy associated with the motion of the additional half plane, it results in

$$U_X = \frac{G \cdot b^3}{4\pi^2 \cdot d}\left[1 - cos\left(\frac{2\pi\varphi}{d}\right)\right] \tag{13}$$

Especially the misalignment displacement is the critical value which tend to constrict the motion of the dislocation through the crystal. This can be seen in Figure 10, where the misalignment displacement increases with the increasing ω/b ratio, whereas the in-plane displacement tends to spread the dislocation and decreases with increasing ratio. The sum of both results in the total misfit energy U_T, with the lowest energy and stable position if the dislocation width w, defined by the half-width of the dislocation, is approximately equal to b.

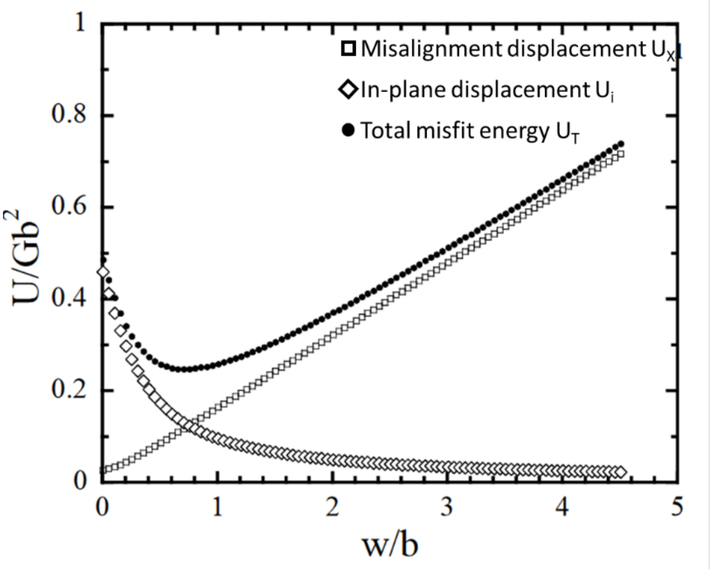

Figure 10: Total misfit energy U_T arises from the misalignment of atoms in a crystal lattice due to dislocations, with the total misfit energy being the sum of these contributions. It quantifies the overall energy cost of dislocation presence. The misalignment potential U_X measures the energy needed to overcome the atomic misalignments associated with dislocations and represents the barrier for dislocation movement through the lattice. The in-plane potential U_i denotes the energy barrier within the crystal plane, reflecting the resistance of the lattice to dislocation motion. Adopted from [9].

This shows that w directly is influenced by the d/b ratio. When the lattice has a small d/b ratio, the atoms are arranged close to each other and the inner planar atom spacing b is larger than the lattice spacing d, which goes hand in hand with a comparatively lower w, and a higher distortion of the bond between A and B (e.g. diamond) than when the lattice has a higher d than b (e.g. fcc copper), where more bonds between A and B are involved in the distortion. So those with a lower d/b ratio result in a radical increase in misfit energy and therefore the dislocation motion requires more energy to move, as seen by the increasing misalignment potential.

If a dislocation now moves a certain distance, the new atomic position u_A or u_B can be determined using a geometric relationship, as a function of the way coordinate x:

$$u_A(x) = -\frac{b}{2\pi}\tan^{-1}\left(\frac{x_A}{w}\right) \; and \; x_A = n \cdot b - \alpha \cdot b \tag{14}$$

$$u_B(x) = -\frac{b}{2\pi}\tan^{-1}\left(\frac{x_B}{w}\right) \; and \; x_B = n \cdot b + \frac{b}{2} - \alpha \cdot b \tag{15}$$

w dislocation width
α moved distance

For the dislocation motion through the crystal lattice Figure 11 illustrates the changes in energies. The total distance is 1, lying between α = 0.5 and α = -0.5. This results in 3 energy states, where all three displayed energies revealing a value of zero, reached at α = -0.25, α = 0 and α = -0.25.

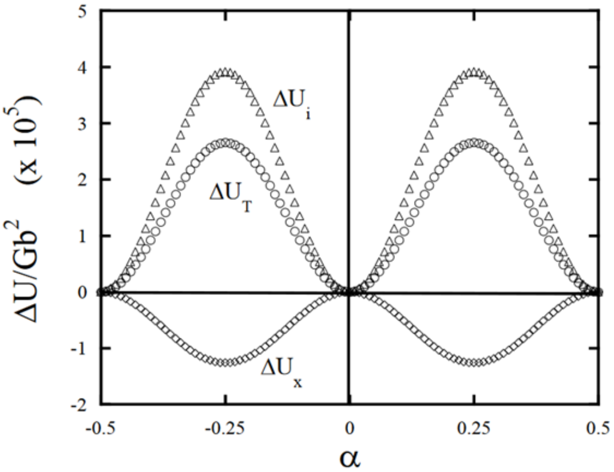

Figure 11: Schematic illustration of the resulting energies when a dislocation moves along x, here α, taken from [9, 11].

The three minima resulting from having first the initial position, where the arrangement from Peierls is given (Figure 9), the resulting minimum, reflecting the state in which the extra half plane moved by 1/2·a, whereas the atoms just moved by b/6. With the next step, overcoming the new maximum, giving the state, where the extra half plane is moved by another 1/2·a and the atoms are now totally shifted by b/3. The maxima reached at α = ±0.25 are equal to this which has to be travelled to move the dislocations and equal to the height of needed external stress which have to be overcome move the dislocation. This shown as ΔU_T, whereas the emerging maximum total misalignment energy ΔU_X cause the main part of the lattice resistance. Coming up to the so-called Peierls stress:

$$\tau_P = \left[\frac{2G}{1-\nu}\right] exp^{\left(-\frac{2\pi}{1-\nu}\cdot\frac{d}{b}\right)} \tag{16}$$

2.2.1 Thermal influence on plasticity

Now the estimation from Peierls defined the needed stress which has to be overcome to move a dislocation through the crystal at 0 K, which we call the Peilers barrier. But to widen up his approach and transfer this to even higher temperatures, whereas also room temperature is a gain of +273.15 K, the flow stress must be calculated. Now we will have a look at how dislocation movement behaves with increasing temperature, as this plays a crucial role in determining the mechanical properties and behaviour of materials, including their plasticity, especially for materials that exhibit high intrinsic resistance against dislocation motion due to the processes of bond breaking and reformation [69]. As temperature rises, thermal activation facilitates the overcome of this barrier for a dislocation by lowering the effective stress required to move a dislocation [70]. This reduction of the effective required stress results due to the start of lattice vibration of atoms in the crystal lattice (function of temperature). With the vibration, some of the atoms will be vibrate in the direction of the Peierls barrier. If these random vibrations happen to cause adjacent atoms to move in the same direction as the Burgers vector of a nearby dislocation, these atoms can surpass the Peierls barrier at lower applied stresses, thereby reducing the yield stress. And by overcoming the barrier, they will pull the atoms on their dislocation over, by contracting the line. This phenomenon is commonly referred to as the double-kink or kink-pair mechanism, where both kinks can interact with each other at short

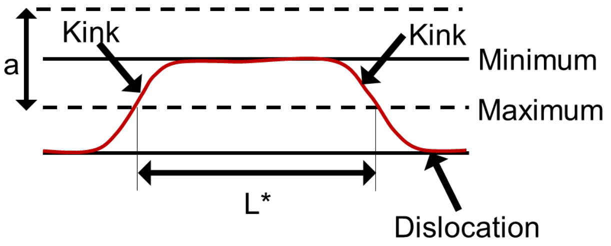

Figure 12: Schematic illustration of the kink-pair mechanism. Based on [2] and **reproduced with permission of Springer Nature.**

range when neighbouring atoms move cooperatively in the same direction as the dislocation [71]. Additionally, with increasing temperature the backwards jumps will be more challenging, directly facilitating the forward motion of atoms.

For the calculation of the flow stress, some previous calculation has to be done, like the speed of a dislocation, which can only be expressed by the overall deformation. The motion of a dislocation causes shear, so the shear per unit time must be estimated. This was first described by Orowan [72], using the shear strain rate $\dot{\gamma}$:

$$\dot{\gamma} = \rho_m \cdot b \cdot v \tag{17}$$

$\dot{\gamma}$	shear strain rate
ρ_m	mobile dislocation density
b	Burgers vector
v	dislocation velocity

The velocity of a dislocation is defined as the jump distance times the number of successful jumps divided by the taken time. This also can be expressed with the distance as the resulting Burgers vector times the Debye frequency ν_A $(10^{13}\ s^{-1})$ describing the vibration energy, which leads the dislocation to overcome and the probability of the successful jumps (ΔG). The strain rate can be formed into the equation:

$$\dot{\gamma} = \rho_m \cdot b \cdot \nu_A \cdot exp^{\left(-\frac{\Delta G}{kT}\right)} \tag{18}$$

$$\dot{\gamma} = \dot{\gamma_o} \cdot exp^{\left(-\frac{\Delta G}{kT}\right)} \tag{19}$$

ΔG	energy barrier
k	Boltzmann constancy
T	temperature

The probability of a successful jump ΔG depends on the lowering the Peierls barrier, ΔF, due to the lattice vibration. The reduction can be defined by the term:

$$n \cdot \tau \cdot b^3 \tag{20}$$

Knowing, that n = 1, because of the tiny number of atoms, and that b3 describes the activation volume V, the probability can be associated with:

$$\Delta G = \Delta F - \tau \cdot V \tag{21}$$

Resulting in:

$$\dot{\gamma} = \rho_m \cdot b \cdot \nu_A \cdot exp^{\left(-\frac{\Delta \mathrm{F} - \tau \cdot V}{kT}\right)} \tag{22}$$

To calculate the critical shear stress for the dislocation motion in the next step, this newly defined shear strain rate can be taken and inserted into equation (5), and be reformed by knowing, that the term defining the critical applied shear stress to move a dislocation is the Peiers stress τ_P in the equation:

$$\tau_C(T, \dot{\gamma}) = \frac{\Delta G_0}{V} + \frac{k \cdot T}{V} \ln\left[\frac{\dot{\gamma}}{\rho_m \cdot b^2 \cdot \nu_A}\right] \tag{23}$$

$$\tau_C(T, \dot{\gamma}) = \tau_P + \frac{k \cdot T}{V} \ln\left[\frac{\dot{\gamma}}{\rho_m \cdot b^2 \cdot \nu_A}\right] \tag{24}$$

Thermal activation can also involve the diffusion of vacancies (missing atoms) in the crystal lattice [2, 69, 70, 73]. At elevated temperatures, vacancies become more mobile, leads to an increase of the dislocation velocity (Orowan relation → equation (17)) and further in a higher strain rate. Moreover, vacancies will rise and migrate to dislocation cores, additionally facilitating the movement of dislocations by providing additional pathways, meaning edge dislocations can climb and cross-slip gets facilitated. Due to the increased mobility dislocations, the thought of an easy deformation way could be expected, but this would result in only having soft materials at higher temperatures, which is not the case. This is grounded in the different kinds of additional obstacles limiting the dislocations moving freely through the crystal lattice. There it can be distinguished between discrete and extended ones, where the first one is correlated with strong to medium strength and the second with weaker strength. The weaker are characterised by the lattice friction and small precipitates, which can be overcome easier with the help of thermal activation. With higher temperature not only dislocations get more mobile, additionally a higher phonon drag force results, because of the increasing lattice vibration and the increasing phonon population [74]. If now the dislocations tangled with each other and need therefore more stress to get remobilised it is called work hardening. Discrete obstacles must be bypassed or cut, which can be solute atoms, precipitates or dispersions. Solute atoms could lie between the regular or at the regular lattice places, mostly revealing a different atomic radius than the substituted atom, leading to a distortion, and hinder the dislocation in its motion. To continue the dislocation motion, the pinned dislocation needs more stress to rid free from the obstacles, which can occur for example with more externally applied stress or higher temperature, this is called solid solution strengthening [75, 76]. If the solute atom diffuses during the deformation to the dislocation and pinned it, the force which is needed to remobilise the dislocation is greater than the force that is required for an unpinned one to move forward, which can be seen in the stress-strain curve as a serrated flow [75, 77-79]. Especially, the size of the obstacle is the critical values. If obstacles exhibiting larger scales thermal activation gets ineffective, and the external stress must be lower than the critical stress to create an additional surface, resulting in cracking instead of deformation. As the strain rate now increases (the dislocation velocity increases) and the temperature remains unaffected, the time for the solute to diffuse and pin a dislocation decreases to a value lower than the dislocation velocity, resulting in a less pronounced solute drag effect. This can lead to a situation where the flow stress decreases with increasing strain rate resulting in a negative strain rate dependency [80]. Therefore, the solute drag effect can influence the strain rate sensitivity of materials. Materials with a significant solute drag effect exhibit a lower strain rate, whereas solute atoms have more time to interact with moving dislocations are able to pin more dislocations leading to higher yield strength and lower ductility, as dislocations are less mobile [77].

2.2.2 Stacking faults

The motion of perfect dislocations has been discussed in the previous chapters, where a dislocation, induced by overcoming the Peierls barrier on a specific slip plane, moves in a specific direction. Especially, the activated slip system exhibits the lowest stress required to overcome the lattice friction, which mostly corresponds to the shortest lattice vector and the highest packed plane, such as {111} for fcc or [0001] for hexagonal close packed (hcp), which can be determined by orientation factors (Schmid factor: how the slip system is oriented concerning the applied stress). This motion leads to a lattice distortion, which can be described as a vector pointing from a reference point in the perfect lattice to a corresponding point in the distorted lattice. Visualising the Burgers vector by drawing its Burgers circuit, resulting in an additional step to close this loop compared to the perfect lattice, this deviation characterises the Burgers vector. As shown by Peierls, the d/b ratio is the key parameter that determines the stress needed to overcome the barrier to allow a dislocation to move through the crystal lattice. This can be influenced by lowering the energy of the Burgers vector, which is often observed for systems that exhibit low stacking fault energy (SFE). Here, the dislocation motion is energetically more favourable by splitting one perfect dislocation into two partials, into dislocations in two alternating directions, following the Frank criterion [81]. For example, for the fcc on the {111} plane, in two <112> directions:

$$|\vec{b}| \rightarrow |\vec{b_1}| + |\vec{b_2}| \tag{25}$$

$$\frac{1}{2}\,[\bar{1}01] \rightarrow \frac{1}{6}\,[\bar{2}11] + \frac{1}{6}\,[\bar{1}\bar{1}2] + \gamma_{SF} \tag{26}$$

γ_{SF} stacking fault energy

This type of stacking fault (SF), called intrinsic SF, results in an interruption of the perfect stacking sequence of the fcc, which is characterised by its continuously repeating ABC sequence and, for hcp, the ABAB sequence. The perfect sequence is a continuous repetition of 'ABCABC' and it may change to 'AB***ABCA***' while the italics part shows the change in stacking order. This change shows that the new stacking order is similar to the hcp stacking order. Besides these intrinsic stacking faults, the stacking sequence can be changed by adding an additional layer, called extrinsic SF, which will form 'AB***A***CABC', as shown in Figure 14 b).

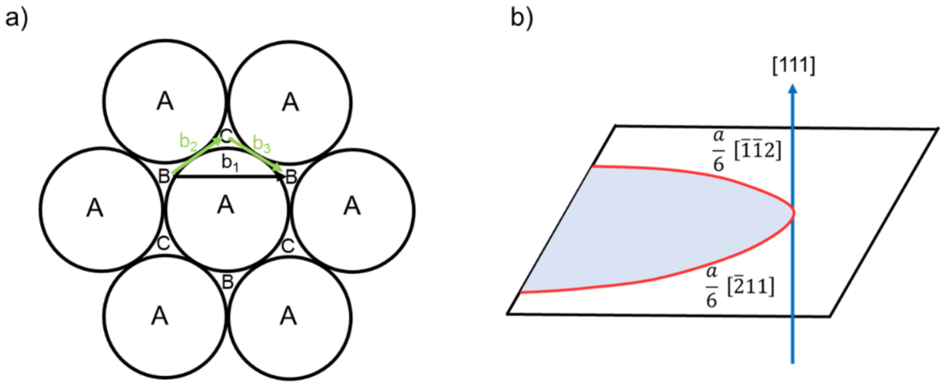

Figure 13: SF process in the fcc lattice, a) shows the dislocation dissociation of $\vec{b}_1$ → $\vec{b}_2$ + $\vec{b}_3$, b) with light blue the hcp stacking is implied. Adopted from [82]. and **reproduced with permission of Springer Nature**

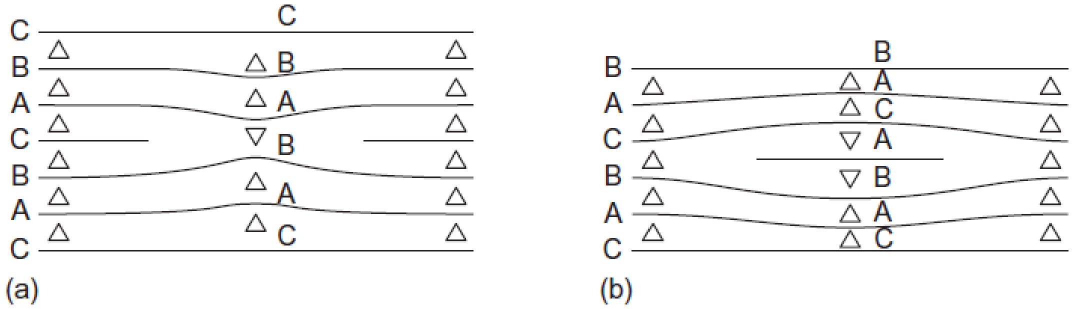

Figure 14: Difference between a) intrinsic and b) extrinsic stacking fault or double SF, taken from [1], **reproduced with permission of Elsevier**.

2.2.3 Plasticity of Laves phases

First investigations on Laves phases, mainly performed on the *C*14 Laves phase prototype $MgZn_2$ by the German 'Forschungsgruppe' in Dresden in the early 1900er, stated that the Peierls mechanism is responsible and the control parameter for the dislocation motion [19, 83-86]. Laves phases exhibit high intrinsic resistance against lattice motion due to the TCP structure, leading to a very small d/b ratio and therefore getting the higher resistance for dislocations to move from the structure itself, and are therefore macroscopically brittle below the BDTT. For these phases this temperature varies between 0.6-0.7$\cdot T_M$. [12, 19, 87, 88] Previous studies of the resulting plasticity have therefore mostly been carried out above this temperature by using the effect of temperature depending on enhancement of the dislocation motion against this lattice resistance, which make macroscopic analysis of mechanical properties, deformation, surface analysis, post mortem TEM (take a deeper look at the deformed structure, analysing the resulting plasticity) possible.

An often-proposed mechanism taking place at higher temperatures is the so called 'synchroshear' mechanism (explained in more detail in: 2.2.4 Stacking faults in Laves phases: Synchroshear mechanism) [23, 89-92]. By establishing the nanomechanical deformation of materials by procedures like nanoindentation tests and micropillar compression tests, plasticity can be locally introduced to these TCP phases below the BDTT.

This allows the characterisation of these phases to be widened and analysed in more detail, starting with the room temperature plasticity. In the following section, a small literature review will give an overview of the previous investigations of the analysed *C*15 Laves phases in terms of plasticity and where labelled with '*', mechanical properties of the CRSS for the micropillar compression test, hardness evaluated by nanoindentation and indentation modulus, are also listed in Table 6.

Table 4 shortly summarise the found slip planes with slip directions from previous studies.

Table 4: Review of *C*15 plasticity, with their corresponding temperature and the "*" labelled, also have CRSS.

Slip system	**Laves phase**	**Temperature**	***Homologous Temperature***
$\{\mathbf{111}\}\frac{\mathbf{1}}{\mathbf{2}}\langle\mathbf{1\bar{1}0}\rangle$	*C*15 [93]	Geometric analysis	
	$MgCu_2$ [83]	650 – 930 K	0.61 – 0.88
	$Fe_2(Dy,Tb)$ [94]	1145 K	0.70
	HfV_2 [95, 96]	570 K	0.40
	$NbCr_2$ [97, 98] *	298 K	0.16
	$NbCo_2$ [99-101] *	298 K	0.17
$\{\mathbf{101}\}\langle\mathbf{010}\rangle$	*C*15 [93]	Geometric analysis	
$\{\mathbf{110}\}\langle\mathbf{1\bar{1}0}\rangle$	$MgCu_2$ [83, 102]	650 – 930 K	0.61 – 0.88
$\{\mathbf{111}\}\langle\mathbf{112}\rangle$ **Twins**	HfV_2 [95, 96]	298 K	0.17
$\{\mathbf{111}\}\frac{\mathbf{1}}{\mathbf{2}}\langle\mathbf{\bar{1}\bar{1}2}\rangle$	$NbCr_2$ [103-106]	1570 – 1600 K	0.81 – 0.87
	$NbCo_2$ [99-101] *	298 K	0.17

The main plasticity was found for the *C*15 Laves phase on the {111} triple layer, which also confirms previous assumptions about dislocation-driven deformation on the close-packed planes. This was given by macroscopic and nanomechanical induced deformation tests, starting at 0.61-0.88·T_M. Krämer et al. [93] suggested in 1968 that the {112} plane would also be the next favourable plane for $\frac{1}{2}\langle 1\bar{1}0\rangle$ dislocations, with the explanation of the less densely packed {111} plane comparable to the fcc lattice. Moreover, plasticity with $\frac{1}{2}\langle\bar{1}\bar{1}2\rangle$ partial dislocation was additionally found to be activatable on RT and at higher temperatures.

The plasticity of the *C*14 Laves phase is briefly summarised in Table 5, in terms of slip systems and where labelled with ‘*’, the mechanical properties of the CRSS for a micropillar compression test, hardness evaluated by nanoindentation and indentation modulus, are also listed in Table 6.

Table 5: Review of *C*14 plasticity with its corresponding temperature and where “*”-labelled also the CRSS for that specific slip system, mostly also the indentation modulus.

Slip system	**Laves phase**	**Temperature**	**Homologous Temperature**
$\mathbf{\{0001\}\frac{1}{3}\langle 11\bar{2}0\rangle}$	*C*14 [93]	Geometric analysis	
	$MgZn_2$ [83]	520 – 770 K	0.61 – 0.90
	Nb(Fe,Ni)$_2$ [74] *	298 K	0.17
	$NbCo_2$ [99, 100] *	298 K	0.17
	$CaMg_2$ [6, 8] *	298 K	0.3
$\mathbf{\{0001\}\frac{1}{3}\langle 10\bar{1}0\rangle}$	*C*14 [93]	Geometric analysis	
	$NbCo_2$ [99, 100] *	298 K	0.17
$\mathbf{\{10\bar{1}0\}\frac{1}{3}\langle \bar{1}2\bar{1}0\rangle}$	*C*14 [93]	Geometric analysis	
	$MgZn_2$ [83]	770 K	0.90
	$NbCo_2$ [99, 100] *	298 K	0.17
	$CaMg_2$ [6, 8] *	298 K	0.30
$\mathbf{\{10\bar{1}0\}\langle 0001\rangle}$	*C*14 [93]	Geometric analysis	
	$CrTa_2$ [107] *	298 K	0.13
$\mathbf{\{11\bar{2}0\}\langle 1\bar{1}00\rangle}$	*C*14 [93]	Geometric analysis	
	$CrTa_2$ [107] *	298 K	0.13

$\boldsymbol{\{\bar{1}101\}\frac{1}{3}\langle\bar{1}2\bar{1}0\rangle}$	*C*14 [93]	Geometric analysis	
	$MgZn_2$ [83]	820 K	0.95
	$NbCo_2$ [99, 100] *	298 K	0.17
	$CaMg_2$ [6, 8] *	298	0.30
$\boldsymbol{\{11\bar{2}2\}\frac{1}{3}\langle\bar{1}\bar{1}23\rangle}$	*C*14 [93]	Geometric analysis	
	$MgZn_2$ [83]	770 – 820 K	0.90 – 0.95
	$CaMg_2$ [6, 8] *	298 K	0.30
	$CrTa_2$ [107]*	298 K	0.13

The resulting *C*14 Laves phase plasticity shows that the predicted slip planes from the geometric analysis of Krämer et al. [93] were found for nanomechanical deformation tests at room temperature and most also for high temperature investigations above the BDTT. This could be based on additional deformation mechanisms that have been thermally facilitated.

To find a reasonable method to compare macroscopic and nano induced plasticity, the theoretical shear stress can be used, which can be calculated for the nanoindentation tests by dividing the CRSS by the shear modulus (= normalised CRSS).

For this case, E is the indentation modulus. In this way, the resulting plasticity can be compared with other Laves phases by comparing the plasticity on the same plane, such as the triple layer $\{111\}_{cub}$ and $\{0001\}_{hex}$.

Table 6: Calculated CRSS/G values for some given Laves phases, using equation (10) for the calculations, for a specific temperature and slip system.

Structure	$\frac{T}{T_M}$	**Slip system**	CRSS	**Indentation Modulus [GPa]**	$\frac{CRSS}{G}$
***C*14 $NbCo_2$ [99, 100]**	0.17	$\{0001\}\langle 1\bar{1}00\rangle$	2.6	273	0.024
		$\{0001\}\langle 11\bar{2}0\rangle$	2.7	273	0.025
		$\{1\bar{1}00\}\langle 11\bar{2}0\rangle$	2.6	273	0.024

		$\{10\bar{1}1\}\langle 10\bar{1}\bar{2}\rangle$	2.5	273	0.023
***C*14 CaMg$_2$ [6, 8]**	0.30	$\{0001\}$	0.52	55	0.023
		$\{10\bar{1}0\}$	0.44	55	0.020
		$\{\bar{1}101\}$	0.53	55	0.024
		$\{11\bar{2}2\}$	0.59	55	0.027
***C*14 CrTa$_2$ [107]**	0.13	$\{10\bar{1}0\}\langle 0001\rangle$	5.1	232 [108]	0.055
		$\{11\bar{2}0\}\langle 1\bar{1}00\rangle$	6.1	232	0.065
		$\{11\bar{2}2\}\frac{1}{3}\langle\bar{1}\bar{1}23\rangle$	5.8	232	0.062
***C*15 NbCo$_2$ [99-101]**	0.17	$\{111\}\langle 1\bar{1}0\rangle$	3.2	290	0.027
		$\{111\}\langle 11\bar{2}\rangle$	3.0	290	0.026
***C*15 NbCr$_2$ [97, 98]**	0.15	$\{111\}\frac{1}{2}\langle 1\bar{1}0\rangle$	4.4 – 4.6	292 [108]	0.047

Previous studies [92, 109, 110] have conducted theoretical investigations of plastic deformation along structurally similar basal and {111} planes in the *C*14 CaMg$_2$ and *C*15 CaAl$_2$ Laves phases using atomistic simulations. In the *C*14 CaMg$_2$ Laves phase, it was demonstrated that the most energetically favourable mechanism for slip on the basal plane involves dislocation motion via synchro-shear [23, 90-92]. Dislocation dissociation, as well as kink-pair nucleation and propagation, were found to be favourable for dislocation motion in *C*14 CaMg$_2$ and *C*15 CaAl$_2$ Laves phases [110]. Whereas the dislocation dissociation was mainly observed at elevated temperatures, indicating thermal activation to reduce the required stress for activation, leading to the assumption that this mechanism is a “high” temperature mechanism [109].

2.2.4 Stacking faults in Laves phases: Synchro-shear mechanism

In Laves phases the dissociations of dislocations are also possible and can take place at the Kagomé layer, for *C*15 at the {111} planes and *C*14 and *C*36 at the [0001] plane, and is termed synchro-shear [23, 90-92, 109-111]. This was first discovered in sapphire by Kronberg et al. [112] and was first transferred into the Laves phase structure by Hazzeldine et al. [90] and Kumar et al. [65, 113]. This mechanism is mostly reported in the hexagonal *C*36 Laves phase [89, 104, 114, 115]. Experimentally, it has been found to occur in $ZrFe_2$ [116] and $MgNi_2$ [117]. For example, in terms of a phase transformation from the hexagonal *C*14 or *C*36 to the cubic *C*15 phase after macroscopic compression tests [114, 115, 118, 119], explainable by the different packings of these structures, which can be transferred by a simple restacking along the basal plane. These phases exhibit a distinct orientation relationship $(111)_{C15}//(0001)_{C36}$ and additionally $[01\bar{1}]_{C15}//[2\bar{1}\bar{1}0]_{C14}$ [116]. The dissociation of dislocation results in two synchro Shockley partials, for the cubic $\frac{1}{6}\langle 2\bar{1}\bar{1}\rangle$ and $\frac{1}{3}\langle 10\bar{1}0\rangle$ for the hexagonal structures, which is the most energetically favourable configuration for this case.

The synchro-shear mechanism results due to a synchronic motion of two Shockley partial dislocations in the tripe layer of the Laves phases. Partial one leads to move the big A atom by b_1, b_2, or b_3 and the second the small B atom by $-b_1$, $-b_2$ or $-b_3$. The total change results in 1b and a stacking fault. Due to the caused rearrangement after the motion of both dislocations, some parts can now reveal some stacking frequence of another Laves phase type, for example the change from *C*36 to *C*15 or vice versa. Previous atomistic calculations by Xie et al. [109, 110, 120] have shown, that this mechanism is highly influenced by the temperature, and can only be activated at elevated temperature, because of the different characters of both synchro-Shockleys. Whereas one of the Shockley is shear sensitive the other is shear intensive and needs additional temperature to reduce the overall Peierls barrier to move.

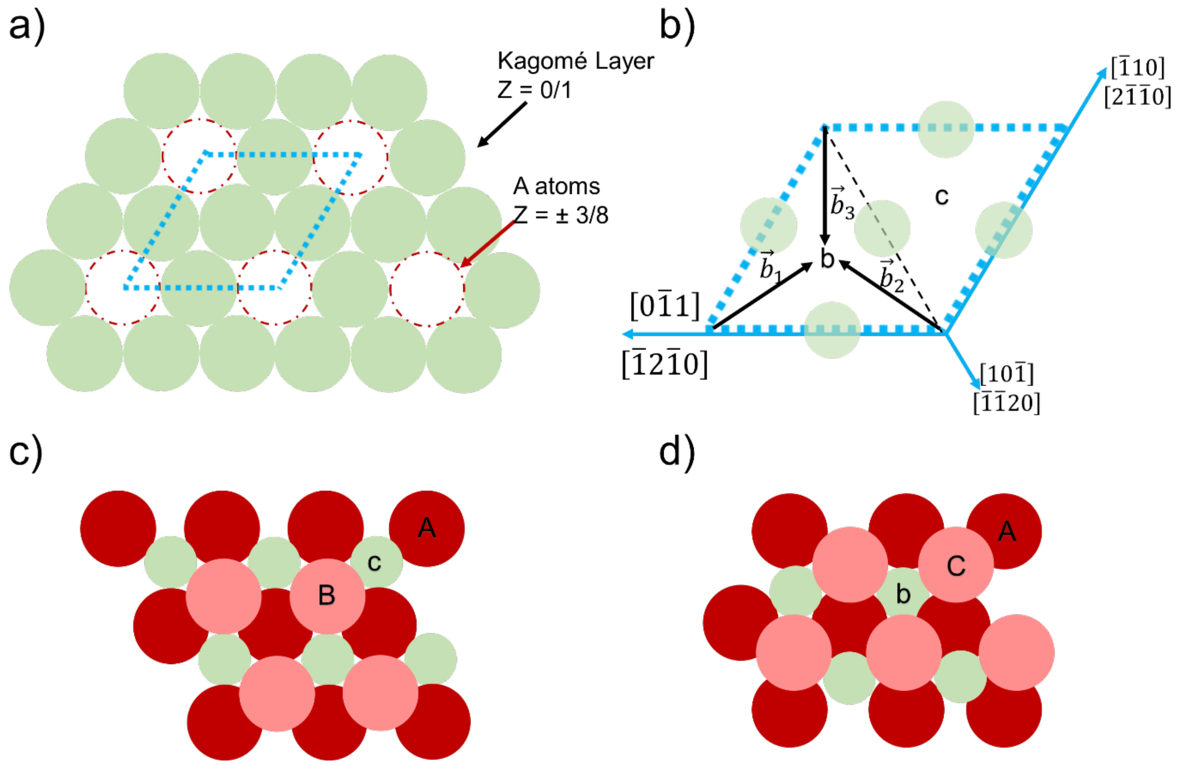

Figure 15: Illustration of the synchro-shear mechanism. In a) the rigid Kagomé layer builds out B atoms, in green, is displaced, and in these holes, the location of the A atoms is implied by red lined circles. b) shows the dissociation of the dislocation for cubic and hexagonal Laves phase. c) and d) showing the triple layer t (c)) and t´(d)), which is placed between the single Kagomé layer building this quadruple stacking. Adopted from [90] **reproduced with permission of Elsevier**.

Shown is the phase transformation from cubic stacking to hexagonal stacking, which is directly characterised by using intrinsic SF.

2.2.5 Chemistry influence on plasticity

Understanding how chemistry influences the mechanical behaviour and phase stability of Laves phases, especially those with defined homogeneity ranges, is valuable for property manipulation [21, 54, 121-130]. Numerous studies indicate that deviations from the perfect stoichiometric composition introduce various defects, such as anti-site atoms and vacancies, which distort the crystal lattice [54]. These deviations can be achieved by altering the internal AB_2 chemistry or by adding an alloying element, which can lead to different defect structures based on the substituted atom [20, 21, 28].

Changes in the ratio of A and B atoms in binary Laves phases affect mechanical properties. Moreover the resulting radius ratio change can impede or facilitate dislocation motion by limiting or opening up the atomic free volume on these planes through the presence of anti-site atoms or vacancies [96, 129]. For instance, Shields et al. [131] found that in $CeNi_2$, vacancy-induced strain fields cause softening at high temperatures and hardening after quenching. In $HfCo_2$, Chen et al. [123, 124] observed a decrease in lattice parameters and mechanical properties with increased Co content due to Co atom substitutions and vacancies. Similarly, studies on $MgZn_2$ revealed decreased hardness and yield stress with deviations from stoichiometry [132]. Introducing a third element, "C," into the Laves phase significantly impacts atomic interactions and mechanical properties. Chen et al. [127] found that alloying $TiCr_2$ with Nb, V, or Mo increased hardness, with V and Mo also enhancing fracture toughness, while Nb decreased it. Takasugi et al. [129, 130] showed that V and Mo substitutions in $NbCr_2$ resulted in hardening or softening based on the specific site they occupied. Phase transformations between different Laves polytypes are closely related to mechanical deformation, with stacking fault formation being a key mechanism. RT compression tests on $ZrFe_2$ demonstrated phase transformation from *C*36 to *C*15 under strain due to synchro Shockley dislocations [114, 116]. Studies also show that adding a ternary element alters dislocation mobility and mechanical properties. For example, Takata et al. [107] observed that increasing Ni content in $NbFe_2$ led to solid solution softening and reduced hardness. Chu et al. [125] found that Nb addition to HfV_2 improved deformability by creating free volume on {111} planes. In summary, manipulating the Laves phase' composition affects mechanical properties through defect structures and phase transformations. While experimental studies provide valuable insights, combining these with computational approaches could further elucidate the underlying mechanisms and optimize property manipulation

2.3 Mg-Al-Ca System

A common lightweight material is displaced by Mg, which exhibits a low density and is therefore one of these well-known lightweight materials [133-137]. Due to the lack of high temperature resistance and poor ductility, the investigations of Mg alloys, especially the most applied combination with aluminium (Al), the Mg-Al alloys, have shown improvements in mechanical properties [138, 139]. These are based on solid solution strengthening affected by the formation of precipitations of the complex $Mg_{17}Al_{12}$ phase in the Mg matrix. These precipitates enhance the room temperature plasticity, but also at temperatures up to 130 °C these precipitates are not stable and cannot influence the above properties [140, 141]. However, many studies have shown that this can be directly improved by the addition of small amounts of rare earth metals or calcium (Ca) [142]. In this case, Ca is the most beneficial and cost-effective choice as the outcome is the same. The addition of the third alloying element results in the formation of various intermetallic phases as a second phase in the Mg matrix [143].

These intermetallic phases are called Laves phases and the Mg-Al-Ca system exhibits all three prototypes. With its three elements, the Mg-Al-Ca system provides the basic building blocks for all three prototypes of the Laves phase. Depending on the composition and with Ca and Al content Laves phases are introduced as a skeleton as a second phase in the Mg matrix. With increasing Mg/Al ratios, precipitates from *C*15 $CaAl_2$ to *C*36 Ca(Mg;Al)$_2$ and finally to *C*14 $CaMg_2$ are found [143-147]. Additionally, the complex β-$Mg_{17}Al_{12}$ Samson phase can form with

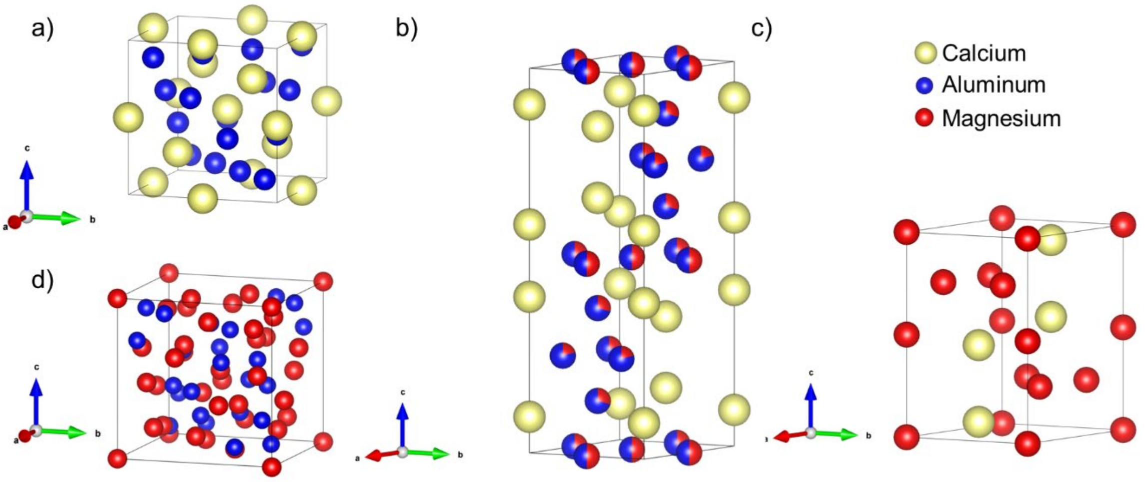

Figure 16: Resulting intermetallic phases in the Mg-Al-Ca system. a) cubic *C*15 $CaAl_2$, b) hexagonal *C*14 $CaMg_2$, c) (di-)hexagonal *C*36 Ca(Al;Mg)$_2$ Laves phase and d) β-$Mg_{17}Al_{12}$ phase, illustrated using VESTA [3].

the addition of Al to Mg, which is mostly found as small precipitates. Atomistic simulations show that in this system two prototypes can exist simultaneously as precipitates in the Mg matrix, which is also observed in the Li-Al-Ca system [55, 56]. This has been attributed to the fact that the structural change is not influenced by the distribution of the B atoms (Al for *C*15 and Mg for *C*14) but by the electron concentration. The solubility range at a constant Ca concentration was determined to be 58.08-66.66 at.% Al and 0-8.52 at.% Mg for the *C*15 phase, whereas the *C*36 phase forms for contributions of 44.22-30.69 at.% Al and 22.44-35.97 at.% Mg and the *C*14 starts at 16.17 at.% and lower Al and 50.49-66.66 at.% Mg [55]. The structures are shown in Figure 16.

3. Research findings of this study

This chapter summarises and links the results obtained during the research years. A distinction is made between already published results and on-going work (in grey), but they are presented together. The following chapter concludes these findings. Dislocation motion in complex intermetallic phases is still poorly understood due to their inherent resistance against dislocation motion, especially their behaviour below the BDTT. This thesis aims to unravel this complexity, close the gap of knowledge regarding the properties and mechanical behaviour of the stoichiometric composition and analysing the influence of a ternary alloying element to the stoichiometric composition. Additionally, it aims to evaluate the influence of the strain rate and the temperature on the analysed systems. For this purpose, the castable Laves phases formed in the Mg-Al-Ca system, the *C*14 and *C*15, namely the $CaMg_2$ and $CaAl_2$ Laves phases, and one ternary *C*14 and two ternary *C*15 Laves phases were investigated (in Figure 17). The compositions of the analysed samples of the Mg-Al-Ca system are shown in Figure 17. The exact compositions of the samples are listed in Table 9, where the stoichiometric compositions are indicated with “S”, the off stoichiometric ones with “NS”. Furthermore, the prototype of the *C*15 Laves phase, the $MgCu_2$ Laves phase was analysed, these is listed “PT” in Table 7.

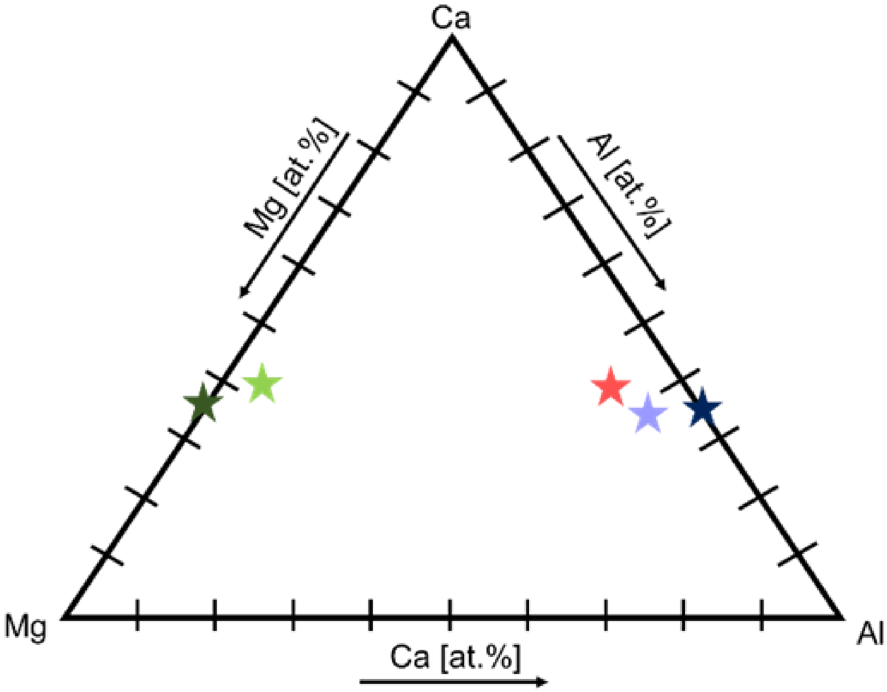

Figure 17: Alignment of the investigated Laves phases in the ternary Mg-Al-Ca diagram. The overall bulk composition is listed in Table 7 below, presented in the diagram as stars with different colour codes: dark green star belongs to the *C*14_S, the light green to *C*14_NS, the dark blue to the *C*15_S, the purple to the *C*15_NS1 and the red star to the *C*15_NS2.

Table 7: Compositions of investigated stoichiometric (S) and off stoichiometric (NS) samples (same colour scheme as Figure 17) and the Prototype (PT).

Sample	Strukturtyp	Mg [at.-%]	Al [at.-%]	Ca [at.-%]
*C*14_S	*C*14	68.7 ± 0.5	31.3 ± 0.5	-
*C*14_NS	*C*14	60.5 ± 0.1	37.4 ± 0.1	2.1 ± 0.0
*C*15_S	*C*15	-	66.5 ± 1.5	33.5 ± 1.3
*C*15_NS1	*C*15	5.7 ± 0.1	61.4 ± 0.2	32.9 ± 0.2
*C*15_NS2	*C*15	10.8 ± 0.8	52.9 ± 0.7	36.3 ± 0.1
Sample	**Strukturtyp**	**Mg [at.-%]**	**Cu [at.-%]**	
*C*15_PT	*C*15	29.7 ± 0.4	70.3 ± 0.4	

The first publication '**Plastic deformation of the $CaMg_2$ C14-Laves phase from 50 - 250°C**', continued the room temperature plasticity investigation of the hexagonal *C*14 $CaMg_2$ Laves phase (*C*14_S), analysed by Zehnder et al. [8]. It deals with the temperature dependent dislocation behaviour in the range from 50 – 250 °C, by presenting a comprehensive study of nanomechanical experiments. Here the mechanical properties, indentation modulus, and hardness remain at one level, measured for three specific areas (Area 1: 48° to the (0001) plane, shown in blue in Figure 18 a) and b), Area 2: 83° to the (0001) plane, shown in red in Figure 18 a) and b) and Area 3: 9° to the (0001) plane, shown in orange in Figure 18 a) and b)) over the temperature range, giving values of 3.3 ± 0.1 GPa to 3.5 ± 0.2 GPa (Figure 18 a)) with indentation modulus values between 53.1 ± 1.3 GPa to 56.3 ± 1.7 GPa (Figure 18 b)). But a change could be observed with the decrease of countable serrations in the stress strain curve with increasing temperature, displayed in Figure 18 c) for 100 °C and Figure 18 d) for 250° C.

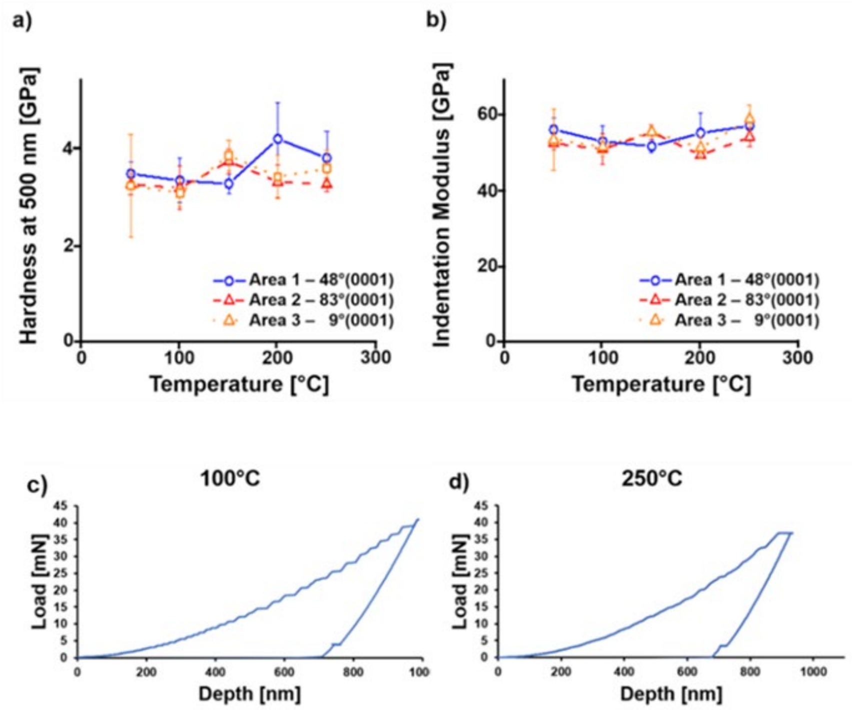

Figure 18: Temperature dependent a) hardness and b) indentation modulus of the C14_S sample of the investigated areas, stays on one level irrespective of temperature and orientation. The load-depth curves at c) 100 °C and d) 250 °C show decreasing serrations with increasing temperature [6].

The statistics of the slip lines show orientation dependent slip line morphologies, with Area 1 showing edges, Area 2 lines and curves and Area 3 curves only. Additionally, an orientation dependent slip line loss with increasing temperature could be observed for all investigated orientations as shown in Figure 19.

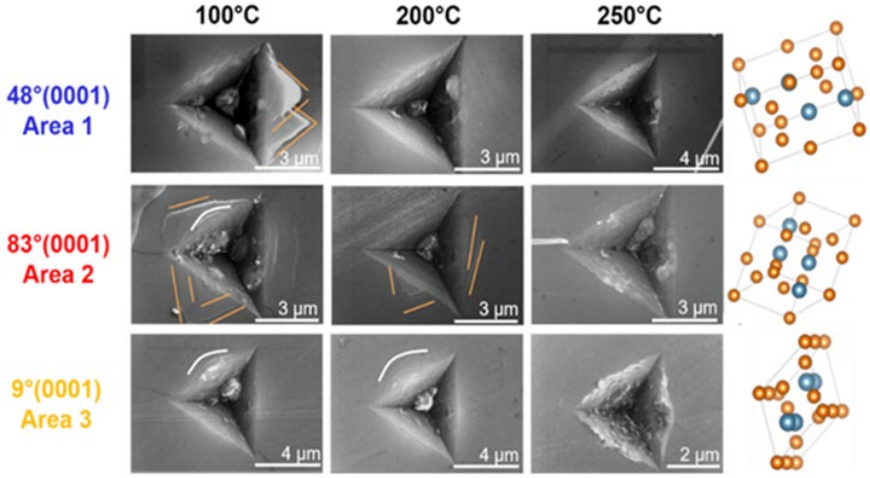

Figure 19: Resulting slip lines shown with the belonging temperature, for all indented orientations [6].

The relative activation frequencies of the slip planes could be evaluated and are illustrated in Figure 20, for Area 1 and Area 2 over the temperature range. A surface trace analysis could only be conducted for traces with straight parts, explaining why this was not possible for Area 3, as only curved lines forming around the indentation mark were observed. For the total amount of surface traces, the pyramidal 1st planes showed the highest activation frequency. The less activated planes for both orientations with respect to the total number of the resulting planes were the basal planes, which could only be detected in Area 1 for indents at 25 °C and 200 °C and in Area 2 at 50 °C and 200 °C. Furthermore, the prismatic 1st order planes were found to be activated in Area 2 for all temperatures and with decreasing frequencies up to 100 °C, showing no activation for Area 1 at 50 °C and 200 °C and the highest at 150 °C, followed by 100 °C and 25 °C.

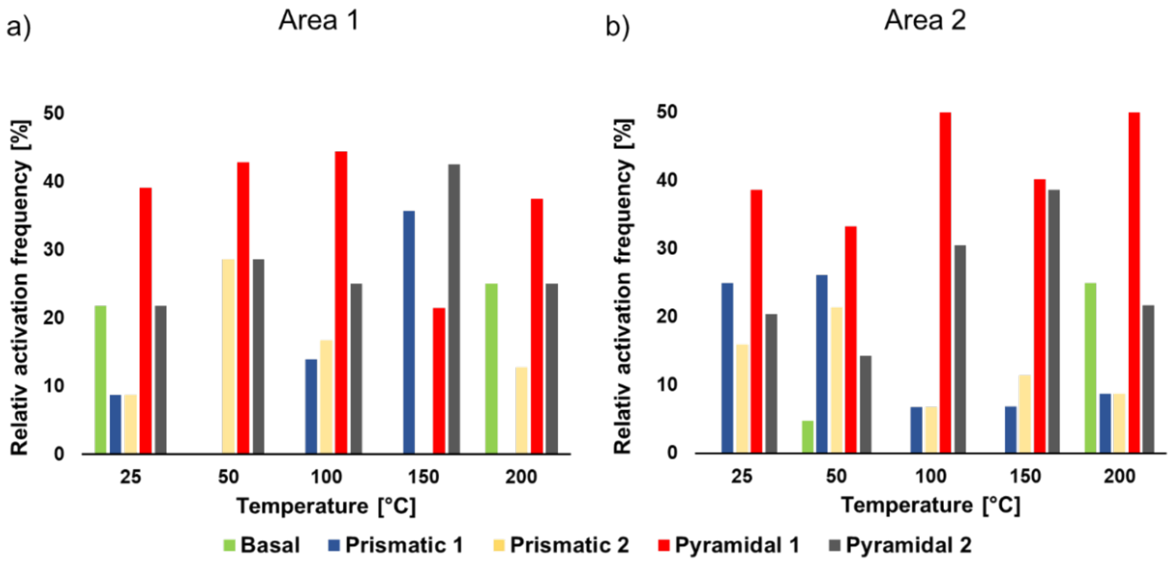

Figure 20: Relative activation frequencies against the investigated temperatures for the *C*14 $CaMg_2$ Laves phase. Room temperature results were taken from [8] and up to 50 °C from [6].

Combined with their CRSS calculated from the micropillar compression test examined at 150 °C and 250 °C, no significant change in activation frequencies or CRSS values was observed with temperature, whereas the number of analysable micropillars was not representative for a statistical statement of slip planes or CRSS. For Area 3, the micropillar compression tests could only be conducted at 150 °C. The values are given in Table 8.

Table 8: Micropillar compression test results from *C*14_S at 150 °C and 250 °C, given the CRSS for the found slip system with their Schmid Factor for Area 1, Area 2 and Area 3.

Area	**Slip system**	**Schmid Factor**	CRSS **150° C**	CRSS **250 °C**
1	(0001)	0.45	0.57	0.46 ± 0.03
	$(10\bar{1}1)$	0.29	0.42	-
	$(\bar{1}100)$	0.24	-	0.22
2	$(11\bar{2}2)$	0.48	0.41	0.49 ± 0.15
	$(10\bar{1}1)$	0.47	0.47	-
3	$(10\bar{1}1)$	0.47	0.58 ± 0.07	
	$(11\bar{2}2)$	0.38	0.28	

In order to gain a more knowledge about the chemical influence and to answer the question of its change of dislocation mechanisms and properties, the off stoichiometric *C*14 Laves phase, sample *C*14_NS, was investigated using the same experimental set up, at RT. The following results are **on-going work** and have not been published to date. The analysed areas are given in Figure 21 displayed in an IPF (inverse pole figure) map with their hardness and indentation modulus, measured by nanomechanical indentation tests, performed (with the same parameter as for *C*14_S) with a constant strain rate of 0.1 s^{-2} up to a depth of 500 nm. The calculated hardness lies between 2.4 and 2.7 GPa and the indentation modulus between 48.2 and 50.7 GPa, which is about 30% lower compared to *C*14_S for the hardness, but stays more or less in the same range for the indentation modulus [8].

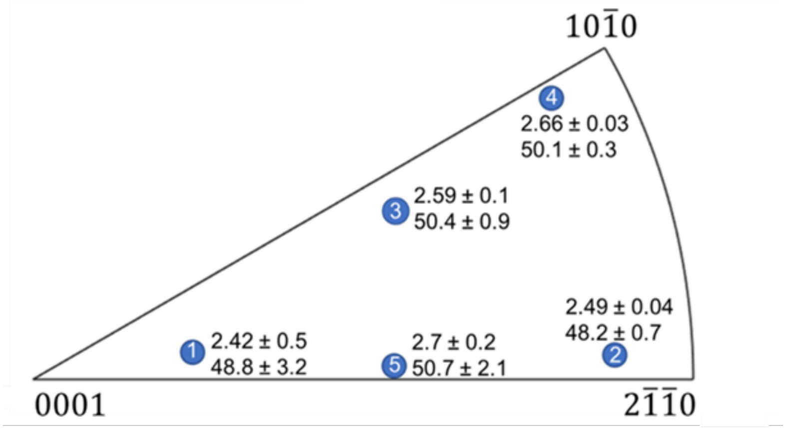

Figure 21: Investigated orientations for the C14_NS sample, with corresponding measured hardness and indentation modulus.

For this sample, 1974 slip traces were analysed and applied against the resulting possible slip planes in Figure 22, showing the same (with the exception of an overall less activation) trend for the activation frequency of the basal slip planes. Figure 22 presents the results of the slip trace analysis (*C*14_NS in light green) compared to *C*14_S (in dark green). In comparison to the *C*14_S sample, the *C*14_NS sample shows less activation of prismatic 1st order slip and slightly more prismatic 2nd order slip and about 10 % more pyramidal 2nd order slip.

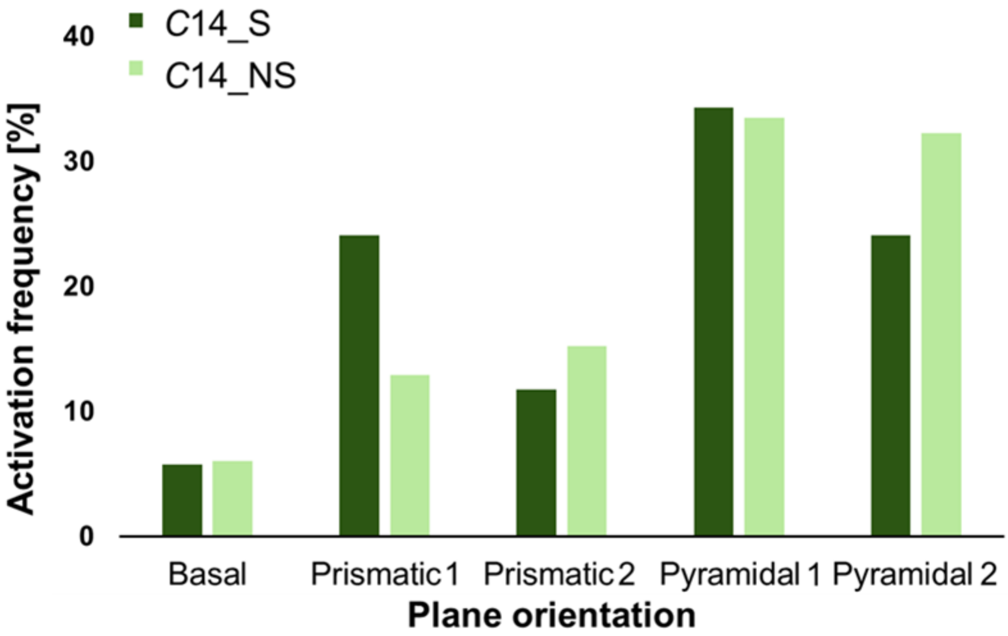

Figure 22: Activation frequencies of the *C*14_S (dark green) and *C*14_NS (light green) Laves phase for the investigated plane orientations.

Micropillar compression tests are performed in the same orientations, where nanoindentation test were applied. An example of each compression test is given in Figure 23 a) – e) and the corresponding engineering stress – engineering strain curves are shown in Figure 23 f).

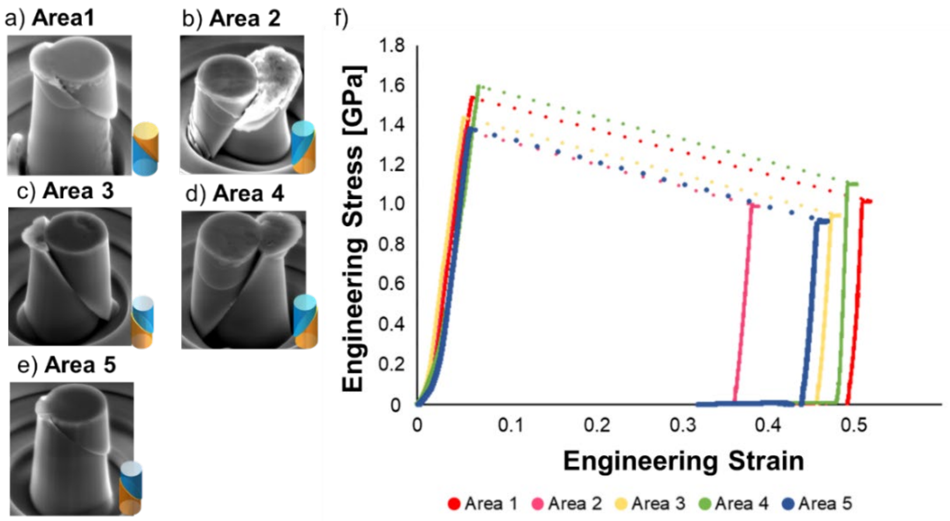

Figure 23: a) – e) illustrate the compressed micropillars for each orientation, whereas the alignment of these could be taken from Figure 21, with the simulation of the slip planes. f) showing the engineering stress-engineering strain curve from the compressed micropillars.

The calculated CRSS obtained from the micropillar compression tests for the specific slip systems can be seen in Table 9, with the highest CRSS for basal and pyramidal 2nd order slip systems. The lowest CRSS were calculated for the prismatic 1st order slip system.

Table 9: Calculated CRSS for the resulting slip systems of *C*14_NS for all analysed orientations, given with their Schmid Factor and engineering stresses.

Area	Slip system	Schmid Factor	Eng. Stress	CRSS
1	$(\bar{1}2\bar{1}\bar{2})\langle 1\bar{2}1\bar{3}\rangle$	0.4168	1.52 ± 0.09	0.63 ± 0.04
2	$(10\bar{1}0)\langle\bar{2}110\rangle$	0.4059	1.35	0.55
3	$(0001)\langle 11\bar{2}0\rangle$	0.4468	1.43 ± 0.06	0.64 ± 0.28
4	$(10\bar{1}0)\langle\bar{2}110\rangle$	0.3655	1.59 ± 0.15	0.58 ± 0.09
5	$(0001)\langle 11\bar{2}0\rangle$	0.4434	1.38 ± 0.17	0.61 ± 0.07

To be able to analyse the influence of the additional ternary element (*C*14_NS), in this case the substitution of 2 at.% Al, the resulting CRSS obtained from the micropillar compression tests, were compared to the results of the binary ones (*C*14_S). These show an about 0.11 GPa higher CRSS for prismatic 1st order slip systems, whereas the CRSS for basal and pyramidal slip systems remains unaffected. But the change in CRSS, the order in terms of which slip system has the lowest value, remains unaffected.

The investigation of the binary *C*15_S ('**Plasticity of the C15-CaAl$_2$ Laves phase at room temperature'**) and ternary *C*15_NS1 and *C*15_NS2 cubic CaAl$_2$ Laves phases ('**Influence of chemical composition on the room temperature plasticity of *C*15 Ca-Al-Mg Laves phases**') were done experimentally by using nanomechanical testing combined with atomistic simulations to verify and confirm experimental sections. By applying the nanomechanical workflow including indentation tests, followed by a slip line analysis, and micropillar compression tests for the *C*15_S and post-mortem TEM investigations, the stoichiometric composition could be analysed. The same workflow was processed for the *C*15_NS1 and *C*15_NS2 except for the micropillar compression test to evaluate the influence of the ternary alloying element.

The mechanical properties of the three samples have shown that by adding the ternary element and with increasing the amount of the ternary element the hardness and indentation modulus decrease, which is given in Table 10.

Table 10: Hardness and indentation modulus for the stoichiometric and off stoichiometric cubic CaAl$_2$ Laves phases.

	***C*15_S**	***C*15_NS1**	***C*15_NS2**
Hardness [GPa]	4.9 ± 0.3	4.6 ± 0.2	4.1 ± 0.3
Indentation Modulus [GPa]	85.5 ± 4.0	80.7 ± 3.0	71.3 ± 1.5

After analysing the binary *C*15_S the additional and equally likely slip plane {112} to {111} could be added to the possible slip planes. Further, after investigating the ternaries, *C*15_NS1 and *C*15_NS2, these could be extended by finding the {113}, {114}, {115}, {116} and {1 1 11} planes. The alignment of these planes is shown in Figure 24 a). The results of the slip plane analysis reveal the {11n} planes as the most activated slip planes for the cubic system, as shown in Figure 24 b). Furthermore, the {100} planes are for all three compositions the least activated ones followed by the {111} planes and the {110} planes.

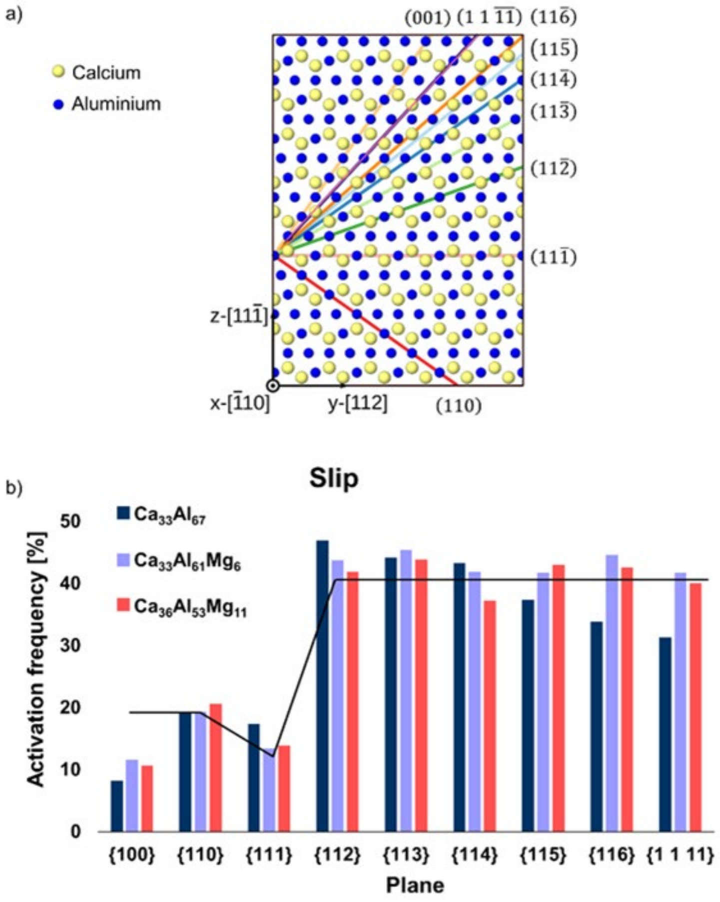

Figure 24: a) alignment of the planes taken for the slip line analysis, displaced in the cubic *C*15 lattice. b) relative activation frequency of the activated slip planes for all three samples. The black line shows the amount of possible slip systems in a related to each other [10].

Besides the slip plane activation, it was found, that the morphology of the resulting slip traces around an indent, was strongly influenced by the orientation, especially for *C*15_S and *C*15_NS1. This phenomenon vanished slightly with the wider distinction of the stoichiometric composition, visible for sample *C*15_NS2, and observable in Figure 25. Especially for *C*15_S and *C*15_NS1, the morphology for surface traces of orientations, lying in its IPF map near to the [111] direction only shows cracks (Figure 25 d) and e)), and no surface traces, whereas it should be mentioned that all indents show at least one crack. For *C*15_S the slip morphology lying in the IPF map near the [011] direction reveals lines and edges, near the [001] direction edges and curves and all in between show a mixture of all surface trace morphologies. *C*15_NS1 therefore shows at [001] directions only curved surface traces and in [011] directions edges. Between [001] and [011] directions a mixture of curves and edges forms around the indent. In between for all three directions edges were mainly observed, only “I” (Figure 25 b, in its IPF map with the light blue/green rectangle)) showed straight lines and edges. The *C*15_NS2 (Figure 25 c)) deviates strongly by showing no cracks and only near the [001] pronounced curved surface traces (Figure 25 f)). The other orientations show either few surface features or none.

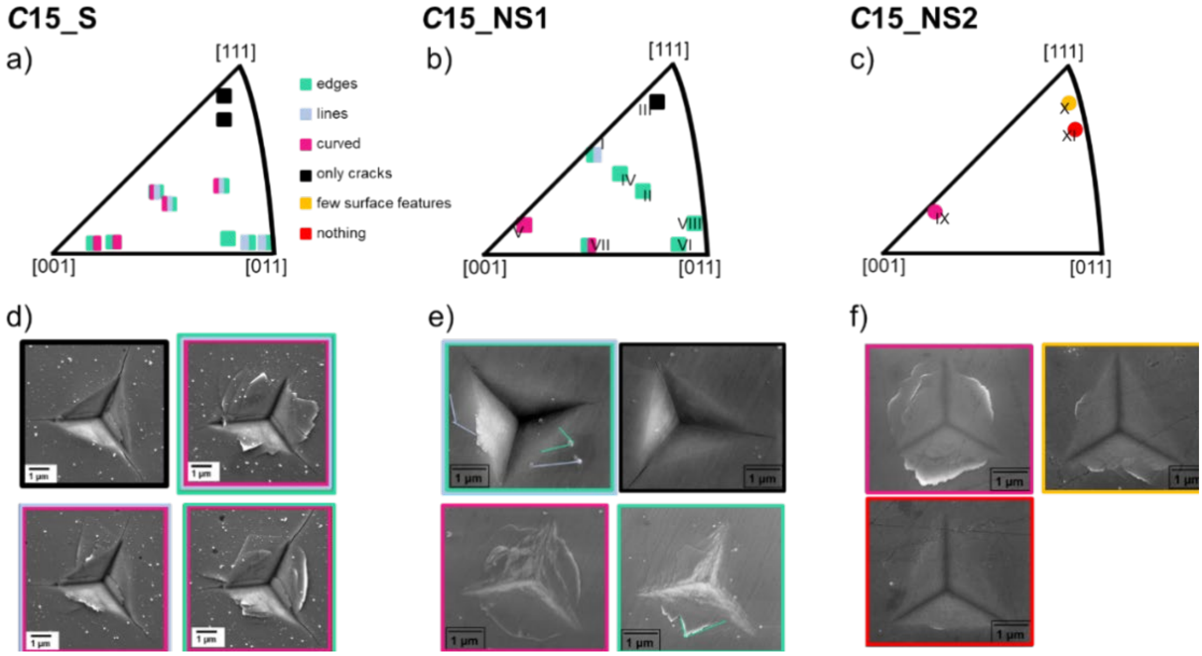

Figure 25: Orientation dependent morphology of resulting slip lines for the cubic $CaAl_2$ Laves phase: a) *C*15_S, b) *C*15_NS1, c) *C*15_NS2 visualised in its IPF map, whereas the colour code gives the different morphologies of surface traces for this orientations: green for edges, blue for lines, pink for curves, black for cracks, yellow for only few surface features and red for nothing, modified from [10, 13].

Atomistic simulations, calculating the energy barrier of some of the slip systems, revealing that for all slip systems, the energy barrier of the full slip {11n}, with n = 1, 2, 4, 5, as well as for the {111} synchro-shear dislocation motion, decreases with increasing offset of the binary stoichiometry substituting the ternary alloy element Mg to the binary $CaAl_2$ Laves phase, as displayed in Figure 26. In Figure 26 a) starting from the initial stoichiometric compound with an energy barrier of 1514 mJ/m^2 the energy barrier decreases just by substituting Al with Mg to 1383 mJ/m^2. By increasing the Ca content simultaneously, the energy barrier increases to 1235 mJ/m^2 for synchro-shear dislocation motion on {111} plane. The initial energy barrier is comparatively lower with 1081 mJ/m^2 for the full slip {111} (Figure 26 b)) as for the synchro-shear {111} dislocation motion and decrease to 884 mJ/m^2. For dislocation motion on the {112} (Figure 26 c)), {114} (Figure 26 d)) and {115} (Figure 26 e)) the initial energy barrier starts between 1226 mJ/m^2 and 1486 mJ/m^2, and reaching up to 998 mJ/m^2, 1147 mJ/m^2 and to 1267 mJ/m^2, respectively, which are values that are relatively higher compared to {111} full dislocation slip but overall lower than for synchro-shear motion.

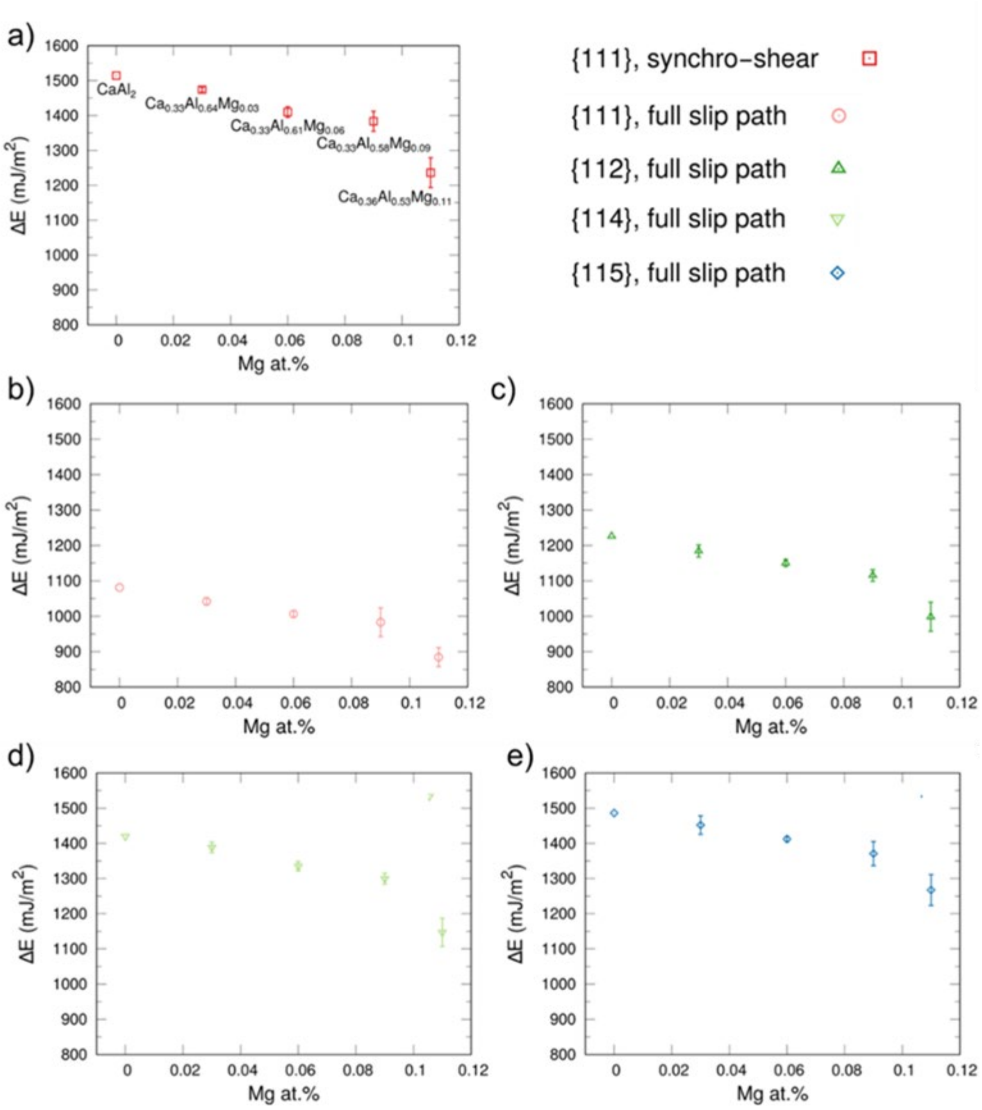

Figure 26: Atomistic simulations for the energy barrier of specific slip systems and its change with the compositions, for a) {111} synchro-shear motion, b) {111} full slip path, c) {112} full slip path and d) {114} full slip path and e) {115} full slip path [10].

In order to investigate the underlying dislocation structure, one specific TEM lamella was taken from each sample and analysed regarding the underlying plasticity. For the off stoichiometric samples, the additional analysis was conducted to prove the phase stability and if the distribution stays constant over the sample depth. All show a high dislocation density. A TEM analysis of sample *C*15_S first confirms the findings of the {112} slip planes, by finding slip bands which can fit both, the {111} and {112} slip planes. The $\vec{g} \cdot \vec{b}$ analysis resulted in the Burges vector to be $\frac{1}{2}[1\bar{1}0]$, fitting also with both planes. Additionally, cracks were forming from the sample surface into the lamella, which could be assigned unambiguously to the $(21\bar{1})$ and $(2\bar{1}1)$ planes, shown in Figure 27 c) with the white dashed lines.

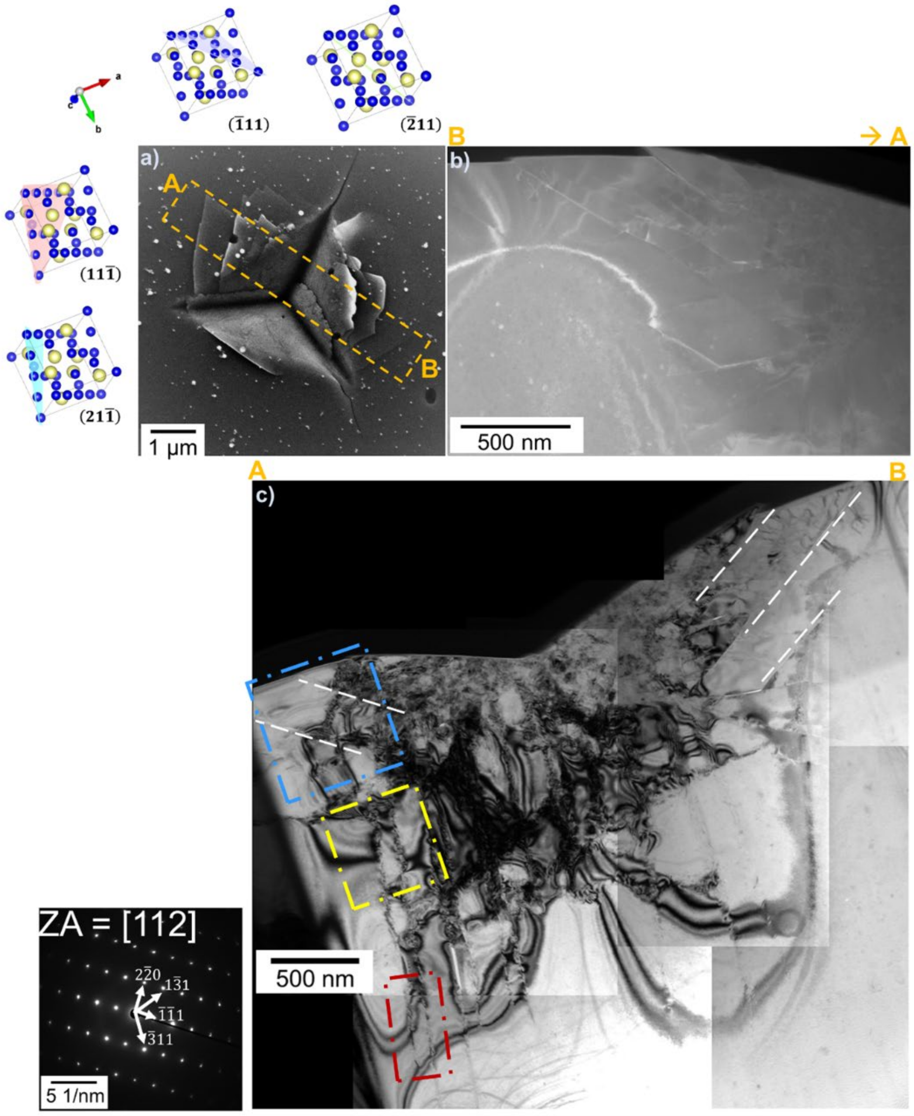

Figure 27: a) SE-image of an nanoindentation imprint including a schematic sketch (dotted orange area), from where the TEM lamella was cut out. letters a and b show the orientation of the membrane and how it was analysed in the further investigations. the slip traces in the vicinity of the indent were furthermore correlated with different planes along with the unit cell using vesta [3]. b) STEM image of the lamella. c) BF-TEM image taken at [112] zone axis. The blue rectangle highlights the area with a high dislocation density, whereas the red rectangle indicates the area where dislocation Burgers vector analysis was performed and the yellow rectangle corresponds to the area where the stacking faults were found [13].

For the sample *C*15_NS1 and *C*15_NS2 the TEM lamella was taken from the indents with curved surface trace morphologies. For *C*15_NS1 the TEM lamella was taken from V (Figure 25 b)) and for *C*15_NS2 (Figure 25 c)) from IX, showing both besides the high dislocation density also areas where dislocation structures could be observed, consisting of more than one dislocation set, which seem to be dislocation dipoles. For *C*15_NS1 slip bands were edge on to the {114} and {115} planes, as well as containing cracks along the {112} planes as shown in Figure 28 a).

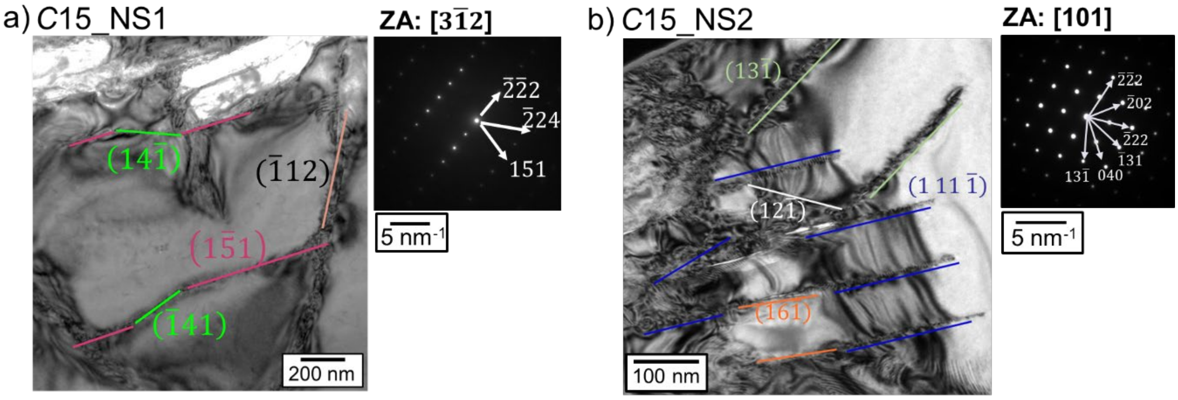

Figure 28: a) *C15_NS1* TEM bright field image in $[3\bar{1}2]$ zone axis, showing slip bands on $(14\bar{1})$ and $(\bar{1}41)$ in light green, $(1\bar{5}1)$ in pink and $(\bar{1}12)$. b) *C15_NS2* in [101] zone axis revealing slip bands on $(1\ 11\ \bar{1})$ in blue. $(13\bar{1})$ in green, $(16\bar{1})$ in orange as well as $(12\bar{1})$ in white. Adopted and modified from [10].

C15_NS2 additionally shows slip bands at the {113}, {116} and {1 1 11} planes, shown in Figure 28 b). Furthermore, both have slip bands with a zig-zag structure, Figure 28. These slip bands lie edge on to the {11n} slip planes. For *C15_NS1* changes between {114} → {115} → {114}, for the *C15_NS2* changes between {1 1 11} → {116} → {1 1 11} are found in the TEM lamella. Furthermore, at higher magnifications more slip plane changes can be observed, taking place at a higher frequency with smaller distances at every plane, presented in Figure 29 b) displaying the yellow rectangle of Figure 29 a). Here changes between $(11\bar{1})$ (in blue) → $(51\bar{1})$ (in pink) → $(21\bar{1})$ (in yellow) → $(51\bar{1})$ → $(21\bar{1})$ →$(11\bar{1})$ can be seen.

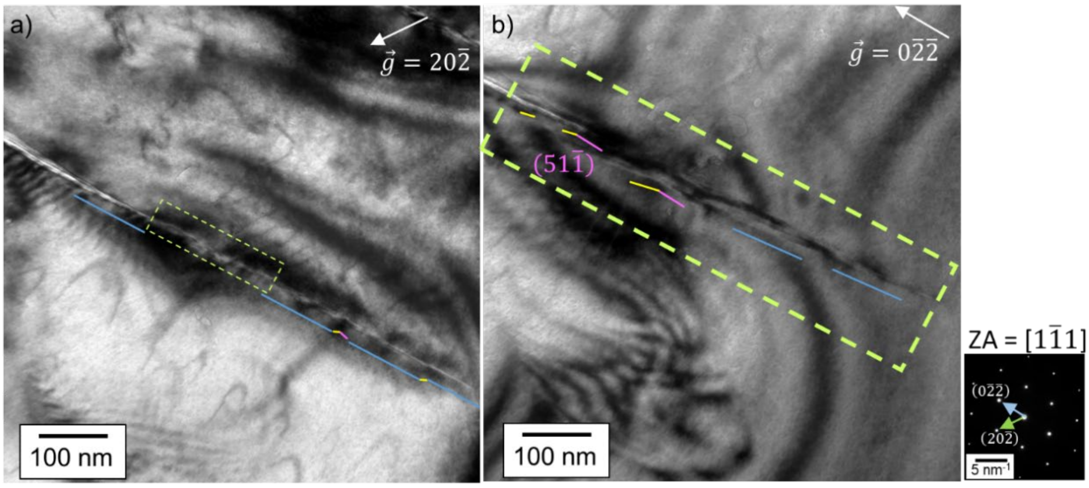

Figure 29: a) and b) TEM bright field images taken in $[1\bar{1}1]$ zone axis. a) with $\vec{g}$=$(20\bar{2})$ two-beam condition at different magnifications, and under b) $\vec{g}$=$(0\bar{2}\bar{2})$ two-beam condition in an indented *C15_NS1* Laves phase. Different coloured lines mark the orientations of the slip plane. The green rectangle shows a quite wavy segment. The zigzag shape of the slip plane indicates the occurrence of multiple cross-slips of dislocations.

Nudge elastic band (NEB) simulations also confirm these findings by using the minimum energy paths (MEPs) and found cross slip events on $(11\bar{2})$, $(11\bar{4})$, $(11\bar{5})$ and $(11\bar{6})$ with dislocation motion periods on varying planes larger than 10 Å. The results are displayed in Figure 30.

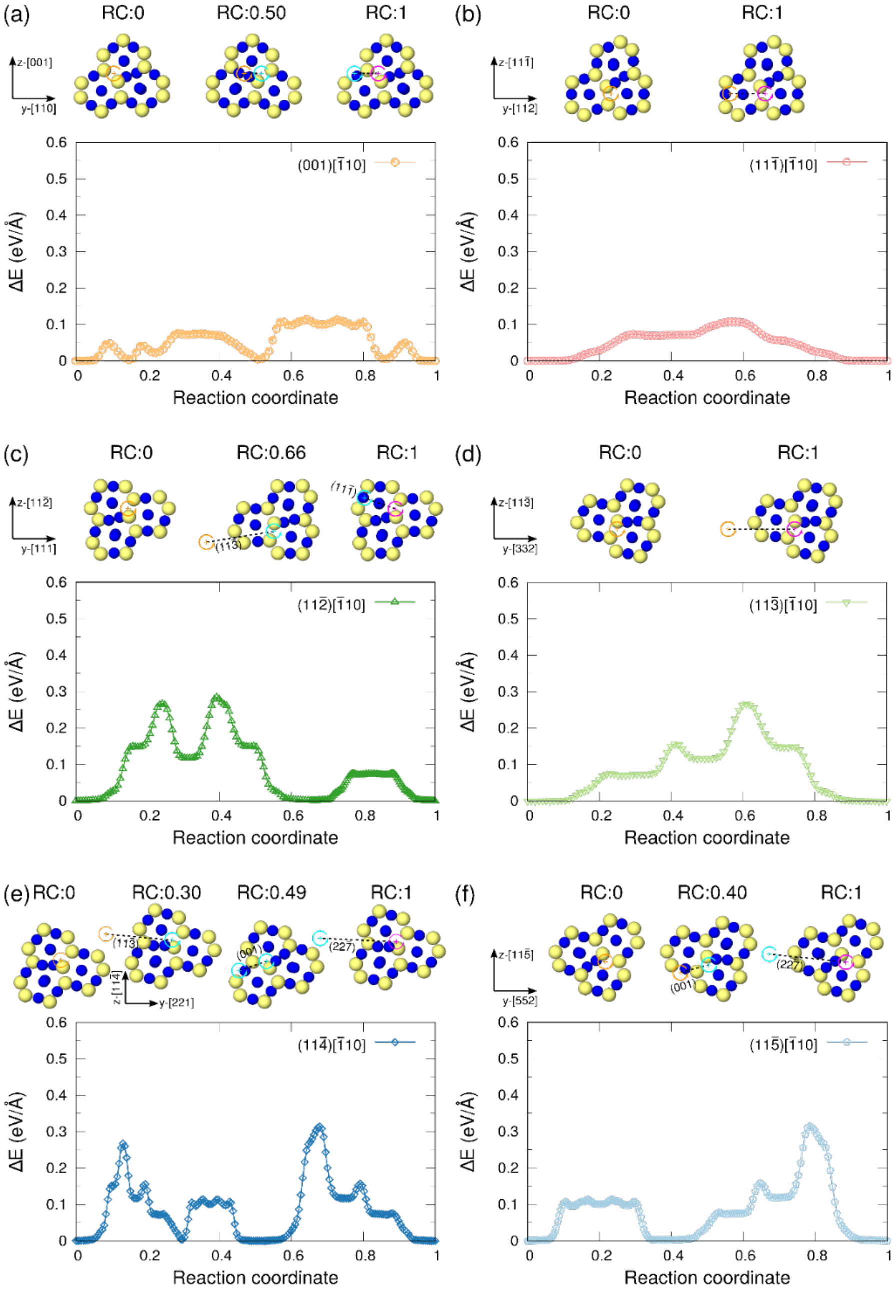

Figure 30: Atomistic configurations and energy profiles along minimum energy paths (MEPs) for the motion of the screw $\frac{a}{2}[\bar{1}10]$ dislocation on (a) (001), (b) $(11\bar{1})$ triple-kagomé interlayer, (c) $(11\bar{2})$, (d) $(11\bar{3})$, (e) $(11\bar{4})$ and (f) $(11\bar{5})$ planes were calculated using the nudged elastic band (NEB) method. Only atoms belonging to the dislocation core, as identified by LaCA, are shown here. The orange and magenta symbols indicate the position of the dislocation line in the initial (reaction coordinate RC:0) and final (RC:1) atomistic configurations, while the cyan symbols represent the position of the dislocation line at the intermediate minima. Dashed lines indicate the glide planes between each local minimum. Performed by Dr. Zhuocheng Xie.

The temperature influence was investigated at a temperature range between 25-580 °C for the *C*15_S by using micropillar splitting and indentation tests with a cube corner, to analyse the resulting fracture toughness and calculating the hardness. Furthermore, TEM lamellae were analysed from an indentation print at RT and 450 °C. However, finding a microplasticity zone before the BDTT is reached, shown in the absence of cracks for the indentation up to 350 °C and no splitting up to 400 °C, but constant hardness in this temperature range. The first hardness drop was than measurable at 450 °C, continued by further decrease at higher temperatures. The dislocation structure observed in the room temperature lamella was different to this in the high temperature lamella, with only exhibiting perfect dislocations compared to this having additional partial dislocations.

Additionally, the *C*15_PT sample was investigated using a nanoindentation test, performing RT indentation tests and afterwards a surface trace analysis. Further tests using nanoindentation at temperatures up to 400 °C followed. The nanoindentation test was performed using a constant strain rate of 0.1 s^{-1}, indenting up to a depth of 500 nm. Here the slip line analysis was limited due to changes on the surface with the result of invisible surface traces. With the RT slip line analysis 1257 surface traces could be analysed, whereas the main plasticity results from the {11n} planes, shown in Figure 31.

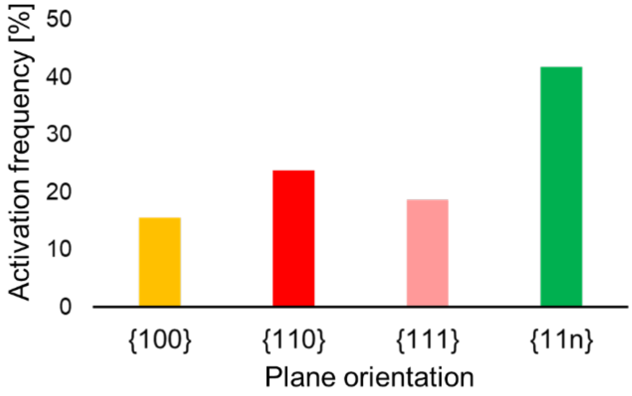

Figure 31: Resulting plane activation in *C*15_PT sample. Showing in yellow the relative activation frequency of the {100}, in red {110}, in rose {111} and in green {11n} planes.

Hardness and indentation modulus were calculated to be 4.4 ± 0.03 GPa and 87.0 ± 1.1 GPa. The changes over the temperature are given in Figure 32. Here the temperature stays at the same range until a specific temperature is reached, which in this case is in the range of between 300 °C and 400 °C, calculated to homologous temperatures ranging from 0.4 to 0.5. After this the hardness drops to 1.1 ± 0.8 GPa and the indentation modulus drops to 55.1 ± 1.8 GPa.

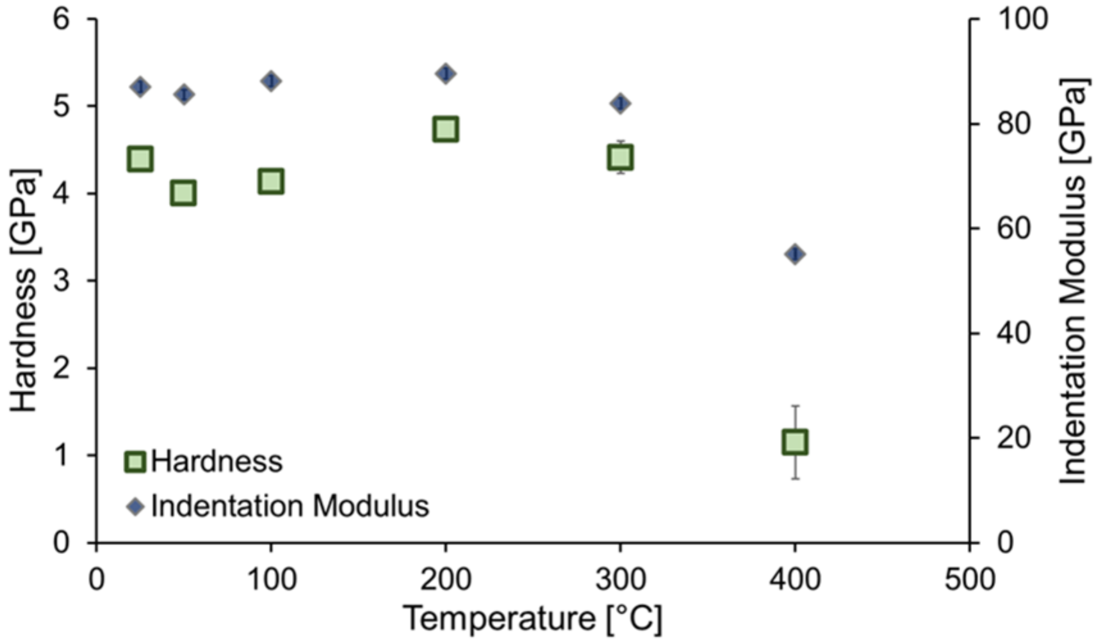

Figure 32: Hardness and indentation modulus evolution over the tested temperature in sample *C*15_PT.

4 Conclusion

The main part of this research was to understand the fundamental plasticity in complex phases. For this task, the forming Laves phases in the Mg-Al-Ca system, namely the *C*14 $CaMg_2$ and the *C*15 $CaAl_2$ and $CuMg_2$ Laves phase, were investigated. With both phases, we gain new insights into the room temperature plasticity and generate information on the general opportunities for dislocation movement, the influence of temperature on dislocation structures, and their change with varying chemistry. To give an overview, the research questions will be answered:

1. Which slip systems can be activated in the Laves phase structure?

Plasticity of the C15-$CaAl_2$ Laves phase at room temperature

Influence of chemical composition on the room temperature plasticity of *C*15 Ca-Al-Mg Laves phases

Besides the common reports of limited occurring plasticity in Laves phases, these studies have shown, that dislocation motion itself is introducible at temperatures below the BDTT. The activation was observed not only on the previously reported low index planes namely the {100}, {110} and {111} planes. The planes can be widened up by finding plasticity on several new {11n} planes, the {112}, {113}, {114}, {115}, {116} and {1 1 11} found by post mortem TEM investigations of deformed areas and afterwards included for the statistical analysis of slip lines, which formed after nanoindentation tests. The difference in resulting slip planes can be grounded by the fact, that previous studies of the Laves phase plasticity only can be done macroscopically above BDTT and will therefore leads to changes in dislocation structures itself, like we could find for the binary $CaAl_2$ Laves phase, which additionally revealed partial dislocation at elevated temperatures.

The analysis of the $CaAl_2$ structure revealed new slip systems for the cubic *C*15 $CaAl_2$ Laves phase structure besides the always reported dislocation motion on the {111} planes. The new slip planes were found to be: {112}, {113}, {114}, {115}, {116} and {1 1 11}, leading to the {11n} planes, visualised in Figure 24, and were also found to be favourable for dislocations to glide on, as shown in the statistical slip line analysis after nanoindentation tests. The critical resolved shear stress calculated after the micropillar compression test of the {112} and {111} planes was found to be in the same range, although the statistic shows, that the {111} planes are together with the {100} planes the less activated ones. This is because the geometrically possible slip systems are three times higher for the {11n} systems than for the {111} planes. NEB analysis also confirms the new planes and shows that no stable stacking fault would be realisable for the {11n} planes. Additionally, atomistic simulations have been performed to calculate the general stacking fault energy and the energy barriers to prove the theoretical capability for these planes, showing that {11n} planes have a comparatively low energy barrier, explaining their activation.

The found Burgers vector for the deformed zone was $\frac{1}{2}[1\bar{1}0]$, giving the dislocations the possibility to glide on the {111} as well as on the {11n} planes, which may be the reason why the zick-zack slip bands which could be found. Besides the straight dislocation slip on one specific slip plane, the cross slip was found to be activated in the cubic system, observable with a slip plane change from {111} → {112} and a more frequent change from {115} → {114} → {115}. Furthermore, the frequent change between the {11n} planes could be explained by their close alignment to each other, where the interplanar space between the {111} and {112} planes include more distance. This directly gives the ability for the dislocation to decompose. This was also confirmed by MEPs simulations. For the hexagonal *C*14 $CaMg_2$ Laves phase the slip systems that were activated were analysed by using a statistical surface trace analysis after the nanoindentation tests. This has shown a more frequent activation of the non-basal planes, which can be explained by its geometrical factor, of the number of geometrical possible slip systems. Whereas for micropillar compression tests no 2nd order prismatic slip system was observed, suggesting that the Schmid factor is too low and the CRSS too high compared to other slip systems.

2. How can the dislocation structure in the complex intermetallic phase and the mechanical properties be influenced by local chemistry, stoichiometry and with elevated temperature?

Influence of chemical composition on the room temperature plasticity of *C*15 Ca-Al-Mg Laves phases

Plastic deformation of the $CaMg_2$ C14-Laves phase from 50-250 °C

Temperature-driven nanoscale brittle-to-ductile transition of the *C*15 $CaAl_2$ Laves phase

The analysis of the influence on the temperature has been investigated in the hexagonal *C*14 $CaMg_2$ Laves phase for temperatures up to 250 °C, in a range from 0.30 – $0.53 \cdot T_M$. Thereby, for Laves phases defined BDTT lying around $0.6 \cdot T_M$ was not reached, which was represented by just negligible changes of the hardness and indentation modulus over the investigated orientations. Meaning the stress which was needed to activate the dislocations to move against the lattice resistance stays in the same range over the activated range. Although the mechanical properties remain unaffected by the temperature, observable decreasing serrations with increasing temperature in the nanoindentation load-depth-curve might result because dislocations nucleate. Otherwise, it could also be connected to the slightly off-stoichiometric composition, leading to the dislocation interaction, here the comparable larger Mg atom has a higher content than the smaller Al atom and might influence the strength of dragging points (hinder the motion of dislocation kinks → reducing dislocation velocity), which further decreases with temperature because the dislocations get more mobile, as visible by decreasing serrations with increasing temperature. Additionally, the BDTT for the cubic *C*15 $CaAl_2$ Laves phase was found to be lower for the nanoindentation test than for the microscopic test, showing a hardness decrease at temperatures of about 450-500 °C, with the BDTT calculated to be $0.55 \cdot T_M$. At 450 °C higher dislocation activity was identified by the drop in hardness and absence of fracture due to pillar splitting.

The dislocation characterisation of the dislocation type after the high temperature test (up to T > 600 °C) differs from that at room temperature where only $\frac{a}{2}\langle 1\bar{1}0\rangle$ dislocations were found, revealing a mixture of perfect $\frac{a}{2}\langle 1\bar{1}0\rangle$ and partial $\frac{a}{6}\langle 1\bar{1}2\rangle$ dislocations, showing the shift in dislocation mechanism from perfect dislocation glide to possible synchro-shear and was reported to be also present for macroscopic tests at high temperatures, mostly above the BDTT. Moreover, the dislocations tend to creep at temperatures above the BDTT.

In terms of anisotropy, no deviations were visible for the *C*14 $CaMg_2$ Laves phase in terms of mechanical properties, but the formation of surface traces seems to be strongly influenced by the orientation. This effect becomes stronger with increasing temperature, which is explainable by the activation of additional temperature activatable dislocation mechanisms, like cross slip or dislocation climbing, especially for not straight surface traces. Cross slip was found for the curved surface structures in the *C*15 $CaAl_2$ Laves phases, whereas the surface morphology strongly depends on the grain orientation. The influence of the chemistry on the anisotropic factor could be analysed and was found to increase with deviation from the binary $CaAl_2$ phase in terms of stiffness and surface traces. The influence of the local chemistry has been analysed for the cubic *C*15 $CaAl_2$ Laves phase by adding Mg and reducing Al. The mechanical properties, here measured as hardness and indentation modulus, show a decreasing trend with increasing Mg addition, which is confirmed by atomistic simulations of the mechanical properties giving the same results. This could be explained by the additional decreasing energy barrier, which was calculated with atomistic simulations, for the resulting slip systems, facilitating dislocation motion by simultaneously reducing the required stress for dislocation motion, resulting in a more ductile compound. Additionally, this could be the reason for the crack formation, whereas the binary compound and the $Ca_{33}Al_{61}Mg_6$ show cracks around the indents, for the $Ca_{36}Al_{53}Mg_{11}$ no cracks could be observed.

For all compounds, the [111] direction shows the highest hardness and indentation modulus but shows only cracks for $Ca_{33}Al_{67}$ and $Ca_{33}Al_{61}Mg_6$ and no surface traces for $Ca_{36}Al_{53}Mg_{11}$ leading to the assumption that the energy for crack nucleation is less than that for dislocation motion. All show in [001] direction curved lines, the lowest Schmid factor for all slip systems except the {110} and the lowest hardness and indentation modulus, which could be explained by having no distinguished easily activatable slip system. This is also shown by the TEM analysis by having a lot of slip bands corresponding to the {11n} planes, but also by observing dislocation dissociation from one plane to the other, for all three compositions.

The overall statistic of the slip traces shows that the local chemistry has no reasonable effect on the activation frequency. For all three compositions, the {11n} planes were the most detected and had the highest Schmid factor.

3. Can we derive general insights into the dislocation behaviour and the mechanical properties of Laves phases from the gained knowledge? And furthermore, predict with this the influence of temperature, strain rate and deviating stoichiometry on dislocations?

Plasticity of the C15-$CaAl_2$ Laves phase at room temperature

Influence of chemical composition on the room temperature plasticity of *C*15 Ca-Al-Mg Laves phases

Plastic deformation of the $CaMg_2$ C14-Laves phase from 50-250 °C

Temperature-driven nanoscale brittle-to-ductile transition of the *C*15 $CaAl_2$ Laves phase

Chapter 10 – on going work

As there were already more than 1400 Laves phases listed in 1991, and this number will continue to grow in the coming years and beyond, it is necessary to consider whether properties and changes can be transferred from one phase to another. Structurally, this would make sense due to the uniformity of arrangement for the respective structure types, and due to the fact, that all Laves phase structures are built up out of the same layers. Of course, the influence of the radius ratios may still play a superordinate role, especially when considering Laves phases with deviations in their stoichiometric composition. However, by studying the *C*15 prototype $MgCu_2$ and the *C*15 $CaAl_2$ Laves phase, it has been possible to gain a first insight into how the mechanical properties change with temperature and how the behaviour of the dislocations is influenced. By calculating the normalised shear stress, it can be seen, that these as well as for $MgCu_2$ as for $CaAl_2$ reveal values of $0.2\text{-}0.3 \cdot T_M$ up to the point between $0.5\text{-}0.6 \cdot T_M$

(shown in Figure 33). Moreover, the measured values of CaMg$_2$ lie in this range, leading to the assumption, that further normalised results will show the same trend. This would directly describe that the inherent stress given by the structure itself, is for every Laves phase in the same range, and hardness values would be predictable. Deformation in the investigated samples and systems was mainly present at the non-basal planes, meaning not on the triple layer planes, which describes a big contrast to previous studies on Laves phases. For both analysed *C*15 Laves phases dislocation slip on the {11n} planes could be found and were dominantly related to their relative activation frequency.

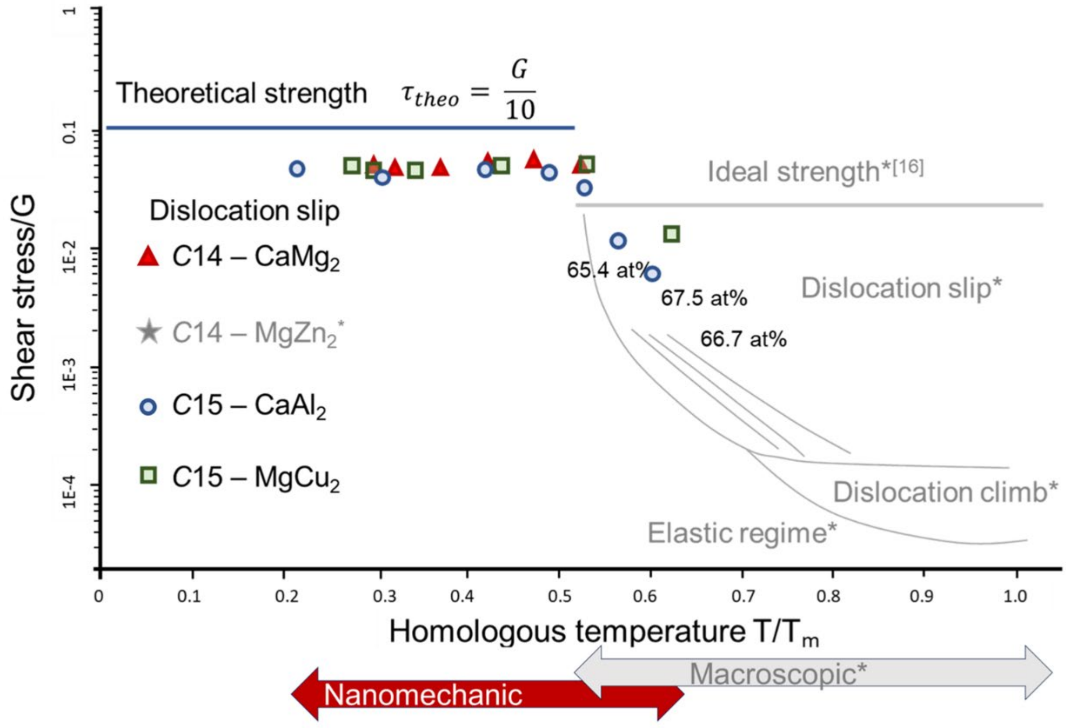

Figure 33: normalised shear stress against homologous T, showing the values for *C*14 CaMg$_2$ with red triangles, for *C*15 CaAl$_2$ with blue circles [7] and *C*15 CuMg$_2$ with green rectangles, gained from nanomechanical experiments. All values are plotted in Pauflers DMM, which he designed for *C*14 MgZn$_2$ in light grey using macroscopic experiments [12], whereas the ideal strength was taken accordingly to Kelly et al. [16].

Full dislocation slip was found to be energetically favourable at RT and changes to partial dislocation were found at 450 °C, which also fits the results from previous studies finding partial dislocations and the synchro-shear mechanism being the main deformation mechanism above the BDTT. The newly found planes make the isostructural comparison more difficult. For the new cubic planes, the stacking of the {112} can be compared with the hexagonal 1st order prismatic $\{10\bar{1}0\}$ planes, observable in Figure 33.

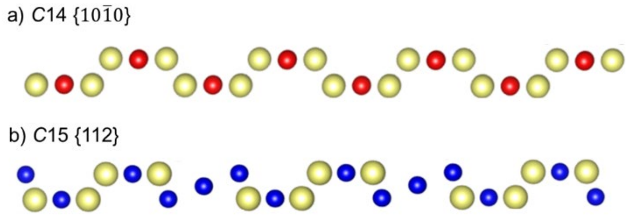

Figure 34: Stacking of a) hexagonal $\{10\bar{1}0\}$ plane and b) cubic $\{112\}$ plane.

The influence of the local chemistry and the temperature appears to have a greater impact on the dislocation behaviour and mechanical properties, but for both parameters, a critical point must be exceeded to observe a measurable influence. But both structures show decreasing mechanical properties, in this case hardness and indentation modulus, with the substitution of a third alloying element. Both reveal the morphological orientation dependency on surface traces, showing for *C*15_NS1 and *C*15_NS2 an increased observation of cross-slip mechanism, by orientations with curved lines, which leads to the assumption, that this will also be the case for *C*14 and *C*14_NS1 with this kind of surface morphologies.

5. Outlook and Future Work

The overall question of the dislocation structure in these complex intermetallic phases and the influence of the stoichiometry, local chemistry, and temperature could be answered by analysing the *C*14 $CaMg_2$ Laves phase up to temperatures of 250 °C and the influence of the local chemistry and its change with the *C*15 $Ca(Mg,Al)_2$ Laves phases at room temperature, but also opens more room for further investigations. The analysis of the pseudo-ternary *C*15 Laves phase indicate the influence of the local chemistry and shows that the new findings in slip systems are also dominant for these systems. The phenomena of change in hardness and modulus indicates that increasing the Mg and Ca content leads to softening, which correlates with atomistic simulations and with the absence of crack planes. In contrast, the number of surface traces decreases, and only tiny segments of straight lines can be seen, which requires more detailed analysis.

To understand and clarify the dislocation behaviour, their interaction, and their changes with the addition of a third alloying element, changing the internal stoichiometry, or increasing the temperature, several additional investigations could be performed and are listed in the following sections:

In this study the systematic analysis of the influence of the ternary element was hindered due to the non-constant Ca content with the substitution of Mg to the *C*15 $CaAl_2$ Laves phase, whereas here the influence of the off-stoichiometric Ca content (increased), can also have contributed to the mechanical changes. A systematic investigation on the effect of the radius variation of the ternary element or for specific binary systems, by just changing the A and leaving B constant or vice versa, on mechanical properties and dislocation behaviour, to be able to predict changes in chemistry more precisely, would be therefore interesting. Furthermore, these insights will help to understand the dislocation mechanisms on atomic size, by small systematic changes of just one atom.

References

1. Hull, D. and D.J. Bacon, Introduction to dislocations. 2001: Butterworth-Heinemann.
2. Conrad, H., Thermally activated deformation of metals. Jom, 1964. 16: p. 582-588.
3. Momma, K. and F. Izumi, VESTA 3 for three-dimensional visualization of crystal, volumetric and morphology data. Journal of applied crystallography, 2011. 44(6): p. 1272-1276.
4. Pearson, W. and C.B. Shoemaker, A system for the coding and generating of layered, tetrahedrally close-packed structures. Acta Crystallographica Section B: Structural Crystallography and Crystal Chemistry, 1969. 25(6): p. 1178-1183.
5. Zhu, J., et al., A thermodynamic interpretation of the size-ratio limits for laves phase formation. Metallurgical and Materials Transactions, 1999. 30(5): p. 1449.
6. Freund, M., et al., Plastic deformation of the CaMg2 C14-Laves phase from 50-250° C. Materialia, 2021. 20: p. 101237.
7. Kanjilal, A., et al., Temperature-driven nanoscale brittle-to-ductile transition of the C15 CaAl2 Laves phase. Materials & Design, 2024: p. 113206.
8. Zehnder, C., et al., Plastic deformation of single crystalline C14 Mg2Ca Laves phase at room temperature. Materials Science and Engineering: A, 2019. 759: p. 754-761.
9. Clegg, W.J., U.o.C. Course M5 - Part III, 2010.
10. Freund, M., et al., Influence of chemical composition on the room temperature plasticity of C15 Ca-Al-Mg Laves phases. arXiv preprint arXiv:2403.13432, 2024.
11. Clegg, W., L. Vandeperre, and J. Pitchford, Energy changes and the lattice resistance. Key Engineering Materials, 2006. 317: p. 271-276.
12. Paufler, P., Deformation-mechanism maps of the intermetallic compound MgZn2. Kristall und Technik, 1978. 13(5): p. 587-590.
13. Freund, M., et al., Plasticity of the C15-CaAl2 Laves phase at room temperature. Materials & Design, 2023. 225: p. 111504.
14. Jagodzinski, H., Polytypism in SiC crystals. Acta Crystallographica, 1954. 7(3): p. 300-300.
15. Jagodzinski, H., Eindimensionale Fehlordnung in Kristallen und ihr Einfluss auf die Röntgeninterferenzen. II. Berechnung der fehlgeordneten dichtesten Kugelpackungen mit Wechselwirkungen der Reichweite 3. Acta Crystallographica, 1949. 2(4): p. 208-214.
16. Kelly, A., W. Tyson, and A. Cottrell, Ductile and brittle crystals. The Philosophical Magazine: A Journal of Theoretical Experimental and Applied Physics, 1967. 15(135): p. 567-586.
17. Komura, Y., Stacking faults and two new modifications of the Laves phase in Mg–Cu–Al system. Acta Crystallographica, 1962. 15(8): p. 770-778.
18. Frank, F.C. and J.S. Kasper, Complex alloy structures regarded as sphere packings. II. Analysis and classification of representative structures. Acta Crystallographica, 1959. 12(7): p. 483-499.
19. Paufler, P., Early work on Laves phases in East Germany. Intermetallics, 2011. 19(4): p. 599-612.

20. Stein, F., M. Palm, and G. Sauthoff, Structure and stability of Laves phases. Part I. Critical assessment of factors controlling Laves phase stability. Intermetallics, 2004. 12(7-9): p. 713-720.

21. Zhu, J., et al., Point defects in binary Laves phase alloys. Acta materialia, 1999. 47(7): p. 2003-2018.

22. Berry, R. and G. Raynor, The crystal chemistry of the Laves phases. Acta Crystallographica, 1953. 6(2): p. 178-186.

23. Chisholm, M.F., S. Kumar, and P. Hazzledine, Dislocations in complex materials. Science, 2005. 307(5710): p. 701-703.

24. Kleber, W., et al., Einführung in die Kristallographie. 2010: Oldenbourg Verlag.

25. Laves, F. and H. Witte, Metallwirtschaft 1935, 14, 645; b) Laves, F. Naturwissenschaften, 1939. 27: p. 65.

26. Schulze, G.E., Zur Kristallchemie der intermetallischen AB2-Verbindungen (Laves-Phasen). Zeitschrift für Elektrochemie und angewandte physikalische Chemie, 1939. 45(12): p. 849-865.

27. Kim, W.Y., et al. Phase Relation and Room Temperature Mechanical Property of Cr2Zr Based Laves Phase. in Materials Science Forum. 2004. Trans Tech Publ.

28. Stein, F. and A. Leineweber, Laves phases: a review of their functional and structural applications and an improved fundamental understanding of stability and properties. Journal of Materials Science, 2021. 56(9): p. 5321-5427.

29. Yartys, V.A. and M.V. Lototskyy, Laves type intermetallic compounds as hydrogen storage materials: A review. Journal of Alloys and Compounds, 2022. 916: p. 165219.

30. Kaiser, T., et al., Probing porosity in metals by electrical conductivity: Nanoscale experiments and multiscale simulations. European Journal of Mechanics-A/Solids, 2023. 97: p. 104777.

31. Brando, M., et al., Logarithmic Fermi-liquid breakdown in NbFe 2. Physical review letters, 2008. 101(2): p. 026401.

32. Horie, Y., et al. Magnetic properties of Ta (Fe1− xTx) 2 with T= V, Cr, Mn, Co and Ni. in Journal of Physics: Conference Series. 2010. IOP Publishing.

33. Rahaman, M.Z. and M.A. Rahman, Novel Laves phase superconductor NbBe2: A theoretical investigation. Computational Condensed Matter, 2016. 8: p. 7-13.

34. Rapp, Ö., J. Invarsson, and T. Claeson, Search for superconductivity in Laves phase compounds. Physics Letters A, 1974. 50(3): p. 159-160.

35. Felten, M., et al., The effect of Laves phases and nano-precipitates on the electrochemical corrosion resistance of Mg-Al-Ca alloys under alkaline conditions. Journal of Magnesium and Alloys, 2024.

36. Song, G.L. and A. Atrens, Corrosion mechanisms of magnesium alloys. Advanced engineering materials, 1999. 1(1): p. 11-33.

37. Wu, P.-p., et al., Effect of extrusion on corrosion properties of Mg-2Ca-χAl (χ= 0, 2, 3, 5) alloys. Corrosion Science, 2017. 127: p. 280-290.

38. Friauf, J.B., The crystal structure of magnesium di-zincide. Physical Review, 1927. 29(1): p. 34.

39. Friauf, J.B., The crystal structures of two intermetallic compounds. Journal of the American Chemical Society, 1927. 49(12): p. 3107-3114.

40. Villars, P. and L. Calvert, Pearson's handbook of crystallographic data for intermediate phases. American Society of Metals, Cleveland, OH, 1985.

41. Villars, P. and L. Calvert, Pearson’s handbook of crystallographic data for intermetallic compounds. 1991, Materials Park, Ohio, USA: American Society for Metals.

42. Komura, Y. and K. Tokunaga, Structural studies of stacking variants in Mg-base Friauf–Laves phases. Acta Crystallographica Section B: Structural Crystallography and Crystal Chemistry, 1980. 36(7): p. 1548-1554.

43. Komura, Y. and Y. Kitano, Long-period stacking variants and their electron-concentration dependence in the mg-base friauf–laves phases. Acta Crystallographica Section B: Structural Crystallography and Crystal Chemistry, 1977. 33(8): p. 2496-2501.

44. Frank, F.C. and J.S. Kasper, Complex alloy structures regarded as sphere packings. I. Definitions and basic principles. Acta Crystallographica, 1958. 11(3): p. 184-190.

45. Shoemaker, D.P. and C.B. Shoemaker, Concerning the relative numbers of atomic coordination types in tetrahedrally close packed metal structures. Acta Crystallographica Section B: Structural Science, 1986. 42(1): p. 3-11.

46. Liu, X.-Y., et al., Self-assembled soft alloy with Frank–Kasper phases beyond metals. Nature Materials, 2024. 23(4): p. 570-576.

47. Sluiter, M.H., A. Pasturel, and Y. Kawazoe. Prediction of site preference and phase stability of transition metal based Frank-Kasper phases. in The Science of Complex Alloy Phases ashfield at the 134th TMS Annual Meeting. San Francisco. 2005.

48. Steurer, W. and J. Dshemuchadse, Intermetallics: structures, properties, and statistics. Vol. 26. 2016: Oxford University Press.

49. Grüner, D., Untersuchungen zur Natur der Laves-Phasen in Systemen der Übergangsmetalle. 2007.

50. Schulze, G.E., Über die Atomabstände in Laves-Phasen. Zeitschrift für Kristallographie-Crystalline Materials, 1959. 111(1-6): p. 249-258.

51. Pearce, P., Structure in Nature is a Strategy for Design. 1990: MIT press.

52. Zhu, J., et al., Enthalpies of formation of binary Laves phases. Intermetallics, 2002. 10(6): p. 579-595.

53. Pearson, W., Laves structures, MgCu2, MgZn2, MgNi2. Acta Crystallographica Section B: Structural Crystallography and Crystal Chemistry, 1968. 24(1): p. 7-9.

54. Thoma, D. and J. Perepezko, A geometric analysis of solubility ranges in Laves phases. Journal of alloys and compounds, 1995. 224(2): p. 330-341.

55. Amerioun, S., S.I. Simak, and U. Häussermann, Laves-Phase Structural Changes in the System CaAl2-x Mg x. Inorganic chemistry, 2003. 42(5): p. 1467-1474.

56. Amerioun, S., et al., Phase Stability in the Systems AeAl2-x Mg x (Ae= Ca, Sr, Ba): Electron Concentration and Size Controlled Variations on the Laves Phase Structural Theme. Inorganic chemistry, 2004. 43(15): p. 4751-4760.

57. Johnston, R.L. and R. Hoffmann, Structure-Bonding Relationships in the Laves Phases. Zeitschrift für anorganische und allgemeine Chemie, 1992. 616(10): p. 105-120.

58. Zhu, J., P. Liaw, and C. Liu, Effect of electron concentration on the phase stability of NbCr2-based Laves phase alloys. Materials Science and Engineering: A, 1997. 239: p. 260-264.

59. Laves, F. and H. Witte, Der einfluß von valenzelektronen auf die kristallstruktur ternärer magnesiumlegierungen. Metallwirtsch, 1936. 15(36): p. 840-842.

60. Nesper, R. and G.J. Miller, A covalent view of chemical bonding in Laves phases CaLixAl2− x. Journal of alloys and compounds, 1993. 197(1): p. 109-121.

61. Nesper, R., Bonding patterns in intermetallic compounds. Angewandte Chemie International Edition in English, 1991. 30(7): p. 789-817.

62. Zhu, J., C. Liu, and P. Liaw, Phase stability and mechanical behavior of NbCr2-based Laves phases. Intermetallics, 1999. 7(9): p. 1011-1016.

63. Von Keitz, A. and G. Sauthoff, Laves phases for high temperatures—Part II: Stability and mechanical properties. Intermetallics, 2002. 10(5): p. 497-510.

64. Livingston, J., Laves-phase superalloys. Physica Status Solidi A (Applied Research);(Germany), 1992. 131(2).

65. Kumar, K., et al., Structural stability of the Laves phase Cr2Ta in a two-phase Cr–Cr2Ta alloy. Acta Materialia, 2000. 48(4): p. 911-923.

66. Peierls, R. The size of a dislocation. 1940.

67. Xu, G. and C. Zhang, Analysis of dislocation nucleation from a crystal surface based on the Peierls–Nabarro dislocation model. Journal of the Mechanics and Physics of Solids, 2003. 51(8): p. 1371-1394.

68. Frenkel, J., Zur theorie der elastizitätsgrenze und der festigkeit kristallinischer körper. Zeitschrift für Physik, 1926. 37(7-8): p. 572-609.

69. Southgate, P. and A. Attard, Thermally activated dislocation kink motion in silicon. Journal of Applied Physics, 1963. 34(4): p. 855-863.

70. Caillard, D. and J.-L. Martin, Thermally activated mechanisms in crystal plasticity. 2003: Elsevier.

71. Seeger, A., The kink picture of dislocation mobility and dislocation-point-defect interactions. Le Journal de Physique Colloques, 1981. 42(C5): p. C5-201-C5-228.

72. Orowan, E., Problems of plastic gliding. Proceedings of the Physical Society, 1940. 52(1): p. 8.

73. Ashby, M.F., A first report on deformation-mechanism maps. Acta Metallurgica, 1972. 20(7): p. 887-897.

74. Fan, H., et al., Strain rate dependency of dislocation plasticity. Nature communications, 2021. 12(1): p. 1845.

75. Cottrell, A. Effect of solute atoms on the behavior of dislocations. in Report of a Conference on Strength of Solids. 1948. The Physical Society London London, UK.

76. Suzuki, H., Chemical interaction of solute atoms with dislocations. Sci. Rep. Res. Inst. Tohoku Univ. A, 1952. 4: p. 455-463.

77. Schmidt, C. and A. Miller, The effect of solutes on the strength and strain hardening behavior of alloys. Acta Metallurgica, 1982. 30(3): p. 615-625.

78. Zhang, F. and W. Curtin, Atomistically informed solute drag in Al–Mg. Modelling and Simulation in Materials Science and Engineering, 2008. 16(5): p. 055006.

79. Kabirian, F., A.S. Khan, and A. Pandey, Negative to positive strain rate sensitivity in 5xxx series aluminum alloys: Experiment and constitutive modeling. International Journal of Plasticity, 2014. 55: p. 232-246.

80. Kuhlmann-Wilsdorf, D., The theory of dislocation-based crystal plasticity. Philosophical Magazine A, 1999. 79(4): p. 955-1008.

81. Frank, F. and J. Nicholas, CXXVIII. Stable dislocations in the common crystal lattices. The London, Edinburgh, and Dublin Philosophical Magazine and Journal of Science, 1953. 44(358): p. 1213-1235.

82. Seeger, A. and U. Dehlinger, Kristallphysik II/Crystal Physics II. 2013: Springer-Verlag.

83. Paufler, P. and G. Schulze, Gleitsysteme innermetallischer Verbindungen. Kristall und Technik, 1967. 2(4): p. K11-K14.

84. Müller, T., et al., Gleitbanduntersuchungen während und nach Verformung der intermetallischen Verbindung MgZn2. Kristall und Technik, 1972. 7(11): p. 1249-1264.

85. Kubsch, H., P. Paufler, and G.E. Schulze, The mobility of grown-in dislocations in the intermetallic compound MgZn2 during prismatic slip. physica status solidi (a), 1974. 25(1): p. 269-275.

86. Müller, T. and P. Paufler, Yield strength of the monocrystalline intermetallic compound MgZn2. physica status solidi (a), 1977. 40(2): p. 471-477.

87. Kirsten, C., P. Paufler, and G. Schulze, Zur plastischen Verformung intermetallischer Verbindungen. Monatsber Dt Akad Wiss Berlin, 1964. 6(2): p. 140-147.

88. Takata, N., et al., Effect of Dislocation Sources on Slip in Fe 2 Nb Laves Phase with Ni in Solution. MRS Online Proceedings Library, 2013. 1516: p. 269-274.

89. Kumar, K. and P. Hazzledine, Polytypic transformations in Laves phases. Intermetallics, 2004. 12(7-9): p. 763-770.

90. Hazzledine, P., et al., Synchroshear of laves phases. MRS Online Proceedings Library (OPL), 1992. 288.

91. Hazzledine, P. and P. Pirouz, Synchroshear transformations in Laves phases. Scripta metallurgica et materialia, 1993. 28(10): p. 1277-1282.

92. Guénolé, J., et al., Basal slip in Laves phases: the synchroshear dislocation. Scripta Materialia, 2019. 166: p. 134-138.

93. Krämer, U. and G. Schulze, Gittergeometrische Betrachtung der plastischen Verformung von Lavesphasen. Kristall und Technik, 1968. 3(3): p. 417-430.

94. Saka, H., et al., Plasticity of single crystals of Fe2 (Dy, Tb) Laves phase at high temperatures. Philosophical Magazine A, 1993. 68(5): p. 871-884.

95. Kim, W.-Y., D.E. Luzzi, and D.P. Pope, Room temperature deformation behavior of the Hf–V–Ta C15 Laves phase. Intermetallics, 2003. 11(3): p. 257-267.

96. Pope, D.P. and F. Chu, Deformation of a C15 Laves phase: Twinning and synchroshear, in Structural intermetallics. 1993.

97. Xue, Y., et al., Critical resolved shear stress of activated slips measured by micropillar compression tests for single-crystals of Cr-based Laves phases. Materials Science and Engineering: A, 2021. 806: p. 140861.

98. Takeyama, M. and C. Liu, Microstructure and mechanical properties of Laves-phase alloys based on Cr2Nb. Materials Science and Engineering: A, 1991. 132: p. 61-66.

99. Luo, W., et al., Crystal structure and composition dependence of mechanical properties of single-crystalline NbCo2 Laves phase. Acta Materialia, 2020. 184: p. 151-163.

100. Luo, W., et al., Composition dependence of hardness and elastic modulus of the cubic and hexagonal NbCo2 Laves phase polytypes studied by nanoindentation. Journal of Materials Research, 2020. 35(2): p. 185-195.

101. Korte, S. and W.J. Clegg, Studying plasticity in hard and soft Nb–Co intermetallics. Advanced Engineering Materials, 2012. 14(11): p. 991-997.

102. Moran, J.B., Mechanical Behavior of MgCu2 Single Crystals. Transactions of the Metallurgical Society of AIME, 1965. 233(8): p. 1473-&.

103. Kazantzis, A., M. Aindow, and I. Jones, Stacking-fault energy in the C15 Laves phase Cr2Nb. Philosophical magazine letters, 1996. 74(3): p. 129-136.

104. Kazantzis, A., et al., On the self-pinning character of synchro-Shockley dislocations in a Laves phase during strain rate cyclical compressions. Scripta Materialia, 2008. 59(7): p. 788-791.

105. Kazantzis, A., et al., The mechanical properties and the deformation microstructures of the C15 Laves phase Cr2Nb at high temperatures. Acta materialia, 2007. 55(6): p. 1873-1884.

106. Kazantzis, A., M. Aindow, and I. Jones, Deformation behaviour of the C15 Laves phase Cr2Nb. Materials Science and Engineering: A, 1997. 233(1-2): p. 44-49.

107. Takata, N., et al., Nanoindentation study on solid solution softening of Fe-rich Fe2Nb Laves phase by Ni in Fe–Nb–Ni ternary alloys. Intermetallics, 2016. 70: p. 7-16.

108. Thoma, D., Intermetallics: laves phases. Encyclopedia of Materials: Science and Technology, 2001: p. 4205-4213.

109. Xie, Z., et al., Thermally activated nature of synchro-Shockley dislocations in Laves phases. Scripta Materialia, 2023. 235: p. 115588.

110. Xie, Z., et al., Unveiling the mechanisms of motion of synchro-Shockley dislocations in Laves phases. Physical Review Materials, 2023. 7(5): p. 053605.

111. Schröders, S., et al., Room temperature deformation in the Fe7Mo6 µ-Phase. International Journal of Plasticity, 2018. 108: p. 125-143.

112. Kronberg, M., Plastic deformation of single crystals of sapphire: basal slip and twinning. Acta Metallurgica, 1957. 5(9): p. 507-524.

113. Kumar, K., et al., Structure and composition of Laves phases in binary Cr–Nb, Cr–Zr and ternary Cr–(Nb, Zr) alloys. Intermetallics, 2003. 11(7): p. 677-685.

114. Liu, Y., S.M. Allen, and J.D. Livingston, Deformation of two C36 laves phases by microhardness indentation at room temperature. Metallurgical and Materials Transactions A, 1995. 26(5): p. 1107-1112.

115. Liu, Y., S.M. Allen, and J.D. Livingston, Deformation mechanisms in a Laves phase. MRS Online Proceedings Library (OPL), 1992. 288.

116. Liu, Y., J.D. Livingston, and S.M. Allen, Room-temperature deformation and stress-induced phase transformation of laves phases in Fe-10 at.% Zr alloy. Metallurgical Transactions A, 1992. 23: p. 3303-3308.

117. Liu, Y., J.D. Livingston, and S.M. Allen, Defect structures and nonbasal slip of C36 laves phase MgNi 2 in a two-phase alloy. Metallurgical and Materials Transactions A, 1995. 26(6): p. 1441-1447.

118. Liu, L., et al., First-principles calculations on the stacking fault energy, surface energy and dislocation properties of NbCr2 and HfCr2. Computational Materials Science, 2017. 140: p. 334-343.

119. Allen, S., Slip, twinning, and transformation in Laves phases. . 1998, Massachusetts Inst. of Technology (MIT), Cambridge, MA (United States).

120. Xie, Z., et al., Laves phase crystal analysis (LaCA): Atomistic identification of lattice defects in C14 and C15 topologically close-packed phases. Journal of Materials Research, 2021. 36(10): p. 2010-2024.

121. Kotula, P., et al., Defects and site occupancies in Nb-Cr-Ti C15 Laves phase alloys. Scripta materialia, 1998. 39(4-5): p. 619-623.

122. Thoma, D., et al., Elastic and mechanical properties of Nb (Cr, V) 2 C15 Laves phases. Materials Science and Engineering: A, 1997. 239: p. 251-259.

123. Chen, K.C., E.J. Peterson, and D.J. Thoma, HfCo2 Laves phase intermetallics—part I: solubility limits and defect mechanisms. Intermetallics, 2001. 9(9): p. 771-783.

124. Chen, K.C., et al., HfCo2 Laves phase intermetallics—part II: elastic and mechanical properties as a function of composition. Intermetallics, 2001. 9(9): p. 785-798.

125. Chu, F., et al., Phase stability and defect structure of the C15 Laves phase Nb (Cr, V) 2. Acta materialia, 1998. 46(5): p. 1759-1769.

126. Fujita, M., Y. Kaneno, and T. Takasugi, Phase field and room-temperature mechanical properties of C15 Laves phase in Nb–Hf–Cr and Nb–Ta–Cr alloy systems. Journal of alloys and compounds, 2006. 424(1-2): p. 283-288.

127. Chen, K.C., S.M. Allen, and J.D. Livingston, Factors affecting the room-temperature mechanical properties of TiCr2-base Laves phase alloys. Materials Science and Engineering: A, 1998. 242(1-2): p. 162-173.

128. Yoshida, M. and T. Takasugi, The alloying effect on the high temperature deformation of Laves phase NbCr2 intermetallic compound. Materials Science and Engineering: A, 1997. 234: p. 873-876.

129. Takasugi, T., M. Yoshida, and S. Hanada, Deformability improvement in C15 NbCr2 intermetallics by addition of ternary elements. Acta materialia, 1996. 44(2): p. 669-674.

130. Takasugi, T. and M. Yoshida, The effect of ternary addition on structure and stability of NbCr2 Laves phases. Journal of materials research, 1998. 13(9): p. 2505-2513.

131. Shields, T., J. Mayers, and I. Harris, Vacancy induced anomalies in the Laves phase CeNi2, in Anomalous Rare Earths and Actinides. 1987, Elsevier. p. 587-590.

132. Eichler, K., et al., Änderung von Verformungseigenschaften der intermetallischen Verbindung MgZn2 im Homogenitätsbereich. Kristall und Technik, 1976. 11(11): p. 1185-1188.

133. Pekguleryuz, M.O. and A.A. Kaya, Creep resistant magnesium alloys for powertrain applications. Advanced engineering materials, 2003. 5(12): p. 866-878.

134. Zubair, M., et al., On the role of Laves phases on the mechanical properties of Mg-Al-Ca alloys. Materials Science and Engineering: A, 2019. 756: p. 272-283.

135. Backes, B., et al., Particle hardening in creep-resistant Mg-alloy MRI 230D probed by nanoindenting atomic force microscopy. Metallurgical and Materials transactions A, 2009. 40: p. 257-261.

136. Baril, E., P. Labelle, and M. Pekguleryuz, Elevated temperature Mg-Al-Sr: creep resistance, mechanical properties, and microstructure. Jom, 2003. 55: p. 34-39.

137. Amberger, D., P. Eisenlohr, and M. Göken, On the importance of a connected hard-phase skeleton for the creep resistance of Mg alloys. Acta materialia, 2012. 60(5): p. 2277-2289.

138. Chung, Y.J., et al. Effects of alloying elements on mechanical properties of Mg-Al alloys. in Materials Science Forum. 2005. Trans Tech Publ.

139. Zhang, L., et al., Effect of Al content on the microstructures and mechanical properties of Mg–Al alloys. Materials Science and Engineering: A, 2009. 508(1-2): p. 129-133.

140. Amberger, D., P. Eisenlohr, and M. Göken, Microstructural evolution during creep of Ca-containing AZ91. Materials Science and Engineering: A, 2009. 510: p. 398-402.

141. Mathur, H., V. Maier-Kiener, and S. Korte-Kerzel, Deformation in the γ-Mg17Al12 phase at 25–278° C. Acta Materialia, 2016. 113: p. 221-229.

142. Sandlöbes, S., et al., A rare-earth free magnesium alloy with improved intrinsic ductility. Scientific reports, 2017. 7(1): p. 10458.

143. Zhang, L., et al., Microstructures and mechanical properties of Mg–Al–Ca alloys affected by Ca/Al ratio. Materials Science and Engineering: A, 2015. 636: p. 279-288.

144. Zhang, H., et al., Thermodynamic properties of Laves phases in the Mg–Al–Ca system at finite temperature from first-principles. Intermetallics, 2012. 22: p. 17-23.

145. Eibisch, H., et al., Effect of solidification microstructure and Ca additions on creep strength of magnesium alloy AZ91 processed by Thixomolding. International journal of materials research, 2008. 99(1): p. 56-66.

146. Ninomiya, R., T. Ojiro, and K. Kubota, Improved heat resistance of Mg-Al alloys by the Ca addition. Acta metallurgica et materialia, 1995. 43(2): p. 669-674.

147. Rzychoń, T., Characterization of Mg-rich clusters in the C36 phase of the Mg–5Al–3Ca–0.7 Sr–0.2 Mn alloy. Journal of Alloys and Compounds, 2014. 598: p. 95-105.

5. Publication 1

Plasticity of the C15-$CaAl_2$ Laves phase at room temperature

M. Freund, D. Andre, P.L. Sun, C.F. Kusche, S. Sandlöbes-Haut, H. Springer, S. Korte-Kerzel

Institute for Physical Metallurgy and Materials Physics, RWTH Aachen University, Aachen, Germany

Materials & Design, Volume 225, 2023, 111504, **reproduced with permission of Elsevier.**

https://doi.org/10.1016/j.matdes.2022.111504

Short Summary

In the Mg-Al-Ca System, three different Laves phases can be formed lying as second phase in the Mg matrix, which influence the mechanical properties and plasticity of the hole system. To understand the interaction of Laves phases with Mg, firstly the basics of Laves phases have to be clarified and be understood before secondly the System and the interaction between matrix phase and intermetallic phases can be unraveled. Especially the room temperature properties are rarely investigated due to its macroscopical brittle failure below the brittle-to-ductile transition temperature. One of the forming Laves phase is the $CaAl_2$ phase, which were analysed using nanomechanical testings, finding the previous studied slip systems and the new {112} planes, which occur to be, with the {111} planes, largely responsible for the plastic deformation at room temperature.

M. Freund: Writing – review & editing, Writing – original draft, Visualization, Investigation, Formal analysis, Conceptualization. D. Andre: Writing – review & editing, Investigation. P.-L. Sun: Visualization. C. F. Kusche: Writing - review. S. Sandlöbes-Haut: Writing - review. H. Springer: Resources. Sandra Korte-Kerzel: Writing –review & editing, Conceptualization, Supervision.

Materials & Design 225 (2023) 111504

Contents lists available at ScienceDirect

Materials & Design

journal homepage: www.elsevier.com/locate/matdes

Plasticity of the C15-$CaAl_2$ Laves phase at room temperature

M. Freund [a,*], D. Andre [a], P.L. Sun [a], C.F. Kusche [a], S. Sandlöbes-Haut [a], H. Springer [b,c], S. Korte-Kerzel [a]

[a] Institute of Physical Metallurgy and Materials Physics, RWTH Aachen University, Germany
[b] Max-Planck-Institut für Eisenforschung GmbH, Düsseldorf, Germany
[c] Institute of Metal Forming, RWTH Aachen University, Aachen, Germany

HIGHLIGHTS

- We find that the {1 1 2} plane seems to be dominant for plasticity, although previous literature lists deformation on the {1 1 1} plane as the dominant mechanism for C15 Laves phases.
- We could quantify the CRSS for both slip systems, namely $\{111\}\langle 1\bar{1}0\rangle$ and $\{112\}\langle 1\bar{1}0\rangle$, as approximately the same at ∼ 1 GPa.
- Our TEM investigations confirm the $[1\bar{1}0]$ Burgers vector type by using the g•b analysis.
- Together, these insights also allow us to explain why the crack and slip trace distribution around indentations varies systematically with crystal orientation.

GRAPHICAL ABSTRACT

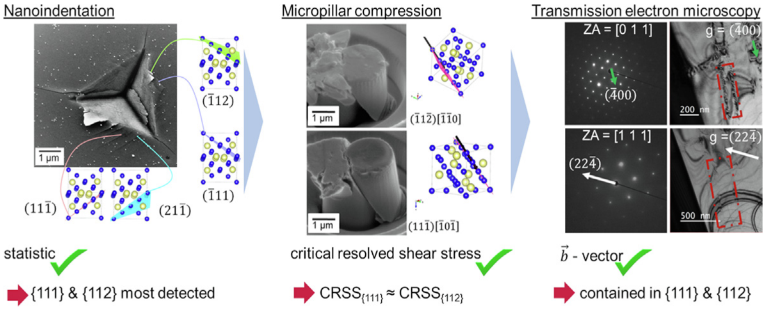

ARTICLE INFO

Article history:
Received 19 October 2022
Revised 2 December 2022
Accepted 12 December 2022
Available online 13 December 2022

Keywords:
Laves phases
$CaAl_2$
Plasticity
Electron microscopy
Nanoindentation
Micropillar compression

ABSTRACT

The room temperature plasticity of the cubic C15 $CaAl_2$ Laves phase was investigated using nanomechanical testing and electron microscopy. The correlation between slip traces in the vicinity of nanoindents and crystallographic orientation data allowed us to gain statistical data on the activated slip and crack planes for 10 different crystallographic orientations. Slip on {1 1 1} and {1 1 2} planes was found to be most favourable for all orientations, whereas cracks predominantly occurred on {1 1 2} planes. A constant hardness of 4.9 ± 0.7 GPa and an indentation modulus of 85.5 ± 4.0 GPa for all investigated orientations for a constant strain rate and a strain rate sensitivity of 0.028 ± 0.019 were measured. Micropillar compression tests and transmission electron microscopy confirmed slip on {1 1 1} and {1 1 2} planes with a Burgers vector of $<1\bar{1}0>$ type. This allowed to determine the critical resolved shear stresses as 0.99 ± 0.03 GPa for $\{111\}<1\bar{1}0>$ and 0.97 ± 0.07 GPa for $\{112\}<1\bar{1}0>$ slip.

1. Introduction

Laves phases are a very common type of intermetallic compound, formed in many binary and ternary systems, as well as being "building blocks" of larger unit cells, such as in the µ-phase, which is a major precipitation phase in steels and superalloys [1,2]. Laves phases were discussed as the basis of future high temperature alloys, and have received recurring attention with a shifting focus on understanding their fundamental structure, stability and mechanical properties [3]. As topologically close packed phases (TCP) with the ideal composition AB_2 formed around an

---

* Corresponding author.
E-mail address: freund@imm.rwth-aachen.de (M. Freund).

https://doi.org/10.1016/j.matdes.2022.111504
0264-1275/© 2022 The Authors. Published by Elsevier Ltd.

ideal ratio of the atomic diameters of $\sqrt{3/2}$, they are also being studied in colloids in the context of photonic crystals with a tunable bandgap [4] and to advance our understanding of amorphous and crystalline phase and defect formation [5,6].

The Laves phase $CaAl_2$ commonly occurs as precipitates in magnesium alloys containing Al and Ca. Despite its inherent brittleness, it can positively influence the plastic deformation of the magnesium alloys at room and moderately elevated temperatures and it is for this reason, and to widen our still limited knowledge about plastic deformation in these brittle crystals, that in this study the room temperature mechanical properties of the $CaAl_2$ Laves phase is investigated.

When Mg is alloyed with both Al and Ca, the Ca/Al ratio determines which intermetallic phase(s) are precipitated and their degree of interconnectivity formed in the magnesium matrix [7,8]. Recent work by Zubair et al. [9] revealed that, during tensile tests, a high interconnectivity provides a preferred growth path for cracks and thus promotes brittle failure, whereas a low connectivity results in an improved overall ductility. However, in creep testing [10], a higher degree of interconnectivity was found to yield an improvement of creep resistance as the intermetallic skeleton hinders dislocation motion [9]. A balance can therefore be struck by carefully choosing alloy composition and solidification conditions to balance sufficient ductility and improved creep resistance depending on the intended technical application. These promising results indicate that Laves phases are potential candidates to improve the creep strength of Mg-Al-alloys for applications above 150 °C, where the more commonly introduced $Mg_{17}Al_{12}$ phase becomes soft [11].

The intermetallic Laves phases formed in Mg-Al-Ca-alloys are the cubic $CaAl_2$ (C15 type), the hexagonal $CaMg_2$ (C14 type) and the hexagonal $Ca(Mg,Al)_2$ (C36 type) phases. The cubic $CaAl_2$ phase is characterised by its high melting temperature (1079 °C for the $CaAl_2$ phase as compared to 715 °C for the $CaMg_2$ phase [12]) and its high creep resistance compared to the hexagonal phases [12]. Creep tests at various temperatures by indentation with a Vickers indenter tip on the $CaAl_2$ phase have shown that for a holding time of 30 s, the microhardness only decreased moderately, from 402 HV to 318 HV and respectively, for a holding time of 3600 s, from 356 HV to 294 HV, with a temperature increase of 280 K from homologous temperatures, T_H, of 0.6 to 0.71 $\cdot T_m$ (T_m=melting temperature in K). In contrast to this, a more pronounced decrease in hardness could be observed for the hexagonal $CaMg_2$ phase showing a decreasing hardness from 156 HV to 47 HV for a 30 s holding period and 149 HV to 10 HV for 3600 s at the same temperature difference [12].

Due to the topologically closed packed structure of Laves phases, plasticity at ambient temperature is mostly impeded, leading to a gap of knowledge regarding mechanisms of plasticity at temperatures below the brittle-to-ductile transition temperature (BDTT), which was measured for Laves phases lying approximately between 60 and 71 % of the melting temperature [13–17]. Therefore, most of the previous literature has investigated Laves phases in temperature ranges above the BDTT, since macroscopic experimental setups can only introduce plasticity in this temperature regime. We summarise these studies on the deformation mechanisms of several cubic C15 Laves phases in the next section.

A theoretical approach of the deformation behaviour of Laves phases by Krämer et al. [16] revealed dislocation motion on the $\{1\,1\,1\}$ plane with $\frac{1}{2}\langle 1\,1\,0\rangle$ perfect dislocations or $\frac{1}{6}\langle 1\,1\,2\rangle$ partial dislocations. Furthermore, possible dislocation motion without dissociation on the $\{1\,0\,1\}$ plane with $\langle 0\,1\,0\rangle$ perfect dislocations and $\frac{1}{4}\langle 1\,2\,1\rangle$ dislocations for the cubic Laves phase was observed. Macroscopic, experimental tests led to similar results as predicted by Krämer for deformation above the BDTT. Studies on the $MgCu_2$ phase found that in addition to the $\{1\,1\,1\}$ plane, the $\{1\,1\,0\}$ and $\{1\,0\,0\}$-planes may act as additional slip planes (380–660 °C, 0.48–0.83 $\cdot T_m$) [18]. In a temperature range of 400–725 °C, 0.50–0.91$\cdot T_m$, other than the $(1\,1\,1)[1\,1\,0]$ slip system, the $(1\,1\,1)[1\,1\,2]$ twinning system was found [19]. Mechanical twinning was also the most frequently detected deformation mechanism for HfV_2 and HfV_2 + Nb for room temperature (RT), 0.02$\cdot T_m$, deformation tests [20,21]. Furthermore, perfect dislocations on the $\{1\,1\,1\}$ plane with $\frac{1}{2}\langle 1\,0\,1\rangle$ were found in $Fe_2(Dy,Tb)$ ($\geq$875 °C, $\geq$ 0.7 $\cdot T_m$), HfV_2 +-Nb (RT) and $NbCr_2$ (1300–1400 °C, 0.75–0.81 $\cdot T_m$), while $NbCr_2$ (1300–1400 °C) also showed dislocations on $\{1\,1\,1\}$ planes dissociating into two $\frac{1}{6}\langle 1\,1\,2\rangle$ Shockley partials [20–24].

Experiments at room temperature were done using micropillar compression tests to suppress cracking below the BDTT [25], so that beside the slip system, critical resolved shear stresses (CRSS) for the observed slip systems could be identified. Micropillar compression studies of $NbCr_2$ and $NbCo_2$ revealed slip on the $\{1\,1\,1\}\langle 1\,1\,0\rangle$ slip system for both, with a CRSS of 4.6 GPa for orientations aligned for single slip and 4.4 GPa ($NbCr_2$) and 3.0–3.1 ± 0.7 GPa ($NbCo_2$) for orientations aligned for multiple slip [25–27]. Moreover, Korte et al. [28] and Luo et al. [29] found both the activation of the $\{111\} < 1\,\bar{1}\,0 >$ slip system for $NbCo_2$ and reported a CRSS of 3.1 ± 0.7 GPa and 3.2 ± 0.7 GPa, while Lou et al. [29] also observed the dislocation motion in the $< 1\,1\,\bar{2} >$ direction on $\{1\,1\,1\}$ planes with nearly the same CRSS of 3.0 ± 0.8 GPa.

The underlying mechanism by which deformation in Laves phases on these slip systems is often reported to occur is the so-called synchroshear mechanism on crystallographic planes containing the characteristic triple layer of Laves phases. The triple layer lies parallel to the $\{1\,1\,1\}$ plane in the cubic C15 and parallel to the basal plane in the hexagonal C14 and C36 phases, and also related intermetallic phases containing Laves phase elements [30–35]. This mechanism is associated with local phase transformations from the hexagonal C14 or C36 to the cubic C15 phase after macroscopic compression tests [36–39], in which case it enables the transition by a simple restacking along the basal plane to create the different packings of these phases. The synchroshear mechanism consists of a synchronous movement of two neighbouring partial dislocations on a triple layer and essentially reverses the stacking direction within the triple layer, giving a local transformation between the prototypical phases or rather forming a stacking fault within the parent structure that corresponds to one of the other structures [30–32].

As seen above, the application of new testing methods on the nanoscale, such as nanoindentation and micropillar compression, now allows us to introduce plasticity in brittle materials below the BDTT. Here, we exploit these methods in conjunction with conventional transmission electron microscopy (TEM) analysis in order to gain a deeper understanding of the mechanisms governing plasticity in Laves phases. For the Mg-Al-Ca system, the hexagonal C14 Laves phase has already been characterised up to a temperature of 250 °C and, interestingly, non-basal slip was found to be predominant at all temperatures in addition to basal slip along the triple layer [40,41]. In contrast, the low temperature deformation behaviour of the cubic C15 is still to be unraveled, especially the qualitative and quantitative determination of the modulus, hardness, the rate dependence and activated slip systems. With this study, we aim to close this gap of knowledge by means of a statistical analysis of slip and crack planes around indentation deformation zones and evaluate possible slip systems and their critical resolved stresses by micropillar compression tests. To achieve a detailed insight into the underlying slip systems and mechanisms, further conventional TEM was used.

2. Experimental methods

2.1. Synthesis and microstructure characterisation

The as-cast samples of nominal $CaAl_2$ composition underwent an annealing procedure in a glass tube furnace under argon atmosphere at 600 °C for 24 h to ensure a homogeneous elemental distribution and obtain grain sizes in the range of a few hundred micrometers. Metallographically the samples were prepared as described in more detail in a previous publication [42]. In a first step, the samples were ground using SiC paper with a grit size of 1200 to 4000, followed by mechanical polishing steps with diamond paste from 6 μm down to 0.25 μm and ethanol with 5 % Polyethylene Glycol 400 (PEG) as a lubricant. A final oxide polishing with a grain size of 0.04 μm and cleaning step with soap and water followed.

Backscattered electron (BSE) imaging in a scanning electron microscope (SEM) (Helios Nanolab 600i, FEI, Eindhoven, NL) at an acceleration voltage of 5 kV revealed a two-phase microstructure with a matrix phase and a secondary phase surrounding the matrix phase (Fig. 1). Additionally, energy dispersive X-ray spectroscopy (EDX) measurements were performed in order to reveal the local chemical composition of the microstructure constituents, by calculating the chemistry over at least 34 point-measurements for both phases. The composition of the matrix phase was found to be 66.5 ± 2.5 at.-% Al and 33.6 ± 1.3 at.-% Ca, which corresponds well to the ideal stoichiometric composition of the $CaAl_2$ phase. The secondary phase consisted of 80.2 ± 1.1 at.-% Al and 19.8 ± 1.0 at.-% Ca and is thus attributed to the $CaAl_4$ phase.

The use of electron backscatter diffraction (EBSD) imaging (Helios Nanolab 600i, FEI, Eindhoven, NL) at an accelerating voltage of 20 kV and a current of 5.5 nA allowed us to identify the grain orientations of the cubic $CaAl_2$ phase, whereas for the tetragonal $CaAl_4$ phase, indexing was not possible because of diffuse Kikuchi patterns. This data was further analysed using orientation imaging microscopy (OIM) analysis^{TM} (EDAX Inc.) in order to obtain the Schmid factors for certain slip systems of the $CaAl_2$ grains used for micropillar compression.

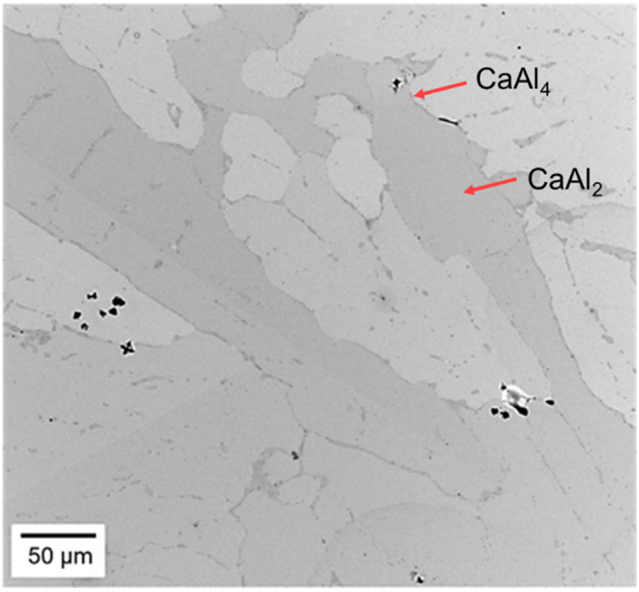

Fig. 1. Backscatter electron image of the microstructure recorded at an acceleration voltage of 5 kV. The matrix phase corresponds to the C15 $CaAl_2$ phase while the surrounding corresponds to the $CaAl_4$ phase.

2.2. Nanoindentation experiments

Nanomechanical tests were performed using an iNano nanoindenter (Nanomechanics Inc., TN, USA) with a diamond Berkovich tip (supplied by Synton MDP, Switzerland) and a dynamic indentation unit (continuous stiffness measurement (CSM)). Prior to testing, the diamond area function (DAF) of the indenter tip was calibrated according to the Oliver and Pharr method [43]. All nanomechanical tests were conducted in the $CaAl_2$ matrix phase at least 10 μm away from the $CaAl_4$ phase [44]. The first nanoindentation tests were performed with a constant strain rate of 0.2 s^{-1} up to a maximum depth of 500 nm. Before unloading, the indenter had a holding period of 2 s. These experiments were analysed for the hardness and indentation modulus as well as for slip traces in the vicinity of the nanoindents. This was done for a total of 120 nanoindents with 890 slip traces in 10 different crystal orientations by correlating the information from EBSD results and secondary electron (SE) images of the indents, as shown in [45].

Furthermore, strain rate jump tests (SRJT) in two different orientations were conducted based on the method first mentioned by Maier-Kiener et al. [46–48] to evaluate the strain rate sensitivity and activation volume of the $CaAl_2$ phase. These were performed at different strain rates of 0.1 s^{-1}, 0.04 s^{-1}, 0.1 s^{-1} and 0.01 s^{-1} with jumps taking place every 100 nm starting at 100 nm indentation depth.

2.3. Micropillar compression experiments

A total number of 15 micropillars with an aspect ratio of approximately 2.5 (pillar top diameter 2.1 μm/ pillar height 5.2 μm) was milled in seven differently oriented grains using focused ion beam (FIB) (Helios Nanolab 600i, FEI, Eindhoven, NL) milling. The compression tests were performed in-situ using an InSEM nanoindenter (Nanomechanics Inc., TN, USA) in an SEM (CLARA, Tescan, Brno, Czech Republic) with an approximate strain rate up to the onset of yielding of 0.1 s^{-1} and were manually stopped when a large strain burst was observed. Post-mortem SE images of the micropillars were taken under a 45° tilt angle using an acceleration voltage of 5 kV and a beam current of 0.69nA. This allowed us to identify the slip planes and potential slip directions for each micropillar. The obtained mechanical data was further corrected for elastic sink deformation of the tip and substrate using the Sneddon correction [49]. Subsequently, the stress at the initial strain burst was converted to the critical resolved shear stress (CRSS) for each slip system.

2.4. TEM experiments

Two TEM lamellae were cut out from indents using site specific FIB milling. The lamellae were then analysed using a JEOL JEM-F200 TEM under different two-beam conditions at 200 kV. A $g \cdot b$ extinction analysis, with g being the diffraction vector and b being the Burgers vector allowed us to identify the Burgers vectors of the dislocations.

3. Results

In order to unravel the mechanical properties and activated slip systems of the $CaAl_2$ phase at ambient temperature, several nanomechanical testing methods were applied: (I) nanoindentation tests to obtain the hardness and indentation modulus, (II) strain rate jump tests in order to determine the strain rate sensitivity and activation volume, (III) slip trace analysis in the vicinity of indents in order to gain a statistical measure of the activated slip systems and (IV) micropillar compression tests to identify the slip planes and calculate the CRSS values using also information from (V) a consecutive TEM analysis, to determine the Burgers vectors of the introduced dislocations from the nanomechanical experiments.

3.1. Nanoindentation

The hardness and indentation modulus were calculated from a continuous stiffness measurement between 350 and 500 nm indentation depth and resulted in an average hardness of 4.9 ± 0.7 GPa and an average indentation modulus of 85.5 ± 4.0 GPa over all 10 orientations, using a constant Poisson ratio of 0.3. A representative load-indentation depth curve is given in Fig. 2. All load-indentation depth curves exhibit serrations, which became more pronounced with higher indentation depths.

Fig. 3 displays the results of the strain rate jump tests, showing a representative curve of the hardness change over the indentation depth with varying strain rate. The average hardness of 5.8 ± 0.8 GPa for the strain rate jump tests agrees, within the standard deviations, with the measured values at the constant strain rate of 0.2 s^{-1}. The averaging over depth for the strain rate jump tests was done over a depth range of 100 – 500 nm, including all measured strain rates. For all orientations, the first jump was conducted at approximately 100 nm followed by strain rate jumps (0.1 s^{-1}; 0.04 s^{-1}; 0.1 s^{-1}; 0.01 s^{-1}) every 100 nm. For the second jump, the hardness increased slightly whereas it decreased between 200 and 300 nm at the next jump to slower strain rates.

From this change in hardness with strain rate, the strain rate sensitivity (m) and the activation volume (V) can be calculated [46–48,50].

The strain rate sensitivity can be calculated based on equation (1):

$$m = \frac{d(\ln H)}{d(\ln \dot{\varepsilon})} \tag{1}$$

with H the hardness and $\dot{\varepsilon}$ the strain rate. The activation volume can then be calculated as

$$V = \frac{3\sqrt{3}\ k\ T}{m\ H} \tag{2}$$

with k the Boltzmann constant and T the absolute temperature in K.

The calculation of the strain rate sensitivity was performed by evaluating the hardness change at the jumps, taking a total amount of 600 values, 300 before and 300 after each hardness jump into account, and calculating the slope of these hardness data before and after the jump. With the extension of these linear trends from each strain rate increment, the hardness difference could be measured at the point of rate change to calculate the strain rate sensitivity. This led to an average strain rate sensitivity of 0.028 ± 0.019 and an activation volume of 0.530 ± 0.780 nm^3, corresponding to 3.75 ± 1.15 b^3, calculated with a lattice parameter of 0.80428 nm and a Burgers vector along the closed packed direction $\frac{a}{2}\langle 110\rangle$ (b = 0.5685 nm).

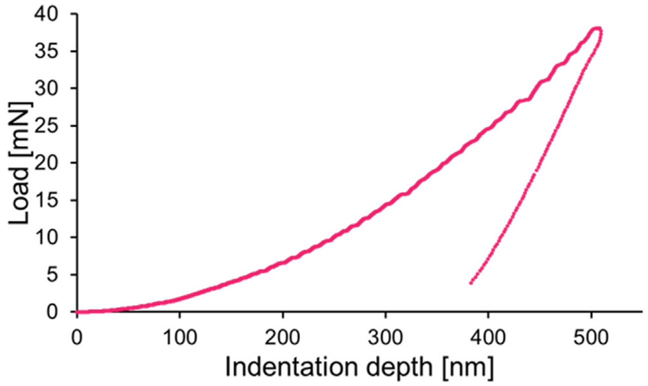

Fig. 2. Representative nanoindentation load-indentation depth curve at a constant strain rate of 0.2 s^{-1} to a maximum depth of 500 nm.

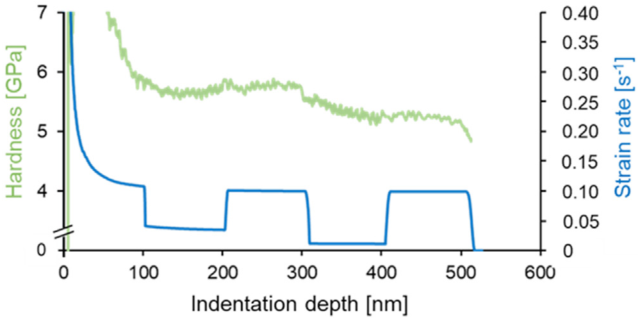

Fig. 3. Hardness and strain rate values over indentation depth for the $CaAl_2$ phase. The strain rate jump test (SRJT) was performed at different strain rates of 0.1 s^{-1}, 0.04 s^{-1}, 0.1 s^{-1}, 0.01 s^{-1}, which was varied every 100 nm.

3.2. Slip line analysis

The slip line analysis was performed on 120 indents, corresponding to 10 different crystallographic orientations. The evaluated indents were performed with a constant strain rate. For all investigated indents, at least one crack was observed to initiate from one of the indent corners, whereas not all indents were surrounded by visible slip lines.

For the slip line analysis, a MatLab® Code was used [45], which, together with the orientation data gained from EBSD measurements, (semi)automatically identified the most probable slip plane from SEM images. For this procedure, a tolerance angle of 3° between the measured angle of the slip trace with the horizontal and the identified plane was chosen. Due to the only small angular deviation in the plane of the sample surface between the {1 1 1} and {1 1 2} planes for some orientations, the automatic analysis has been manually corrected as described in [45] where the angle between both planes was found to be smaller than 3°. If more than one slip plane was assigned to the occurring slip plane, both possibilities were counted, so that the overall activation frequency in this case amounts to more than 100 %. The slip traces around the indents were then subdivided into three categories according to their morphology, namely lines, edges and curves, as suggested by Schröders et al. [51] (Fig. 4). All grain orientations are displayed in Fig. 4 within the inverse pole figure (IPF) map with a colour code visualising the morphology of the surface traces and those orientations in which only cracks were observed. As each indent for which slip traces were observed also had at least one adjacent crack, they were not included as an additional category in Fig. 4.

Fig. 5 displays examples of the slip trace analysis. For the identification of slip planes only straight lines and edges were used.

A total of 890 surface traces, including slip lines and cracks formed around a total of 120 indentations, were evaluated in order to obtain a statistical analysis. 625 of these surface traces pertain to plastic deformation and 265 to cracks, both were analysed separately. The corresponding results are depicted in Fig. 6. For the plastic deformation, 58 % of the resulting slip traces were correlated to {1 1 1} planes, followed by the {1 1 2} planes with an activation frequency of 48 % (the total activation frequency reaches over 100 % as a result of double counting of slip planes when the angle of different candidate slip planes is less than 3°). For the cracks, ori-

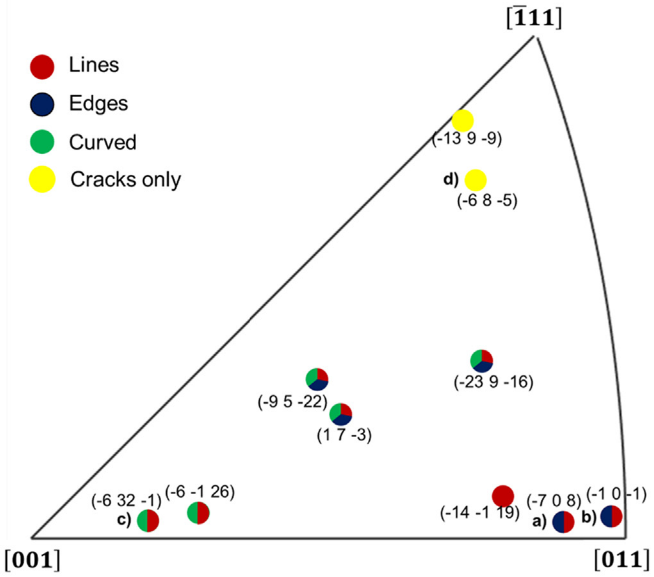

	{111}	{112}	{110}	{100}
(-13 9 -9)	0.35	0.40	0.29	0.50
(-6 8 -5)	0.38	0.35	0.32	0.50

	{111}	{112}	{110}	{100}
(-23 9 -16)	0.35	0.49	0.45	0.47
(1 7 -3)	0.35	0.43	0.35	0.22
(-9 5 -22)	0.48	0.46	0.44	0.37

	{111}	{112}	{110}	{100}
(-1 0 -1)	0.41	0.48	0.41	0.35
(-7 0 8)	0.47	0.33	0.43	0.35
(-14 -1 19)	0.47	0.19	0.45	0.35

	{111}	{112}	{110}	{100}
(-6 32 -1)	0.46	0.49	0.39	0.15
(-6 -1 26)	0.49	0.49	0.35	0.16

Fig. 4. Orientations of all analysed grains for slip line analysis as an inverse pole figure map with corresponding morphology of surface traces, such as in the publication of Schröders et al. [51], see Fig. 5 for images of the different morphologies here. All indents contain cracks, but with yellow, the orientation is shown, where only cracks were observed, red shows straight slip lines, blue edges and green rounded surface traces. The orientations labelled (a), (b), (c) and (d) are shown in a detailed slip line analysis in the corresponding subfigures of Fig. 5. Additionally, the highest Schmid factor for each slip system is given in the table. The Schmid factors were calculated by assuming uniaxial compression. (For interpretation of the references to colour in this figure legend, the reader is referred to the web version of this article.)

entations along {1 1 2} and {1 1 0} planes were mostly detected with 37 % and 28 %, respectively. 4 % of slip planes and 19 % of crack planes could not be assigned to any plane. The comparatively high number of not indexed crack planes results from the curved crack path and the changing morphology along the crack, which may nucleate at small depths and progress outwards as the indent is pushed further into the surface. In contrast, slip traces form and are successively flattened by the proceeding indentation, so that only the final traces remain visible outside the contact zone.

3.3. Micropillar compression

A total of 15 micropillars corresponding to 7 different orientations were deformed until strain bursts occurred. Representative micropillars for each orientation are depicted in Fig. 7 a) including their correspondingly oriented unit cells (Fig. 7 b)) and the engineering stress strain curves (Fig. 8). For slip plane determination, the 45° tilted SE-images of the micropillar were compared to the 90° tilted unit cell taken from VESTA, to realise the side view [52]. The slip angles of both images were compared taking the tilt during imaging of 45° into account using $\gamma_{90} = \tan^{-1}\left(\tan(\gamma_{45})\cdot\sqrt{2}\right)$. The corresponding slip planes were again assigned with a tolerance of ± 3°. For the slip direction the best fitting slip plane and Burgers vector with the highest Schmid factor were assumed. The slip planes found to show deviation angles of $\leq 3°$ were the {1 1 1} and {1 1 2} slip planes. The distinction of these planes was not as difficult as in the slip plane analysis of the deformation zone around indents, as the angular difference was more clearly visible in the geometry of a micropillar.

The CRSS was determined by taking the engineering stress, at the point at which the first strain burst happened, multiplied with the Schmid factor of the determined slip system.

All compressed micropillars are listed in Table 1 including their identified slip systems, Schmid factors (m_S), compression axes, yield stresses (σ_y) and CRSS values.

Overall, 10 of the 15 pillars slipped on the {1 1 1} planes and 5 on the {1 1 2} planes. Slip on the {1 1 1}<1 $\bar{1}$ 0 > slip systems occurred at an average yield stress of 2.96 ± 0.54 GPa resulting in an average CRSS of 0.99 ± 0.07 GPa (Table 1), whereas slip on the {1 1 2}<1 $\bar{1}$ 0 > slip systems occurred at a yield stress ranging from 2.67 GPa to 3.69 GPa resulting in an average of 2.94 ± 0.24 GPa and an average CRSS value of 0.97 ± 0.03 GPa (Table 1). The error is given as the standard deviation for the specific slip systems.

For micropillar 13 and 14, the CRSS could not be determined unambiguously, and is therefore marked with a "*" in Table 1 and not included in the average values given above. This is due to the activation of two slip systems and the impossibility of assigning the strain bursts to one of the slip systems. Fig. 9 depicts the slip events observed for pillar 13. From the front (Fig. 9 a)), only one slip system, $\left(\bar{1}\,2\,1\right)\left[\bar{1}\,0\,\bar{1}\right]$, is visible, whereas in the back view (Fig. 9 b)), two slip systems are visible, both belonging to the {1 1 2} <1 $\bar{1}$ 0 > slip system.

In Table 2 all measured mechanical properties and their corresponding values are listed.

3.4. TEM

For TEM analysis, a site-specific lamella was lifted out from an indent for which the {1 1 1} and {1 1 2} planes could not be distinguished by surface analysis alone. Fig. 10 a) displays the alignment of the lamella, where letters "A" and "B" represent the two sides of the lamella. Additionally, the possible slip planes, $(1\,1\,\bar{1})$, $(2\,1\,\bar{1})$, $(\bar{1}\,1\,1)$ and $(\bar{2}\,1\,1)$, determined by the slip line analysis are shown in the unit cells. In Fig. 10 b), a scanning transmission electron microscopy (STEM) image of the deformation zone is shown. Some clear lines next to the indent at the "A" side are observed to go from the bulk material to the surface. In addition, the surface slip traces were assigned to be the edged lines on the surface and thus correlated to ductile deformation. Looking at the deformation zone below the indentation, cracks can be seen emanating from these edged slip lines.

Fig. 10(c) displays a bright field (BF) TEM image taken along the [1 1 2] zone axis. It can be seen that the deformed microstructure is

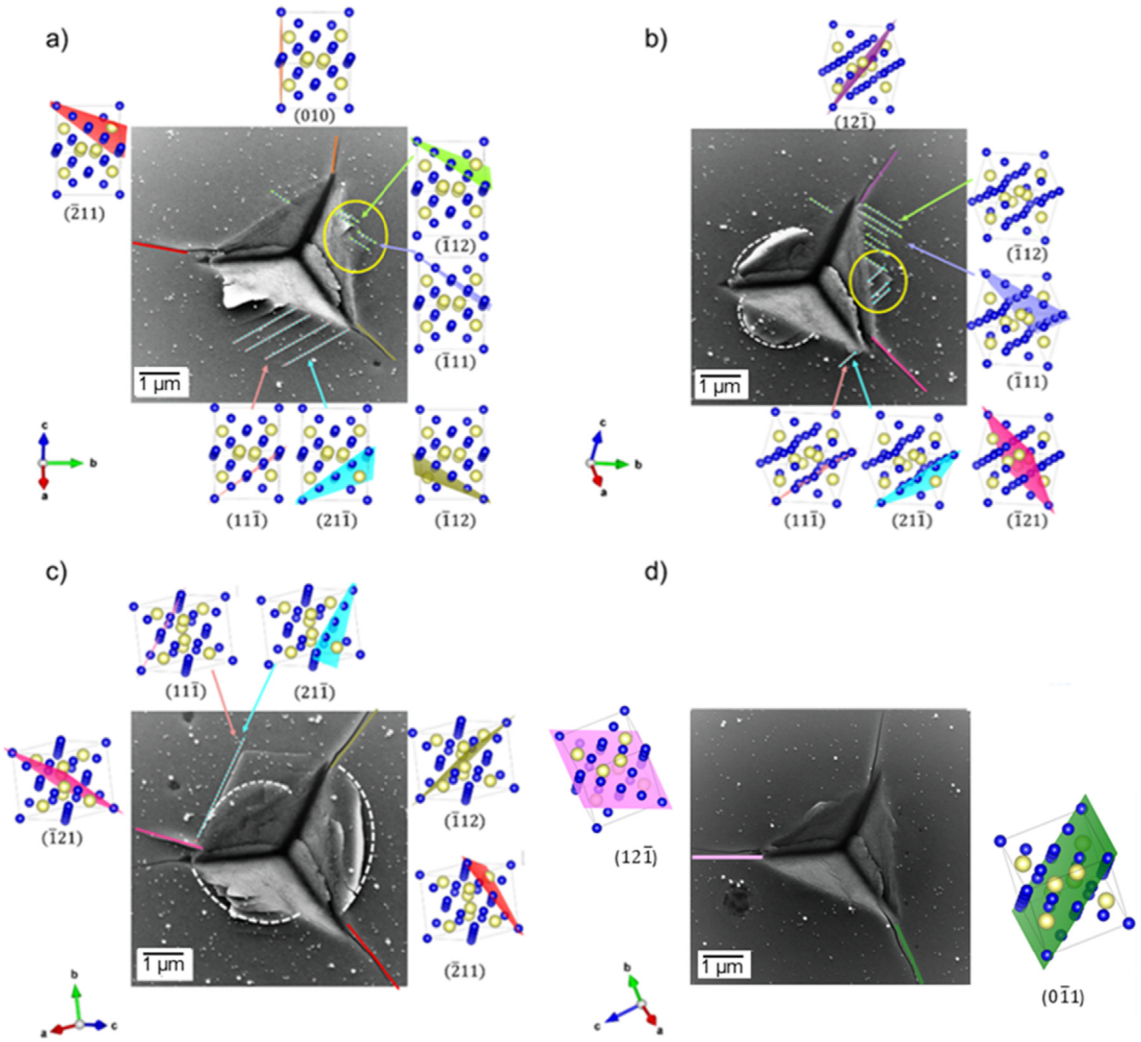

Fig. 5. Examples of the representation of the slip trace analysis for four different orientations: The traces in the vicinity of the indent are subdivided into the following categories depending on their morphology: straight slip lines (correlated with their slip plane in the $CaAl_2$ phase using VESTA (Visualization for Electronic and Structural Analysis [52])), edges marked by yellow circles, and curved lines indicated by white dotted curved lines. The latter were not further analysed. Next to the SE images in a-d), the top view on the correspondingly orientated $CaAl_2$ unit cell including the observed slip planes is depicted. The compression axes are a) $\left(\bar{7}\ 0\ \bar{8}\right)$, b) $\left(\bar{1}\ 0\ \bar{1}\right)$, c) $\left(\bar{6}\ 32\ \bar{1}\right)$ and d) $\left(\bar{6}\ 8\ \bar{5}\right)$. (For interpretation of the references to colour in this figure legend, the reader is referred to the web version of this article.)

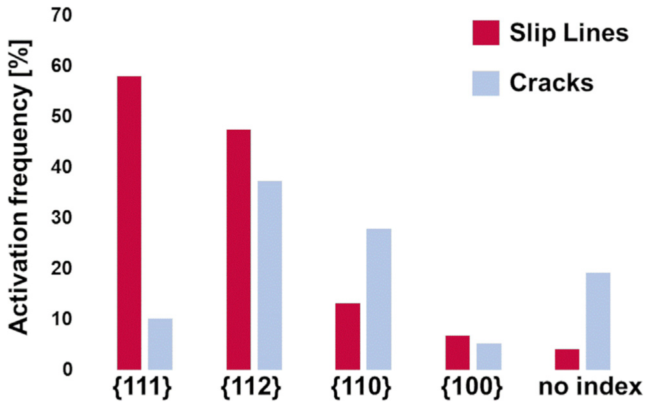

Fig. 6. Activation frequency of the slip and crack planes in the vicinity of the analysed nanoindents.

not homogeneous. The dislocation density is high under the indent, which indicates the occurrence of large plastic deformation. Multiple slip systems should have been activated under the indent. The dislocation density is observed to decrease away from the indent. Slightly away from the indent, deformation is confined within some bands, which will be named "slip bands" in the following sections. At least two sets of slip bands appear in this area. Further away from the indent, only one set of slip band is observed. However, the finding that dislocations with different Burgers vectors exist in the same slip band, makes it more difficult to index the dislocations' Burgers vectors. This is discussed in more detail below. Similarly, it is noted that horizontally away from the indent, in the area of low dislocation density, some slip bands can be more clearly observed and are indicated by white dotted lines in Fig. 10 c). In order to determine the orientations of these slip bands, the lamella was further tilted to the [011] zone axis and the slip bands on both "A" and "B" sides are determined to be $(2\bar{1}1)$ and $(21\bar{1})$ plane traces, respectively. These slip bands are also observed to lie parallel to the straight crack planes. Moreover, the blue dotted rectangle represents the area where slip bands were observed lying also on the $(2\bar{1}1)$ plane (Fig. 10), which also can be seen in more detail in Fig. 11. Within the red dotted rectangle, the region where the Burgers vector was analysable is marked (in more detail Fig. 12), also the yellow rectangle signs the area,

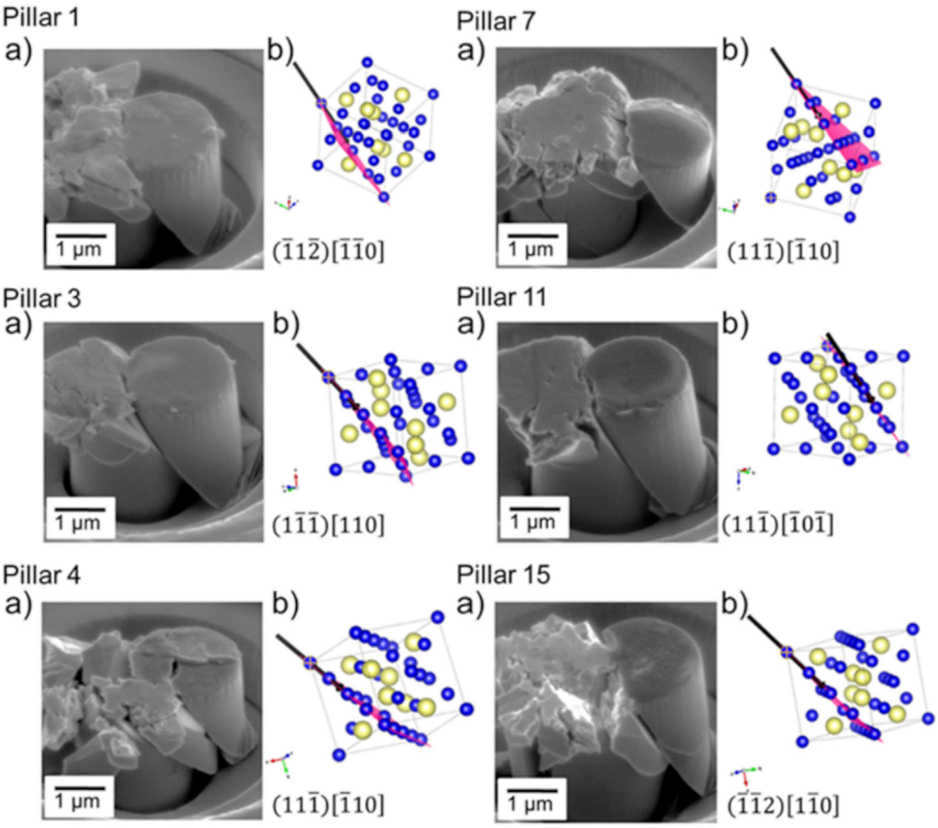

Fig. 7. Images and crystal orientation for selected micropillars. a) SE-images of the deformed micropillars taken under a tilt angle of 45°, b) the correspondingly oriented unit cell including the identified slip plane and the possible slip direction under 90° tilt angle using VESTA [52].

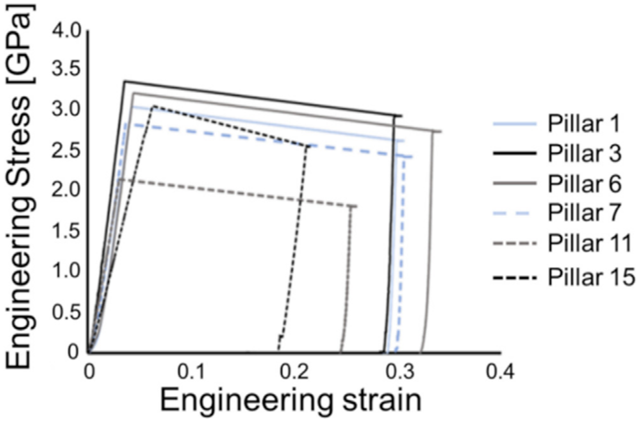

Fig. 8. Engineering stress - engineering strain curves of the deformed micropillars shown in Fig. 7.

where structures can be observed, which can be interpreted as stacking faults (Fig. 13).

Especially the evidence of dislocations on a {1 1 2} plane was found by rotating the lamella around 180°, shown in Fig. 11, where slip bands lie parallel to the $(\bar{2}\,1\,\bar{1})$.

In the area away from the indent marked by a red rectangle in Fig. 10 c), two slip bands with a high dislocation density were observed and either one or two sets of dislocations were noticed within these two slip bands. These two slip bands were further analyzed under different two-beam conditions (Fig. 12). The left slip band includes two different parallel dislocation sets lying antiparallel to each other and including an intersection. Both slip bands were evaluated in more detail for Burgers vector analysis. For this, dislocations within these slip bands were observed after tilting to three different zone axes namely [0 1 1], [1 1 2] and [1 1 1], and six different two-beam conditions, g = $(\bar{3}\,1\,1)$, g = $(\bar{3}\,1\,\bar{1})$, g = $(\bar{1}\,3\,\bar{1})$, g = $(\bar{2}\,2\,0)$, g = $(2\,2\,\bar{4})$ and g = $(\bar{2}\,\bar{2}\,2)$ were applied. Dislocations within the right slip band are visible using zone axis [1 1 2] and g = $(\bar{1}\,3\,\bar{1})$ (Fig. 12 a)), g = $(\bar{2}\,2\,0)$ (Fig. 12 b)) g = $(\bar{3}\,1\,1)$ (Fig. 12 c)) as well as zone axis [0 1 1] with g = $(\bar{3}\,1\,\bar{1})$ (Fig. 12 d)), whereas these dislocations are invisible under the combinations of zone axis [1 1 1] with g = $(2\,2\,\bar{4})$ (Fig. 12 e)) and zone axis [0 1 1] with g = $(\bar{2}\,\bar{2}\,2)$ (Fig. 12 f)).

According to the visibility/invisibility of dislocations under different two-beam conditions owing to the corresponding lattice strain, the Burgers vector of this set of dislocations can be determined and it is $[1\,\bar{1}\,0]$, which lies on the $(1\,1\,\bar{1})$ and (1 1 1) planes. However, dislocations with Burgers vector of $[1\,\bar{1}\,0]$ can also slip on the (1 1 2) plane. It is therefore not possible to distinguish between {1 1 1} and {1 1 2} planes for the underlying slip planes from this analysis.

Besides the high dislocation density and the associated dislocations in the slip bands, small straight lines that may be related to stacking faults have also been observed (indicated by arrows in Fig. 13). One set of these straight lines were found to lie predominantly on the $\left(1\,1\,\bar{1}\right)$ plane, which are marked by a yellow arrow in Fig. 13. For the other stacking faults the corresponding planes could not be identified. The presence of stacking faults indicates that dislocations dissociate into partials leading misfits in stacking

Table 1
Micropillars 1–15 including their compression axes, the observed slip systems, Schmid factors (m_s), yield stresses (σ_y), and CRSS values.

Pillar	Pillar axis	Slip System	m_S	σ_y [GPa]	CRSS [GPa]
1	$(1\,7\,10)$	$(\bar{1}\,1\,\bar{2})[\bar{1}\,\bar{1}\,0]$	0.32	3.05	0.98
2		$(\bar{1}\,\bar{1}\,\bar{2})[\bar{1}\,10]$	0.34	2.67	0.94
3	$(\bar{9}\,1\,11)$	$(1\,\bar{1}\,\bar{1})[110]$	0.33	3.37	1.11
4–6	$(1\,\bar{5}\,9)$	$(11\,\bar{1})[\bar{1}\,10]$	0.30	3.34	1.02
				3.13	0.94
				3.22	0.97
7 + 8	$(6\,\bar{13}\,21)$	$(11\,\bar{1})[\bar{1}\,10]$	0.35	2.67	0.93
				3.05	1.07
9	$(13\,\bar{7}\,21)$	$(\bar{1}\,1\,\bar{1})[0\,\bar{1}\,\bar{1}]$	0.36	2.43	0.87
10		$(11\,\bar{1})[\bar{1}\,0\,\bar{1}]$	0.30	2.25	0.98
11				2.24	0.97
12–14	$(12\,\bar{15}\,7)$	$(111)[0\,\bar{1}\,1]$	0.26	3.88	1.01
		$(\bar{1}\,21)[\bar{1}\,0\,\bar{1}]\,(11\,\bar{2})[\bar{1}\,10]$	0.46 0.31	3.56	* (1.64/1.10)
		$(\bar{1}\,21)[\bar{1}\,0\,\bar{1}]\,(11\,\bar{2})[\bar{1}\,10]$	0.46 0.31	3.69	* (1.70/1.14)
15	$(\bar{7}\,1\,\bar{14})$	$(\bar{1}\,\bar{1}\,2)[1\,\bar{1}\,0]$	0.32	3.11	1.00

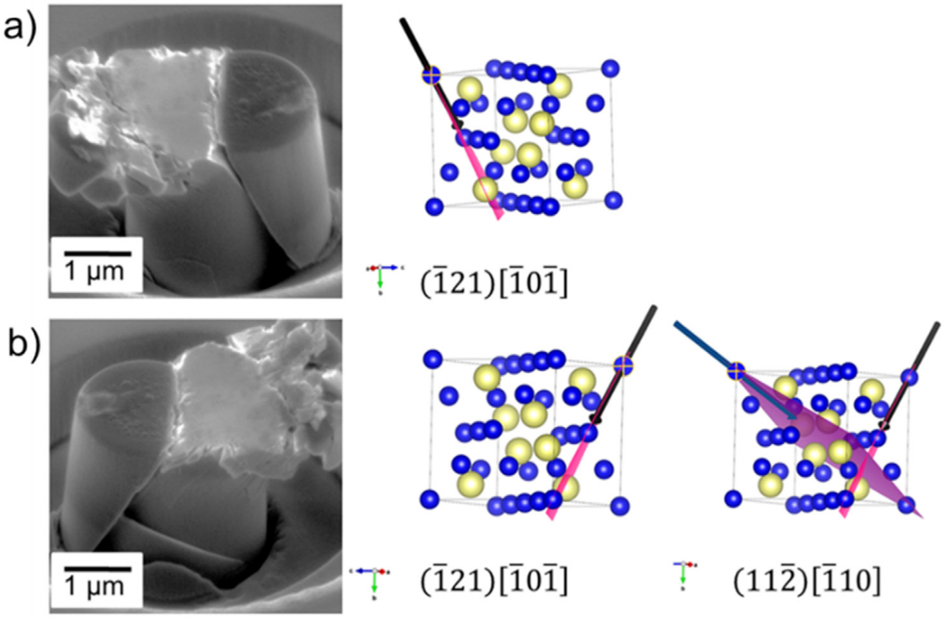

Fig. 9. SE-images of pillar 13 after deformation in a) front view including the corresponding unit cell and b) back view including the corresponding unit cell using VESTA [52].

Table 2
Presenting all nanomechanical measured properties of the $CaAl_2$ Laves phase.

Mechanical properties	Measured values
Hardness CSM	4.9 ± 0.7 GPa
Indentation Modulus	85.5 ± 4.0 GPa
Hardness SRJT	5.8 ± 0.8 GPa
Strain rate sensitivity	0.028 ± 0.019
	0.530 ± 0.780 nm^3
Activation volume	3.75 ± 1.15 b^3
CRSS $\{111\}\frac{1}{2}\langle 1\,\bar{1}\,0\rangle$	2.96 ± 0.54 GPa
CRSS $\{112\}\frac{1}{2}\langle 1\,\bar{1}\,0\rangle$	2.94 ± 0.24 GPa

after their motion. Moreover, the occurrence of stacking faults on one of the triple layers is often correlated with the synchroshear process, which is thought to take place on the {1 1 1} planes.

4. Discussion

4.1. Mechanical properties

The measured hardness and indentation modulus at an indentation depth of 500 nm were consistent over all 10 different crystallographic orientations with a value of 4.9 ± 0.7 GPa and 85.5 ± 4.0 GPa. A recent study by Lou et al. [53] on $CaAl_2$ particles in a magnesium matrix revealed a hardness of 5.7 ± 0.4 GPa and an average Young's modulus of 82.9 ± 1.0 GPa, in good agreement with the values measured in the present study. The measured Young's modulus is also in good agreement with measurements on macroscopic single crystals by Schiltz and Smith [54], who measured elastic constants corresponding to a polycrystalline Young's modulus of 98 GPa, very close also to that predicted by ab initio calculations by Yu et al. [55], with an expected Young's modulus

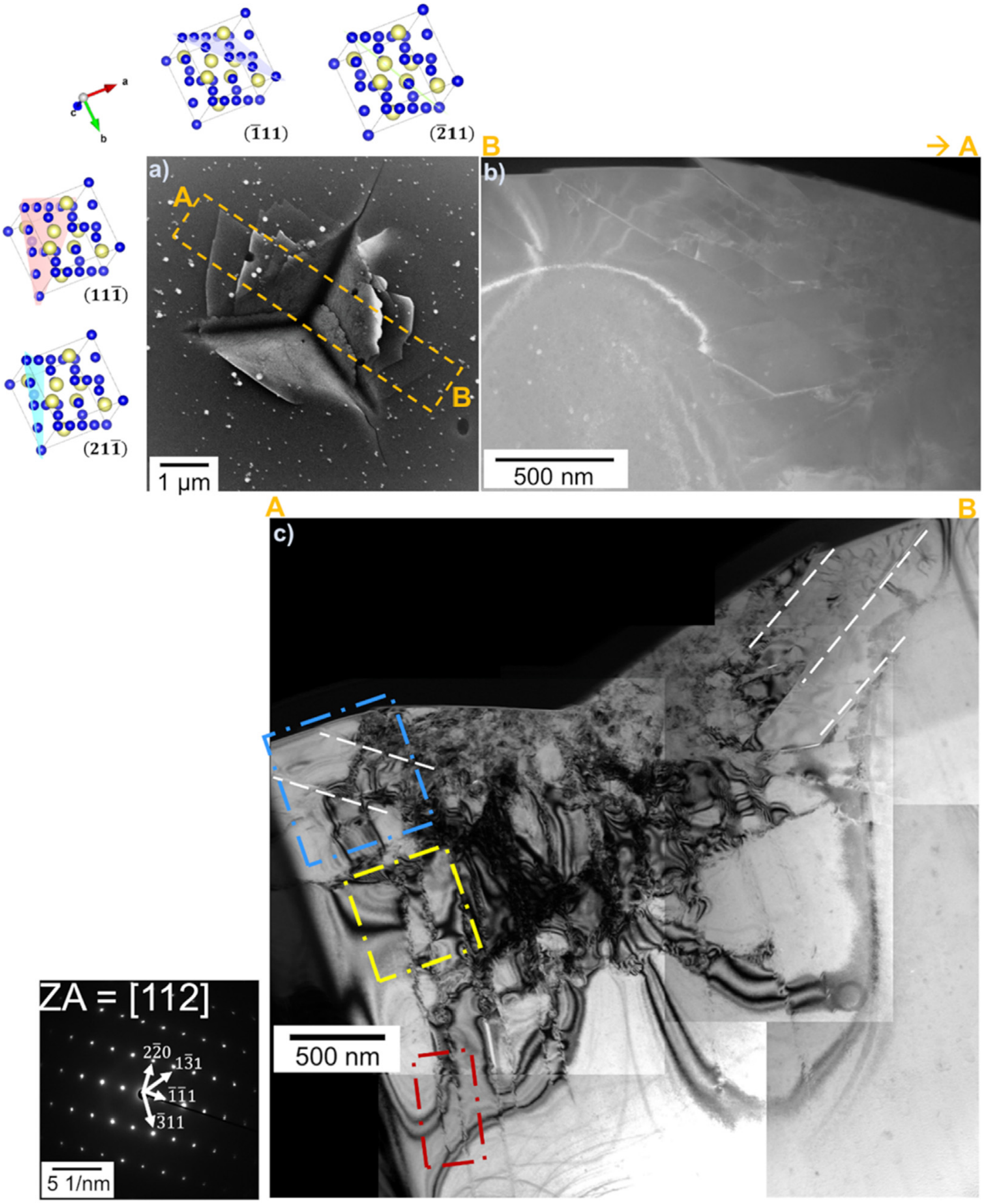

Fig. 10. A) se-image of a nanoindent including a schematic sketch (dotted orange area), from where the tem lamella was cut out. letters a and b show the orientation of the membrane and how it was analysed in the further investigations. the slip traces in the vicinity of the indent were furthermore correlated with different planes along with the unit cell using vesta[52]. b) STEM image of the lamella. c) BF-TEM image taken at [112] zone axis. The blue rectangle highlights the area with a high dislocation density (Fig. 11), whereas the red rectangle indicates the area where dislocation Burgers vector analysis was performed (Fig. 12) and the yellow rectangle corresponds to the area where the stacking faults from Fig. 13 were found. (For interpretation of the references to colour in this figure legend, the reader is referred to the web version of this article.)

at 0 K of 92 GPa. Measurements of the microhardness by Rokhlin et al. [12] for different holding periods (30 s and 3600 s) at 20 °C, resulting in 402 HV for 30 s and 354 HV for 3600 s, show the presence of creep for this duration and pressure. However, hardness values from macroscopic hardness measurements can be converted into values comparable to nanohardness using the equation from Fischer-Cripps [56,57] where hardness values from Vickers tests (HV) can be calculated in nanomechanical hardness (HN) by using the linear fit: $HV = 94.5 \cdot HN$, resulting in 3.94 GPa and 3.49 GPa respectively. These values are consistent with the calculated macroscopic hardness from our data using the Nix-Gao model, giving a value of 3.46 GPa [58].

Single crystal measurements of the elastic constants of $CaAl_2$ [54] gave a consistent absence of directional variation with an anisotropy factor of 0.98, i.e. very close to 1. Investigations of the hardness dependence on the crystal orientation for the $NbCo_2$ C15 Laves phase were performed by Luo et al. [26]. They investigated the hardness dependence on the orientation and stoichiometry applying nanoindentation tests on a diffusion couple and found that the hardness and the indentation modulus were unaffected by a change in orientation, which is consistent with the findings obtained here. Similar results were obtained by Zehnder et al. [40] for the hardness and indentation modulus of the hexagonal C14 $MgCa_2$ Laves phase after nanoindentation tests in different ori-

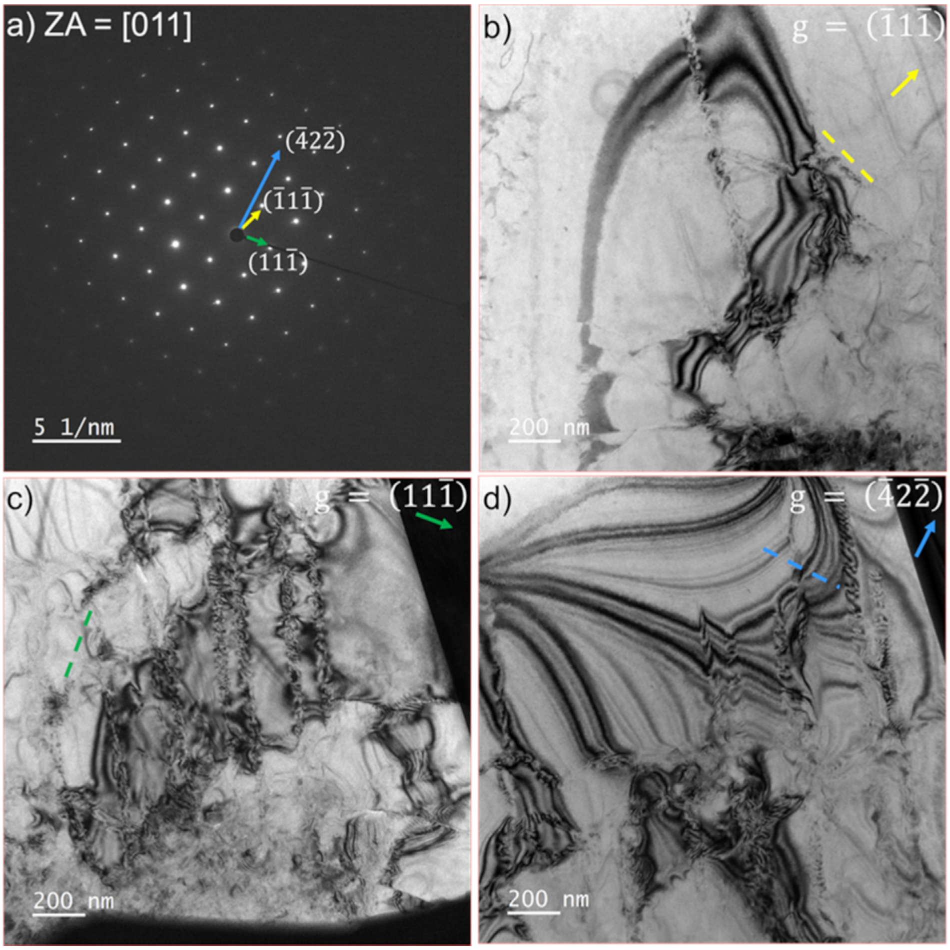

Fig. 11. TEM BF images showing dislocation substructure under the nanoindent (Fig. 10 a)) under 3 two-beam conditions with the same zone axis (a)). b) shows slip bands g = $(\bar{1}\,1\,\bar{1})$, the yellow dashed line shows the alignment of the $(\bar{1}\,1\,\bar{1})$ slip plane. c) displays the dislocation structure with g = $(1\,1\,\bar{1})$, the green dashed line symbolises the $(1\,1\,\bar{1})$ plane trace and in d) with g = $(\bar{4}\,2\,\bar{2})$ the dislocations on the $(2\,\bar{1}\,\bar{1})$ plane (blue dashed line) are shown. These images were taken in TEM with a 180° rotation of the lamella shown in Fig. 10. (For interpretation of the references to colour in this figure legend, the reader is referred to the web version of this article.)

entations, showing a constant hardness and indentation modulus for all measured orientations.

To compare the mechanical properties with the measured mechanical properties of Laves phases from previous room temperature deformation studies, the normalised CRSS will be determined by dividing the CRSS by the shear modulus. To compare these values, calculations were done analysing deformation along the planes containing the triple layer, i.e. for the C15 structure the (1 1 1) plane and for the C14 Laves phase the (0001) plane. For the $CaAl_2$ C15 Laves phase investigated in this study, a CRSS/G = 0.027 (with G ≈ 36 GPa) ratio was obtained. For the cubic $NbCo_2$ Laves phase, the normalized CRSS can be calculated to lie between 0.027 and 0.033 [28,29], while for the C14 Laves phase of the Mg-Al-Ca alloy it comes up to 0.023 at ambient temperature [40]. For the hexagonal $NbCo_2$ phase it results in 0.023, respectively, taking the results by Luo et al. [29]. As the available data below the BDTT is largely restricted to room temperature, with the exception of the lowest melting phase, which was also tested at elevated temperature [40], this comparison is necessary for slightly varying homologous temperatures. However, the melting points of the C15 and C14 phases in the Nb-Co system are very close. The finding that all values lie in the same range, while a trend to higher values can be observed for the cubic phases when comparing both structures.

Whether this is in fact the case or a result of a variation in shear modulus on the active slip plane compared to the isotropic shear modulus [59], could be investigated further by dedicated ab initio calculations of the triple layer slabs' stiffness and experiments at identical homologous temperatures on single crystalline micropillars oriented for slip on the {1 1 1} and {0001} planes.

4.2. Active slip systems

The statistical evaluation of the activated slip planes in the vicinity of the nanoindents (Fig. 6) revealed the activation of four different slip planes. The predominant slip plane was found to be the {1 1 1} plane (58.1 %), which is consistent with a previous publication by Paufler et al. [1] and studies [16,18,19] on the cubic $MgCu_2$ phase at elevated temperatures. However, the activation of the {1 1 2} plane was observed with a frequency of 47.5 %, which is only 10.6 % less often than the {1 1 1} plane.

There are several things to consider in interpreting this data, most importantly, the chance of double assignment of a slip trace where the traces of two (or more) planes are identical or very close to one another. The cubic system exhibits a total of four {1 1 1} planes but 12 {1 1 2} planes. This leads to a higher number of unambiguously identifiable {1 1 2} planes than {1 1 1} planes. Therefore, the expectation that those traces counted as a {1 1 2} trace, a greater fraction is in fact uniquely assigned, while many more {1 1 1} assignments also correspond to a possible {1 1 2} plane. A total number of 625 surface traces were correlated with plastic deformation, whereby the total amount of plane traces

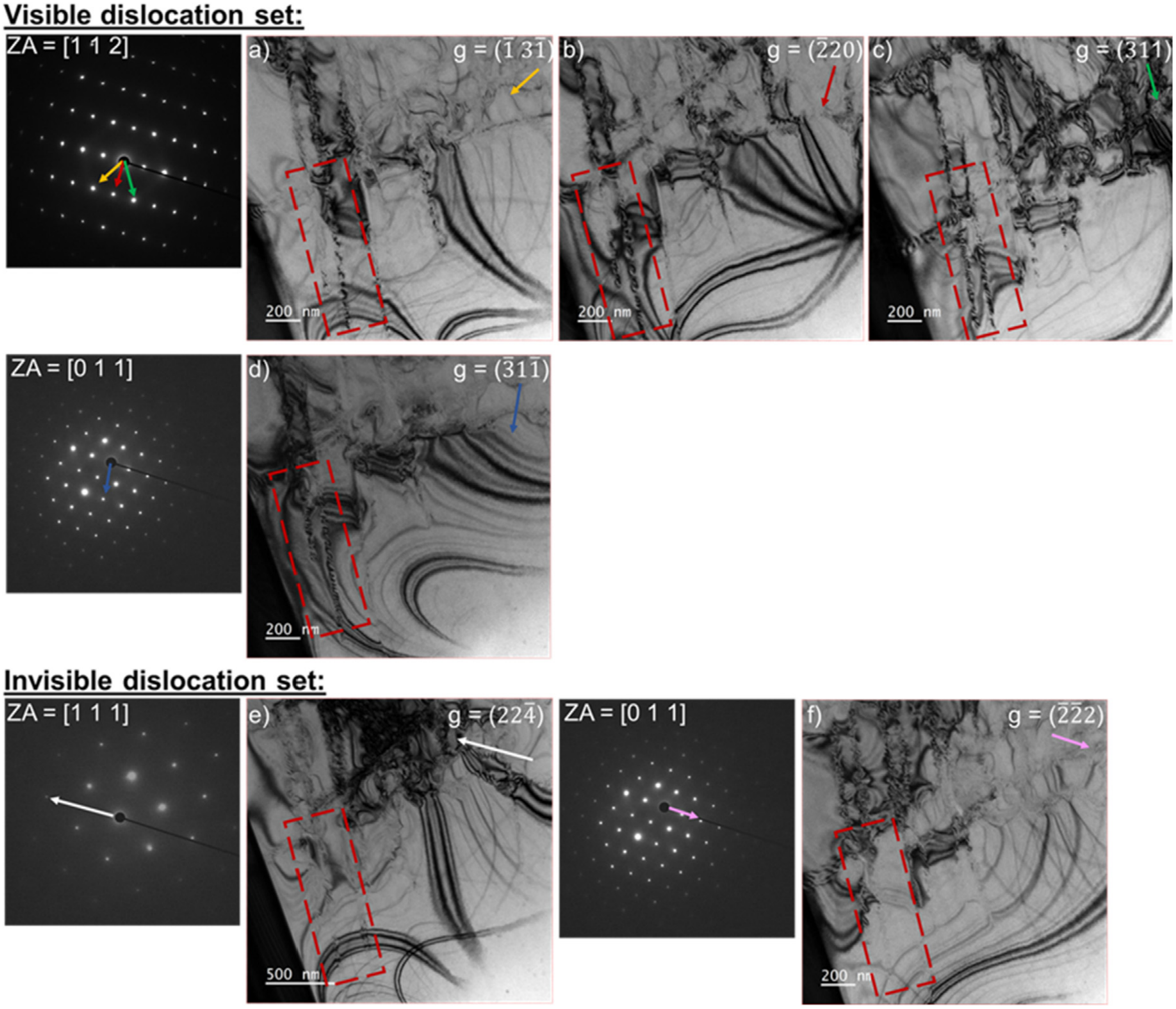

Fig. 12. TEM BF images showing dislocation substructure under the nanoindent (Fig. 10 a)) under different two-beam conditions. The red rectangle indicates the slip band, where the dislocation Burgers vector was analysed. The dislocation set is visible under a) g = ($\bar{1}$ 3 $\bar{1}$), b) g = ($\bar{2}$20) and c) g = ($\bar{3}$11) in [112] zone axis and under d) g = ($\bar{3}$ 1 $\bar{1}$) in [001] zone axis. They become invisible under e) g = (22$\bar{4}$) in [111] zone axis and f) g = ($\bar{2}$ $\bar{2}$2) in [011] zone axis. (For interpretation of the references to colour in this figure legend, the reader is referred to the web version of this article.)

was summed up to 811, because of double counting for those planes for which the deviation angle was below 3°. 23 % of the surface traces were counted twice. The double counted slip planes can be divided in 54 % (101 surface traces) for the {1 1 1} planes and 46 % (85 surface traces) for the {1 1 2} planes. With this knowledge about both corresponding to more or less the same number of double counting events, a purely geometrical artefact giving rise to the previously unexpected {1 1 2} slip plane can be excluded, because without double counting 212 surface traces were assigned to the {1 1 2} planes.

Now, a more detailed consideration of the geometry of the crystal and surface slip trace analysis, with its inherent double counting for planes yielding the same surface intersection or trace will follow. Given the higher probability of double counting for each of the 12 {1 1 2} planes compared to the 4 {1 1 1} planes, one might expect that for an equal division of unique slip traces, the {1 1 1} plane is softer, as it should otherwise only show a third of the number of traces. However, due to the different inclination of the two planes, there is also a difference in their likelihood of activation. While each of the 4 {1 1 1} planes possesses 3 independent Burgers vectors, giving a total of 12 independent slip systems, each of the 12 {1 1 2} planes contains only one possible Burgers vector, so that for a given identifiable plane, the {1 1 1} has a three times higher probability of having a favourably aligned Burgers vector giving a slip system with a high resolved shear stress. Overall, it would therefore appear that the slip trace analysis suggests no real difference in activation of the two slip systems on either {1 1 1} or {1 1 2} planes. This is in fact consistent with the observation from microcompression that there is no significant difference in CRSS between the two systems for slip on either {1 1 1} or {1 1 2} planes.

Since it is not possible to unambiguously identify the Burgers vector from micropillar compression experiments, although it is needed to estimate a critical resolved shear stress, TEM investigations were performed on nanoindents with their greater variety of active slip planes and greater gradient in dislocation density enabling a better selection of conditions for dislocation strain field imaging towards the edge of a plastic zone. By conducting a $g \cdot b$ extinction analysis, the Burgers vector could be identified as <10$\bar{1}$>, which is contained in both identified slip planes. Furthermore, besides perfect dislocations, the presence of stacking faults, especially on a {1 1 1} planes, points towards the motion of at least partly dissociated dislocations by the well-known synchroshear mechanism in the triple layer [30–33].

The CRSS for plastic deformation on both slip systems in microcompression was then found to be 0.99 ± 0.03 GPa for {1 1 1}<1 $\bar{1}$ 0 > and 0.97 ± 0.07 GPa for {1 1 2}<1 $\bar{1}$ 0 >. There are no other studies on round micropillars from bulk $CaAl_2$ for a direct quanti-

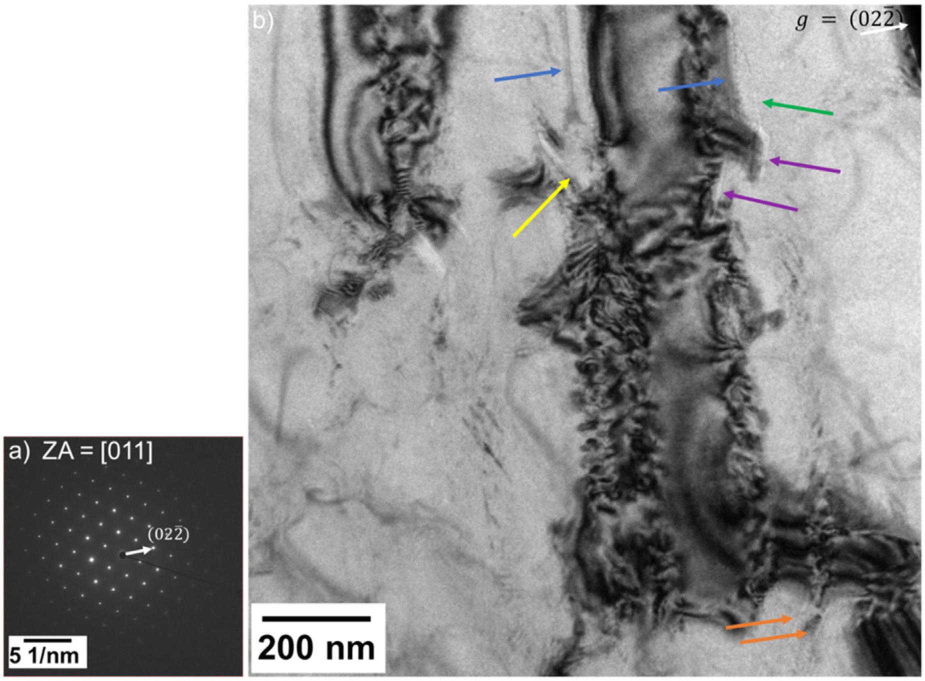

Fig. 13. Higher magnification TEM BF image showing the area marked by the yellow rectangle in Fig. 10. This image was taken under g vector (02$\bar{2}$) in [011] zone axis. Stacking faults with different orientations are indicated by arrows with different colours. The yellow ones show stacking faults parallel to the (11$\bar{1}$) plane trace. (For interpretation of the references to colour in this figure legend, the reader is referred to the web version of this article.)

tative comparison with our data, but agreement can be found with respect to the work on square pillars in $CaAl_2$ precipitates, since this work must also take into account the effects of stoichiometry on the plasticity of the Laves phase, which are largely unknown.

A previous study by Luo et al. [53] also reported the {1 1 1} <1 $\bar{1}$ 0 > slip system in $CaAl_2$ precipitates to represent the major slip system after performing micropillar compression tests at ambient temperature. Their measured CRSS value was 164.9 MPa, which is a factor of 6 lower than measured in our experiments. However, considering that their micropillars had a square cross-section of 4 μm × 4 μm compared to our round micropillar with a diameter of 2.1 μm, the deviation might in part originate from the size effect on dislocation motion and easier dislocation nucleation at the edges of square pillars, giving a smaller contribution from nucleation to the overall stress level and a potentially higher dislocation density, which would lead to a reduction in CRSS in a lattice resistance controlled material. A micropillar study using round and square micropillars [60,61] showed that for both types, mechanisms of collective cross-slip were observed between two planes of the same plane family and with the same high Schmid factor, whereas the measured initial stress was greater for the round geometry. From the Laue analysis and post mortem SEM, the deformation zone of the square micropillar was found to be more pronounced and showed different activated slip systems.

In addition, a deviation from the stoichiometric composition may influence the mechanical properties [53], because the C15 Laves phase particles, embedded in a Mg matrix phase, compressed by Luo et al. showed a deviation of ~ 5.7 at.-% for Al and ~ 2.0 at.-% for Ca from the ideal composition. However, it is still not clear how a deviation from the ideal stoichiometry influences the mechanical properties and therefore how to estimate an expected change in CRSS with composition. Some studies [1,62,63] suggest a decreasing hardness for a deviation from the ideal composition, whereas another study [26] reported an increase of the hardness.

On a qualitative level, our detection of {1 1 1}<1 $\bar{1}$ 0 > slip is very typical for C15 Laves phases at room temperature and in good agreement with previous studies by Luo et al. for $CaAl_2$ [53], Xue et al. [27] for the $CrNb_2$ phase, Luo et al. [29] and Korte et al. [28].

On the other hand, deformation on the {1 1 2} plane has not yet been reported for intermetallic phases of C15 type at room temperature so far, to the authors' best knowledge. However, the high frequency and often unique assignment of slip traces to {1 1 2}, its identification by TEM and on the surface of micropillars, prove the occurrence of slip on {1 1 2} planes.

Preferential deformation was expected along the triple layer, which lies along the {1 1 1} planes in the C15 structure, but deformation on non-basal planes, away from the triple layer (along {0001} planes), has in fact previously been described for hexagonal Laves phases with the C14 structure in several studies at ambient and elevated temperature [40,41]. Additionally, micropillar compression tests of the $CaMg_2$ C14 Laves phase at room temperature have revealed that the CRSS is comparatively low for the 1st order prismatic slip system [27,40].

For a comprehensive comparison, the CaMg2 Laves phase was chosen because of its similar structure and also the presence of similar elements on the A site of the AB2 Laves phase structure. Additionally, for this phase more data are available in the literature including the slip line activation on different planes and CRSS values.

For the evaluation of the {1 1 2} slip system, a comparison of the analysed structure of the cubic C15 and the hexagonal C14 Laves phases was done. It could be observed that a similar stacking to the cubic {1 1 2} plane can be found in the hexagonal structure and can be related to previously reported non-basal slip plane. In Fig. 14 both structures are displayed. The black line shows the plane along the triple layer (in C15 the (1 1 1) and C14 the (0001) plane) for both packings. The position of three parallel (1 1 2) planes is shown for the cubic C15 Laves phase with pink lines. A comparatively similar stacking sequence is in fact found along the {10 $\bar{1}$ 0} plane (1st order prismatic plane) of the hexagonal C14 Laves phase (Fig. 14 pink line). Both reveal a triple stacking with an A-B-A (Ca-Al-Ca or Ca-Mg-Ca) stacking. For the C14 struc-

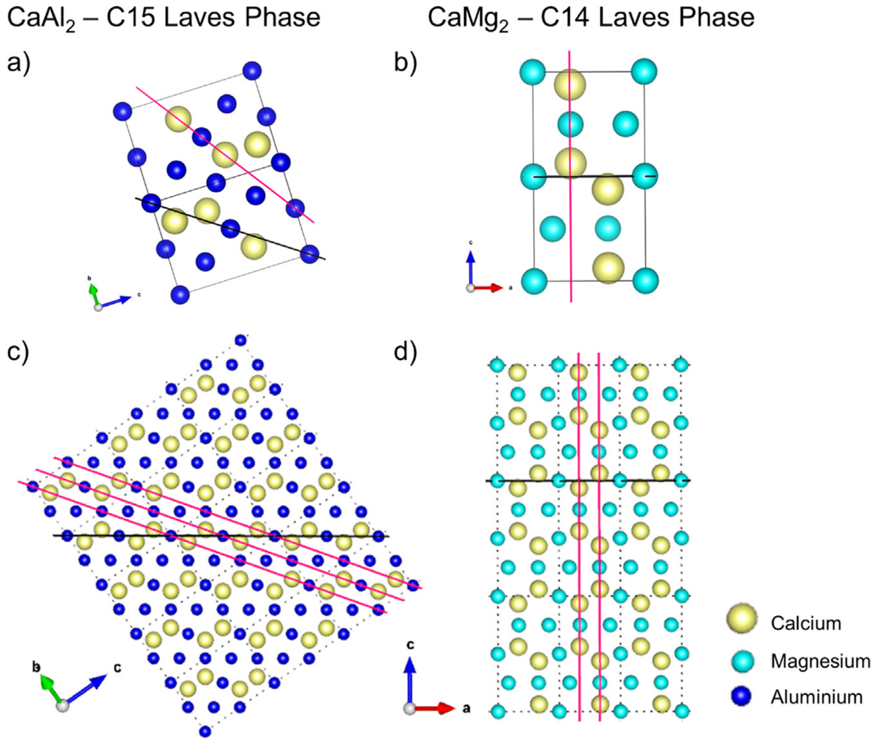

Fig. 14. Visualisation of the (111) plane (black line) and (112) plane (purple line) in the $CaAl_2$ phase and the (0001) plane (black line) and the $(10\bar{1}0)$ plane (purple line) in the $CaMg_2$ phase by using VESTA, whereby a) and b) displays the different unit cells aligned for a crystallographic comparison for the planes [52]. (For interpretation of the references to colour in this figure legend, the reader is referred to the web version of this article.)

ture these repeat continuously along the prismatic plane, while for the C15 structure the Kagomé layer is intersected, placing the repeating unit at some distance and with an Al atom in between. Considering that the prismatic plane is the easiest slip plane in the $CaMg_2$ C14 phase, deformation by a similar mechanism on the {112} plane in C15 does not appear too unreasonable. The effect of the disturbed repeat unit along the plane on dislocation glide cannot be readily anticipated as so little is known about glide on this type of plane. The curved slip lines found frequently at the indents might be indicative of high cross-slip activity. Cross slip might be a preferential slip mode due to a reduced confinement of dislocations to a specific set of parallel {112} planes and a tendency to follow the repeating motif to make the glide path more similar to the prismatic plane in the C14 phase.

In addition to considering the qualitative possibility of slip on the {112} planes, the expected quantitative values for the CRSS can also be compared, at least relatively speaking, based on the interplanar spacing of the slip plane, which strongly affects the dislocation width and consequently Peierls stress for a given Burgers vector [64]. For the triple layer, the $CaAl_2$ phase reveals a closer interplanar spacing. These values are listed in Table 3 compared with the $CaMg_2$ phase. The interplanar spacings of both (ideal) structures are caused by the different constituent atoms and their atomic radii. Ca possesses the largest radius with 197 pm, followed by Mg with 160 pm and Al with 143 pm [65,66]. This leads to the closer interplanar spacing in the triple sequence of the (112) plane in $AlCa_2$ than for the $(10\bar{1}0)$ plane in $CaMg_2$. The difference between these distances amounts to 0.32 Å. The continuously repeating triple sequence of the $(10\bar{1}0)$ plane in $CaMg_2$ has a smaller interplanar spacing than the distance between the triple sequence and the intersecting Al atom from the Kagomé layer of the (112) plane in $CaAl_2$. Additionally, the arrangement of the parallel {112} planes repeats continuously, revealing a small overlap from the triple layer on one plane to the triple layer on the next parallel plane with a lattice distance of 1.64 Å (distance between the purple lines displaced in Fig. 14). Looking at the alignment of the $(10\bar{1}0)$ plane, there are only two parallel layers, with a lattice spacing of 1.78 Å, which also is smaller than the full distance to the next triple layer in the plane.

Table 3
Interplanar spacing of the triple layers and the (112) and $(10\bar{1}0)$ planes. The distances were measured along the plane from the center of one atom to the other.

$CaAl_2$	spacing	$CaMg_2$	spacing
(111)		**(0001)**	
Al ↔ Ca	3.33 Å	Mg ↔ Ca	3.65 Å
Ca ↔ Ca	3.47 Å	Ca ↔ Ca	3.82 Å
Ca ↔ Al	3.33 Å	Ca ↔ Mg	3.65 Å
(112)		$(10\bar{1}0)$	
Ca ↔ Al ↔ Ca (spacing in triple sequence)	3.33 Å	Ca ↔ Mg ↔ Ca (spacing in triple sequence)	3.65 Å
Al ↔ triple sequence ↔ Al	7.70 Å	Between triple sequences	6.37 Å
Lattice distance	1.64 Å	Lattice distance	1.78 Å

With the comparison of these planes and the knowledge of the low CRSS for 1st order prismatic slip systems in C14 Laves phases, the possibility of the activation of {112} slip cannot be entirely explained or connected with a distinct dislocation mechanism, but its occurrence can be rationalised from this comparison.

4.3. Active fracture planes

In contrast, the nucleated cracks could clearly be measured to be the {112} plane. The identification of the crack planes is clearer than that of the slip lines due to smaller encountered overlaps in these cases for the {111} and {112} planes compared to the slip line analysis. The TEM analysis (Fig. 10) further revealed planar cracks within the volume and along slip traces extending from the volume to the surface on the $(2\bar{1}1)$ and $(21\bar{1})$ planes. During indentation, the applied pressure would provide a driving force for these cracks to open. Therefore, this leads to the assume that plasticity occurred first on these planes and that upon unloading, the accumulation of dislocation defects further promoted decohesion along these apparently favourable {1 1 2} fracture planes. A very similar observation has been made by Schröders et al. [51] during indentation and microcompression of the structurally related μ-phase and crack nucleation at intersecting slip bands in general is a commonly observed phenomenon at large and small scales [25,67,68].

4.4. Orientation dependence of slip morphology

Beside the straight lines and edges, which could be used to clearly identify active slip systems that were confirmed in both microcompression and TEM, curved traces were also detected around the indents (Fig. 5), which could not be assigned to individual underlying slip planes. This occurrence of both curved and straight slip traces is similar to what was observed by the authors in deformation of the $CaMg_2$ C14 Laves phase at elevated temperatures [41] and also for the Fe_7Mo_6 μ-phase at ambient temperature [51], but could not yet be assigned to a specific deformation mechanism beyond speculation that possible reasons may be easy cross-slip or promotion of cross-slip where slip systems interact.

One might expect these to result in an orientation dependence in terms of the prevalent slip morphology and this is indeed observed (Fig. 4). Grains near the [0 1 1] direction exhibit edged and straight lines around the deformation zone, while grain orientations near [111] only reveal cracks. For orientations near [0 0 1] direction straight lines and further curved deformation can be seen. The orientations between these three directions in the centre of the standard triangle exhibit all deformation morphologies concurrently.

This can be rationalise as follows:

For deformation with the major stress along [1 1 1] (either as a close approximation in microcompression of a (1 1 1) oriented crystal or a rough approximation for indentation on the same surface plane), there is no {1 1 1} plane with a non-zero Schmid factor as all planes are either perpendicular to the surface or the Burgers vector within the surface plane. In case of the {1 1 2} planes, there are three sets of planes, those lying perpendicular to the surface (one indicated in yellow in Fig. 15), those with the Burgers vector in the surface plane (red in Fig. 15) and those inclined to the surface at a shallow angle and the Burgers vector also out of the surface plane (grey and violet in Fig. 15). Only the latter achieve a non-zero Schmid factor. While the first can leave no slip trace, the second would be more likely to crack for a favourable fracture plane and the last are at the very least unlikely to form slip traces unless slip can very easily expand outwards from the highest pressure zone to intersect the surface at some horizontal distance away. For the two identified slip system families and the {1 1 2} a favourable crack plane, the observed cracks and an absence of slip traces is therefore consistent with expectations.

In [0 1 1] and [0 0 1] orientation, straight traces as well as edges (i.e. very short, connected segments of different orientations) or curves, respectively, occurred. This can also be rationalised based on the orientation of the available slip planes. Leaving again those unconsidered which are unlikely to form slip traces (those {2 1 1} planes with a shallow inclination to a {0 1 1} surface plane or those (nearly) normal to the surface, which would rather serve as fracture planes), suitable slip planes with intermediate Schmid factors can be found for both the {1 1 1} and {2 1 1} planes. However, while in case of a {0 1 1} surface these form a twofold symmetry with an orientation spread from 4 potential slip planes (a central {1 1 1} and 3 {2 1 1}) each, in case of a {0 0 1} surface these are grouped around the 4 {1 1 1} poles to give a much more continuous orientation spread. The observation of the more ragged edges in case of the first case of a {0 1 1} surface and more continuously curved traces in case of the {0 0 1} surface is therefore equally consistent with deformation on the two slip plane families and cross-slip occurring between them owing to the shared Burgers vector.

Finally, further away from the low index axis orientations, where both slip systems have systems with high Schmid factors (Fig. 4) and many differently oriented planes, a mixture of these regimes is expected and observed.

In addition to dislocation slip, twinning was mostly reported as occurring deformation mechanism at room temperature for cubic Laves phases in macroscopic studies [12,13], but was not observed in our study doing micropillar compression tests or in the analysed TEM lamella.

4.5. Activation volume

Strain rate jump tests revealed a strain rate sensitivity of 0.02 8 ± 0.019 for the C15 phase and an overall average activation volume of 3.75 ± 1.15 b^3, for a Burgers vector along the closed packed direction $\frac{a}{2}\langle 110\rangle$ (b = 0.5685 nm). Due to the close packed structure of the Laves phases, the intrinsic resistance against plastic deformation is assumed to be comparatively high, especially compared to metals with a simple face centred cubic structure. Additionally, the fact of having a BDTT shows the strong influence of thermal activation for plasticity, and therefore the activation volume should be comparatively low, as measured in the strain rate jump test. An activation volume around $\sim$ 10 b^3 is usually correlated with the mechanisms of overcoming the Peierls barrier, giving rise to the lattice resistance, by forming and moving kink pairs, in contrast to overcoming a field of discrete obstacles like other dislocations or precipitates [70]. However, other mechanisms are associated with similar activation volumes, particularly cross-slip and climb. Both are difficult to be observed directly by TEM, but at least climb, which is based on the diffusion of vacancies to dislocations, may be considered unlikely here as experiments were carried out at low homologous temperatures, where diffusional processes of flow are not usually dominant. In contrast, dislocation motion affected by solute drag and the diffusion speed of the solutes in comparison to the dislocation velocity, is known to lead to strong experimental signatures in the form of serrated flow.

Serrations have been reported in the loading curves for different intermetallic phases like the hexagonal $CaMg_2$ as well as for the cubic $Mg_{17}Al_{12}$ for nanoindentation tests at room temperature or 50 °C, decreasing with increasing temperature [11,41]. The room temperature activation volume for the γ-$Mg_{17}Al_{12}$ phase was estimated as 4.8 b^3 by Mathur et al. [11], however, the authors could also not unambiguously assign this volume to either dislocation motion controlled by overcoming the Peierls barrier or solute drag effects.

In the literature on high temperature Laves phase deformation in bulk samples, in particular $MgZn_2$, attempts to provide deformation mechanism maps suffer from similar limitations [71]. Macroscopically, data on yield stresses is only available down to the BDTT at a homologous temperature of around 0.6. In the plastic regime (in compression) above this temperature and up to the point of the onset of dislocation climb at higher temperatures and low stresses, dislocation glide and climb are thought to be the governing mechanisms with glide assumed to be rate limiting [71]. Observations of yield drops support the assumption that such mechanisms with a strong inverse dependence of the stress on mobile dislocation density are operating [15,72]. However, the

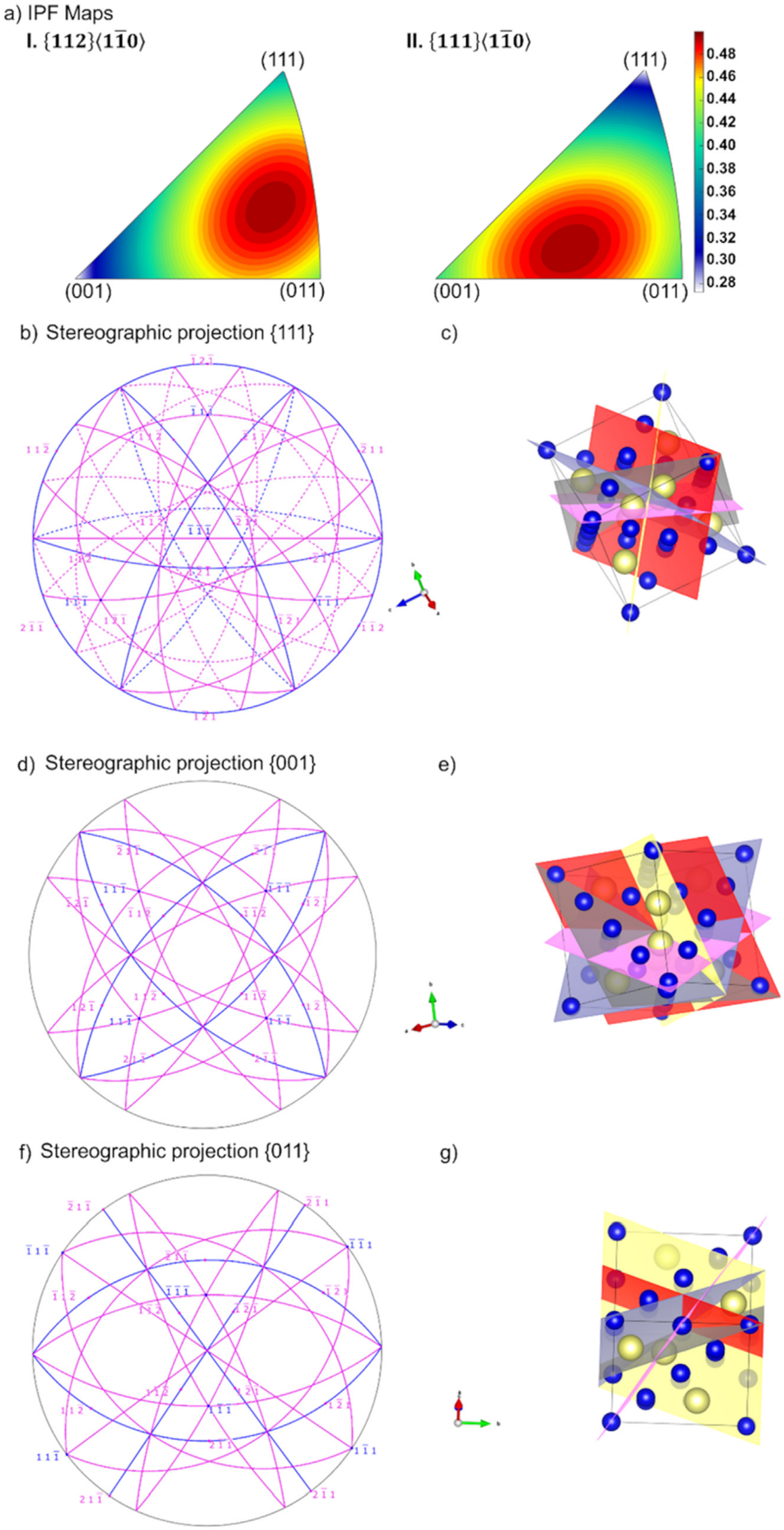

Fig. 15. A) displays the schmid factor distribution for i. $\{1\,1\,2\}< 1\,\bar{1}\,0 >$ and II. $\{1\,1\,1\}< 1\,\bar{1}\,0 >$ in an IPF map. In b), d), f) the stereographic projection of the b) {1 1 1}, d) {0 0 1} and f) {0 1 1} traces (in blue) with ⟨2 1 1⟩ poles (in pink) is shown using Crystal Maker [69]. c), e), g) visualises [52] the alignment of the {1 1 2} planes in the unit cells of the experimentally found orientations that were the closest to the c) {1 1 1}, e) {0 0 1} and g) {0 1 1} (surface) plane normal (here facing upwards). (For interpretation of the references to colour in this figure legend, the reader is referred to the web version of this article.)

observation of serrations and also immobilisation of dislocations in interrupted mechanical tests [15], also points to a further role of point defects in the deformation of Laves phase crystals. Given that off-stoichiometric composition has been found to lead to softening in many but not all cases, it can be concluded here that in the $CaAl_2$ C15 Laves phase it is likely that at low temperature the lattice resistance provides the rate limiting mechanism, but that cannot infer if or in how far this is also affected by solutes. Additionally, studies above the BDTT on cubic Laves phases calculated a decreasing strain rate sensitivity and the activation volume with increasing temperature and correlating it also with the overcoming of the Peierls barrier, which could also be correlated diffusion or climb processes at these experimental temperatures [73,74].

However, the work presented here and elsewhere on Laves phases in recent years now puts us into a position to investigate these effects in more detail and with hopefully more definite conclusions. With respect to the $CaAl_2$ phase, future work towards elevated temperatures and also towards off-stoichiometric or alloyed compositions can follow. Taking into account the new insights on the active dislocation slip systems and the dependence of likely cross-slip opportunities on crystal orientation in indentation presented above, the expectation that work at temperatures between room temperature and the BDTT as well as on alloys will be able to draw firmer conclusions on the individual roles of the lattice resistance on individual slip systems and solutes, anti-site defects or vacancies in governing dislocation motion in Laves phases. In experiments, the different point defects may not be possible to control separately, however, in simulations, first efforts are already being made to explore their role on dislocation motion [75].

5. Conclusions

The plasticity of the $CaAl_2$ C15 phase was investigated at ambient temperature using nanoindentation in conjunction with a slip trace analysis, strain rate jump tests, micropillar compression and TEM analysis. The combination of these testing methods allowed us to draw the following conclusions:

- The average hardness and indentation modulus are 4.9 ± 0.7 GPa and 85.5 ± 4.0 GPa and do not vary significantly with orientation.
- Strain rate jump tests reveal a strain rate sensitivity of 0.028 ± 0.019 and a corresponding activation volume of 3.75 ± 1.15 b^3.
- All nanomechanical experiments have shown that the predominate slip systems are $\{111\}\langle 1\bar{1}0\rangle$ and $\{112\}\langle 1\bar{1}0\rangle$ and are activated with more or less the same CRSS of 0.99 ± 0.07 GPa and 0.97 ± 0.03 GPa, respectively, whereby TEM investigations allowed to identify the $[1\bar{1}0]$ Burgers vector type by using the $g \cdot b$ analysis.
- Cracks at the edge of the indents were found on the $\{112\}$ plane for all investigated orientations.
- TEM analysis on a nanoindent allowed to identify dislocation motion on both $(11\bar{1})$ and $(\bar{2}1\bar{1})$ planes. Stacking faults were found and could be located on the $(11\bar{1})$ plane.

Data availability

The authors do not have permission to share data.

Declaration of Competing Interest

The authors declare that they have no known competing financial interests or personal relationships that could have appeared to influence the work reported in this paper.

Acknowledgements

The authors gratefully acknowledge financial support by the Deutsche Forschungsgemeinschaft (DFG) to all projects involved in this paper A05, Z and S the SFB1394 Structural and Chemical Atomic Complexity – From Defect Phase Diagrams to Material Properties, project ID 409476157. This project has received funding from the European Research Council (ERC) under the European Union's Horizon 2020 research and innovation programme (grant agreement No. 852096 FunBlocks). H. Springer gratefully acknowledges funding through the Heisenberg program of the DFG (project number 416498847).

References

[1] P. Paufler, Early work on Laves phases in East Germany, Intermetallics 19 (4) (2011) 599–612.
[2] F. Stein, A. Leineweber, Laves phases: a review of their functional and structural applications and an improved fundamental understanding of stability and properties, J. Mater. Sci. 56 (9) (2021) 5321–5427.
[3] J. Livingston, Laves-phase superalloys?, Phys Status Solidi A 131 (2) (1992) 415–423.
[4] A.-P. Hynninen et al., Self-assembly route for photonic crystals with a bandgap in the visible region, Nat. Mater. 6 (3) (2007) 202–205.
[5] B. van der Meer et al., High antisite defect concentrations in hard-sphere colloidal laves phases, Soft Matter 16 (17) (2020) 4155–4161.
[6] B.A. Lindquist, R.B. Jadrich, T.M. Truskett, From Close-Packed to Topologically Close-Packed: Formation of Laves Phases in Moderately Polydisperse Hard-Sphere Mixtures. arXiv preprint arXiv:1803.03327, 2018.
[7] A. Suzuki et al., Structure and transition of eutectic (Mg, Al) 2Ca Laves phase in a die-cast Mg–Al–Ca base alloy, Scr. Mater. 51 (10) (2004) 1005–1010.
[8] H.A. Elamami et al., Phase selection and mechanical properties of permanent-mold cast Mg-Al-Ca-Mn alloys and the role of Ca/Al ratio, J. Alloy. Compd. 764 (2018) 216–225.
[9] M. Zubair et al., On the role of Laves phases on the mechanical properties of Mg-Al-Ca alloys, Mater. Sci. Eng. A 756 (2019) 272–283.
[10] D. Amberger, P. Eisenlohr, M. Göken, Microstructural evolution during creep of Ca-containing AZ91, Mater. Sci. Eng. A 510 (2009) 398–402.
[11] H. Mathur, V. Maier-Kiener, S. Korte-Kerzel, Deformation in the γ-$Mg_{17}Al_{12}$ phase at 25–278° C, Acta Mater. 113 (2016) 221–229.
[12] L. Rokhlin et al., Calcium-alloyed magnesium alloys, Met. Sci. Heat Treat. 51 (3–4) (2009) 164.
[13] T. Müller et al., Gleitbanduntersuchungen während und nach Verformung der intermetallischen Verbindung $MgZn_2$, Krist. Tech. 7 (11) (1972) 1249–1264.
[14] D. Hinz, P. Paufler, G. Schulze, Temperature change experiments during secondary creep of the intermetallic compound $MgZn_2$, physica status solidi (b) 36 (2) (1969) 609–615.
[15] T. Müllerr, P. Paufler, Yield strength of the monocrystalline intermetallic compound $MgZn_2$, physica status solidi (a) 40 (2) (1977) 471–477.
[16] U. Krämer, G. Schulze, Gittergeometrische Betrachtung der plastischen Verformung von Lavesphasen, Krist. Tech. 3 (3) (1968) 417–430.
[17] A. Von Keitz, G. Sauthoff, Laves phases for high temperatures—Part II: Stability and mechanical properties, Intermetallics 10 (5) (2002) 497–510.
[18] P. Paufler, G. Schulze, Gleitsysteme innermetallischer Verbindungen, Krist. Tech. 2 (4) (1967) K11–K14.
[19] J. Moran, Mechanical behavior of $MgCu_2$ single crystals, Trans. Metall. Soc. AIME 233 (8) (1965) 1473.
[20] D.P. Pope, F. Chu, Deformation of a C15 Laves phase: Twinning and synchroshear, Structural intermetallics (1993).
[21] W.-Y. Kim, D.E. Luzzi, D.P. Pope, Room temperature deformation behavior of the Hf–V–Ta C15 Laves phase, Intermetallics 11 (3) (2003) 257–267.
[22] A. Kazantzis, M. Aindow, I. Jones, Deformation behaviour of the C15 Laves phase Cr_2Nb, Mater. Sci. Eng. A 233 (1–2) (1997) 44–49.
[23] A. Kazantzis et al., The mechanical properties and the deformation microstructures of the C15 Laves phase Cr_2Nb at high temperatures, Acta Mater. 55 (6) (2007) 1873–1884.
[24] A. Kazantzis, M. Aindow, I. Jones, Stacking-fault energy in the C15 Laves phase Cr_2Nb, Philos. Mag. Lett. 74 (3) (1996) 129–136.
[25] S. Korte-Kerzel, Microcompression of brittle and anisotropic crystals: recent advances and current challenges in studying plasticity in hard materials, MRS Commun. 7 (2) (2017) 109–120.
[26] W. Luo et al., Composition dependence of hardness and elastic modulus of the cubic and hexagonal $NbCo_2$ Laves phase polytypes studied by nanoindentation, J. Mater. Res. 35 (2) (2020) 185–195.
[27] Y. Xue et al., Critical resolved shear stress of activated slips measured by micropillar compression tests for single-crystals of Cr-based Laves phases, Mater. Sci. Eng. A 806 (2021) 140861.
[28] S. Korte, W.J. Clegg, Studying plasticity in hard and soft Nb–Co intermetallics, Adv. Eng. Mater. 14 (11) (2012) 991–997.

[29] W. Luo et al., Crystal structure and composition dependence of mechanical properties of single-crystalline $NbCo_2$ Laves phase, Acta Mater. 184 (2020) 151–163.
[30] M.F. Chisholm, S. Kumar, P. Hazzledine, Dislocations in complex materials, Science 307 (5710) (2005) 701–703.
[31] Hazzledine, P., et al., *Synchroshear of Laves phases.* MRS Online Proceedings Library (OPL), 1992. **288**.
[32] P. Hazzledine, P. Pirouz, Synchroshear transformations in Laves phases, Scr. Metall. Mater. 28 (10) (1993) 1277–1282.
[33] J. Guénolé et al., Basal slip in Laves phases: the synchroshear dislocation, Scr. Mater. 166 (2019) 134–138.
[34] Z. Xie et al., Laves phase crystal analysis (LaCA): Atomistic identification of lattice defects in C14 and C15 topologically close-packed phases, J. Mater. Res. 36 (10) (2021) 2010–2024.
[35] S. Schröders et al., On the structure of defects in the Fe_7Mo_6 μ-Phase, Acta Mater. 167 (2019) 257–266.
[36] Y. Liu, J.D. Livingston, S.M. Allen, Defect structures and nonbasal slip of C36 laves phase $MgNi_2$ in a two-phase alloy, Metall. Mater. Trans. A 26 (6) (1995) 1441–1447.
[37] Liu, Y., S.M. Allen, and J.D. Livingston, *Deformation mechanisms in a Laves phase.* MRS Online Proceedings Library (OPL), 1992. **288**.
[38] Y. Liu, S.M. Allen, J.D. Livingston, Deformation of two C36 laves phases by microhardness indentation at room temperature, Metall. Mater. Trans. A 26 (5) (1995) 1107–1112.
[39] Allen, S., *Slip, twinning, and transformation in Laves phases.* , A.-.-J. Final technical report, 1997, Editor. 1998, Massachusetts Inst. of Technology (MIT), Cambridge, MA (United States).
[40] C. Zehnder et al., Plastic deformation of single crystalline C14 Mg_2Ca Laves phase at room temperature, Mater. Sci. Eng. A 759 (2019) 754–761.
[41] M. Freund et al., Plastic deformation of the $CaMg_2$ C14-Laves phase from 50–250° C, Materialia 20 (2021) 101237.
[42] D. Andre et al., Metallographic preparation methods for the Mg based system Mg-Al-Ca and its Laves phases, Mater Charact (2022) 112187.
[43] W.C. Oliver, G.M. Pharr, An improved technique for determining hardness and elastic modulus using load and displacement sensing indentation experiments, J. Mater. Res. 7 (6) (1992) 1564–1583.
[44] P.S. Phani, W. Oliver, A critical assessment of the effect of indentation spacing on the measurement of hardness and modulus using instrumented indentation testing, Mater. Des. 164 (2019) 107563.
[45] J.-S.-L. Gibson et al., Finding and Characterising Active Slip Systems: A Short Review and Tutorial with Automation Tools, Materials 14 (2) (2021) 407.
[46] V. Maier-Kiener, K. Durst, Advanced nanoindentation testing for studying strain-rate sensitivity and activation volume, JOM 69 (11) (2017) 2246–2255.
[47] V. Maier et al., An improved long-term nanoindentation creep testing approach for studying the local deformation processes in nanocrystalline metals at room and elevated temperatures, J. Mater. Res. 28 (9) (2013) 1177–1188.
[48] V. Maier et al., Nanoindentation strain-rate jump tests for determining the local strain-rate sensitivity in nanocrystalline Ni and ultrafine-grained Al, J. Mater. Res. 26 (11) (2011) 1421–1430.
[49] D. Singh et al., Micropillar compression of Al/SiC nanolaminates, Acta Mater. 58 (20) (2010) 6628–6636.
[50] B. Lucas, W. Oliver, Indentation power-law creep of high-purity indium, Metall. Mater. Trans. A 30 (3) (1999) 601–610.
[51] S. Schröders et al., Room temperature deformation in the Fe_7Mo_6 μ-Phase, Int. J. Plast 108 (2018) 125–143.
[52] K. Momma, F. Izumi, VESTA 3 for three-dimensional visualization of crystal, volumetric and morphology data, J. Appl. Cryst. 44 (6) (2011) 1272–1276.
[53] S. Luo et al., Micro-compression of Al_2Ca particles in a Mg-Al-Ca alloy, Materialia 21 (2022) 101300.
[54] R. Schiltz Jr, J. Smith, Elastic constants of some M Al2 single crystals, J. Appl. Phys. 45 (11) (1974) 4681–4685.
[55] W.-Y. Yu et al., First-principles investigation of the binary AB2 type Laves phase in Mg–Al–Ca alloy: Electronic structure and elastic properties, Solid State Sci. 11 (8) (2009) 1400–1407.
[56] K.L. Johnson, K.L. Johnson, Contact mechanics, Cambridge University Press, 1987.
[57] A. Fischer-Cripps, P. Karvankova, S. Vepřek, On the measurement of hardness of super-hard coatings, Surf. Coat. Technol. 200 (18–19) (2006) 5645–5654.
[58] W.D. Nix, H. Gao, Indentation size effects in crystalline materials: a law for strain gradient plasticity, J. Mech. Phys. Solids 46 (3) (1998) 411–425.
[59] P. Howie et al., Softening non-metallic crystals by inhomogeneous elasticity, Sci. Rep. 7 (1) (2017) 1–9.
[60] C. Marichal et al., 110 Slip with 112 slip traces in bcc Tungsten, Sci. Rep. 3 (1) (2013) 1–7.
[61] H. Van Swygenhoven, S. Van Petegem, In-situ mechanical testing during X-ray diffraction, Mater Charact 78 (2013) 47–59.
[62] J. Zhu et al., Point defects in binary Laves phase alloys, Acta Mater. 47 (7) (1999) 2003–2018.
[63] K. Eichler et al., Änderung von Verformungseigenschaften der intermetallischen Verbindung $MgZn_2$ im Homogenitätsbereich, Krist. Tech. 11 (11) (1976) 1185–1188.
[64] R. Peierls, The size of a dislocation, in: Selected Scientific Papers Of Sir Rudolf Peierls: (With Commentary), World Scientific, 1997, pp. 273–276.
[65] Forbes, R.G., *The prediction of zero-barrier evaporation field: Datasheet from Condensed Matter · Volume 45B: "Physics of Solid Surfaces" in SpringerMaterials (https://doi.org/10.1007/978-3-662-53908-8_158)*, G. Chiarotti and P. Chiaradia, Editors., Springer-Verlag GmbH Germany.
[66] M. Spittel, T. Spittel, Influence of chemical composition and forming conditions on flow stress, in: Part 3: Non-ferrous Alloys-Heavy Metals, Springer, 2016, pp. 18–64.
[67] S. Korte et al., Deformation of silicon–insights from microcompression testing at 25–500 C, Int. J. Plast 27 (11) (2011) 1853–1866.
[68] Cottrell, A.H., *The Bakerian Lecture, 1963. Fracture.* Proceedings of the Royal Society of London. Series A. Mathematical and Physical Sciences, 1963. **276** (1364): p. 1-18.
[69] D.C. Palmer, Visualization and analysis of crystal structures using CrystalMaker software, Zeitschrift für Kristallographie-Crystalline Materials 230 (9–10) (2015) 559–572.
[70] H. Conrad, Thermally activated deformation of metals, JOM 16 (7) (1964) 582–588.
[71] P. Paufler, Deformation-mechanism maps of the intermetallic compound $MgZn_2$, Krist. Tech. 13 (5) (1978) 587–590.
[72] P. Paufler, G. Schulze, Plastic deformation of the intermetallic compound $MgZn_2$, physica status solidi (b) 24 (1) (1967) 77–87.
[73] Y. Ohba, N. Sakuma, High temperature-room temperature deformation behavior of $MgCu_2$ laves phase intermetallic compound, Acta Metall. 37 (9) (1989) 2377–2384.
[74] H. Saka et al., Plasticity of single crystals of Fe_2(Dy, Tb) Laves phase at high temperatures, Philos. Mag. A 68 (5) (1993) 871–884.
[75] Z. Xie, et al., Unveiling the mechanisms of motion of synchro-Shockley dislocations. arXiv preprint arXiv:2205.02669, 2022.

6. Publication 2

Plastic deformation of the $CaMg_2$ C14-Laves phase from 50 - 250°C

Martina Freund, Doreen Andre, Christoffer Zehnder, Hanno Rempel, Dennis Gerber, Muhammad Zubair, Stefanie Sandlöbes-Haut, James S. K.-L. Gibson, Sandra Korte-Kerzel,

Institute for Physical Metallurgy and Materials Physics, RWTH Aachen University, Aachen, Germany

Materialia, Volume 20, 2021, 101237, **reproduced with permission of Elsevier.**

https://doi.org/10.1016/j.mtla.2021.101237.

Short Summary

Intermetallic phases can significantly improve the creep resistance of magnesium alloys, extending their use to higher temperatures. However, little is known about the deformation behaviour of these phases at application temperatures, which are commonly below their macroscopic brittle-to-ductile-transition temperature. In this study, we therefore investigate the activation of different slip systems of the $CaMg_2$ phase and the occurrence of serrated yielding in the temperature range from 50°C to 250°C. A decreasing amount of serrated flow with increasing temperature suggests that solute atoms govern the flow behaviour when the $CaMg_2$ phase is off-stoichiometric.

Martina Freund: Writing – review & editing, Visualization, Investigation, Formal analysis. Doreen Andre: Writing – review & editing, Investigation. Christoffer Zehnder: Conceptualization, Writing – original draft. Hanno Rempel: Formal analysis. Dennis Gerber: Formal analysis. Muhammad Zubair: Formal analysis. Stefanie Sandlöbes-Haut: Writing - review. James S.-K.-L.: Formal analysis, Writing - review. Sandra Korte-Kerzel: Writing –review & editing, Supervision.

Materialia 20 (2021) 101237

Contents lists available at ScienceDirect

Materialia

journal homepage: www.elsevier.com/locate/mtla

Full Length Article

Plastic deformation of the $CaMg_2$ C14-Laves phase from 50 - 250°C

Martina Freund[a,*], Doreen Andre[a], Christoffer Zehnder[a], Hanno Rempel[a], Dennis Gerber[a], Muhammad Zubair[a,b], Stefanie Sandlöbes-Haut[a], James S. K.-L. Gibson[a], Sandra Korte-Kerzel[a]

[a] *Institute for Physical Metallurgy and Materials Physics, RWTH Aachen University, Aachen, Germany*
[b] *Department of Metallurgical and Materials Engineering, UET, Lahore, Pakistan*

ARTICLE INFO

Keywords:
Plasticity
Laves phase
Temperature
Stoichiometry
Nanoindentation
Microcompression

ABSTRACT

Intermetallic phases can significantly improve the creep resistance of magnesium alloys, extending their use to higher temperatures. However, little is known about the deformation behaviour of these phases at application temperatures, which are commonly below their macroscopic brittle-to-ductile-transition temperature. In this study, we therefore investigate the activation of different slip systems of the $CaMg_2$ phase and the occurrence of serrated yielding in the temperature range from 50°C to 250°C. A decreasing amount of serrated flow with increasing temperature suggests that solute atoms govern the flow behaviour when the $CaMg_2$ phase is off-stoichiometric.

1. Introduction

1.1. Application of $CaMg_2$ Laves phases

Magnesium, as the lightest structural metal, has great potential for light-weight applications, but the use of its alloys in applications above 100°C is limited due to their low creep resistance. Recently-developed alloys containing aluminium and calcium exhibit minimum creep rates up to three orders of magnitude lower than pure magnesium [1–10]. This improved creep resistance is due to the formation of an interconnected network of intermetallic phases [7-9,11-13]. This network reduces creep taking place via grain boundary sliding or other diffusion-dominated creep mechanisms along grain boundaries. However, once this network begins to crack, the creep rates significantly increase [14,15]. Consequently, there is a need to understand the mechanical response and plasticity mechanisms of the intermetallic phases to predict deformation and creep-related failure in these Mg-Al-Ca alloys from room- to application-temperatures and to pursue purposeful alloy design.

In Mg-Al-Ca alloys, several intermetallic phases form [10,16-20], including two hexagonal Laves phases C14 $CaMg_2$ and C36 $Ca(Mg,Al)_2$, the cubic C15 $CaAl_2$, the β-Mg_2Al_3 Laves phase and $Mg_{17}Al_{12}$ precipitates with a complex body-centred cubic structure (α-Mn type). The $Mg_{17}Al_{12}$ phase exhibits a significant hardness drop once temperatures reach 150°C [21]. Hence, it is assumed that for Mg-Al-Ca alloys with favourable high-temperature behaviour, the $Mg_{17}Al_{12}$ phase should be avoided, which can be realised by increasing the Ca content [15]. The mechanical properties of the Mg-Al-Ca alloy at high temperature will subsequently be determined by the deformation of the α-Mg matrix and the Laves phases.

1.2. Deformation mechanisms of Laves phases

Reports on macroscopic low-temperature deformation behaviour of the $Ca(Mg_x,Al_{1\text{-}x})_2$ and most other Laves phases are sorely lacking, with a solitary publication by Kirsten et al. [22] who reported slip on $\{01\bar{1}0\}\langle 2\bar{1}\bar{1}0\rangle$ at ambient temperature after their Brinell hardness tests on the $CaMg_2$ phase. However, extensive studies on the high temperature (HT) mechanical properties of Laves phases have been conducted by Paufler, Schulze, Kubsch and others [23–34]. Specifically, they have conducted compression and creep tests at high homologous temperatures, T_H, mainly on C14 $MgZn_2$ single crystals. Generally, these studies have shown that it is not possible to induce bulk plastic flow in macroscopic specimens at homologous temperatures lower than approximately $T_H = 0.6$. For lower temperatures, plastic deformation can only be introduced locally in Laves phases, such as in indentation or using micropillar compression [22,29,35,36]. As an example, a recent nanoindentation study by Lou et al. [37] analysed the influence of the orientation on the hardness of the C14 $NbCo_2$ phase. It was found that the hardness was about 5% higher for an orientation close to (0001) compared to the other investigated orientations.

For a long time, hardness tests were the only available method allowing the determination of the mechanical properties of Laves phases over a large range of temperatures. Kirsten et al. [22] conducted hardness tests on the $MgZn_2$ and the $CaMg_2$ C14 Laves phases and revealed a de-

---

[*] Corresponding author.
E-mail address: freund@imm.rwth-aachen.de (M. Freund).

https://doi.org/10.1016/j.mtla.2021.101237
Received 15 June 2021; Accepted 25 September 2021

creasing hardness of approximately 10% up to a transition temperature, after which a pronounced loss in hardness was observed. This transition temperature was 0.59^*T_m (T_m being the melting temperature) for the $CaMg_2$ phase also investigated within this study and 0.61^*T_m for the $MgZn_2$ phase. Correspondingly, this trend was also found for the yield strength in dynamic compression tests on the $MgZn_2$ phase [28].

Regarding deformation mechanisms above the transition temperature, Paufler et al. [29] postulated a deformation regime at low stresses and high temperatures ($T > 0.7\ T_m$) where dislocation climb is thought to be active. However, Kubsch et al. [32] did not observe this in their experiments. Furthermore, Paufler et al. [26,27,31] showed that the dislocation velocity on basal and prismatic slip planes is exponentially dependent on the applied stress at conditions of constant temperature and stress (e.g. during creep) in Laves phases. From these findings, the authors concluded that a thermally activated Peierls mechanism is the limiting factor for dislocation motion at high temperatures [26,27,31]. It has also been observed that the critical stresses for dislocation motion associated with the lattice resistance (thermally activated flow over the Peierls barrier) for basal and prismatic slip are of the same order of magnitude at high temperatures [27]. Furthermore, a significant amount of thermally activated cross-slip has been found between 250°C and 500°C [31]. Most dislocations present after high temperature deformation were observed to be on the basal or the prismatic planes [31], however, it should be noted that the single crystals tested were purposely aligned for the activation of these slip systems. Recent atomistic simulations by Guénolé et al. [38] have shown that the propagation mechanism for dislocations on the basal plane is a synchroshear mechanism, rather than conventional dislocation glide.

Though experiments at several temperatures have revealed that $\langle a \rangle$-type dislocations on basal planes are the most frequently observed dislocation type [25,31,39-41], several studies have shown that non-basal slip systems can also be activated in Laves phases [39,42-45]. It has further been reported that slip planes normal to the basal plane can be activated when Laves phase containing alloys are deformed at elevated temperatures [46]. A publication by Paufler et al. [47] further listed the observed slip systems of several intermetallic phases at different temperature ranges. For $MgZn_2$, which has the same crystal structure (C14) as that of the $CaMg_2$ investigated here, basal slip was reported to occur for temperatures between 250°C and 550°C, whereas at temperatures of 500°C and above, prismatic and pyramidal slip were reported. Furthermore, uniaxial compression experiments by Paufler et al. [48] on nearly (0001) oriented $MgZn_2$ single crystals at 450°C revealed mechanical twinning as an additional deformation mechanism. Studies by Kazantzis et al. [49–51] on the deformation behaviour of the C15 $NbCr_2$ phase confirm the deformation via slip and twinning at elevated temperatures, which is assumed to be due to a low stacking fault energy.

In addition to these effects of crystal orientation and temperature, the stoichiometry – or rather the off-stoichiometry, i.e. the deviation from the exact stoichiometry – also has a significant effect on the deformation mechanisms and the mechanical properties of Laves phases. It has been seen that with increasing off-stoichiometry, deformation becomes less uniform in Laves phases and Lüders bands begin to form during plastic deformation [28,30-33,52]. Furthermore, several publications by Luo et al. [36,37,53] who studied the composition dependence of the mechanical properties of C14 and C36 $NbCo_2$, as well as C15 $NbCo_2$ Laves phases, revealed an effect of the composition on the critical resolved shear stress (CRSS), elastic modulus and hardness, but no effect on the fracture toughness. These effects were explained by a reduced shear modulus, stacking fault energy and Peierls stress, respectively. More information regarding the fundamental aspect of Laves phases can be found in a recent review by Stein et al. [54].

Kubsch et al. [31] reported a strong effect of the stoichiometry on the deformation mechanisms, reporting in $MgZn_2$ that slight deviations (±2 at.-%) from the stoichiometric composition cause a significant decrease of the dislocation velocity, particularly on the Mg-rich side. In intermetallic structures, off-stoichiometry can induce pinning points for dislocations, thus hindering the motion of dislocation kinks and therefore reducing the velocity of dislocations [26,31]. This is considered in the model proposed by Celli et al. [32] where the rate-controlling mechanism of plastic deformation is proposed to be the nucleation of double kinks and their lateral movement across pinning points [32]. A similar mechanism is reported by Kazantzis et al. [55] regarding the self-pinning nature of synchro-Shockleys in the C15 Laves phase at elevated temperatures.

Similar effects on the dislocation velocity have been reported elsewhere [28,30-33,52], implying that especially for the exact stoichiometric composition, dislocation starvation is a limiting factor at the beginning of deformation. Subsequently, dislocations are then able to travel large distances without being pinned [28,33]. This is in good agreement with micropillar compression experiments by Takata et al. [35,42] who found that the critical stress required to activate shear deformation in Fe_2Nb micropillars was drastically reduced when the pillars were slightly pre-deformed with a Berkovich indenter prior to compression, indicating that dislocation nucleation is a critical factor for plastic deformation of Laves phases [35,42]. In metals, this effect can also be observed, but only in samples that have been prepared to achieve a low dislocation density by solidification, annealing and avoidance of damage from the focussed ion beam (FIB) [56,57]. None of these special conditions have been applied in our work. It has been further reported that temperature does not affect the mean distance that dislocations travel before being pinned, but that the number of activated dislocation sources is instead increased with increasing temperature [28]. Finally, it has been shown that if several Laves phases are present in one system at the same temperature, the C15 phase can typically be found at the exact stoichiometric composition while the C14 and the C36 phase both tend to crystallise with an off-stoichiometric composition [58].

A previous study by the authors [59] elucidated the critical resolved shear stresses of different slip systems in the C14 $CaMg_2$ Laves phase at room temperature. The critical resolved shear stresses obtained for slip on these planes in microcompression follow the sequence: 1st order prismatic planes (0.44 GPa) < basal (0.52 GPa) and 1st order pyramidal (0.53 GPa) planes < 2nd order pyramidal planes (0.59 GPa) < 2nd order prismatic planes, for which no critical stress could be measured directly [59]. The authors further identified the presence of both $\langle a \rangle$ and $\langle c+a \rangle$-dislocations on the 1st order pyramidal planes by transmission electron microscopy of lamellae extracted from under nanoindents [59].

The aim of the present study is to extend these investigations and to study the activation and critical resolved shear stresses of slip systems in the $CaMg_2$ Laves phase at intermediate elevated temperatures where plastic deformation still cannot be achieved macroscopically. Hence, we aim to close the gap between deformation at room temperature and high temperatures. To this end, elevated temperature nanoindentation and micropillar compression between 50°C and 250°C ($< 0.53\ T_m$) were performed in conjunction with microstructure characterisation using scanning electron microscopy (SEM), electron backscatter diffraction (EBSD) and transmission electron microscopy (TEM).

2. Experimental methods

As-cast samples of the $CaMg_2$ (C14) phase prepared from a pre-alloy were mechanically ground and polished with diamond paste down to 0.25 µm, followed by a final polishing step with 0.05 µm aluminium oxide polishing solution (OPA). EBSD (Hicari, EDAX (NJ, USA)) was used to determine the crystal orientations. Three grains with angles of 48°, 83° and 9° between the (0001) plane normal and normal direction (ND) were selected for micromechanical testing (Fig. 1). EDX measurements were performed on all three areas of interest. The mean Mg-content was measured as 68.7 ± 0.5 at.-% which is a deviation of approximately 2 at.-% from the exact stoichiometric composition. A wet-chemical analysis of the pre-alloy revealed an impurity content of <0.32 wt.-% with aluminium the major impurity element (0.24 wt.-%).

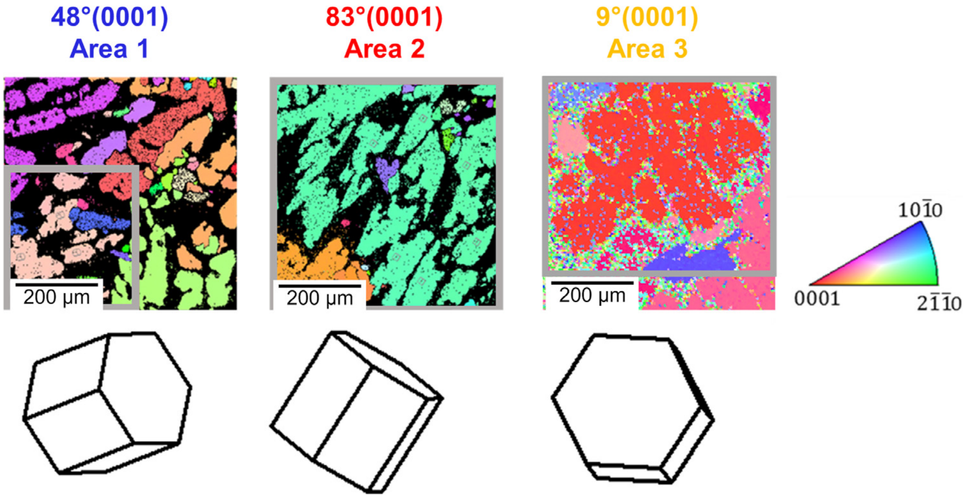

Fig. 1. EBSD maps of the three grain orientations with position of the investigated areas marked by grey rectangles. Their unit cell orientation viewed from the normal direction is also given.

2.1. Nanoindentation

Indentation experiments were performed between 50°C and 250°C in 50°C steps in the three crystal orientations resulting in a total of 80 indents using an in-situ SEM nanoindenter (InSEM-III, Nanomechanics Inc, TN, USA / Tescan Vega-3, TESCAN Brno, Czech Republic) using continuous stiffness measurements. A diamond Berkovich indenter tip (supplied by Synton MDP, Switzerland) was used, which was calibrated prior to indentation at room temperature on fused silica [60]. All indentation tests were performed at a constant strain rate of approximately 0.04 s^{-1} up to a maximum load of 20 mN or a maximum depth of 600 nm. Furthermore, for better visibility of potential slip traces, indents up to a maximum load of 1000 nm were performed using a loading rate of 0.2 s^{-1}. The thermal drift rate was below 0.4 nm/s for all measurements. The resulting data were then further evaluated according to the method published by Oliver and Pharr [60]. After indentation, secondary electron (SE) images of the indents were recorded by SEM (Helios Nanolab 600i, FEI, Eindhoven, NL) and the surface slip lines around the indents were compared to the plane traces of different slip planes obtained from the EBSD maps; a full description of this procedure is given elsewhere [61,62]. This approach gives the relative frequency of slip plane-surface intersections for the crystal orientations selected experimentally and, hence, elucidates the activation frequency of different slip planes. TEM investigations were conducted at 200 kV (Philips CM20) on lamellae taken from indents performed at 250°C in the 48°(0001) and the 83°(0001) orientations. The lamellae were cut using a focused ion beam.

2.2. Micropillar compression experiments

Micropillars were manufactured in all three grains using a focused ion beam (FIB) (FEI Helios Nanolab 600i, FEI, Eindhoven, NL) at a voltage of 30 kV and currents between 21 nA and 80 pA. The micropillars with a circular cross section had an average aspect ratio (height : top diameter) of 2.8 and were compressed ‘in-situ’ inside an SEM, using a diamond flat punch at a constant loading rate of 0.9 mN/s at temperatures of 150°C and 250°C. The thermal drift was below 0.4 nm/s for all measurements. After successful compression of 17 micropillars, they were imaged at 45° in a SEM (FEI Helios Nanolab 600i, FEI, Eindhoven, NL) and the angles of the slip events were measured, corrected for the stage tilt, and compared to the intersections of crystal planes with the pillar surface using Matlab® in order to assign them to possible slip planes [62]. It was further assumed that slip in the direction of the highest Schmid factor was activated. The resulting slip direction was then further verified with the post compression SE-images. Finally, the original upper diameter of the pillar was used to calculate the critical resolved shear stress (CRSS).

3. Results

3.1. Nanoindentation

Fig. 2 shows representative hardness-depth curves from indentation tests performed at 50°C and 250°C. These exhibit the commonly-observed indentation size effect, with a higher hardness towards smaller depths. To compare the hardness across different temperatures and orientations, the value at 500 nm was taken, as at the point the indentation size effect is vanishingly small for all measured orientations and temperatures. These data are given in Fig. 3a and show no clear trends over the studied temperature range. Averaging the hardness values over all temperatures and orientations gives a value of 3.5 ± 0.3 GPa. The indentation modulus was similarly constant within the standard deviation at all temperatures and orientations and amounts to 53.3 ± 4 GPa (Fig. 3b). For determining these values, a mean Poisson ratio of 0.24 was taken based on the values reported elsewhere [63,64].

Fig. 4 shows representative load-displacement curves for the 48°(0001) orientation between 50°C and 250°C revealing serrated flow at all testing temperatures, which decreases with increasing testing temperature. The occurrence of serrated flow causes a relatively high noise level when hardness is evaluated using a continuous stiffness measurement (Fig. 2a for example).

3.2. Slip line analysis

SE images of slip lines formed around the indents were compared to the traces of surface/crystal plane intersections of potential slip planes using the local orientation information from EBSD. This evaluation yields statistical information using a total number of 249 evaluated slip traces on the activation of different slip systems and presents a useful first step to guide and interpret subsequent uniaxial compression experiments [61,62]. Principally, all indents could be sorted into three categories depending on the amount and shape of slip lines around them. At low temperatures, clear and straight slip lines were observed that could unambiguously be correlated with potential crystallographic plane traces (**Fig.** 5, orange, straight lines). With increasing temperature either no slip lines formed (Fig. 5, no markings) or the slip lines followed a curved shape, presumably following the stress field in very narrow steps (Fig. 5, white, curved lines).

In this last case, the error from falsely assigning one slip line increased with a decreasing number of interpretable slip traces. Consequently, only those experiments where at least ten sufficiently straight

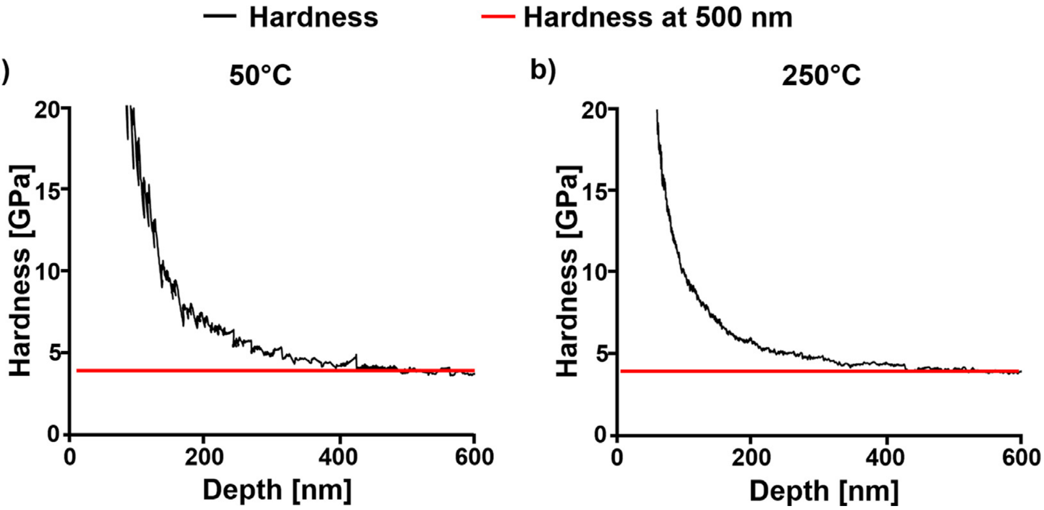

Fig. 2. Hardness with indentation depth for the 48°(0001) oriented grain at 50°C (a) and 250°C (b). The red line displays the average hardness value at 500 nm.

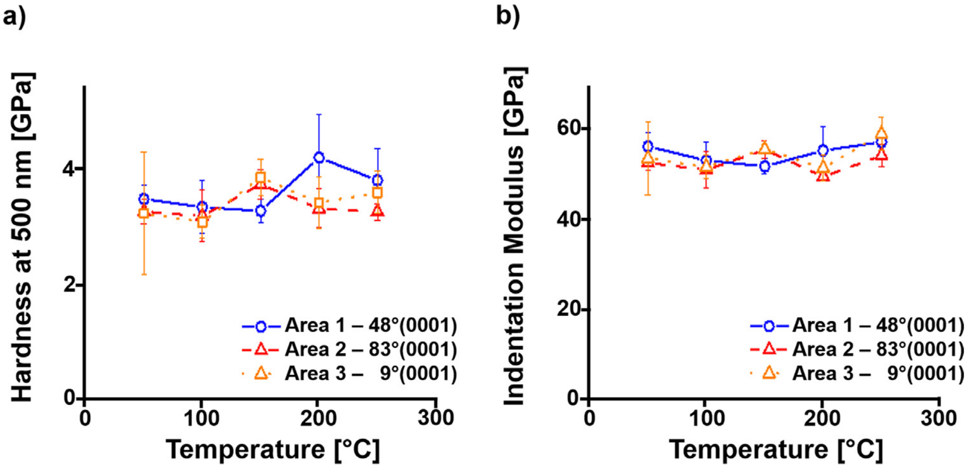

Fig. 3. a) Hardness at 500 nm and b) indentation modulus for all three orientations and temperatures between 50°C and 250°C including their standard deviation.

slip trace segments could be identified in total for each orientation were analysed further.

Fig. 6 shows the glide planes to which the slip lines were assigned for the 83° and 48°(0001) grain orientations that could be analysed as a function of temperature. Also included are CRSS values for each slip system which were determined via micropillar compression, as discussed later.

In the 83°(0001) oriented grain (red data points), the relative frequency of activation of basal slip traces first increased slightly, but then decreased to zero at temperatures above 100°C. The relative frequency of activation of 1st order prismatic slip traces decreased from 15% to 8% between room temperature and 200°C. The relative frequency of activation of 2nd order pyramidal and 2nd order prismatic slip traces stayed constant at around 40% and 10%, respectively. The fraction of 1st order pyramidal slip traces fluctuated around a value of 35%, but overall slightly increased with temperature.

In the grain with 48°(0001) orientation (blue data points), similar trends were seen: the occurrence of basal slip decreased with temperature, vanishing at 150°C. The relative frequency of activation of 1st order prismatic slip traces decreased slightly, from 26% at room temperature to 20% at 150°C, and similar to the 83°(0001) oriented grain, the fraction of 2nd order prismatic slip traces remained constant. Differences between the two grains occurred regarding the pyramidal slip systems. In the 48°(0001) orientation, the relative frequency of activation of 1st order pyramidal slip traces stayed constant with 33% up to a temperature of 100°C and then decreased to 20% at 150°C, while the relative frequency of activation of the 2nd order pyramidal slip traces increased sharply from 32% at room temperature to 50% at 150°C.

3.3. Micropillar compression

A total of seventeen micropillars were compressed and found to deform plastically within the course of this study. Eleven micropillars were compressed at 150°C and six at 250°C within the three differently orientated grains. For each orientation and temperature, one representative compressed micropillar including its simulated slip plane and engineering stress strain curve is given in Fig. 7. Note that for the 9°(0001) orientation, due to experimental difficulties, no micropillar analysis could be conducted at 250°C. The number of pillars exhibiting the indicated slip planes are given in Fig. 8 for each grain orientation.

The 48°(0001) oriented micropillars showed slip planes corresponding predominately to the basal plane for both elevated temperatures, which has a high Schmid factor of 0.49. However, slip on the 1st order prismatic and 1st and 2nd order pyramidal planes was also observed.

For the 83°(0001) orientated pillars, some pillars slipped along the basal and 1st order prismatic plane at ambient temperature, but more pyramidal slip was observed for all temperatures. Despite its high Schmid factor of 0.48, prismatic slip was only activated for two pillars.

For the 9°(0001) orientated micropillars, the activated slip planes correspond to the pyramidal slip systems, which also have the highest Schmid factor of 0.47 to 0.49. For the 9°(0001) orientation at ambient temperature, one pillar slipped on the 1st order pyramidal plane, vs two

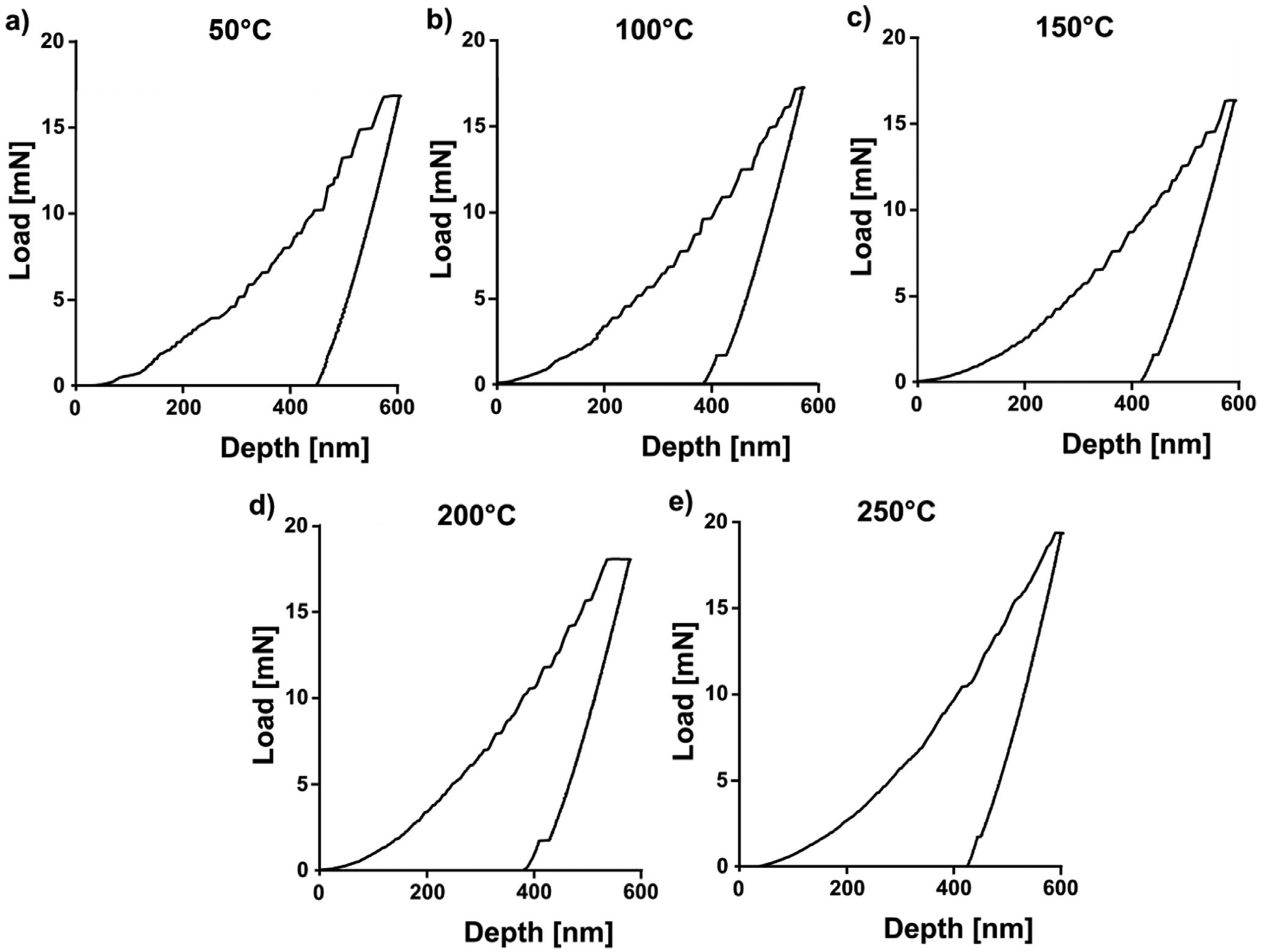

Fig. 4. Load-displacement curves performed under a constant strain rate of approximately 0.04 s^{-1} from the 48°(0001) oriented grain at 50°C (a), 100°C (b), 150°C (c), 200°C (d) and 250°C (e). Tests were performed until a limit of 600 nm was reached. At low temperatures, plastic instabilities are visible, which decrease with increasing temperature and almost vanish at 250°C.

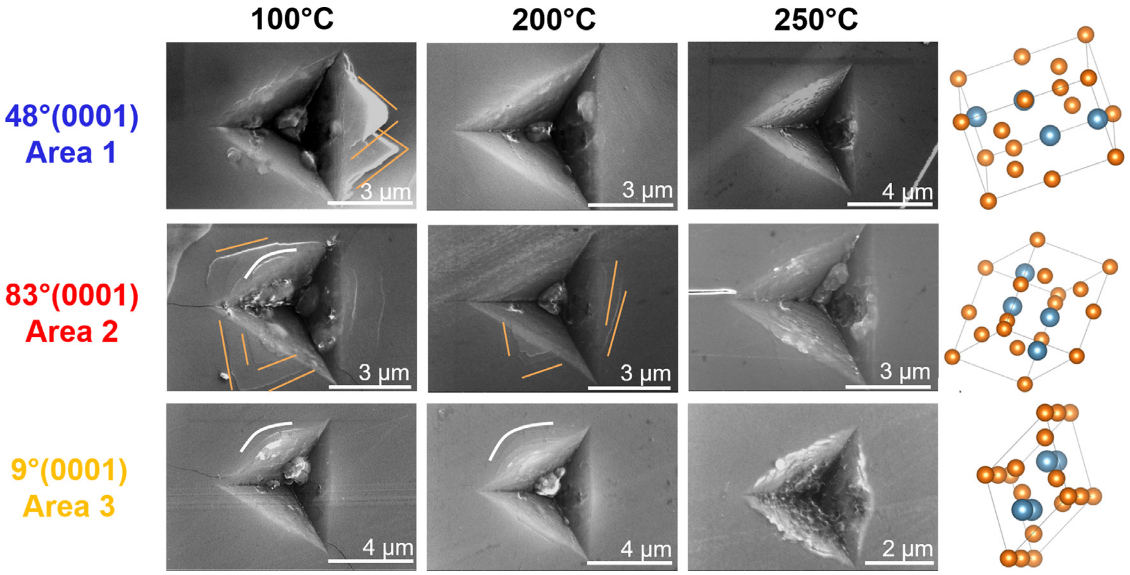

Fig. 5. SE images of indents performed at 100°C, 200°C and 250°C for all three orientations, as depicted on the right. Three different kinds of slip lines were observed: clear, straight lines (orange lines, e.g. 83°(0001) at 100°C and 200°C), no slip lines (e.g. 48°(0001) at 200°C and 250°C) and curved slip lines, presumably following the stress field in narrow steps (white, curved lines, e.g. 9°(0001) at 100°C and 200°C).

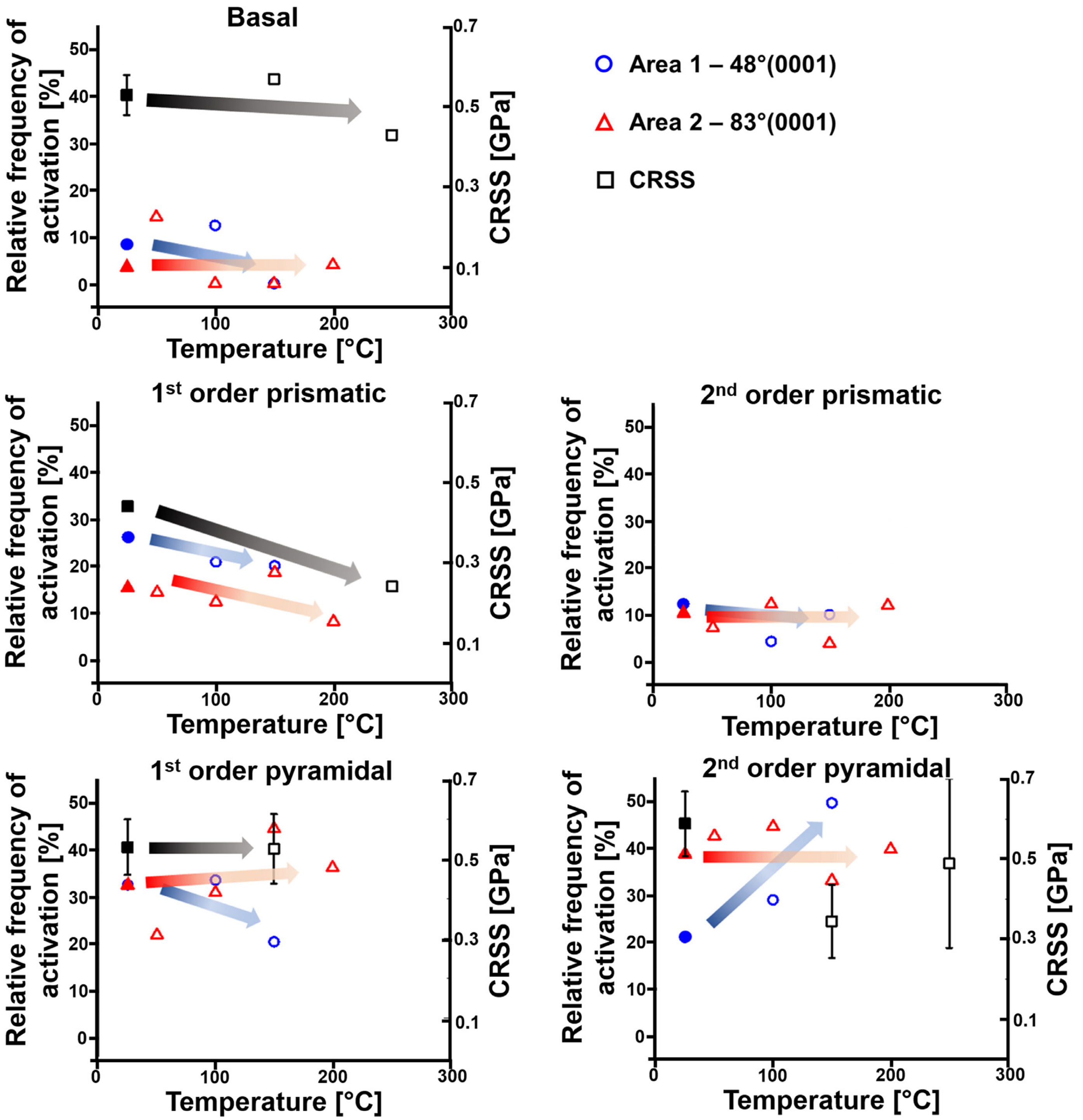

Fig. 6. Relative frequency of activation of different slip planes determined from the slip traces analysis in nanoindentation experiments for the 83°(0001) (red triangles) and 48°(0001) (blue circles) oriented grains at different temperatures. These data points refer to the left axis and the trends are highlighted by the same-coloured arrows. The CRSS values determined by micropillar compression are displayed in black squares and refer to the right axis. The filled symbols are room temperature data taken from reference [59] whereas all open symbols represent data from this work.

pillars on the 2nd order pyramidal plane, whereas at 150°C, three pillars slipped on the 1st order pyramidal plane and one pillar on the 2nd order pyramidal plane.

Consequently, CRSS values spanning the entire range of testing temperatures could only be determined for slip on 2nd order pyramidal and basal planes, shown by the black squares in Fig. 6.

4. Discussion

The hardness as well as the indentation modulus were measured for different temperatures and different orientations, see Fig. 3. Both only varied within the standard deviation over all measured temperatures. The hardness at 500 nm of 3.5 ± 0.3 GPa for temperatures between

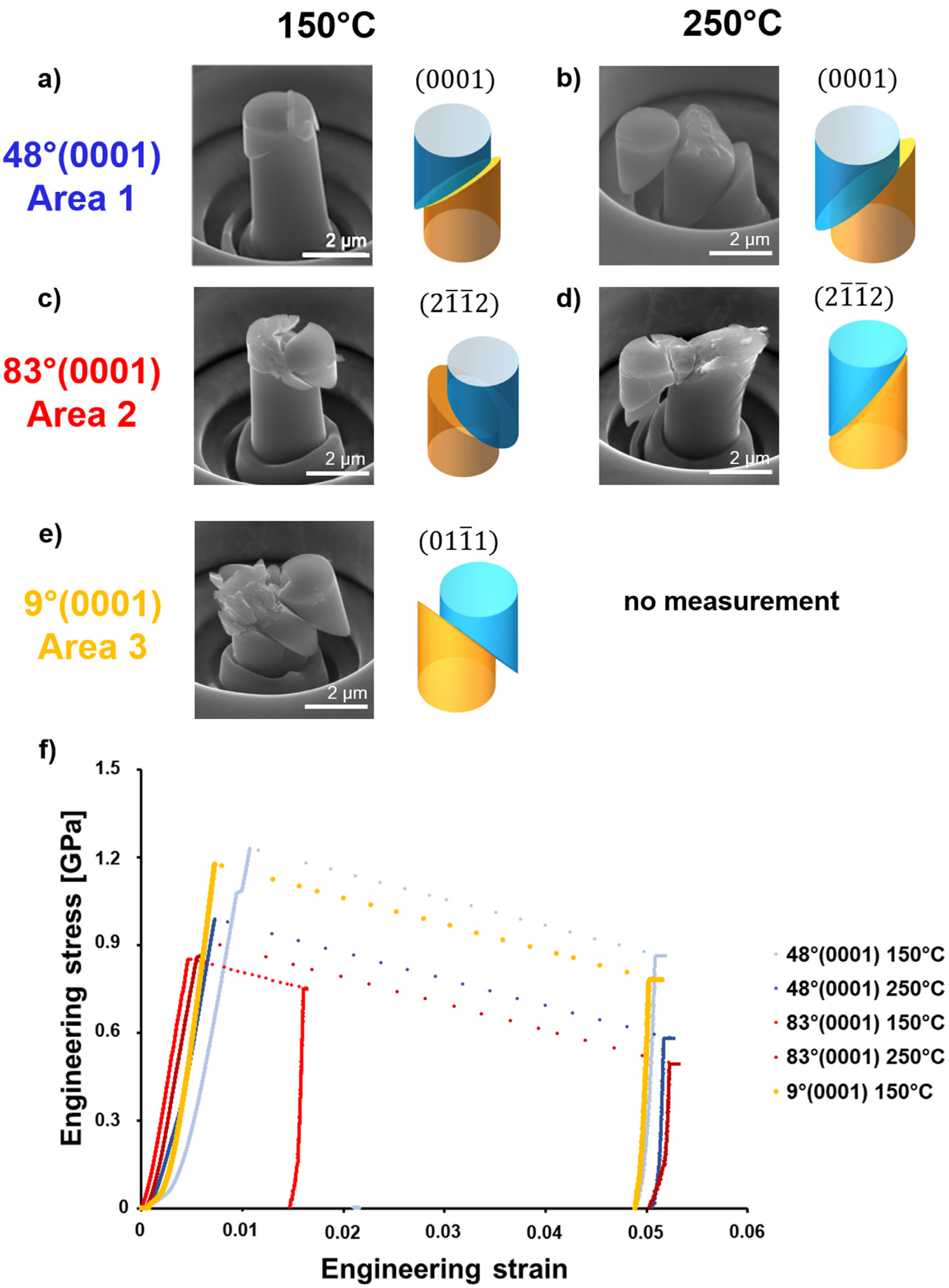

Fig. 7. a-e) SE-images of typical compressed micropillars for all three investigated orientations including the simulated slip planes for the same orientation. f) Representative stress-strain curves for different orientations and temperatures are also given. In almost all cases the loading is perfectly elastic until the critical stress is reached, after which uncontrolled deformation occurs (due to the use of a load-controlled nanoindenter) until the flat punch arrests at the bottom of the trench around the pillar, at approximately 5% strain.

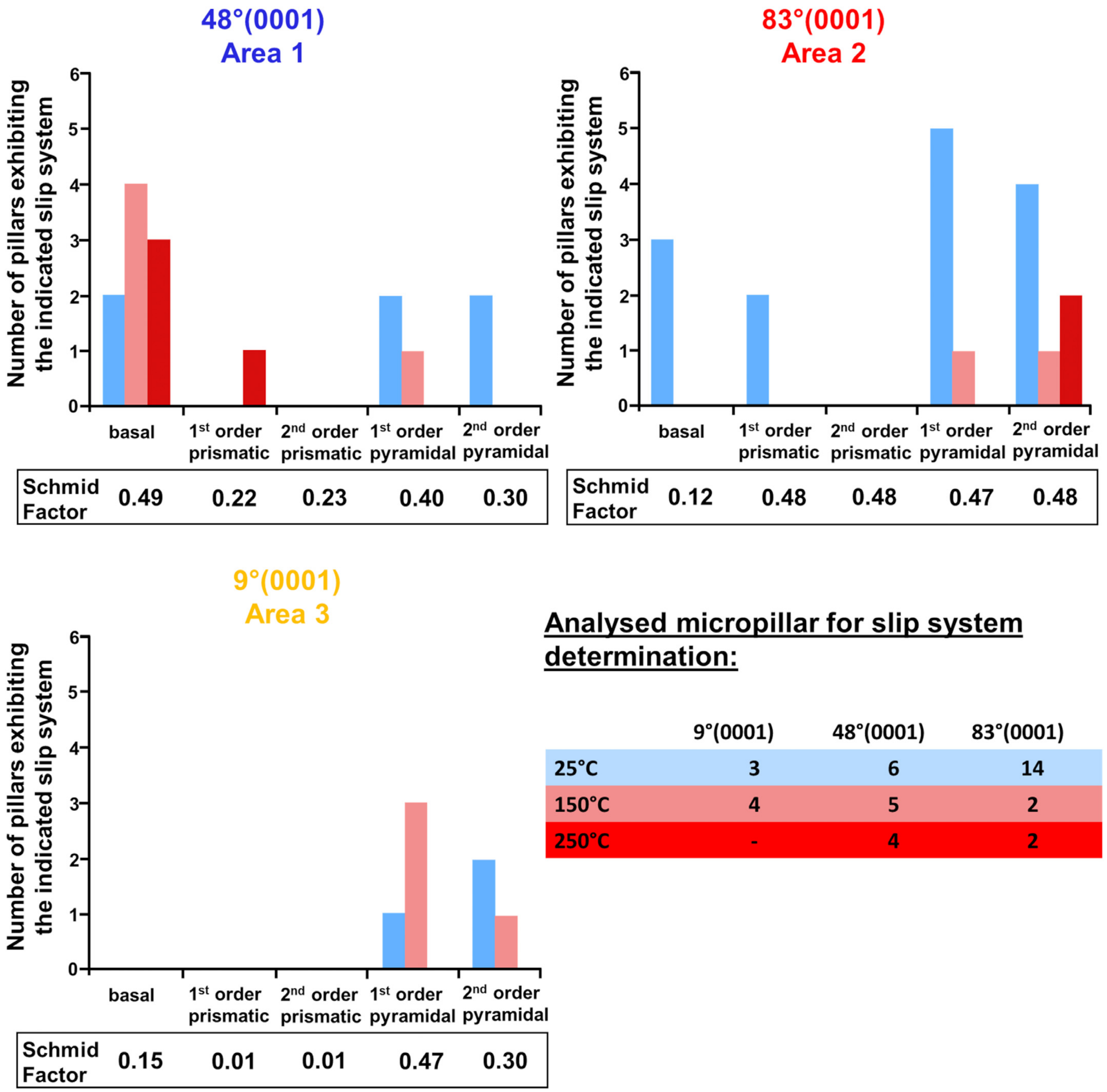

48°(0001) Area 1

Schmid Factor	0.49	0.22	0.23	0.40	0.30

83°(0001) Area 2

Schmid Factor	0.12	0.48	0.48	0.47	0.48

9°(0001) Area 3

Schmid Factor	0.15	0.01	0.01	0.47	0.30

Analysed micropillar for slip system determination:

	9°(0001)	48°(0001)	83°(0001)
25°C	3	6	14
150°C	4	5	2
250°C	-	4	2

Fig. 8. Number of pillars exhibiting the indicated slip system in microcompression for all three orientations at different testing temperatures and their corresponding Schmid factors. The room temperature data have been taken from reference [59] and are represented in blue for each orientation.

50 and 250°C is in agreement with the authors' previously published ambient temperature hardness of 3.4 ± 0.2 GPa measured at the same indentation depth [59]. Furthermore, no strong effect of the crystallographic orientation occurred. Similar investigations on the hardness of the $CaMg_2$ phase over a vast range of temperatures were also performed by Kirsten et al. [22]. They measured the Brinell hardness from ambient temperature up to 800 K and reported a transition temperature above which the hardness decreased significantly. This transition temperature was found to be 0.59^*T_m. Since our results only cover the temperature range of $0.33^*T_m – 0.53^*T_m$, they are below the transition temperature, and therefore our observed constant hardness trend is similar to the reported results by Kirsten et al. [22], who observed a loss in hardness of about 10 percent in a temperature range from $0.25^*T_{m\,–}\ 0.59^*T_m$.

However, the isotropy of our hardness values differs from results reported by Kirsten [65]. He found both anisotropic and lower microhardness values of 2.23 ± 0.06 and 1.87 ± 0.06 for (0001) and $(10\bar{1}1)$ oriented crystals, respectively. These are reasonably comparable orientations to Area 3 - 9°(0001) and Area 1 - 48°(0001). While the lower values are likely attributable to the indentation size effect, the anisotropy is difficult to explain. This might occur due to compositions deviating from stoichiometry, or possible alignment of the microindenter to activate specific slip systems. However, these exact details are unfortunately not available in the cited work. In a recently published work by Luo et al. [37], the orientation dependence of the hardness of the C14 $NbCo_2$ phase was also investigated using nanoindentation. They reported an increased hardness of about 5% for orientations close to (0001) compared to the other investigated orientations. This much smaller variation compared to the results from Kirsten [65] corresponds to ~0.18 GPa, well within the scatter of the results given here. Luo et al. [37] also report that deformation behaviour only changes when the composition approaches a phase boundary (i.e. C14/C15 or C14/C36). Whether this is related to the exact composition – NbCo$_2$ compared to CaMg$_2$ – remains a subject of further investigation.

Similar to the hardness trend observed within our study, the measured indentation modulus neither varied significantly with temperature nor with crystallographic orientation. The average value over all temperatures and orientations was calculated to be 53.3 ± 4 GPa and is in good agreement with DFT calculations by Yu et al. [66] who calculated an elastic modulus of 55.74 GPa at 0K. The invariance of modulus with temperature observed here likely contributes to the agreement between the experimental data and these calculations.

4.1. Serrated yielding

It is further under discussion how an off-stoichiometric composition might affect the deformation behaviour of Laves phases [28,30-33]. So far, it is known that the dislocation velocity as well as the initial dislocation density can be affected by the chemical composition [31,67]. One reasonable explanation for the lowered dislocation velocity with increasing off-stoichiometry proposed by Kubsch is that off-stoichiometry might hinder the free motion of dislocation kinks and thus reduce the mobility of dislocations, which is indeed observed [31]. The dislocation velocity was further found to increase with increasing temperature due to thermally activated mechanisms [31]. Moreover, specimens with off-stoichiometric compositions are reported to have a higher dislocation density prior to deformation. This is assumed to be due to internal stresses induced by anti-site defects, i.e. substitutional solute atoms [67–69].

The CaMg$_2$ Laves phase investigated within this study has a 2 at.-% higher Mg content than the stoichiometric composition and contains aluminium as an impurity element (0.24 wt.-%), which would be expected to also occupy the same sites as the Mg atoms. It is therefore likely that the phase contains a high number of initial dislocations which move at a low velocity at ambient temperature. This, together with the excess Mg is the ideal prerequisite for serrated yielding, where solute atoms might hinder dislocation motion by pinning free dislocation segments.

With increasing temperature, the dislocation velocity as well as the diffusivity of solute atoms is increased, which lowers the pinning effects. In order to visualise the loss in displacement jumps, the number of observed displacement jumps is evaluated as function of temperature for all three investigated orientations (Fig. 9). Our findings indicate that in the investigated CaMg$_2$ phase solute atoms govern the movement of dislocations below the transition temperature at 0.59*T$_M$.

The off-stoichiometric crystallisation of the CaMg$_2$ phase is not surprising. It has already been reported by Stein et al. [58] that in systems where cubic and hexagonal polytypes are present at the same temperature (as in the Mg-Al-Ca system), the C15 phase usually forms at the stoichiometric composition while the C14 (investigated here) and the C36 phase crystallise off-stoichiometrically.

For the sake of completeness, we point out that the determined composition of 68.7 ± 0.5 at.-% Mg is subject to the typical systematic errors in EDX measurement accuracy [70,71]. Therefore, the exact extent as to which the sample is off-stoichiometric is impossible to quantify solely with this technique. Other techniques, such as atom probe tomography, are correspondingly much more involved and beyond the scope of this work. However, we are nevertheless confident that the sample is off-stoichiometric. As standardless EDX quantification, as performed here, can approach an accuracy of ±2% [72], our EDX measurements are above the threshold at which off-stoichiometry is present (i.e. the true composition lies between 68.7 at.% ±2%). This, in combination with previous, more detailed investigations on the off-stoichiometry of Laves phases [28,30-33,67], corroborates the assumption that the material tested in this study deviates from the exact stoichiometric composition and that plasticity in the CaMg$_2$ phase is strongly affected by the excess Mg atoms or trace Al atoms on presumably the same sites, i.e. the presence of solute atoms in the low temperature regime.

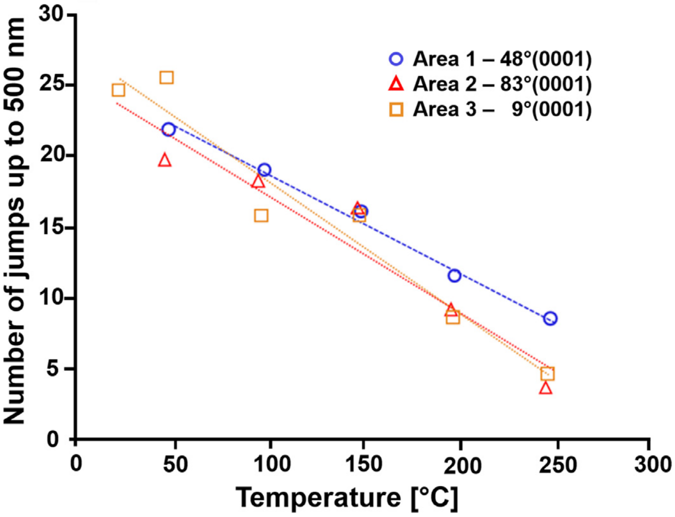

Fig. 9. Extent of serrated flow as a function of temperature for the three orientations. As a measure, the number of displacement jumps that occurred up to a depth of 500 nm is taken. The number of serrations diminishes with increasing temperature.

4.2. Slip line analysis

The slip line analysis showed a decreasing number of identifiable slip lines on the sample surface with increasing temperature for all orientations. Possible explanations of this effect could be surface oxidation, indenter orientation effects, dislocation climb, thermally activated cross-slip or an increase in the homogeneity of slip. We assume that surface oxidation does not play a significant role in the observed loss in slip traces during the elevated temperature deformation as the experiments were conducted under high vacuum (10^{-5} Pa) and surface features (e.g. within the indent) are still clear (Fig. 5).

We also assume that the orientation of the indenter faces with respect to the grain orientation also does not play a strong role in these materials. This relative orientation was not controlled between the data presented here at high temperature and that previously published at room temperature (Fig. 6 open and closed symbols), yet the data form consistent trends. Additionally, in studies of indenter orientation on deformation [73], deformation strongly confined to one face of the residual impression is reported. No such phenomenon has been observed in any of the indents in these materials in SE/BSE imaging. This might be related to deformation here forming discrete slip lines, rather than homogenous pile-up, but it remains to be explored.

Regarding dislocation climb, a similar loss in slip steps was already reported by Mathur et al. [21] around indents in the intermetallic Mg$_{17}$Al$_{12}$ phase. However, in their study, this activation of dislocation climb was accompanied not only by a change in dislocation structures without concentration on individual planes but also by a significant change in the strain rate sensitivity and a pronounced drop in hardness with temperature. These effects were not found for the CaMg$_2$ Laves phase studied here in the temperature range between 50°C and 250°C.

The third possibility of thermally activated cross-slip of screw dislocations causing a loss of slip lines at the sample surface was studied via TEM investigations on an ambient temperature indent and an indentation test performed at 250°C (Fig. 10). These investigations showed that the dislocation structures are similar for samples deformed at 25°C and 250°C. A change of the dominant slip system can be seen, but no sig-

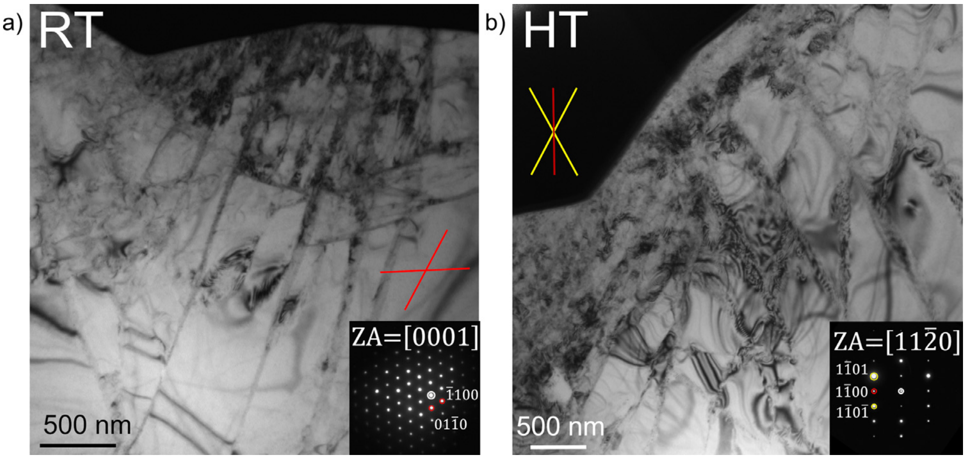

Fig. 10. TEM images of $CaMg_2$ samples deformed at room temperature (a) and 250°C (b). The orientation of $\{1\bar{1}00\}$ and $\{1\bar{1}01\}$ plane traces is indicated by the red and yellow lines respectively, based on the position of the corresponding diffraction spots in the inset selected area diffraction patterns with [0001] and $[11\bar{2}0]$ zone axis (ZA).

nificant change in dislocation structure is visible. Therefore, the results suggest no occurrence of cross-slip up to 250°C.

It seems most likely, therefore, that the activation of further slip systems (Fig. 6) together with a reduction in the amount of serrated yielding (Fig. 9) leads to less localised deformation and consequently less pronounced slip steps. Since the CRSS of slip systems can change with temperature, as discussed in the next section, the activation of further slip systems might lead to more evenly-distributed slip between a larger number of available slip systems, which consequently reduces the visibility of distinct slip traces. Furthermore, a decrease of localised deformation due to a diminishing amount of serrated yielding effect might result in more homogeneous deformation, as also reported by Klose et al. [74].

The relative frequency of activation of slip on different slip planes and their temperature-dependence was measured, though restricted to the 48°(0001) and 83°(0001) grains due to the rapid loss of visible slip lines in the 9°(0001) grain.

For the 48°(0001) orientation, basal slip has the highest Schmid factor of 0.49 and 1st order pyramidal slip also has a high Schmid factor of 0.4. For the 83°(0001) orientation, all prismatic and pyramidal slip systems have high Schmid factors of 0.47 - 0.48. The relative frequency of activation of basal slip was slightly higher for the 48°(0001) orientation than for the 83°(0001) orientation. A higher relative frequency of activation of the slip systems with higher Schmid factor can also be found for the 1st order pyramidal and 2nd order pyramidal slip systems, corresponding to the 83°(0001) orientation. However, for the 1st and 2nd order prismatic planes, this trend was not seen. This might be related to the sufficient accommodation of the induced strain by the activation of the pyramidal slip systems already.

A quantitative comparison of the relative frequency of activated slip planes between all slip systems can however not be easily drawn, as the anisotropy of the hexagonal unit cell and the consequently different numbers of equivalent slip planes need to be taken into account here too (see reference [59] for further details).

Furthermore, CRSS values for basal, 1st order prismatic and 1st and 2nd order pyramidal slip are given. However, due to the small number of compressed micropillars, no general conclusion on the development of the CRSS with temperature can be drawn.

Quantitative measurements of CRSS using micropillar compression are difficult due to the limited amount of data points over the range of orientation and temperature. However, these results suggest that basal and 1st order prismatic slip show a decreasing CRSS with temperature, whereas 1st and 2nd order pyramidal slip do not show significant changes.

Paufler et al. found that the lattice resistance due to the Peierls barrier for basal and prismatic slip is of the same magnitude at a temperature of 390°C [27]. Additionally, they found that most dislocations present after high temperature deformation were on the basal or prismatic planes [27], albeit in single crystals aligned for this purpose. However, the specific alignment as well as the different testing temperatures used compared to our tests, impede a direct comparison.

So far, the occurrence of basal slip was often reported after macroscopic elevated temperature tests on the C14 phase [23,25,27,31,33,41,47]. However, hardness tests on the $MgZn_2$ phase also revealed the basal plane as predominant slip plane at temperatures between room temperature and 500 K [22] and basal slip was found after ambient temperature indentation tests by Takata et al. [39]. Luo et al. [36] observed basal and non-basal slip by compressing $NbCo_2$ micropillars, which is consistent with our findings, where basal slip was found after nanoindentation as well as microcompression at all temperatures if the Schmid factor was high.

Prismatic slip was also mostly reported to occur at elevated temperatures (above 390°C) in macroscopic tests in the C14 phase [27,32,47]. However, a study by Kirsten et al. [22] on the $CaMg_2$ phase, which is also investigated here, reported 1st order prismatic slip after ambient temperature hardness tests. And indeed, slip traces corresponding to the 1st order prismatic planes were also observed for both, the 48°(0001) orientation and the 83°(0001) orientation, within our study. Micropillars in the 83°(0001) orientation, have a high Schmid factor of 0.48 for 1st order prismatic slip, and this system was also observed in ambient temperature micropillar compression.

Interestingly, 1st order prismatic slip could also be activated for the 48°(0001) orientation at 250°C even though the Schmid factor was as low as 0.22. However, if the decreasing CRSS of 1st order prismatic slip with increasing temperature (Fig. 7) is considered, the occurrence of 1st order prismatic slip at 250°C can be explained, suggesting that this slip system is thermally activated.

Slip on the 1st and 2nd order pyramidal plane in the C14 phase is, to the authors' best knowledge, only reported to occur above 500°C [47]. However, the lack of reported pyramidal slip at lower temperatures might also be a result of the limited number of studies on ambient temperature deformation of the C14 Laves-phases.

5. Conclusions

The deformation behaviour of the $CaMg_2$ C14 Laves phase at temperatures between 50°C and 250°C ($0.33{*}T_m$ – $0.53{*}T_m$) was investigated for different grain orientations. In-situ nanoindentation in conjunction with SE, EBSD and TEM imaging allowed an analysis of the deformation behaviour in various aspects:

- The average hardness and indentation modulus over all temperatures were 3.5 ± 0.3 GPa and 53.4 ± 4 GPa, respectively, with negligible anisotropy or temperature sensitivity.

- Up to 200°C, serrated yielding was observed in the indentation curves, which decreased with increasing temperature. This is associated with solute atoms governing the dislocation mobility by pinning slipping dislocation segments.
- The activation of different slip systems from nanoindentation was evaluated in a statistical manner between 50°C and 250°C. The number of identifiable slip traces around indents and the number of serrations decreased with increasing temperature, which is assumed to be due to the activation of additional slip systems at elevated temperatures together with a decreasing effect of solute atoms.
- CRSS values were determined by micropillar compression experiments for basal, 1st order prismatic and pyramidal as well as 2nd order pyramidal slip. While the data should be interpreted with caution due to the limited number of pillars, the results initially suggest that basal and 1st order prismatic slip show a decreasing CRSS with temperature, whereas 1st and 2nd order pyramidal slip do not show significant changes.

Declaration of Competing Interest

None.

Acknowledgement

The authors gratefully acknowledge the financial support of the Deutsche Forschungsgemeinschaft (DFG) within project A05 of the Collaborative Research Center (SFB) 1394 “Structural and Chemical Atomic Complexity - from defect phase diagrams to material properties” – project number 409476157. This project has received funding from the European Research Council (ERC) under the European Union’s Horizon 2020 research and innovation programme (grant agreement No. 852096 FunBlocks).

References

[1] Y. Terada, et al., A thousandfold creep strengthening by Ca addition in die-cast AM50 magnesium alloy, Metall. Mater. Trans. A 35 (9) (2004) 3029–3032.
[2] W. Qudong, et al., Effects of Ca addition on the microstructure and mechanical properties of AZ91magnesium alloy, J. Mater. Sci. 36 (12) (2001) 3035–3040.
[3] T. Sato, M.V. Kral, Microstructural evolution of Mg–Al–Ca–Sr alloy during creep, Mater. Sci. Eng.: A 498 (1–2) (2008) 369–376.
[4] M. Vogel, O. Kraft, E. Arzt, Creep behavior of magnesium die-cast alloy ZA85, Scr. Mater. 48 (8) (2003) 985–990.
[5] N.D. Saddock, et al., Grain-scale creep processes in Mg–Al–Ca base alloys: Implications for alloy design, Scr. Mater. 63 (7) (2010) 692–697.
[6] T. Rzychoń, Characterization of Mg-rich clusters in the C36 phase of the Mg–5Al–3Ca–0.7Sr–0.2Mn alloy, J. Alloys Compd. 598 (0) (2014) 95–105.
[7] A. Luo, B.R. Powell, M. Balogh, Creep and microstructure of magnesium-aluminum–calcium based alloys, Metall. Mater. Trans. A 33 (3) (2002) 567–574.
[8] B. Backes, et al., Particle Hardening in Creep-Resistant Mg-Alloy MRI 230D Probed by Nanoindenting Atomic Force Microscopy, Metall. Mater. Trans. A 40 (2) (2009) 257–261.
[9] D. Amberger, P. Eisenlohr, M. Göken, Microstructural evolution during creep of Ca–containing AZ91, Mater. Sci. Eng.: A (0) (2009) 398–402 510–511.
[10] H. Cao, et al., Experiments coupled with modeling to establish the Mg-rich phase equilibria of Mg–Al–Ca, Acta Mater. 56 (18) (2008) 5245–5254.
[11] A. Suzuki, et al., Precipitation Strengthening of a Mg-Al-Ca–Based AXJ530 Die-cast Alloy, Metall. Mater. Trans. A 39 (3) (2008) 696–702.
[12] H. Eibisch, et al., Effect of solidification microstructure and Ca additions on creep strength of magnesium alloy AZ91 processed by Thixomolding, Int. J. Mater. Res. 99 (1) (2008) 56–66.
[13] M.P. Liu, et al., Mechanical Properties and Creep Behavior of Mg–Al–Ca Alloys, Mater. Sci. Forum 488 (2005) 763–766.
[14] D. Amberger, P. Eisenlohr, M. Göken, On the importance of a connected hard-phase skeleton for the creep resistance of Mg alloys, Acta Mater. 60 (5) (2012) 2277–2289.
[15] M. Zubair, et al., On the role of Laves phases on the mechanical properties of Mg-Al-Ca alloys, Mater. Sci. Eng.: A 756 (2019) 272–283.
[16] S. Amerioun, S.I. Simak, U. Häussermann, Laves-Phase Structural Changes in the System CaAl2-xMgx, Inorg. Chem. 42 (5) (2003) 1467–1474.
[17] E. Deligoz, et al., The first principles investigation of lattice dynamical and thermodynamical properties of Al2Ca and Al2Mg compounds in the cubic Laves structure, Comput. Mater. Sci. 68 (0) (2013) 27–31.
[18] J. Gröbner, et al., Experimental investigation and thermodynamic calculation of ternary Al–Ca–Mg phase equilibria, Z. Metallkd. 94 (9) (2003) 976–982.
[19] S.M. Liang, et al., Thermal analysis and solidification pathways of Mg–Al–Ca system alloys, Mater. Sci. Eng.: A 480 (1–2) (2008) 365–372.
[20] A. Suzuki, et al., Structure and transition of eutectic (Mg,Al)2Ca Laves phase in a die-cast Mg–Al–Ca base alloy, Scr. Mater. 51 (10) (2004) 1005–1010.
[21] H.N. Mathur, V. Maier-Kiener, S. Korte-Kerzel, Deformation in the γ-Mg17Al12 phase at 25–278°C, Acta Mater. 113 (2016) 221–229.
[22] C. Kirsten, P. Paufler, G. Schulze, Zur plastischen Verformung intermetallischer Verbindungen, Monatsber Dt Akad Wiss Berlin 6 (2) (1964) 140–147.
[23] D. Hinz, P. Paufler, G. Schulze, Temperature change experiments during secondary creep of the intermetallic compound MgZn2, Phys. Status Solidi 36 (2) (1969) 609–615.
[24] U. Krämer, G. Schulze, in: Gittergeometrische Betrachtung der plastischen Verformung von Lavesphasen, 3, Kristall und Technik, 1968, pp. 417–430.
[25] P. Paufler, G. Schulze, Plastic deformation of the intermetallic compound MgZn2, Phys. Status Solidi 24 (1) (1967) 77–87.
[26] P. Paufler, J. Marschner, G.E.R. Schulze, The Mobility of Grown-in Dislocations in the Intermetallic Compound MgZn2 I. Stress Dependence for Edge Dislocations in Prism Slip at 390°C, Phys. Status Solidi 40 (2) (1970) 573–579.
[27] P. Paufler, J. Marschner, G.E.R. Schulze, The mobility of grown-in dislocations in the intermetallic compound MgZn2 II. Stress dependence of basal slip at 390°C, Physica Status Solidi 43 (1) (1971) 279–282.
[28] T.H. Mueller, P. Paufler, Yield strength of the monocrystalline intermetallic compound MgZn2, Phys. Status Solidi 40 (2) (1977) 471–477.
[29] P. Paufler, Deformation-mechanism maps of the intermetallic compound MgZn2, Krist. Tech. 13 (5) (1978) 587–590.
[30] P. Paufler, Early work on Laves phases in East Germany, Intermetallics 19 (4) (2011) 599–612.
[31] H. Kubsch, P. Paufler, G. Schulze, The Mobility of Grown-in Dislocations in the Intermetallic Compound MgZn2. III. Dependence of Basal Slip on Chemical Composition within the Homogeneity Range and on Temperature, Phys. Status Solidi 56 (1) (1973) 231–234.
[32] H. Kubsch, P. Paufler, G. Schulze, The mobility of grown-in dislocations in the intermetallic compound MgZn2 during prismatic slip, Phys. Status Solidi 25 (1) (1974) 269–275.
[33] T. Müller, et al., Gleitbanduntersuchungen während und nach Verformung der intermetallischen Verbindung MgZn2, Krist. Tech. 7 (11) (1972) 1249–1264.
[34] J. Livingston, E. Hall, E. Koch, Deformation and Defects in Laves Phases, MRS Online Proc. Lib. Arch. (1988) 133.
[35] N. Takata, et al., Effect of Dislocation Sources on Slip in Fe2Nb Laves Phase with Ni in Solution, MRS Proc. 1516 (2012) 269–274.
[36] W. Luo, et al., Crystal structure and composition dependence of mechanical properties of single-crystalline NbCo2 Laves phase, Acta Mater. 184 (2020) 151–163.
[37] W. Luo, et al., Composition dependence of hardness and elastic modulus of the cubic and hexagonal NbCo2 Laves phase polytypes studied by nanoindentation, J. Mater. Res. 35 (2) (2020) 185–195.
[38] J. Guénolé, et al., Basal slip in Laves phases: the synchroshear dislocation, Scr. Mater. 166 (2019) 134–138.
[39] N. Takata, et al., Nanoindentation study on solid solution softening of Fe-rich Fe2Nb Laves phase by Ni in Fe–Nb–Ni ternary alloys, Intermetallics 70 (2016) 7–16.
[40] L. Machon, G. Sauthoff, Deformation behaviour of Al-containing C14 Laves phase alloys, Intermetallics 4 (6) (1996) 469–481.
[41] S. Voß, Mechanische Eigenschaften von Laves-Phasen in Abhängigkeit von Kristallstruktur und Zusammensetzung am Beispiel der Systeme Fe–Nb–Al und Co–Nb, RWTH Aachen, Aachen, Germany, 2011.
[42] N. Takata, et al., Plastic deformation of the C14 Laves phase (Fe,Ni)2Nb, Scr. Mater. 68 (8) (2013) 615–618.
[43] S.M. Allen, Technical Progress Report: August 1, 1990 - January 31, 1997, MIT, Departement of Materials Science and Engineering, 1998.
[44] Y. Liu, S.M. Allen, J.D. Livingston, Deformation Mechanisms in a Laves Phase, MRS Proc. (1992) 288.
[45] Y. Liu, J.D. Livingston, S.M. Allen, Room-temperature deformation and stress-induced phase transformation of laves phases in Fe-10 At. Pct Zr alloy, Metall. Trans. A 23 (12) (1992) 3303–3308.
[46] Y. Liu, S.M. Allen, J.D. Livingston, Deformation of two C36 laves phases by microhardness indentation at room temperature, Metall. Mater. Trans. A 26 (5) (1995) 1107–1112.
[47] P. Paufler, G. Schulze, Gleitsysteme innermetallischer verbindungen, Krist. Tech. 2 (4) (1967) K11–K14.
[48] P. Paufler, G.E. Schulze, Zur Zwillingsbildung in MgZn2, Krist. Tech. 2 (2) (1967) 231–244.
[49] A. Kazantzis, et al., The mechanical properties and the deformation microstructures of the C15 Laves phase Cr2Nb at high temperatures, Acta Mater. 55 (6) (2007) 1873–1884.
[50] A. Kazantzis, M. Aindow, I. Jones, Deformation behaviour of the C15 Laves phase Cr2Nb, Mater. Sci. Eng.: A 233 (1–2) (1997) 44–49.
[51] A. Kazantzis, M. Aindow, I. Jones, Stacking-fault energy in the C15 Laves phase Cr2Nb, Philos. Mag. Lett. 74 (3) (1996) 129–136.
[52] T. Müller, Inhomogeneities of the plastic deformation of MgZn2 single crystals, Krist. Tech. 10 (8) (1975) 805–811.
[53] W. Luo, et al., Influence of composition and crystal structure on the fracture toughness of NbCo2 Laves phase studied by micro-cantilever bending tests, Mater. Des. 145 (2018) 116–121.
[54] F. Stein, A. Leineweber, Laves phases: a review of their functional and structural applications and an improved fundamental understanding of stability and properties, J. Mater. Sci. 56 (9) (2021) 5321–5427.
[55] A.V. Kazantzis, et al., On the self-pinning character of synchro-Shockley dislocations in a Laves phase during strain rate cyclical compressions, Scr. Mater. 59 (7) (2008) 788–791.

[56] M. Lowry, et al., Achieving the ideal strength in annealed molybdenum nanopillars, Acta Mater. 58 (15) (2010) 5160–5167.

[57] H. Bei, et al., Effects of pre-strain on the compressive stress–strain response of Mo-alloy single-crystal micropillars, Acta Mater. 56 (17) (2008) 4762–4770.

[58] F. Stein, M. Palm, G. Sauthoff, Structure and stability of Laves phases part II—structure type variations in binary and ternary systems, Intermetallics 13 (10) (2005) 1056–1074.

[59] C. Zehnder, et al., Plastic deformation of single crystalline C14 Mg2Ca Laves phase at room temperature, Mater. Sci. Eng.: A 759 (2019) 754–761.

[60] W.C. Oliver, G.M. Pharr, Measurement of hardness and elastic modulus by instrumented indentation: Advances in understanding and refinements to methodology, J. Mater. Res. 19 (1) (2004) 3–20.

[61] S. Schröders, et al., Room temperature deformation in the Fe7Mo6 μ-Phase, Int. J. Plast. 108 (2018) 125–143.

[62] J.S.-L. Gibson, et al., Finding and characterising active slip systems: a short review and tutorial with automation tools, Materials 14 (2) (2021) 407.

[63] P. Mao, et al., First-principles calculations of structural, elastic and electronic properties of AB2 type intermetallics in Mg–Zn–Ca–Cu alloy, J. Magnesium Alloys 1 (3) (2013) 256–262.

[64] M. De Jong, et al., Charting the complete elastic properties of inorganic crystalline compounds, Sci. Data 2 (1) (2015) 1–13.

[65] Kirsten, C., Über Festigkeitseigenschaften intermetallischer Verbindungen- Doctoral thesis in Technical University Dresden. 1963.

[66] W.-Y. Yu, et al., First-principles investigation of the binary AB2 type Laves phase in Mg–Al–Ca alloy: electronic structure and elastic properties, Solid State Sci. 11 (8) (2009) 1400–1407.

[67] K. Eichler, et al., Änderung von Verformungseigenschaften der intermetallischen Verbindung MgZn2 im Homogenitätsbereich, Krist. Tech. 11 (11) (1976) 1185–1188.

[68] J. Zhu, et al., Point defects in binary Laves phase alloys, Acta Mater. 47 (7) (1999) 2003–2018.

[69] J. Zhu, et al., Enthalpies of formation of binary Laves phases, Intermetallics 10 (6) (2002) 579–595.

[70] K.E. MacArthur, et al., Probing the effect of electron channelling on atomic resolution energy dispersive X-ray quantification, Ultramicroscopy 182 (2017) 264–275.

[71] K.E. MacArthur, et al., Quantitative energy-dispersive X-ray analysis of catalyst nanoparticles using a partial cross section approach, Microsc. Microanal. 22 (1) (2016) 71.

[72] P. Pinard, et al., Development and validation of standardless and standards-based X-ray microanalysis, in: IOP Conference Series: Materials Science and Engineering, IOP Publishing, 2020.

[73] S. Jakob, et al., Influence of crystal orientation and Berkovich tip rotation on the mechanical characterization of grain boundaries in molybdenum, Mater. Des. 182 (2019) 107998.

[74] F. Klose, et al., Analysis of portevin-le chatelier serrations of type bin Al–Mg, Mater. Sci. Eng.: A 369 (1–2) (2004) 76–81.

7. Publication 3

Influence of chemical composition on the room temperature plasticity of C15 Ca-Al-Mg Laves phases

Martina Freund [a], Zhuocheng Xie [a], Pei-Ling Sun [a], Lukas Berners [a], Joshua Spille [b], Hexin Wang [a], Carsten Thomas [c], Michael Feuerbacher [c], Marta Lipinska-Chwalek [b] [c], Joachim Mayer [b] [c], Sandra Korte-Kerzel [a]

[a] Institute for Physical Metallurgy and Materials Physics, RWTH Aachen University, Aachen, Germany

[b] Central Facility for Electron Microscopy, RWTH Aachen University

[c] Ernst Ruska-Centre for Microscopy and Spectroscopy with Electrons, Forschungszentrum Jülich GmbH

Acta Materialia, Volume 276, 2024, 120124, **reproduced with permission of Elsevier.**

https://doi.org/10.1016/j.actamat.2024.120124

Short Summary

The influence of the deviation of the stoichiometric composition is still under debate, and contrary findings are reported in previous studies. To analyse the effects of a off-stoichiometric composition, two samples with $CaAl_2$ Laves phase structures, which revealing Mg as ternary alloying element, were nanomechanical investigated. The hardness and modulus decrease with the decreases with further deviation from the stoichiometric composition, which were also confirmed by atomistic simulations. The visibility of slip lines, resulting from nanoindentation tests, also decrease with the higher off-stoichiometric composition. Additional slip systems were found, being mainly included in the plasticity of the *C*15 $CaAl_2$ phases.

Martina Freund: Writing – review & editing, Writing – original draft, Visualization, Investigation, Formal analysis, Conceptualization. Zhuocheng Xie: Writing – review & editing, Investigation. Pei-Ling Sun: Visualization. Lukas Berners: Methodology. Joshua Spille: Visualization. Hexin Wang: Investigation. Carsten Thomas: Resources. Michael Feuerbacher: Resources. Marta Lipinska-Chwalek: Supervision. Joachim Mayer: Supervision. Sandra Korte-Kerzel: Writing – review & editing, Conceptualization, Supervision.

Acta Materialia 276 (2024) 120124

Contents lists available at ScienceDirect

Acta Materialia

journal homepage: www.elsevier.com/locate/actamat

Full length article

Influence of chemical composition on the room temperature plasticity of *C*15 Ca-Al-Mg Laves phases

Martina Freund [a,*], Zhuocheng Xie [a,*], Pei-Ling Sun [a], Lukas Berners [a], Joshua Spille [b], Hexin Wang [a], Carsten Thomas [c], Michael Feuerbacher [c], Marta Lipinska-Chwalek [b,c], Joachim Mayer [b,c], Sandra Korte-Kerzel [a]

[a] *Institute of Physical Metallurgy and Materials Physics, RWTH Aachen University, Germany*
[b] *Central Facility for Electron Microscopy, RWTH Aachen University, Germany*
[c] *Ernst Ruska-Centre for Microscopy and Spectroscopy with Electrons, Forschungszentrum Jülich GmbH, Germany*

ARTICLE INFO

Keywords:
Laves phase plasticity
Off-stoichiometry
Electron microscopy
Nanoindentation
Atomistic simulation

ABSTRACT

The influence of chemical composition changes on the room temperature mechanical properties in the binary $Ca_{33}Al_{67}$ *C*15 $CaAl_2$ Laves phase were investigated in two ternary alloys with off-stoichiometric compositions with 5.7 at.% Mg substitution ($Ca_{33}Al_{61}Mg_6$) and 10.8 at.% Mg and 3.0 at.% Ca substitution ($Ca_{36}Al_{53}Mg_{11}$) and compared to the stoichiometric ($Ca_{33}Al_{67}$) composition. Cubic Ca-Al-Mg Laves phases with multiple crystallographic orientations were characterised and deformed using nanoindentation. The hardness and indentation modulus were measured to be 4.1 ± 0.3 GPa and 71.3 ± 1.5 GPa for $Ca_{36}Al_{53}Mg_{11}$, 4.6 ± 0.2 GPa and 80.4 ± 3.8 GPa for $Ca_{33}Al_{61}Mg_6$ and 4.9 ± 0.3 GPa and 85.5 ± 4.0 GPa for $Ca_{33}Al_{67}$, taken from our previous study, respectively. The resulting surface traces as well as slip and crack planes, were distinguished on the indentation surfaces, revealing the activation of several different {11n} slip systems, as further confirmed by conventional transmission electron microscopic observations. Additionally, the deformation mechanisms and corresponding energy barriers of activated slip systems were evaluated by atomistic simulations.

1. Introduction

Laves phases are some of the most common intermetallic structures and are attractive for strengthening of structural materials. They consist of two elements with different atomic radii, with an ideal radius ratio in AB_2 binary Laves phases of $r_A/r_B = 1.225$ [1–6].

The topologically closed packed (TCP) structure of the Laves phases poses a challenge to the introduction of macroscopic plasticity due to its inherent resistance to dislocation motion. As a result, there is limited knowledge on the plastic behaviour and little documentation of dislocation motion below the brittle to ductile transition temperature (BDTT), typically encountered at around $0.6 \cdot T_H$ (T_H = homologous temperature) for Laves phases [7–11].

For the cubic *C*15 Laves phases, a review of the commonly reported slip systems and the corresponding BDTT temperatures was included in a previous publication [12]. Dislocation slip is predominantly reported on {111} planes at and above the BDTT [10,11,13–21]. Several studies using micropillar compression to introduce plasticity at room temperature also revealed slip on {111} planes [22–26]. However, investigations on $CaAl_2$ Laves phases have shown significant contributions from {112} slip planes to plasticity [12].

Theoretical studies using atomistic simulations have shed further light on the plasticity mechanisms in Laves phases [27–29]. Dislocation motion by synchro-shear [5,30,31] was demonstrated as the most energetically favourable slip mechanism on the basal plane in the hexagonal *C*14 $CaMg_2$ Laves phase [27], while kink-pair nucleation and propagation are preferred in both *C*14 $CaMg_2$ and *C*15 $CaAl_2$ Laves phases [29] and thermal assistance was found to be indispensable in activating the motion of synchro-Shockley dislocations, implying that this type of plastic event is impeded at low temperatures [28]. Point defects, such as vacancies, introduced with deviations from the stoichiometric AB_2 composition [32], significantly affect dislocation motion energy barriers [2].

To better understand the plasticity of Laves phases with off-stoichiometric compositions, we investigate the deformation of the *C*15 $CaAl_2$ Laves phase with different Mg contents (presumably

---

* Corresponding authors.

E-mail addresses: freund@imm.rwth-aachen.de (M. Freund), xie@imm.rwth-aachen.de (Z. Xie).

https://doi.org/10.1016/j.actamat.2024.120124
Received 19 March 2024; Received in revised form 11 June 2024; Accepted 20 June 2024

replacing Al in the lattice) and a change in Ca concentration. This study aims to elucidate the impact of compositional changes on plasticity in Laves phases, building on previous research on compositional stability and the effects of chemical composition on plasticity.

1.1. Influence of chemical composition on Laves phase stability and plasticity

The knowledge of the influence of chemical composition on the mechanical behaviour and phase stability of Laves phases, particularly those with well-defined homogeneity ranges, can be helpful for specific property manipulation. Amerioun et al. [33] investigated the structural changes in Laves phases when substituting Al atoms with Mg. They found transformations from the C15 Laves phase (homogeneity range from $CaAl_2$ to $CaAl_{1.76}Mg_{0.24}$) to the C36 phase (homogeneity range from $CaAl_{1.34}Mg_{0.66}$ to $CaAl_{0.93}Mg_{1.07}$), and further to the hexagonal C14 Laves phase (homogeneity range from $CaAl_{0.49}Mg_{1.51}$ to $CaMg_2$).

The mechanical behaviour of Laves phases is significantly influenced by composition, with deviations from stoichiometry leading to the insertion of various types of defects into the lattice, such as anti-site atoms and vacancies [3,34–37]. Altering the composition away from the ideal binary stoichiometry, either by varying the internal chemical composition or adding alloying elements, results in different defect structures [3,4,34,36–42]. This can lead to a distortion of the ideal lattice and changes in lattice parameters, subsequently affecting mechanical properties [32]. The introduction of a ternary element also plays a crucial role, with the atomic radius and quantity of the element determining how it is incorporated into the lattice [2,3,32]. Moreover, the radius ratio in cubic Laves phases significantly affects dislocation motion on {111} planes, influencing the atomic free volume and dislocation mobility [15,39]. The presence of anti-site atoms or vacancies can impede or facilitate dislocation motion, highlighting the intricate relationship between composition, defect structures, and mechanical behaviour in Laves phases [15,39].

1.1.1. Binary Laves phases

In terms of the changes in mechanical properties resulting from a changing Laves phase composition, we focus first on the effect of altering the ratio of A and B atoms in the binary AB_2 Laves phases, before considering the inclusion of a third element:

Shields et al. [43] explored the microhardness of quenched binary rare-earth cubic $CeNi_2$ Laves phases and found that strain fields induced by vacancies in the lattice could result in softening at high temperatures and hardening after quenching at low temperatures. They also observed that in a comparison of Ni and Co as the B element, vacancy formation is much more preferable for Ni, as reported by Mansey et al. [44], which they related to the variable valency of the Ce A atoms. On this basis, further investigations estimated that Laves phases combining transition elements with rare-earth elements may exhibit unique properties due to their extreme radius ratios [44–47]. The RNi_2 (R: rare earth) Laves phases have received particular attention also beyond $CeNi_2$. In these phases, the atomic radius ratios r_A/r_B significantly exceed the ideal ratio of 1.225, structural vacancies at the A site are prevalent, and their density increases with the atomic radius of R [48]. Particularly in $LaNi_2$ Laves phases with the highest r_A/r_B, the formation of a superstructure with ordered vacancies (La_7Ni_{16}) is energetically more favourable compared to the stoichiometric C15 phases. In how far structural vacancies differ in their effect on mechanical properties compared to disordered vacancies has not yet been explored to the best of our knowledge, but due to their integration into the crystal structure, they can be stabilised to reach higher densities of over 10 % on the A-site lattice [48].

Similar investigations by Chen et al. [36,37] on cubic $HfCo_2$ Laves phases demonstrated a decrease in lattice parameter and mechanical properties with increasing Co content, attributed to Co atom substitutions and vacancies. Elastic moduli and Poisson's ratio as well as hardness, measured at room temperature (RT) were found to drop with deviation from the stoichiometric composition. The authors proposed that the observed softening was due to easier synchro Shockley dislocation motion on {111} planes facilitated by increased free volume from decreasing packing density and Co substitutions.

Moreover, deviations from stoichiometry in hexagonal $MgZn_2$ Laves phases [1,49–51] have been associated with decreased hardness, yield stress, and dislocation velocity. In a summary of this work, Paufler [1] proposes an intricate interplay of grown-in point and line defects. While an increased density of the first leads to dislocation pinning, associated with the observed time- and temperature dependent formation of a strong upper yield point in the undeformed crystal towards lower temperatures, the off-stoichiometric samples were also thought to contain a higher number of (mobile) dislocations, which the authors proposed to counterbalance the hardening effect they otherwise expected from point defect/dislocation interactions. Kubsch et al. [51] have observed that the off-stoichiometric composition results in a decreasing dislocation velocity and increasing need for dislocation activation enthalpy, between 340- 456°C. Shao et al. [52] performed density functional theory calculations to explore the influence of chemical composition on point defects in $MgZn_2$, indicating that anti-site defects have low formation energies.

Zhu et al. [3] observed hardening in both over- and under-stoichiometric compositions at room temperature (RT) in cubic $NbCr_2$, $NbCo_2$, and hexagonal $NbFe_2$ alloys, attributing it to anti-site defects in the absence of constitutional vacancies. Luo et al. [23] found increased hardness towards the stoichiometric composition in the cubic C15 $NbCo_2$ Laves phase. Interestingly, micropillar compression tests by the same authors across the same compositional range of the C15 $NbCo_2$ phase revealed a constant critical resolved shear stress for slip on {111} planes [24].

Phase transformations between different Laves polytypes are also closely related to mechanical deformation, with stacking fault formation occurring due to the movement of synchro-Shockley dislocations on adjacent slip planes [5,30,31]. This is enabled by the construction of three different Laves structures, which are stacking variants normal to their characteristic triple layer lying parallel to the {111} or (0001) planes in the cubic and hexagonal phases, respectively [53,54]. Importantly, Laves phases exhibit such phase transformations between polytypes through the accumulation of stacking faults (SFs). These may occur as a result of chemical and atomic order at the stacking fault leading to the formation of a segregation stabilised planar defect phase [55] and as a consequence of the different polytypes being structurally distinguished by their stacking of the characteristic Laves phase layers. As changes in chemical composition affect the stability of the polytypes, they may also change the unstable and stable stacking fault energies on the planes between the characteristic layers in each phase [15,42,56].

RT compression tests of the $ZrFe_2$ Laves phase have shown phase transformations from C36 to C15 under compressive strain, driven by the motion of synchro-Shockley dislocations on {111} planes [57]. Manipulating Laves phase composition therefore not only alters plasticity based on point defects and lowers the energy barrier for dislocation motion but also simplifies phase transformations via SFs [5,30,31].

So far, the effect of different point defects on dislocation mobility in binary Laves phases remains unclear based on experimental literature. As well as phase transformations necessitates a combination of many experiments. Modelling efforts have started to contribute to this field, for example by predicting the formation energies of the different defect types from density functional theory [52] and studying their interaction with dislocations in atomistic simulations [29].

1.1.2. Ternary Laves phases

The influence of a third element, on the mechanical properties of Laves phases has been extensively studied, primarily focusing on phases formed by transition metals [34,38,39,58,59]. These investigations have revealed intricate relationships between composition and mechanical behaviour.

In the Fe-Nb-Ni ternary system, Fe-rich $NbFe_2$ Laves phases experienced solid solution softening with increasing Ni content, leading to reduced hardness and elastic modulus [59]. Similar observations were made in the Nb-Cr-Ti system, where SFs and dipoles were observed, affecting mechanical behaviour [40].

Chen et al. [35] explored the effects of ternary alloying elements (Nb, V, Mo) on the cubic $TiCr_2$ Laves phase. They found that while all three elements increased hardness, V and Mo led to increased fracture toughness, whereas Nb decreased it. Additionally, V and Mo substitutions on specific sites affected lattice strain and free volume, influencing dislocation motion. Similar investigations by Takasugi et al. [39] on the cubic $NbCr_2$ Laves phase showed that V and Mo substitutions resulted in either hardening or softening, depending on the specific sites they occupied. The addition of W and Mo induced phase transformations and SFs, affect mechanical properties differently. Yoshida et al. [38] expanded this work to also include 5% W replacing either Nb or Cr in the alloys' composition. They found significant hardening when substituting Cr but only weak hardening when W was added instead of Nb. However, this study lacked measurements of lattice parameters to validate the hypothetical replacements based on alloy composition. The authors observed SFs and initial phase transformations to hexagonal polytypes upon the addition of W and Mo, which was not observed with V addition. Consequently, there was no apparent correlation between the presence of SFs on {111} planes (seen in Mo and W-containing alloys) and overall softening (observed only in $(Nb,Mo)Cr_2$). Further research by Thoma et al. [41] investigated the effects of V addition to the cubic $NbCr_2$ Laves phase, showing changes in moduli and transition temperatures.

Overall, these investigations highlight the complexity of ternary alloying effects on Laves phases, with mechanisms such as synchro-shear emerging as crucial for understanding mechanical behaviour. However, gaps in understanding persist, particularly regarding low-temperature plasticity mechanisms and their dependence on composition.

Studies also considered equal substitution of A- and B-sites, such as Nb addition to HfV_2, [42,60,61], resulting in improved deformability attributed to the creation of free volume on {111} planes. In addition, while the hypothesis of creating free volume in the triple layer through ternary alloying has been explored in several studies where a growing support for the role of synchro-shear in relating site-specific element substitution to mechanical properties, conclusive evidence is still lacking. Furthermore, dislocation mechanisms other than slip on a given plane, e.g. dislocation cross-slip, are often overlooked in experimental studies, which primarily focus on determining the type of present point defects or identifying deformation mechanisms based on macroscopic observations of slip and its thermal activation alone.

1.2. Correlative nanomechanical testing and atomistic simulations

From this review of the existing literature, we identify two current gaps in knowledge concerning Laves phase plasticity, which we aim to address in this work: a general lack of understanding of low temperature plasticity mechanisms and how these are affected by changes in composition. To address these gaps, a closer integration of experimental and computational approaches is essential. By combining these methods, we can better understand the underlying dislocation mechanisms and identify potential defects. This integrated approach is particularly crucial given the increasing complexity of investigations involving varying compositions and exploring fundamental mechanisms at perfect stoichiometry.

Advancements in nanomechanical testing now offer the capability to introduce plasticity without being constrained by the BDTT, as fracture can be successfully suppressed [25]. By utilizing a combination of scanning electron microscopy (SEM) and transmission electron microscopy (TEM) to examine the slip planes and Burgers vectors of dislocations, it becomes possible to analyse the resulting defect structures and relate these to critical stresses for dislocation-mediated plasticity at room temperature. The impact of adding ternary alloying elements and deviations from stoichiometric compositions in Laves phases remains a debated topic. This study therefore aims to evaluate the influence of chemical composition by comparing it with the authors' previous investigation on the room temperature plasticity of the stoichiometric $C15$ $CaAl_2$ Laves phase [12]. In that study, deformation primarily occurred due to dislocation motion on {111} and {112} slip planes, which may be expected to change with the addition of Mg and/or Ca atoms. Atomistic simulations serve to rationalise experimental observations on composition-dependent mechanical properties and activation of slip systems, particularly focusing on the associated energy barriers. The present analysis aims to delve deeper into this change, seeking to bridge the gap in knowledge by understanding the influence of ternary alloying elements on deformation mechanisms in cubic Laves phases.

2. Experimental methods

2.1. Sample preparation

In this work, two off-stoichiometric compositions of the ternary $C15$ $CaAl_2$ Laves phase were studied. Both substitute Al, first with 6 at.% Mg, $Ca_{33}Al_{61}Mg_6$, and for the second with 11 at.% Mg and 3.0 at.% Ca, $Ca_{36}Al_{53}Mg_{11}$.

For sample synthesis, two methods were used and in both cases, starting elements were added to yield an approximate $C36$ composition with near equal amounts Ca, Al, and Mg. However, as the $C36$ was not observed to form, we use here two parts of the resulting castings which contained the stated phase compositions with a high volume fraction and grain sizes large enough for nanomechanical analysis.

A first ingot was prepared by flux-growth. A melt of composition $Ca_{32.7}Al_{31.9}Mg_{35.4}$ was sealed in a tantalum crucible under 500 mbar argon atmosphere, which was in turn sealed in a protecting quartz tube. This ensemble was placed in a buffered box furnace and heated to a temperature of 870 °C where it was kept for 2 h for homogenization. Cooling was carried out by lowering the temperature to 850 °C at a rate of 10 °C/h and subsequently to 750 °C at a rate of 1 °C/h. Then the ensemble was rapidly removed from the furnace, and the remaining melt and the solidified part were separated by centrifugation. Finally, it was slowly cooled down to room temperature within about 2 to 3 h.

A cross cut of the resulting ingot was prepared for phase analysis in the scanning electron microscope (SEM) (Fig. 1). It contained several phases. The main phase in the area investigated in this work was determined using energy dispersive X-ray spectroscopy (EDX) (FIB, Helios Nanolab 600i, FEI) measurements. A large volume fraction of $Ca_{33}Al_{61}Mg_6$ regions were found, and the composition was determined as 61.4 ± 0.2 at.% Al, 32.9 ± 0.2 at.% Ca and 5.7 ± 0.1 at.% Mg.

A second ingot was prepared by Bridgman growth. A tantalum ampoule was charged with raw elements of composition $Ca_{32.7}Al_{31.9}Mg_{35.4}$ and sealed under a 600 mbar argon atmosphere. The ampoule was placed in a vertical Bridgman furnace on a water-cooled cold finger and heated to 900 °C, where it was kept 1 h for homogenization. Then the growth process was run by withdrawing the melt out of the hot zone of the furnace at a rate of 5 mm/h, which was proceeded for 40 h, i.e. 200 mm.

A cross cut of the resulting ingot again displayed the presence of several phases. Regions of $Ca_{36}Al_{53}Mg_{11}$ were found with a composition according to EDX measurements of 52.9 ± 0.7 at.% Al, 36.3 ± 0.1 at.% Ca and 10.8 ± 0.8 at.% Mg.

For metallographic preparation, the samples were embedded in copper paste to provide a stable sample environment and to hinder fracture or porosity. Afterward the sample was ground using 1200 to 4000 grit SiC paper. An additional grinding step followed with POLARIS M diamond grinding plates of 3 μm and 1 μm and polishing in 4 steps with 6, 3, 1, and 0.25 μm diamond paste with isopropanol with 5 % PEG as lubricant. Final polishing with an aluminium oxide polishing solution

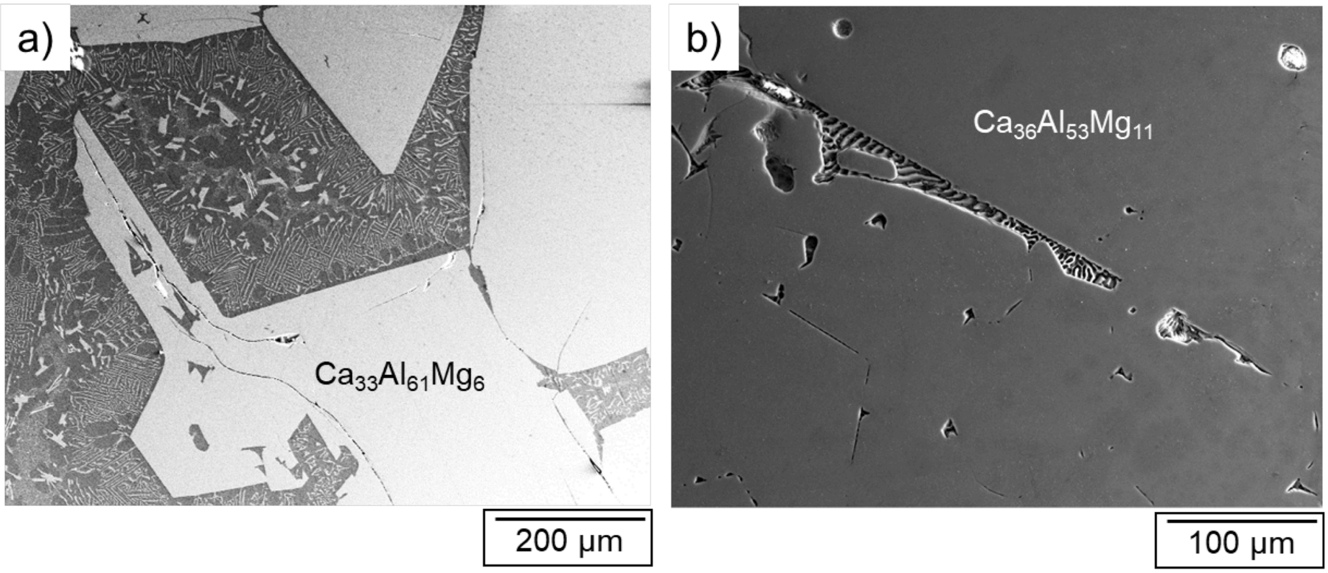

Fig. 1. Secondary electron micrographs of the samples containing a) $Ca_{33}Al_{61}Mg_6$. and b) $Ca_{36}Al_{53}Mg_{11}$. Both samples contain large grains of *C*15 phase and eutectic Mg/intermetallic.

(OPA; a mixture of 5 % silica dissolved in isopropanol and added polyethylene glycol (PEG)) and a cleaning step with water and dishwashing liquid followed.

The use of electron backscatter diffraction (EBSD) (Hikari, EDAX Inc.) at an accelerating voltage of 20 kV and a current of 5.5 nA allowed us to identify the grain orientation of the cubic $CaAl_2$ phase for both samples and also identify, $Ca_{33}Al_{61}Mg_6$, the pure Mg matrix lying around the individual $CaAl_2$ + Mg areas (Fig. 1). This data was further analysed using OIM analysis™ (EDAX Inc.) to obtain the Schmid factors of the grains used for an approximation of first activated slip systems, assuming uniaxial compression along the surface normal.

For imaging of the plastic zone around the indents, secondary electron (SE) images were acquired by SEM in high-resolution mode (CLARA, Tescan, Brno, Czech Republic) with an accelerating voltage of 2 kV at a current of 100 pA.

2.2. Nanoindentation experiments

Continuous stiffness measurement (CSM) nanoindentation tests (iNano, Nanomechanics Inc., TN, USA) were performed using a diamond Berkovich tip (Synton-MDP AG, CH). Prior to testing, the diamond area function (DAF) and frame stiffness of the indenter tip were calibrated according to the Oliver and Pharr method [62,63]. The determination of hardness and indentation modulus for all investigated areas was performed at indentation depths between 350 and 500 nm and assuming a constant Poisson's ratio of 0.3. For $Ca_{33}Al_{61}Mg_6$, eight grains with different orientations were indented with two arrays of 5 × 5 indents. The two arrays were placed with a relative rotation of 30° about the surface normal, to investigate the influence of the tip geometry on the slip and crack behaviour. All nanoindentation tests were conducted with a constant strain rate of 0.2 1/s up to a maximum depth of 500 nm. Slip traces observed in the direct vicinity of the indents were analysed by correlating the information from EBSD data and corresponding SE-images.

2.3. TEM experiments

In total three TEM lamellae were milled out in two different orientations by site specific focussed ion beam (FIB) milling in both off-stoichiometric materials, two for $Ca_{33}Al_{61}Mg_6$ and one for $Ca_{36}Al_{53}Mg_{11}$. All were then analysed by TEM (JEOL JEM-F200 and FEI Tecnai F20 TEM) with a double tilt holder. Under two-beam conditions, a $\vec{g}\cdot\vec{b}$ analysis, with $\vec{g}$ is the diffraction vector and $\vec{b}$ is the Burgers vector of the dislocations, was applied to determine the Burgers vectors of the dislocations. In addition, selected area electron diffraction (SAED) was applied to confirm the presence of the cubic *C*15 Laves phase structure underneath the indent and acquire orientation information for slip plane identification, (cf. Figs. 5 and 6).

2.4. Atomistic simulations

The atomistic simulations in this work were performed using the software package LAMMPS [64]. The interatomic interactions were modelled by a machine-learning moment tensor potential (MTP) [65,66] for Al-Ca-Mg [67]. This potential provides more accurate prediction for the lattice parameter, elastic constants and stacking fault energy of the *C*15 $CaAl_2$ Laves phase than a modified embedded atom method (MEAM) potential for Al-Ca-Mg [68] when compared with experimental data and ab-initio calculations (see Table S1 in the supplementary material). *C*15 $CaAl_2$ atomistic samples were constructed using Atomsk [69], and off-stoichiometric compositions were generated by randomly substituting atoms using five different random configurations for each composition. To model a chemical composition close to that of $Ca_{33}Al_{61}Mg_6$ in the experiments, the Ca content remains at 33 at.% and Mg solutes (3, 6 and 9 at.%) substitute the Al sublattice. For $Ca_{36}Al_{53}Mg_{11}$, the Ca sublattice remains intact and an additional 3 at.% Ca and 11 at.% Mg solutes substitute the Al sublattice.

Generalized stacking fault energy (GSFE) lines and surfaces were calculated by incrementally shifting one-half of the crystal across the slip direction and plane. Periodic boundary conditions (PBC) were applied in the directions parallel to the slip plane. Fixed boundary conditions were applied along the slip plane normal, where the outermost atomic layers with a thickness of 14 Å at both top and bottom were fixed. The aspect ratio of the simulation samples is greater than 10. The crystal was relaxed in the direction perpendicular to the slip plane after each displacement step using the FIRE [70,71] algorithm with a force tolerance of 10^{-8} eV/Å. Climbing image nudged elastic band (NEB) [72,73] calculations were performed on the simulation setup with the same boundary conditions as mentioned above to find saddle points and minimum energy paths (MEPs) of slip events. The spring constants for parallel and perpendicular nudging forces are both 1.0 eV/Å^2. Quickmin [74] was used to minimize the energies across all replicas until the force norm was below 0.01 eV/Å.

3. Results

For the evaluation of the effects of chemical composition changes (as variation of Mg and/or Ca content) on the mechanical properties in the cubic $CaAl_2$ Laves phase at ambient temperature, a combination of nanomechanical testing with EDX, EBSD and TEM experiments was applied. With the employed approach, hardness and indentation modulus variations determined from nanoindentation tests were compared with local chemical composition, orientation, and resulting deformation defects. In particular, EDX and TEM were used to measure the chemical composition. The slip traces formed in the vicinity of the indents were analysed for the different grain orientations (Table 1 and Fig. 2) to statistically reveal the activated slip planes. Moreover, TEM investigations were performed in selected areas, where dislocations were introduced by the nanomechanical tests, to analyse the Burgers vectors directions of these dislocations. Atomistic simulations were conducted to investigate the influence of the chemical composition on the mechanical properties and slip activation.

3.1. Nanoindentation

For $Ca_{33}Al_{61}Mg_6$, the average hardness of the indentation experiment is calculated to be 4.6 ± 0.2 GPa, and the average indentation modulus is 80.7 ± 3.0 GPa. The average values calculated for $Ca_{36}Al_{53}Mg_{11}$ were determined to be 4.1 ± 0.3 GPa and 71.3 ± 1.5 GPa, respectively.

Because of the large grains for the indented orientations of $Ca_{33}Al_{61}Mg_6$, we were able to extract orientation dependent hardness and indentation modulus data. Fig. 2 shows all measured grain orientations located in an inverse pole figure (IPF). Table 1 gives information on the chemical compositions, hardness and indentation moduli of all analysed orientations for $Ca_{33}Al_{61}Mg_6$. The hardness values and indentation moduli are calculated as an average over both indentation experiments for each orientation (random and +30° rotated states). This was done because of their minor deviation.

3.2. Surface trace analysis

For the statistical analysis of the resulting slip and crack planes, a total of 7172 surface traces was carefully analysed following the method by Gibson et al. [75] using aligned EBSD data and SE images. The tolerance angle between the alignment of the identified slip traces and the ideal orientation of potential slip plane traces was chosen to be 3° to account for small deviations from perfect alignment during normal imaging and EBSD analysis under 70°. The plastic zones around the indentation marks showed three different morphologies: straight lines, edges and curves, the same as in the earlier publications of Laves phases and μ-phases [12,76,77]. We also encountered areas where only cracking occurred or no visible surface traces formed.

Table 1
Summary of the chemical composition, hardness and indentation modulus for all orientations for $Ca_{33}Al_{61}Mg_6$, whereby the orientation numbers relate to the numeration of these orientations in the IPF of Fig. 2.

	Chemical composition			Hardness [GPa]	Indentation Modulus [GPa]
	Mg [at.%]	Al [at.%]	Ca [at.%]		
I	5.9 ± 0.2	61.2 ± 0.2	32.9 ± 0.2	4.7 ± 0.4	78.3 ± 2.1
II	5.8 ± 0.2	61.5 ± 0.2	32.7 ± 0.1	4.6 ± 0.2	80.8 ± 1.9
III	6.2 ± 0.2	61.1 ± 0.2	32.8 ± 0.2	5.5 ± 0.4	89.5 ± 1.9
IV	5.9 ± 0.2	61.5 ± 0.2	32.5 ± 0.1	4.8 ± 0.1	77.1 ± 1.5
V	5.9 ± 0.2	61.1 ± 0.3	33.0 ± 0.2	4.8 ± 0.2	81.7 ± 1.6
VI	5.8 ± 0.3	61.2 ± 0.3	33.0 ± 0.1	4.8 ± 0.6	78.9 ± 1.8
VII	5.9 ± 0.1	61.2 ± 0.1	33.0 ± 0.1	4.8 ± 0.3	80.4 ± 1.5
VIII	6.0 ± 0.1	60.9 ± 0.2	33.1 ± 0.2	4.6 ± 0.3	78.6 ± 1.9

Fig. 2 displays the indentation surfaces with the six different morphologies and their orientations in the IPF map (see Fig. 2a). Fig. 2b–f shows representative morphologies of the surface traces forming around indentations in of $Ca_{33}Al_{61}Mg_6$. Fig. 2b shows straight lines mixed with edges around the indent in area I. Fig. 2c presents only cracks appearing around the indent in area III, located near {111}. Fig. 2d reveals a curved slip trace morphology in area V, oriented most closely towards {001}. Fig. 2e shows edges around the indent in area VI and Fig. 2f the mixture of edges and curves for area VII. The rotation of the sample does not affect any resulting surface traces and morphologies of the tested orientation.

Fig. 2g–i shows representative morphologies of the surface traces forming around indentations in $Ca_{36}Al_{53}Mg_{11}$. In Fig. 2g, only the curved slip morphology is evident around the indent in area 1, while Fig. 2i illustrates the absence of visible surface deformation in area 3. Fig. 2h displays all defined morphology types observed in area 2.

The analysis of the surface traces can only be performed on those traces which contain straight components, such as the straight lines (Fig. 2b), cracks (Fig. 2c) and parts of the edges (Fig. 2e). For the curved traces, an evaluation of possible slip planes is not feasible, therefore, the resulting plasticity of area V as well as area 1 and area 3 (because of the absence of slip lines) (Fig. 2d, g, i) is not taken into account for the statistical evaluations of the activated slip planes.

For the statistical analysis of the resulting slip traces forming around the indents, we considered in the present work more planes than in a previous study [12]: the low index {100}, {110} slip planes as well as the {111} and {11n} planes with $n = 2, \ldots, 6$ and 11. This decision was based on new observations of plastic events on these slip planes in the TEM analysis in the present work. The alignment of the considered planes with respect to the unit cell is shown in Fig. 3a.

Surface traces related to plasticity were analysed statistically on samples of $Ca_{33}Al_{67}$, $Ca_{33}Al_{61}Mg_6$, and $Ca_{36}Al_{53}Mg_{11}$, yielding 892, 3902, and 992 traces, respectively. As in case of the indexation of slip planes, considering all possible slip systems within the deviation angle, the total number of slip planes over the total number of surface traces in percent, which we refer to as activation frequency is around 300 %. This suggests multiple potential solutions per slip line due to the tolerance angle of the slip trace analysis algorithm and orientations where unique solutions may not exist. The activation frequency of slip planes remained consistent across different indenter rotations, although the number of detected surface traces varied, with more traces generally observed around 30° clockwise rotated indentations.

To analyse the influence of the change in chemical composition in the C15 phase with respect also to the stoichiometric $CaAl_2$ Laves phase without Mg, the results of the slip line analysis of the stoichiometric $CaAl_2$ Laves phase [12] were reanalysed and plotted next to the results of the off-stoichiometric samples (Fig. 3), where the total amount of activated slip systems is represented by blue bars for $Ca_{33}Al_{67}$, and by purple and light red bars for $Ca_{33}Al_{61}Mg_6$ and $Ca_{36}Al_{53}Mg_{11}$, respectively. Overall, all samples have in common, that the highest slip plane activation frequency was detected on the new {11n} planes, which, to the best of our knowledge, have never been reported in previous work. The {110} and {100} were detected less often, irrespective of the composition of the Laves phases.

Differences between the compositions emerge for the activation of the {111} plane and the higher order {11n} planes. In the case of the {111} plane, activation decreases for both samples containing Mg (from 18.7 % in $Ca_{33}Al_{67}$ to 13.4 % in $Ca_{33}Al_{61}Mg_6$ and 13.9 % in

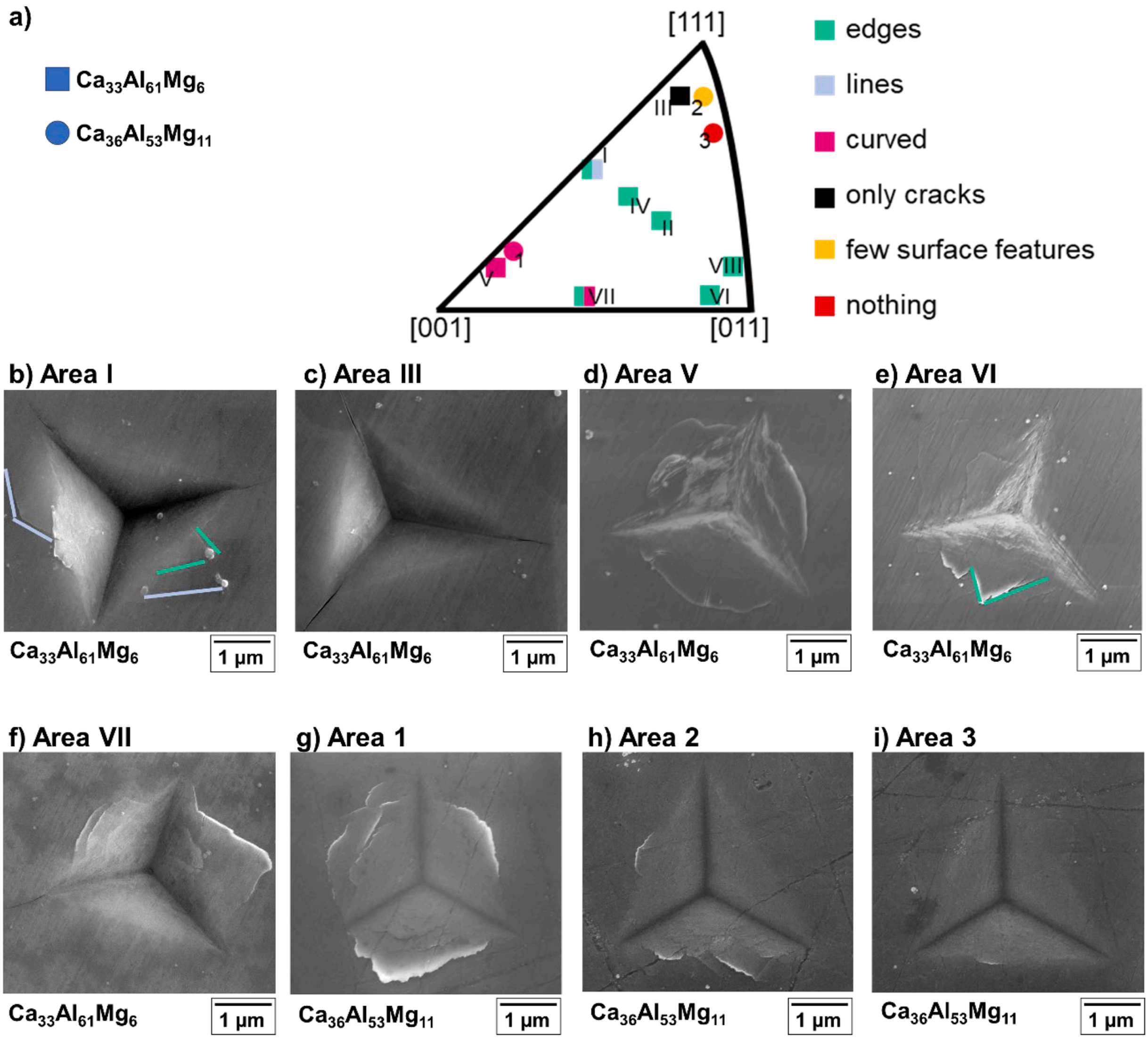

Fig. 2. Different morphologies of the plastic zones around the indents, where the square symbols with Roman numbers represent the resulting morphology for $Ca_{33}Al_{61}Mg_6$, and circles with Arabic numbers represent the morphology for $Ca_{36}Al_{53}Mg_{11}$. In the IPF in a), the pink squares/circles indicate the orientation where curved slip lines were observed in d) for area V and g) for area 1 The black square shows the orientation where only cracks occurred, comparable with the SE images of area III in c). Green squares mark the orientations where edge slip traces formed, shown for areas VII and VI in e), f). Light blue squares highlight the orientations where straight slip lines are visible, which only occurred together with edge slip lines for area I. Examples are indicated in b), where the light blue lines correspond to the line traces and the green lines highlight surface traces of edge type. The orange circle denotes the case where only a few surface features were observed, as in area 2 in h). Lastly, the red circle corresponds to the orientation of area 3 in which no surface signature was identified, as shown in i).

$Ca_{36}Al_{53}Mg_{11}$). Furthermore, the activation of the {11n} planes hovers at or above 40 % (with the sole exception of {114} in $Ca_{36}Al_{53}Mg_{11}$) in the Ca-Al-Mg alloys.

Regarding the crack planes, the same procedure as for the slip planes was used. The general activation frequency for the resulting orientations is shown in Fig. 3c. As the indented areas around the indents of $Ca_{36}Al_{53}Mg_{11}$ were crack free, this sample is not included in Fig. 3c. The dominant crack planes in terms of activation frequency were the {11n} planes. In total, $Ca_{33}Al_{67}$ showed 394 cracks for 144 indents, while $Ca_{33}Al_{61}Mg_6$ revealed 992 cracks for 400 indents, resulting in a similar propensity for crack formation of 2.7 and 2.5 cracks per indent, respectively. Again, the indexation resulted in 3 times as many potential crack planes as indexable cracks in the micrographs, given a total activation frequency of the order of 300 % in both cases.

Both compositions show a similar distribution of crack planes with the {11n} planes at the higher activation frequencies and, as seen in the activation of slip, crack propagation on the {100}, {110} and {111} planes were also detected, but comparable to the {11n} planes at a significantly reduced frequency. For a better visualisation of the origin of multiple assignments of slip planes and the difficulty in distinguishing {11n} planes, in Fig. 4 an example for orientation IV of $Ca_{33}Al_{61}Mg_6$ of two parallel surface traces is given, where, in addition to the $(\bar{1}13)$, $(\bar{1}14)$, $(\bar{1}15)$ planes, the (011) plane could be found. The (011) plane exhibits a deviation angle of 2° (from the ideal trace assuming perfectly accurate determination of the surface plane and crystal orientation), a deviation angle of $(\bar{1}14)$ was calculated to be 3°, whereas the {113} and {115} can be assigned twice with deviation angles of approximately 2°.

3.3. TEM analysis

Detailed investigation of the deformation microstructure in both non-stoichiometric $Ca(Al,Mg)_2$ Laves phases was performed by TEM analysis. Electron transparent FIB Lamellae were prepared from the material volumes located next to or directly beneath of the selected indents presented in Fig. 2.

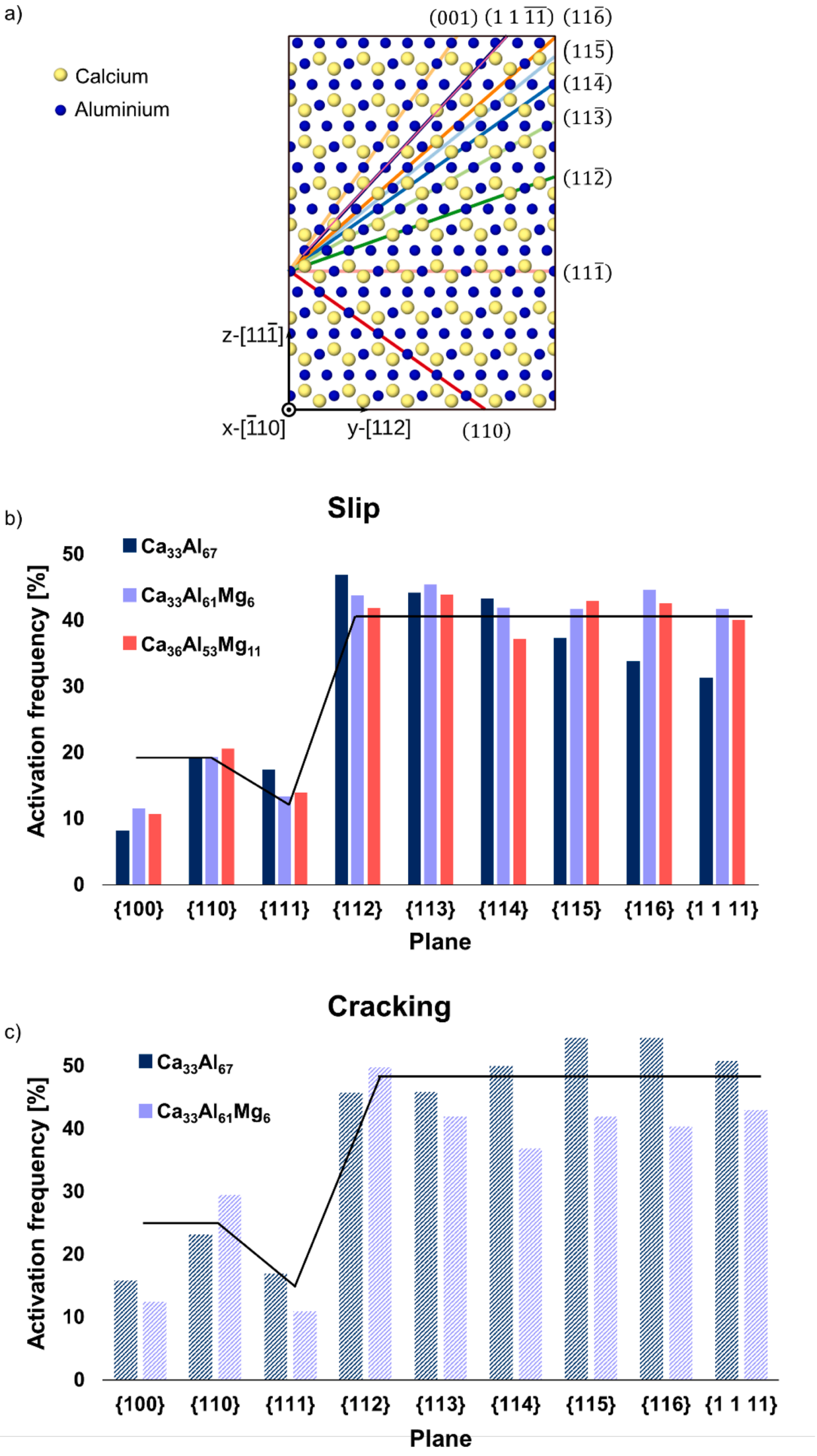

Fig. 3. a) Alignment of the identified slip planes in the cubic *C*15 $CaAl_2$ Laves phase. b) Activation of these planes from indentation slip trace analysis. c) Indexed crack planes from indentation considering the same plane families. Data for the binary $Ca_{33}Al_{67}$ phase taken from [12] (slip) and [24] (cracking). The black lines visualise the relative number of available planes of each family and would therefore correspond to the expected relative activation in case of equal resistance to dislocation slip or cracking.

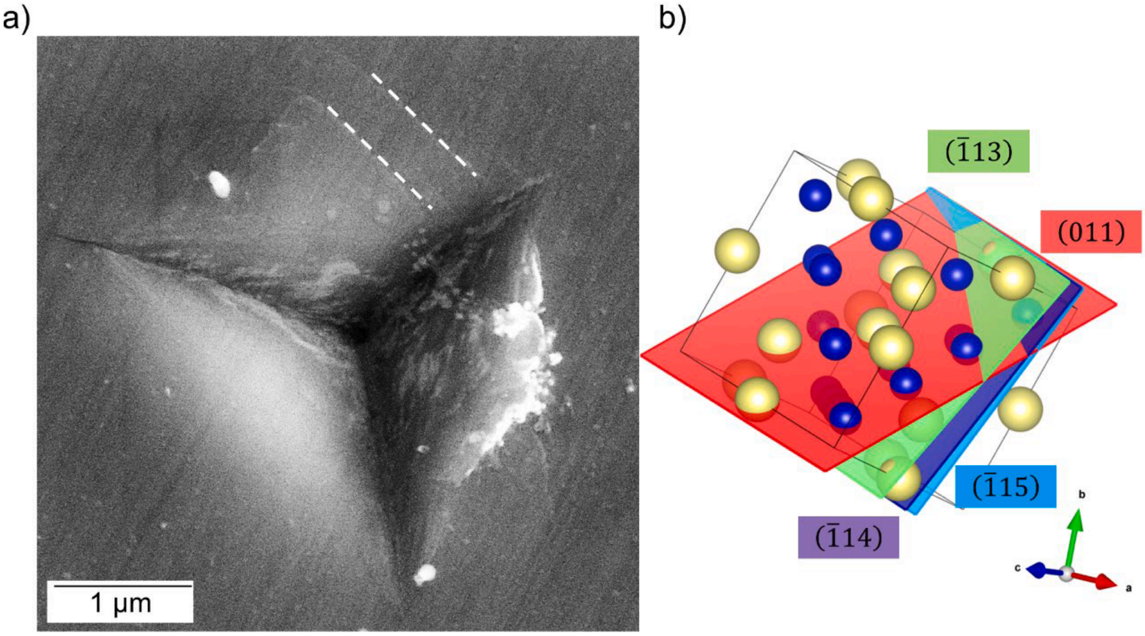

Fig. 4. Exemplary visualisation of the surface analysis, showing in a) the SE image taken from orientation IV with the analysed surface trace with edge character marked with the white dashed line. In b) the $CaAl_2$ unit cell shows the possible solution taken from the slip line detection results, but only plotting one for every plane family. The colours underlying the indices are those used to draw the planes in the unit cell, taking VESTA [91].

A TEM lamella was milled from orientation V in $Ca_{33}Al_{61}Mg_6$ to identify the curved slip planes (cf. Fig. 2d), which cannot be identified by the surface trace analysis. Here, the TEM lamella was milled to obtain the foil plane possibly parallel to one of the {110} planes. In this way, six zone axes were accessed for this TEM analysis: the [101], $[1\bar{1}1]$, [323], [312], $[2\bar{1}3]$ and $[3\bar{1}2]$ zone axes.

The image taken at the $[1\bar{1}1]$ zone axis is shown in Fig. 5a. The dislocations located just under the indent are found to be confined onto specific planes. A region of interest is highlighted by a yellow square in Fig. 5a and presented in Fig. 5b at a higher magnification. The three “main” slip bands are highlighted in Fig. 5b by the numbers 1, 2 and 3. The activated slip planes of the slip bands can be determined from the TEM images taken at different zone axes when the slip planes are edge-on, i.e. the slip planes are oriented parallel to the electron beam direction and therefore observed as thin lines in the TEM images. Some segments of slip bands 1 and 2 are found to be close to edge-on in the $[1\bar{1}1]$ zone axis, (Fig. 5-1)), and show the same behaviour under the analysed two beam conditions. Slip band 3 was found to be close to edge-on at the $[3\bar{1}2]$ zone axis orientation. In order to determine the orientations of the slip bands precisely, the lamella was tilted to different zone axes, as mentioned in the previous section. The lamella (foil) plane was determined by calculating the tilting angles between the foil normal direction and different zone axes to be (75 2 69). The intersection lines of the possible slip plane and the lamella plane within the unit cell are labelled by differently coloured lines in Fig. 5. These coloured lines (intersections) were compared with the slip band orientations on the TEM images taken at different zone axes. The indexed slip planes are given in Fig. 5c-i next to the images taken in the $[1\bar{1}1]$ zone axis and $[3\bar{1}2]$ zone axis (Fig. 5-1) and 2), respectively).

With multi-beam diffraction conditions, dislocation contrast was found to obscure the slip plane orientations. Slip band 1 consists of segments with variating habit plane orientation. The bottom segment of slip band 1 was found to be parallel to the $(11\bar{1})$ plane (trace indicated by the blue line in Fig. 5e). The middle segment of slip band 1 appears parallel to the $(21\bar{1})$ plane (orange trace in Fig. 5d), while the top segment lies parallel to the $(31\bar{1})$ plane (purple line in Fig. 5c).

Fig. 5-2) shows slip band 3 imaged at the $[3\bar{1}2]$ zone axis. This slip band consists of different segments, which lie on different slip planes. The left segment lies parallel to the $(\bar{1}41)$ plane (shown in red in Fig. 5g), while the right segment aligns with the (151) plane trace (shown in pink in Fig. 5i). In addition to slip band 3, two other slip bands on both the left and right sides were also analysed (Fig. 5f and h) and assigned to the $(21\bar{1})$ and $(\bar{1}12)$ slip planes, respectively.

The deformation structures below an indent in orientation 1 in $Ca_{36}Al_{53}Mg_{11}$ were also examined by TEM (Fig. 6). The lamella was milled to align its orientation close to that of the lamella from $Ca_{33}Al_{61}Mg_6$ in Figs. 5 and 6 where the lamella plane coincides with one of the {110} planes. The overview TEM BF image of this lamella from $Ca_{36}Al_{53}Mg_{11}$ is displayed in Fig. 6a, where the dashed square shows the region of interest containing dislocation structures investigated further in detail. This region is also shown at a higher magnification in Fig. 6b at the [101] zone axis. The microstructure under the indent is similar to that of the first lamella of $Ca_{33}Al_{61}Mg_6$ with a homogenous plastic zone in which multiple slip systems are activated. Slightly away from the indent, deformation is again found to be confined to specific planes. Some of the slip bands are seen close to edge-on, while many of them are not edge-on. To characterise the orientations of the slip bands, the lamella was tilted to six zone axes, [101], $[1\bar{1}2]$, [211], [213], $[1\bar{1}1]$, and [103]. The slip bands have a higher visible density of dislocations in some zone axes in Fig. 6b as well as under many two-beam conditions (shown in Fig. 6). This makes it difficult to determine the slip active planes in these slip bands and indicates that there may be more than one set of dislocations on the slip bands. Therefore, a more in-depth analysis was performed under different two-beam conditions and will be shown in the following sections.

The slip bands imaged along the [101] zone axis and the corresponding selected area electron diffraction (SAED) pattern are displayed in Fig. 6b. At the [101] zone axis, some slip bands are observed to be close to edge-on. The upper two slip bands are found to be parallel to the $(1\bar{3}\bar{1})$ plane (Fig. 6c), while a $(12\bar{1})$ plane (Fig. 6d) appears between the two $(1\bar{3}\bar{1})$ slip bands. In the middle of the image, several parallel slip bands can be seen. These bands again consist of segments with slightly different orientations (Fig. 6e), which are indexed to be on the $(16\bar{1})$ and $(1\ 11\ \bar{1})$ planes (illustrated in Fig. 6e and f, respectively). This feature of

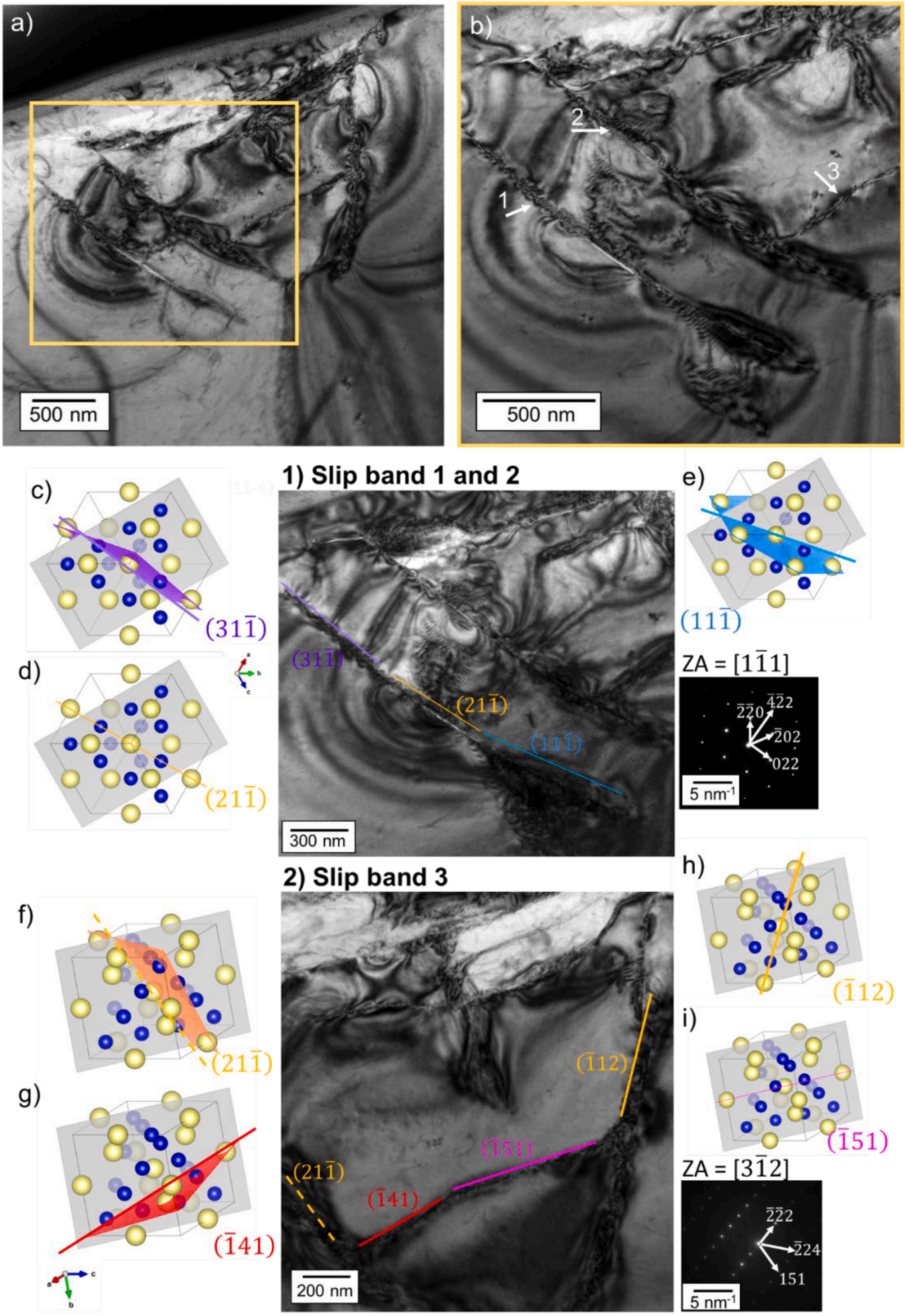

Fig. 5. Dislocation structure beneath the indent zone in $Ca_{33}Al_{61}Mg_6$ from area V. a) Overview TEM BF image taken at $[1\bar{1}1]$ zone axis. The yellow square highlights the region of interest and is displayed in b) at a higher magnification and a difference of 0.6° in tilting angle. Moreover, the numbers 1 to 3 show different slip bands, which were further analysed. TEM BF images taken at the 1) $[1\bar{1}1]$ zone axis and 2) $[3\bar{1}2]$ zone axis. Some segments of slip bands 1 and 2 are close to edge-on at $[1\bar{1}1]$ zone axis. A segment of Slip band 3 is close to edge-on at $[3\bar{1}2]$ zone axis. c) – e) show the unit cell, lamella plane (grey plane) and the indexed slip plane (colour plane) using VESTA [78]. The colour lines are the intersections of the lamella plane and the slip plane and they are shown next to the slip bands for guidance. In 1), the slip band is observed to have segments with various orientations: the upper (purple), middle (orange) and lower (blue) sections, which are indexed to be on the $(31\bar{1})$, $(21\bar{1})$ and $(11\bar{1})$ planes, respectively. Slip band 3 in 2) consists of two segments parallel to the $(\bar{1}41)$ plane (red, f)) and the (151) plane (pink, i)). The orange lines are determined to be lie parallel to the {112} planes on $(21\bar{1})$ and $(\bar{1}12)$ planes, respectively.

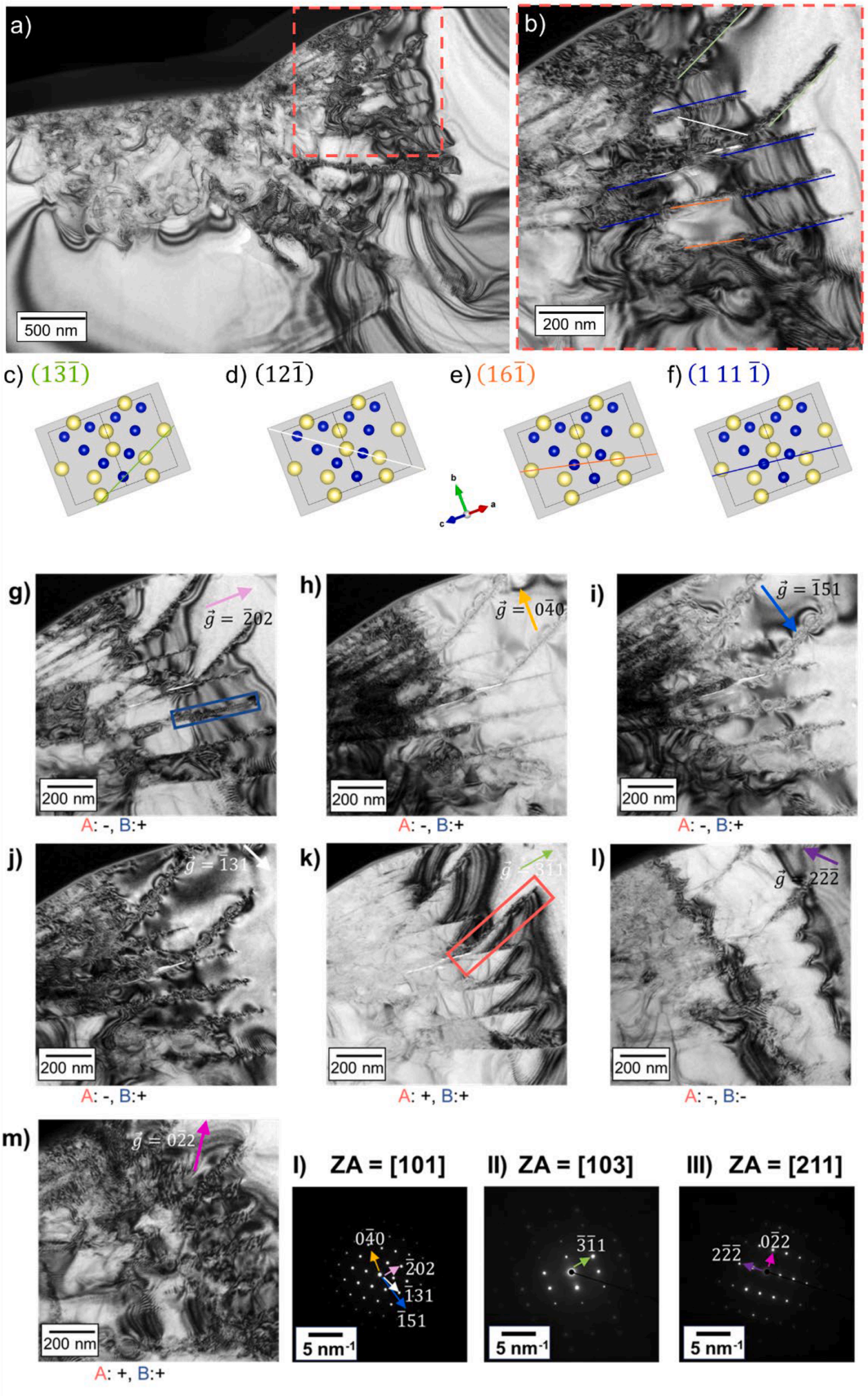

Fig. 6. Deformed microstructure beneath the indent zone in $Ca_{36}Al_{53}Mg_{11}$. a) TEM BF overview image of the lamella at [101] zone axis, of area 1 (Fig. 2). The area marked by the dashed square is shown at b) a higher magnification. The assignment of the slip bands is additionally visualised with coloured lines, and these are shown in c)-f) orientated in the $CaAl_2$ unit cell, shown with VESTA [78]. The applied two-beam conditions in g)-j) belong to I) the [101] zone axis, k) was taken at II) the [103] zone axis, and l) and m) were recorded in III) the [211] zone axis., whereby the $\vec{g}$-vectors are shown in the zone axis image with the different colours and also in the BF images, the corresponding $\vec{g}$-vectors are: a) $(\bar{2}02)$ in light pink (I), b) $(0\bar{4}0)$ in yellow (I),c) $(\bar{1}51)$ in blue (I) and d) $(\bar{1}31)$ in white (I). The visibility (+) or invisibility (-) of the dislocations, dislocation A (indicated by red rectangle) and B (blue rectangle), are listed under the images.

the slip band is the same as observed in $Ca_{33}Al_{61}Mg_6$, which indicates that a similar deformation mechanism may have taken place in both samples.

As noted above, there is often more than one set of dislocations on the slip bands and the images taken exactly along the zone axes have a high strain contrast resulting from all of the dislocations. Therefore, two-beam conditions were applied to selectively view individual sets of dislocations based on their Burgers vector $\vec{b}$. There are two sets of dislocations, which are named “dislocation A” (Fig. 6 red rectangle) and “dislocation B” (Fig. 6 blue rectangle), on a given slip plane. In the $\vec{g}\cdot\vec{b}$ analysis, it was found that under two-beam conditions: $\vec{g}=(\bar{2}02)$, $(0\bar{4}0)$, $(\bar{1}51)$ and $(\bar{1}31)$, dislocations with $\vec{b}=[101]$ are all invisible (dislocations A). The $(1n\bar{1})$ slip planes containing $\vec{b}=[101]$ are all edge-on. However, there is still a strain field visible along some of the slip bands (in Fig. 6g), h), i) and j)). This indicates that on some of the slip bands, there may be more than one slip plane with different Burgers vectors in close proximity or with direct overlap. Therefore, it is considered that there is another set of dislocations with different Burgers vectors (dislocations B) on another slip plane. According to the $\vec{g}\cdot\vec{b}$ analysis (the visibility/invisibility criterion), the Burgers vector of dislocations B is indexed to be $\vec{b}=½\,[110]$ or $½[01\bar{1}]$, which is on the $(1\bar{1}n)$ and (n11) plane, respectively. However, finding out all the slip planes of different dislocations is not the main focus of the present study, and consequently, no further experiment was carried out on finding out the slip plane of dislocations B.

At the bottom part of the lamella, some SFs were observed (Fig. 7) which presumably did not contribute to or originate from the plastic deformation during indentation. They present as straight lines arranged in parallel and at a relative angle of 70° viewed along the [101] zone axis, as indicated in Fig. 7. The alignment of these lines is visualised in the cubic $CaAl_2$ unit cell; they correspond to the $(11\bar{1})$ and $(1\bar{1}\bar{1})$ planes.

3.4. Atomistic simulations

The effects of the chemical composition on the elastic properties of C15 Ca-Al-Mg Laves phases, including Young’s modulus E, bulk modulus B, shear modulus G, and Poisson’s ratio ν, were investigated using atomistic simulations. For the stoichiometric C15 $CaAl_2$ phase, $B = 52.5$ GPa, $E = 91.7$ GPa, $G = 37.9$ GPa, and $\nu = 0.209$. As the Mg content increases to 6 at.% (corresponding to the chemical composition of $Ca_{33}Al_{61}Mg_6$), the values of B, E, and G decrease to 51.7, 88.1, and 36.2 GPa, respectively, as shown in Fig. 8. By the introduction of an over-stoichiometric Ca content, corresponding to the experimentally studied sample $Ca_{36}Al_{53}Mg_{11}$, the reduction of elastic moduli becomes more prominent, i.e., the values of B, E, and G decrease to 50.4, 81.3, and 33.0 GPa, respectively.

The influence of the orientation-dependent behaviour of the mechanical properties is listed in Table 2 for the resulting Young’s modulus and universal anisotropy index A_U [79]. Values for the [111], [110] and [100] oriented Young’s moduli for the tested compositions are given. Overall, the decreasing values can be seen for every composition, starting from [111] → [110] → [100], and from $Ca_{33}Al_{67}$ → $Ca_{33}Al_{61}Mg_6$ → $Ca_{36}Al_{53}Mg_{11}$. Additionally, with increasing Mg content the anisotropy index increases from 0.009 to 0.022. However, it remains at a low level of anisotropy, consistent with the experimental results of C15 $CaAl_2$ ($A_u = 0.0005$) reported in [80].

In order to form a direct connection between the experimental and computational results, we further investigated the energy changes during many different potential slip events on the experimentally observed slip systems. To this end, we first compare all slip systems in $Ca_{33}Al_{67}$ before approaching the effect of chemical composition for a subset of these planes. The experimentally identified slip systems were assessed by calculating the corresponding GSFE lines (Fig. 9a and γ-surfaces (Figure S2) as well as the correlated minimum energy paths via the NEB calculations (Fig. 9b) in C15 $CaAl_2$. The energy barriers for all slip systems are summarized in Table S 2 in the supplementary material. For the GSFE calculation of the $1/6\ [\bar{2}1\bar{1}]$ partial slip on the $(11\bar{1})$ triple layer, the rigid-body shift was interpolated according to the path of the

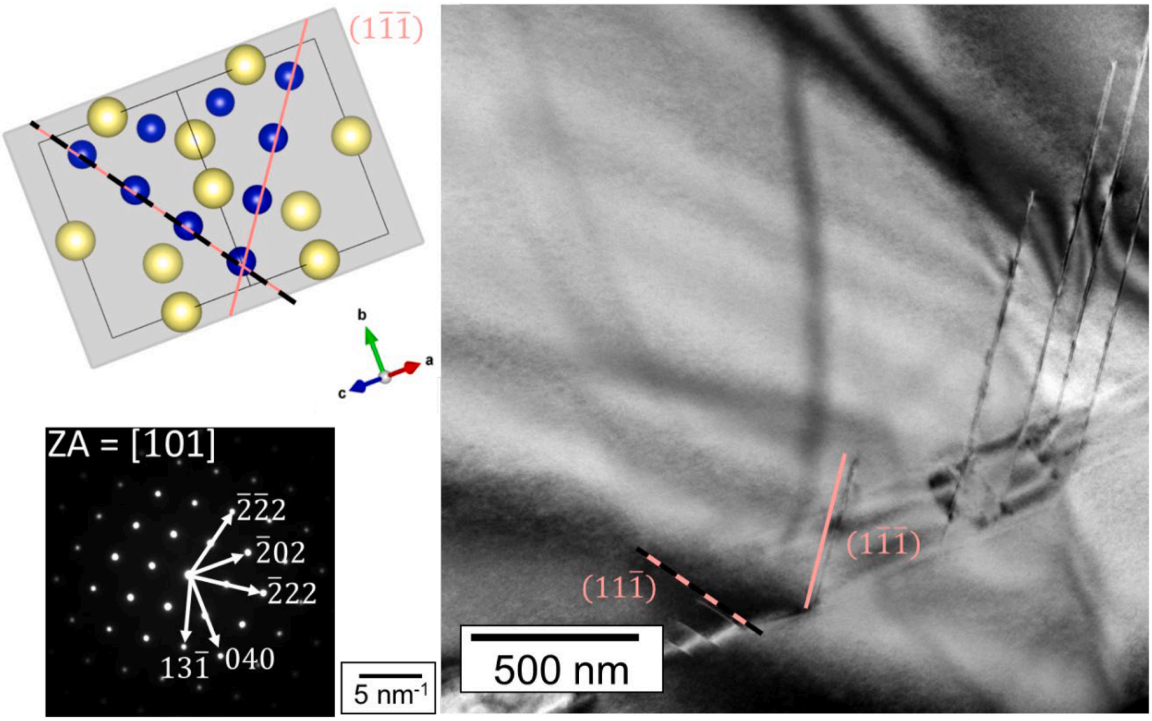

Fig. 7. {111} stacking fault structures in a TEM BF image of the lower part of the $Ca_{36}Al_{53}Mg_{11}$ lamella in [101] zone axis, having two different orientated parallel assigned lines with a 70° rotation between them. In a) these lines are shown in the unit cell, being parallel to the $(11\bar{1})$ and $(1\bar{1}\bar{1})$ plane, visualised using VESTA [78].

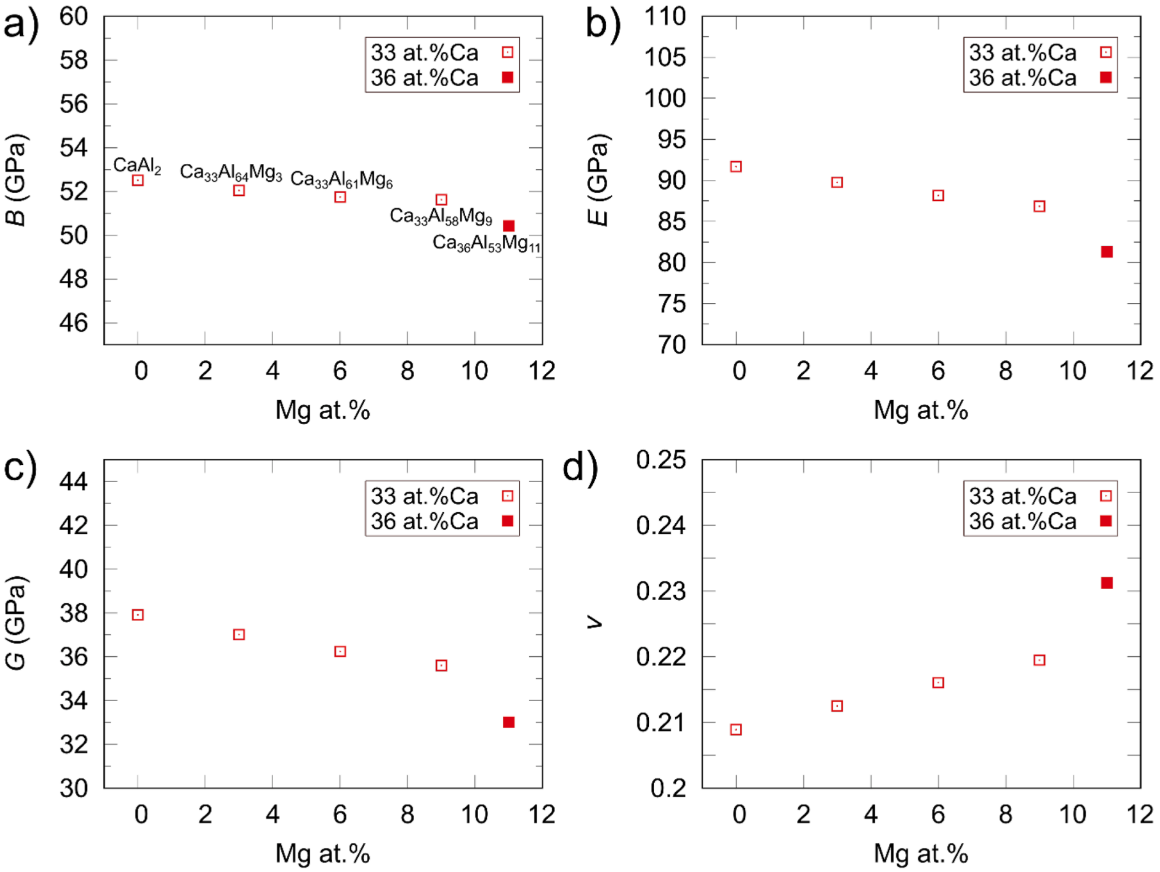

Fig. 8. Elastic properties calculated through atomistic simulations on *C*15 Ca-Al-Mg Laves phases. a) Bulk modulus (*B*), b) Young's modulus (*E*), c) shear modulus (*G*) and d) Poisson's ratio (*ν*).

Table 2
Calculated orientation dependent Young's modulus and anisotropy factor (A_U) for the three compositions.

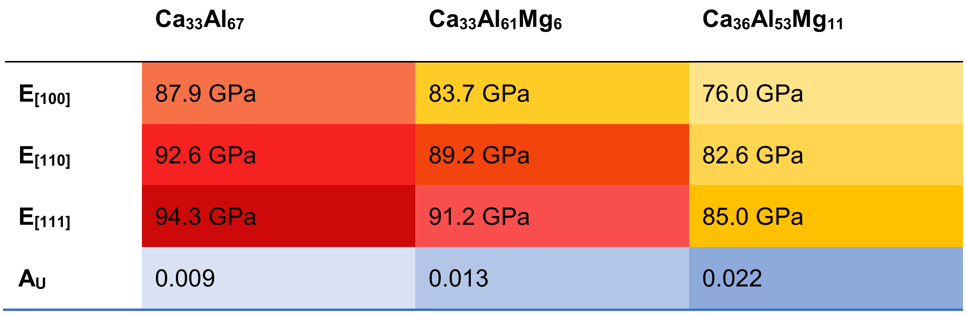

	$Ca_{33}Al_{67}$	$Ca_{33}Al_{61}Mg_6$	$Ca_{36}Al_{53}Mg_{11}$
$E_{[100]}$	87.9 GPa	83.7 GPa	76.0 GPa
$E_{[110]}$	92.6 GPa	89.2 GPa	82.6 GPa
$E_{[111]}$	94.3 GPa	91.2 GPa	85.0 GPa
A_U	0.009	0.013	0.022

synchro-shear slip mechanism [27]. The energy barriers based on the GSFE lines for all slip systems range from approximately 1000 to 1600 mJ/m^2, where the (001) $[\bar{1}10]$ exhibits the highest barrier (1570 mJ/m^2) and $(11\bar{1})_{tk}[\bar{1}10]$ slip, that is slip between the triple and Kagomé layer (index *tk*) exhibits the lowest (1081 mJ/m^2) energy barrier among all slip events. The slip events along the minimum energy path (MEP) were obtained via the NEB calculation. The synchro-shear slip event $(11\bar{1})_t[\bar{1}10]$, index *t* to indicate synchro-shear taking place in the triple layer) exhibits the greatest change in energy level with the activation energy of this mechanism becoming the lowest (907 mJ/m^2) among all calculated slip events, as shown in Fig. 9b and Table S1. Notably, (001) $[\bar{1}10]$ slip retains the highest activation energy (1564 mJ/m^2) along the MEP, followed by (110) $[\bar{1}10]$ slip (1210 mJ/m^2). The energy barriers along the MEP for other $(11\bar{n})$ $[\bar{1}10]$ slip events range from 983 to 1190 mJ/m^2. Among all slip events considered here, stable stacking fault states exist only along the MEP of the synchro-shear slip event ($(11\bar{1})_t[\bar{1}10]$).

The investigation into the effects of chemical composition on plasticity involved the calculation of GSFE lines for selected slip systems, varying solute concentrations and distributions in *C*15 Ca-Al-Mg Laves phases. Across all considered slip systems, the energy barriers decrease in off-stoichiometric compositions with an increase in Mg content and the lowest values are again obtained for the $Ca_{36}Al_{53}Mg_{11}$ composition (with over-stoichiometric Ca content), see Fig. 10.

Additionally, the synchro-shear-induced {111} stacking fault energy dramatically decreases by 50 % from 123.2 mJ/m^2 in the stoichiometric composition to 60.4 ± 9.6 mJ/m^2 in the off-stoichiometric

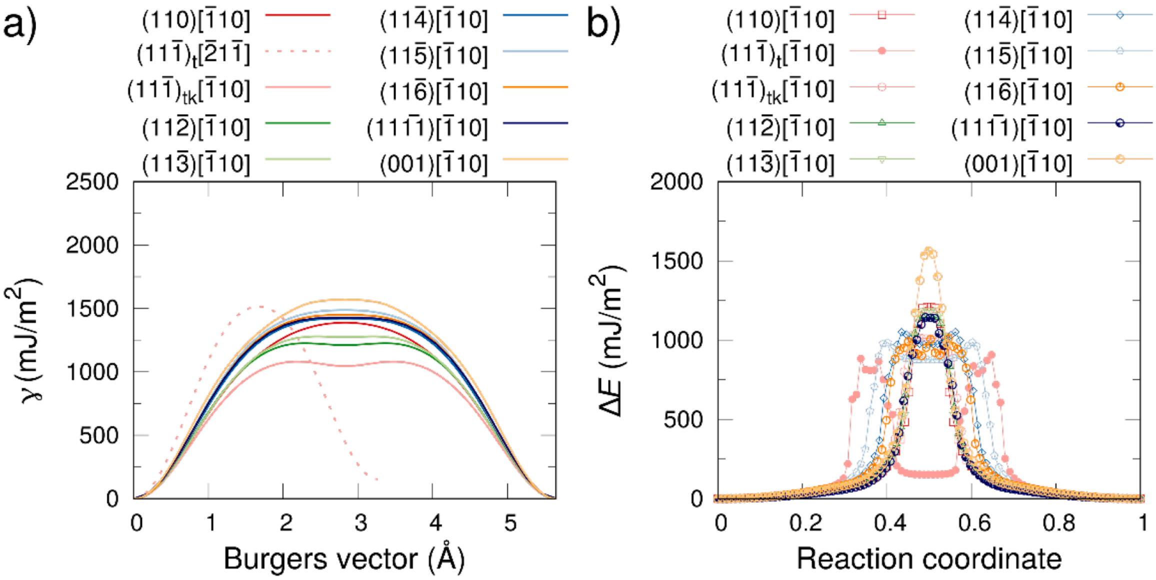

Fig. 9. Assessment of $[\bar{1}10]$ slip systems in $C15$ $CaAl_2$ Laves phase. a) GSFE (γ) lines of full or partial $[\bar{1}10]$ slip on different slip planes. b) Excess energy (ΔE) versus reaction coordinate of $[\bar{1}10]$ slip calculated using NEB.

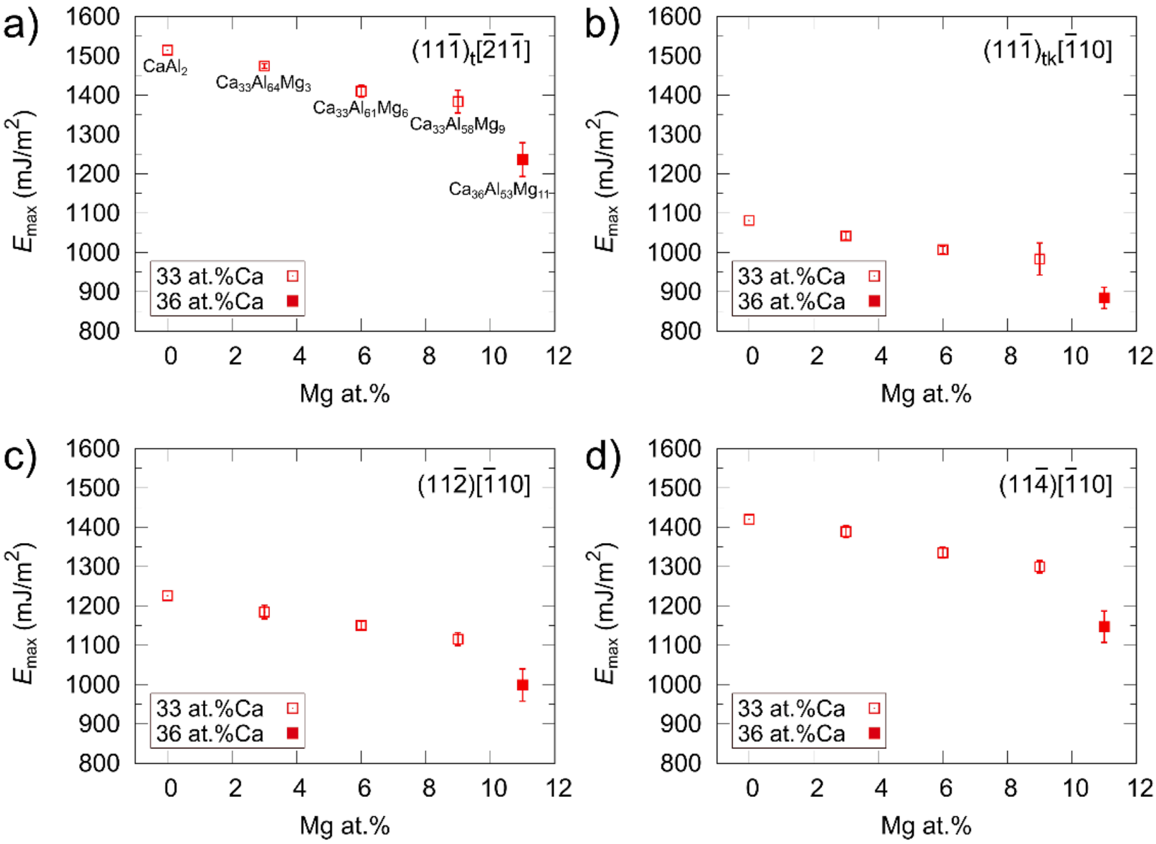

Fig. 10. Energy barriers (E_{max}) in GSFE lines of $[\bar{1}10]$ slip in stoichiometric and off-stoichiometric $C15$ Ca-Al-Mg Laves phases. a) Partial $[\bar{1}10]$ ($1/6\ \bar{2}1\bar{1}$) slip on the $(11\bar{1})$ triple layer along the synchro-shear slip path. b) Full $[\bar{1}10]$ slip on the $(11\bar{1})$ triple-Kagomé layer along the crystallographic slip path. Full $[\bar{1}10]$ slip on c) $(11\bar{2})$ and d) $(11\bar{4})$ planes.

$Ca_{36}Al_{53}Mg_{11}$ composition as shown in Fig. 11.

4. Discussion

4.1. Phase analysis

We confirmed the presence of the cubic $C15$ Laves phase for both

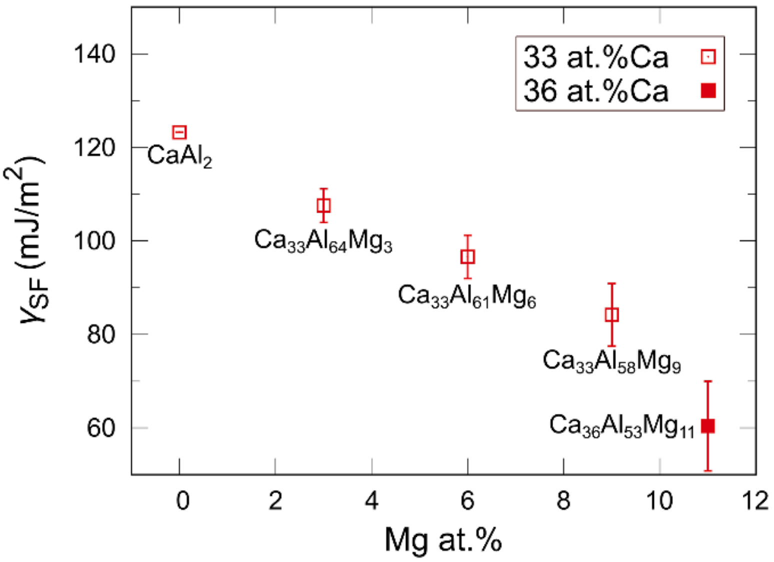

Fig. 11. Synchro-shear-induced {111} stacking fault energies (γ_{SF}) in stoichiometric and off-stoichiometric C15 Ca-Al-Mg Laves phases.

samples, $Ca_{33}Al_{61}Mg_6$ and $Ca_{36}Al_{53}Mg_{11}$, using both SAED and EBSD, with chemical compositions for the C15 grains determined by SEM-EDX to 61.4 ± 0.2 at.% Al, 32.9 ± 0.2 at.% Ca and 5.7 ± 0.2 at.% Mg and 52.9 ± 0.7 at.% Al, 36.3 ± 0.1 at.% Ca and 10.8 ± 0.8 at.% Mg, respectively. Amerioun et al. [33] and Tehranchi et al. [81] used first principles calculations to estimate the stability range of $CaAl_{2\text{-}x}Mg_x$, i.e. for a stoichiometric Ca content. They proposed a stability limit for the C15 phase near 8 at.% and 13 at.% Mg, respectively at 0 K, that is either below or above in terms of the Mg content found here in the C15 phase, with the 13 at.% Mg both compounds fit. At 0 K Tehranchi et al. [81] conclude from their data that the C36 phase should directly decompose into a mixture of C15 + C14 phase as the C36 phase remains above the hull at 0 K. Hallstedt and Moori [82] note in their work on the Mg-Al-Ca ternary phase diagram that the energy difference between C15 and C36 is often small and the phase stability window therefore remains uncertain in particular for the C36 phase, which they also propose decomposes into C15 + C14 for temperatures below 200 °C. Zubair et al. [83] considered the three Laves polytypes as part of a metallic-intermetallic composite and found phase transitions between as-cast and heat-treated conditions. Most of their Laves phase precipitates proved under-stoichiometric in terms of Ca, however, the highest Ca-content of 34.2 at.% was found in a C15 precipitate (after heat treatment for 48 h at 500 °C and subsequent slow cooling) with a 4.6 at.% Mg and 61.2 at.% Al. These work on phase stability of the C15 $Ca(Al,Mg)_2$, together with our results, indicate that the Mg content investigated here is stable in the C15 phase and that the slightly increased Ca content also appears to be contained within the same phase width. In the present work, we do not observe any indication of a bulk phase transformation to any of the hexagonal Laves phases. Although individual SFs on {111} planes were observed in the $Ca_{36}Al_{53}Mg_{11}$ and the stacking fault energy was found to drop with the addition of Mg and Ca in our atomistic simulations, consistent with expectations based on the first principles studies [33], no transition in the form of e.g. massive stacking fault formation could be observed. In terms of the mechanical properties, we therefore interpret all our data in the context of the C15 phase, but with the influence on the plastic deformation of the phase stability and the phase transformation path via synchro-shear in the triple layer in mind [5,30,31,57].

4.2. Mechanical properties

We obtained indentation data for various orientations and three compositions when including the related binary C15 $Ca_{33}Al_{67}$ [12]. Average hardness and modulus decreased slightly, albeit not statistically significantly through addition of Mg in $Ca_{33}Al_{61}Mg_6$ and a notable decrease was found for $Ca_{36}Al_{53}Mg_{11}$, with hardness and indentation modulus each approximately 16 % lower than $Ca_{33}Al_{67}$.

Atomistic simulations corroborate the experimental findings and demonstrate that a substitution of Al for Mg decreases hardness and elastic moduli values. The trend in calculated bulk elastic properties follows a pattern with increasing Mg content (Fig. 8), which is very consistent with the experimental findings. The observed softening is consistent with the dielastic effect, characterized by a reduction in modulus, and solute/vacancy-assisted dislocation motion, as reported in previous atomistic simulations [29].

The trend identified in this study aligns with the measurements of Luo et al. [23], who also found a softening behaviour, that is a decrease in hardness, with the deviation from the stoichiometric $NbCo_2$ C15 phase by increasing either Nb or Co content [23].

In addition to the dielastic effect, this softening behaviour can be interpreted by considering the effect of lattice distortion caused by introducing misfit solute atoms on plastic deformation. For the current phase, with the atomic radius of Mg being 17pm larger than that of an Al atom, taking the atomic radius forming in the Laves phase [84], the incorporation of Mg atoms into the sublattice of Al would lead to a change of Laves phase structure and may cause lattice distortion. The atomistic mechanisms of the softening effects by anti-site defects in the C14 $CaMg_2$ Laves phase have been demonstrated using atomistic simulations [29]. The activation energy of kink-pair nucleation, which serves as the rate-limiting step of synchro-Shockley dislocation motion on the basal or {111} plane, can be lowered by the presence of Ca_{Mg} or Mg_{Ca} anti-sites at the dislocation core region. This softening behaviour in off-stoichiometric compositions was also demonstrated for other {11n} slip systems (see Fig. 10), the mechanisms through which anti-site effects influence dislocation motion and the associated activation energies require further investigation.

Previous studies on the influence of ternary element additions have shown that the hardness and modulus typically remain stable or are minimally affected until surpassing a certain threshold of the additional element [23,34,38,39,58,59,85]. For instance, the addition of V to $NbCr_2$ at low concentrations (3 and 5 at.%) did not significantly alter mechanical properties, despite an increase in lattice parameter due to the replacement of smaller Cr atoms by V atoms [39,58]. However, higher V concentrations (10, 18, and 25 at.%) elevated the brittle to ductile transition temperature (BDTT) [41], indicating that the amount of the added element is critical for property changes. In contrast to the

RNi$_2$ Laves phases, the $C15$ CaAl$_2$ phase, having a relatively low r_A/r_B value and therefore is not expect to exhibit structural vacancy. Instead, constitutional vacancy at the Al site is found to be more energetically favourable than other constitutional point defects, as indicated by atomic-scale modelling [29,86]. Thus, introducing additional Ca, can lead to an increased concentration of constitutional vacancies at A sites in $C15$ CaAl$_2$ Laves crystal structures, thereby facilitating synchro-Shockley dislocation motion more effectively than anti-site defects. These factors may explain why the Ca$_{36}$Al$_{53}$Mg$_{11}$ composition, with additional Ca and Mg, exhibits more significant changes in hardness and modulus compared to Ca$_{33}$Al$_{61}$Mg$_6$ with only Mg substitutions. Additionally, phase stability influences mechanical properties; for example, ab-initio calculations predict the formation of the ternary $C36$ phase of Ca(Al,Mg)$_2$ with a specific Mg content, suggesting a transition in properties [33].

4.3. Orientation dependence of mechanical properties

We also assessed orientation dependence in two ways: (1) by rotating the triangular impression of the indenter by 30° around the indentation axis and (2) by indenting along different crystal orientations. The first gave negligible changes in properties and no qualitative differences in the formation of slip traces or the distribution of identified planes apart from an overall greater number of slip traces. The assessment of orientation-dependent hardness and modulus was carried out in the greatest depth on the intermediate sample in terms of composition, Ca$_{33}$Al$_{61}$Mg$_6$, which allowed the placement of many indents into each of the large grains. This is in contrast to the other samples, for example in case of the Ca$_{36}$Al$_{53}$Mg$_{11}$ only 4 to 6 indents per orientation could be placed. For Ca$_{33}$Al$_{61}$Mg$_6$, the hardness and modulus were consistent in 7 out of 8 areas, with only area III, closest to [111] (Fig. 2) diverging towards higher values. This area gave a hardness of 5.5 ± 0.4 GPa and an indentation modulus of 89.5 ± 1.9 GPa. We assume that this may be due to two reasons. First, for the hardness, the absence of visible slip traces around the indent (Fig. 2c), indicating the absence of easily activated slip planes for this orientation, which revealed only crack nucleation. A similar behaviour was reported for the stoichiometric Laves phase in a similar orientation [12], and it will be further discussed in the next section. Second, the influence of the anisotropy of this phase. Atomistic simulation calculates the modulus for all three compositions (Table 2) which shows that Young's modulus reveals the highest values in [111] direction and the lowest at [100], at values of 91.2 GPa and 83.7 GPa, respectively, matching with the experimental data for Ca$_{33}$Al$_{61}$Mg$_6$. Additionally, an increasingly anisotropic fracture with increasing deviation from the binary composition was observed.

4.4. Deformation mechanisms

For the assessment of the activated slip planes, the activation frequencies were plotted for nine slip planes: the {100}, {110}, {111}, {112}, {113}, {114}, {115}, {116} and {1 1 11} planes. The alignment of these planes is displayed in Fig. 3. All planes were further identified and confirmed with TEM investigations in Fig. 6. In addition, the Burgers vectors identified by TEM ($\frac{1}{2}$ [101] on the $(1\ 11\ \bar{1})$ and $(16\bar{1})$ planes as shown in Fig. 3) were also confirmed by the atomistic simulations. The gamma surfaces and NEB calculations results indicate that no stable SF state exists as a result of simple shear or on the MEPs in {11n} planes, where $n \geq 2$, revealing full dislocation slip as the dominant dislocation mechanism on these planes (while partial formation is possible on the {111} planes containing the triple layer).

For Ca$_{33}$Al$_{61}$Mg$_6$, two different indentation tests were performed (initial state and +30° rotated sample) in order to analyse the influence of the indenter geometry on the resulting slip activation.

If we now consider the slip plane activation across all analysed compositions, Ca$_{33}$Al$_{61}$Mg$_6$, Ca$_{36}$Al$_{53}$Mg$_{11}$ and also Ca$_{33}$Al$_{67}$ [12], it can be seen that the {11n} planes dominate and not, as initially expected, the {111} planes. It is important to note that the activation frequencies stated here for Ca$_{33}$Al$_{67}$ deviate from those previously reported in [12], especially obvious for the reduced activation of {111} planes. This results from a change in the analysis protocol in that here we not only allowed double indexation in terms of different slip planes possessing a consistent surface trace orientation within the threshold (which remained constant), but we also counted individual planes of the same family separately. This allows us to not only weigh the relative occurrence of the different planes but also to assess their activation frequency with respect to the number of different available planes within a given family of planes, as indicated in the diagrams showing the activation frequencies of the different slip and crack planes (Fig. 3b and c). For example, for the {11n} plane family with $n \geq 2$, the geometric probability of indexation is higher, as there are 12 different {11n} planes, compared to 4 for the {111} and 6 for the {100} and {110} plane families. A comparison of the relative activation frequencies in the view of this number of available slip planes gives a first indication of those planes which are easier or harder to activate than the average slip plane, as confirmed by a comparison of a slip trace analysis and micro compression in other intermetallics including the hexagonal CaMg$_2$ Laves phase [76,87]. Here, we note that the relative activation of {110}, {111} and {11n} follows the number of available slip planes for all three samples with the sole exception of the slightly higher activation of {111} slip in the binary Ca$_{33}$Al$_{67}$ sample, which lies in the error bar. Also consistent across all three samples is the reduced activation of slip and cracking on the {100} planes, as these lie lower than the {110} plane family that offers the same number of slip planes and below half the value measured for the {11n} planes with twice the number of independent slip planes.

Atomistic simulations confirm the experimental observation of the slip line statistics from the perspective of the expected energy barrier for slip. The minor detection of dislocation activity on the {001} planes is entirely consistent with the highest energy barrier on this plane both for simple shear and following the MEP as shown in Fig. 9a and b. Slip on the {110} plane may be expected to occur in principle based on the atomistic simulations, as the energy barrier is the second highest along the MEP, but of the same order of magnitude as for the other {11n} planes. However, the plane was not observed in our TEM analysis. This finding is consistent with our slip trace analysis when considering the sampled orientations and slip trace morphology. Overall, the most dominantly activated slip planes are the {11n} planes with $n \geq 2$ (Fig. 3), showing slight differences that depend on the grain orientation. For the activation of the different slip planes differentiated by orientation, the reader is referred to Figure S1 in the supplementary materials.

Fig. 12 is broken down for the analysable orientations, the orientation-dependent Schmid factor M of the {11n} slip systems (Fig. 12c-h) including the {111} plane (Fig. 12b), is visualised in the IPF using a colour code for showing the magnitude of the calculated M. Here, the distribution of its maximum shows for the {11n} system starting with $n = 2$ and ending with $n = 11$, that the corner is shifting with increasing n from the location between [011] and [111], where the analysable surface traces (edges and straight lines) were located (Fig. 12a), to [111]. For all these slip systems the [001] part always reveals the lowest M. For the $\{111\}\langle 1\bar{1}0\rangle$ system the maximum of M is central between [001] and [011], showing the lowest M at [111] but also a relatively low M for [001]. The highest M is present in $\langle 100\rangle$ orientation. However, the slip trace morphology of indentations indented along a surface normal near [100] show curved slip traces, indicative of no single easily activated slip system. If {110} were viable slip planes with a comparable critical resolved shear stress and highest Schmid factor (assuming compression along the indentation axis) compared to the other {11n} planes, straight slip traces along {110} traces would be expected in this particular orientation, but are not found for any of the three compositions. We therefore assume that indexation

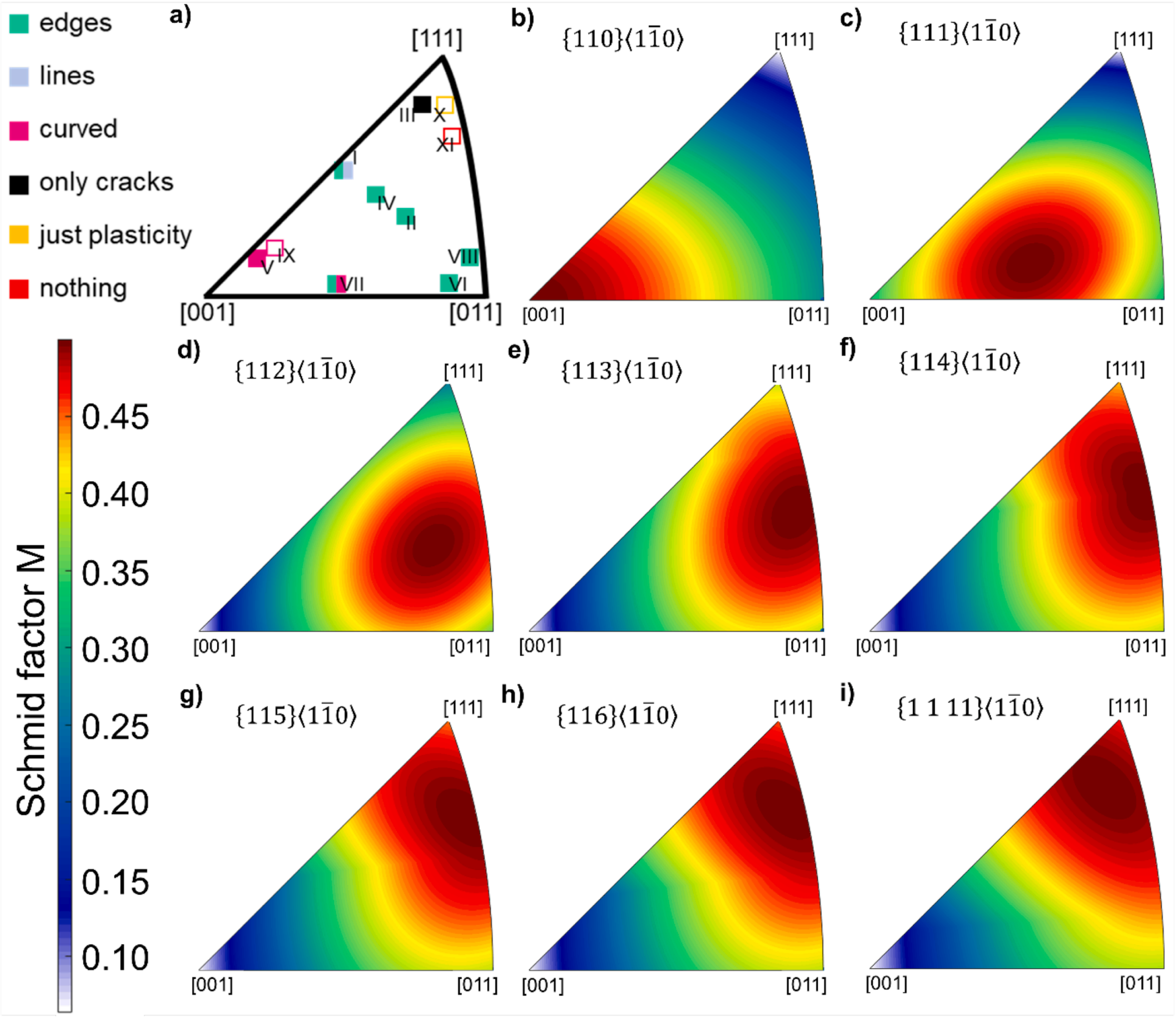

Fig. 12. a) Orientation dependent slip morphology from Fig. 3 with the Schmid factor M of the {110} – {1 1 11} slip systems (b)-i)) for deformation along the surface normal.

of both {100} and {110} predominately results from the ambiguity of the method with different planes producing identical or closely aligned surface intersections depending on crystal orientation [75]. Taking a look at the deviation angle between the surface trace and the orientation of the plane trace, it is observable, that the counted {110} plane reveals a slightly different angle than one of the {11n} planes and lays often in the range of the {1 1 11}, {115}, {113} as well as the {112} plane. The other {11n} slip systems exhibit similar energy barriers, consistent with similar activation frequencies in nanoindentation tests for $n \geq 2$ and a proportionally lower frequency for {111} with a third of the number of distinguishable planes for the two Ca(Al,Mg)$_2$ alloys.

So far, we have purposefully dealt with the {112} to {1 1 11} planes as one group of {11n} planes, as distinguishing these planes is difficult in experiments outside of edge-on viewing with correlated diffraction information in the TEM, which revealed the activation of these planes. In the slip trace analysis, an additional difficulty arises from the alignment of the plane traces and small deviations between these planes. For different n in the {11n} index, the angle between these planes continuously decreases with increasing n, i.e., the deviation between $(11\bar{1})$ and $(11\bar{2})$ is 20°, which decreases to 3° between $(11\bar{5})$ and $(11\bar{6})$. For the slip line analysis, the threshold for assignment of a possible slip plane to a slip trace was set to 3°, i.e. the same order of magnitude as the difference in inclination between the planes themselves (not necessarily the surface traces, which may lie at even more similar angles).

The difficulty of exact slip plane determination is further visualised in Fig. 12, in that the distribution of the resolved shear stress becomes more similar as the planes' orientations converge in the higher order {11n} systems. The close alignment may of course result in a relative overestimation of the higher order {11n} planes where these are counted together perhaps more frequently than low index planes. However, we note that while these aspects result in difficulties in the differentiation of individual slip planes for large n, neither on its own is sufficient to result in indexation of these planes. If the planes possess substantially different critical resolved shear stresses, the similar Schmid factor would result in clear preferences for those with a lower activation barrier and the difference in alignment exceeds the experimental threshold with respect to the entire range of planes and in particular the lower order {11n} planes in most orientations.

We therefore conclude that the highest fraction of plasticity is carried on the {11n} planes with $n \geq 1$. Two further aspects remain to be considered: the effect of chemical composition on the activation of these planes (and competing planes for fracture) and the likely slip system operating on the {111} planes, which is the only plane on which partials and the synchro-shear mechanism may operate.

As TEM confirms the presence of the new {11n} slip planes but indentation suggests very similar critical stresses for these planes, we refer to atomistic simulations in interpreting and bringing these results together to understand the dislocation-mediated plasticity in the Ca-Al-

Mg Laves phases. The simulation results concerning the related energy barriers suggest that for the experimentally detected dominant {11n} plasticity, all barriers decrease with the addition of Mg and Ca (see Fig. 10) in addition to the drop in elastic moduli (see Fig. 8). Plastic deformation therefore becomes easier with increasing off-stoichiometric components and the stoichiometric *C*15 sample ($Ca_{33}Al_{67}$) exhibits the highest energy barriers for all slip events. This potentially explains the observed increasing dislocation and slip band densities from the $Ca_{66}Al_{67}$ phase to both $Ca_{33}Al_{61}Mg_6$ and $Ca_{36}Al_{53}Mg_{11}$. In addition, the observation of dislocation dipoles is consistent with more easily activated plasticity the *C*15 phase containing additional Mg [88,89], as dipoles may form more readily when the line energy is comparatively lower, allowing the more mobile dislocation structures to interact and rearrange. The computational results also reveal that by introducing Ca, the energy barriers significantly decrease and deviate from the linearly descending trend observed when only substituting Mg. This is entirely consistent with the sharper drop in hardness and modulus observed for the $Ca_{36}Al_{53}Mg_{11}$, which in terms of Mg addition increases by about the same increment as $Ca_{33}Al_{61}Mg_6$ relative to the binary alloy, but leads to a drop in hardness and stiffness that is more than twice as large. Furthermore, the finding that the energy barriers drop similarly on all systems is consistent with a chemical composition-independent activation of the different slip planes in the statistical indentation slip trace analysis, particularly as they all share the same Burgers vector according to our TEM and atomistic simulation results, enabling cross-slip between them.

In close relation to these observations of {11n} plasticity and orientation dependence of flow, we also note that, for all three compositions, the indented orientation near the [111] direction exhibits no or very few surface slip traces. In $Ca_{33}Al_{61}Mg_6$ and $Ca_{33}Al_{67}$, cracks were found instead, but not in $Ca_{36}Al_{53}Mg_{11}$. In the [111] direction, the Schmid factors for the {11n} slip systems are high, with the maximum found for the {1 1 11} planes. The fact that no distinct surface plasticity is observed leads to the hypothesis that the resolved (normal) stress for crack nucleation on easy fracture planes is lower than that for dislocation motion. Therefore, the competition between cracking and slipping is resolved in favour of cracking. This is consistent with several planes lying nearly or, in case of the {112} planes directly, normal to the sample surface, giving a high elastic stress release during crack opening along the circumferential tensile component of the stress field during indentation.

Moreover, these [111]-like orientations exhibit higher values for hardness and indentation modulus as mentioned above (Table 1, area III and Table 2). The higher order {11n} planes lie closer together than lower index planes, giving overall not as many geometric options for slip on high Schmid factor planes in the three-dimensional stress field of the indentation along a [111] axis, compared with the centre of the standard triangle, where the different lower index {11n} planes are also highly stressed. TEM and also the formation of curved surface traces provide additional indications that dislocations move under frequent cross-slip along the easiest planes around the imprinting indenter tip. In the {111} direction, the lack of variability in slip plane orientation coupled with the favourable orientation for cracking may therefore give rise to the observed transition toward cracking. Interestingly, $Ca_{36}Al_{53}Mg_{11}$ showed the same anisotropy in surface traces, but no cracks were observed in any orientation (Fig. 2h). This is in contrast to $Ca_{33}Al_{61}Mg_6$ and $Ca_{33}Al_{67}$, where only cracks occurred in similar indentation orientations [12]. It could be rationalised by the decrease in the energy barrier for slip events (as illustrated in the atomistic simulations in Fig. 10) in that the barrier for crack nucleation is not reached before plasticity takes place beneath the indent. In addition, the higher dislocation mobility may be associated with a lower rate of crack nucleus formation as dislocations are also found to occur on a greater number of slip planes, suggesting that lock formation and subsequent crack opening due to pile-up of dislocations is delayed in the $Ca_{36}Al_{53}Mg_{11}$ composition. Such an increase in the crack nucleation barrier with chemical composition was also demonstrated by previous studies where the ternary Laves phase or the deviation from the stoichiometric composition results in higher fracture toughness [85,90–93], but not related as directly to changes in dislocation mobility and morphology.

Lastly, we consider the activation of synchro-shear in the cubic Laves phase. In the majority of the literature, this mechanism is assumed to constitute not just the major but sole dislocation mechanism accommodating plastic deformation in *C*15 Laves phases. Here, we find that slip among many different {11n} is vital to comprehending the cubic Laves phase's plasticity. Deformation on the {111} planes containing the triple layer is, however, also the only mechanism of dislocation motion that is associated with the occurrence of SFs or phase transformations between the different Laves polytypes.

Multiple previous studies on the dislocation structures of Laves phases with chemical variations reveal that the density of SFs is heavily influenced by the chemical composition [23,38,40,58,59]. For the cubic *C*15 $NbCo_2$ Laves phase with a Nb content of 25.6 at.%, SFs occur on the {111} planes, whereas with increasing Nb content, the microstructure consists of dislocations and low-angle grain boundaries [23]. The same microstructural transition was also reported with the addition of ternary alloying elements to $NbCr_2$ by Yoshida et al. [38]. The structure remains a cubic Laves phase with the addition of relatively smaller atoms, while bigger atoms first reduce the stability of the cubic phase and then invoke micro-twins and SFs. In *C*15 Ca-Al-Mg Laves phases, the observation of SFs in $Ca_{36}Al_{53}Mg_{11}$ along the $(11\overline{1})$ and $(1\overline{1}\overline{1})$ planes, as shown in Fig. 7, correlates well with the atomistic simulations, where a 50 % decrease in γ_{SF} was obtained in the off-stoichiometric sample with a similar composition as $Ca_{36}Al_{53}Mg_{11}$.

However, in spite of these observations of planar defect formation and dislocations aligned along {111} planes, it has been demonstrated that synchro-shear slip on the {111} plane is a thermally activated event in the sense that thermal assistance is indispensable for activating this slip event [28]. The required thermal fluctuation in atom positions is largely suppressed at room temperature in Laves phases with melting points much above 300 K, and hence, we tend to consider the {111} synchro-shear slip a high-temperature mechanism. This is the reason why the activation frequency of the {111} plane is lower than that of other {11n} planes despite having a similar energy barrier level.

5. Conclusions

The influence of chemical composition on plasticity in *C*15 Ca-Al-Mg Laves phases at room temperature was investigated using a combination of nanoindentation tests to obtain a statistical distribution of activated slip and crack planes, along with TEM analysis to characterize the introduced dislocation structures. Atomistic simulations were employed to reveal the energy barriers associated with these slip events. This work leads us to the following conclusions:

- The addition of Mg and Ca leads to a decrease in the hardness and indentation modulus relative to the binary composition.
- The cubic $Ca(Al,Mg)_2$ Laves phases are anisotropic with respect the formation of surface traces from plastic deformation.
- The statistical analysis of the relative activation frequency of the surface traces revealed that the {11n} planes were the most activated slip planes, and this is rationalised by the comparably low energy barriers of these slip events obtained in atomistic simulations.
- {111} stacking faults were identified in the off-stoichiometric composition due to the significant decrease in stacking fault energy. However, it is not clear how this affects plastic properties as synchro-shear slip on the {111} plane requires thermal activation and, in agreement with this requirement, was found to be less activated compared to other {11n} planes across all compositions in our room temperature indentation experiments.
- Cracking was suppressed in nanoindentation of $Ca_{36}Al_{53}Mg_{11}$.

In summary, we find that the $Ca(Al,Mg)_2$ phase exhibits softening behaviour away from the $CaAl_2$ composition that is associated with distinct dislocation mechanisms, which we were able to infer using a combination of statistical indentation slip trace analysis, TEM and atomistic simulations. We believe that, in the future, this approach may also help elucidate the many conflicting results found elsewhere in the literature on chemical composition-dependent Laves phase plasticity.

CRediT authorship contribution statement

Martina Freund: Writing – review & editing, Writing – original draft, Visualization, Investigation, Formal analysis, Conceptualization. **Zhuocheng Xie:** Writing – review & editing, Investigation. **Pei-Ling Sun:** Visualization. **Lukas Berners:** Methodology. **Joshua Spille:** Visualization. **Hexin Wang:** Investigation. **Carsten Thomas:** Resources. **Michael Feuerbacher:** Resources. **Marta Lipinska-Chwalek:** Supervision. **Joachim Mayer:** Supervision. **Sandra Korte-Kerzel:** Writing – review & editing, Supervision.

Declaration of competing interest

The authors declare that they have no known competing financial interests or personal relationships that could have appeared to influence the work reported in this paper.

Acknowledgement

The authors gratefully acknowledge financial support by the Deutsche Forschunugsgemeinschaft (DFG) to all projects involved in this paper (A03, A05 and Z) of the SFB1394 Structural and Chemical atomic Complexity – From Defect Phase Diagrams to Material Properties, project ID 409476157. This project has received funding from the European Research Council (ERC) under the European Union's Horizon 2020 research and innovation programme (grant agreement No. 852096 FunBlocks). We would also like to express our gratitude to Marvin Poul and Jörg Neugebauer for early access to the Mg-Al-Ca machine learning potential used in this work. The authors gratefully acknowledge the computing time provided to them at the NHR Center NHR4CES at RWTH Aachen University (project number p0020431 and p0020267). This is funded by the Federal Ministry of Education and Research, and the state governments participating on the basis of the resolutions of the GWK for national high performance computing at universities (www.nhr-verein.de/unsere-partner). We would also like to thank the anonymous reviewer for reading our manuscript in great detail and providing very constructive and detailed criticism.

Supplementary materials

Supplementary material associated with this article can be found, in the online version, at doi:10.1016/j.actamat.2024.120124.

References

[1] P. Paufler, Early work on Laves phases in East Germany, Intermetallics 19 (4) (2011) 599–612.
[2] F. Stein, A. Leineweber, Laves phases: a review of their functional and structural applications and an improved fundamental understanding of stability and properties, J. Mater. Sci. 56 (9) (2021) 5321–5427.
[3] J. Zhu, et al., Point defects in binary Laves phase alloys, Acta Mater. 47 (7) (1999) 2003–2018.
[4] D. Thoma, J. Perepezko, A geometric analysis of solubility ranges in Laves phases, J. Alloys. Compd. 224 (2) (1995) 330–341.
[5] M.F. Chisholm, S. Kumar, P. Hazzledine, Dislocations in complex materials, Science 307 (5710) (2005) 701–703.
[6] R. Berry, G. Raynor, The crystal chemistry of the Laves phases, Acta Crystallogr. 6 (2) (1953) 178–186.
[7] T. Müller, et al., Gleitbanduntersuchungen während und nach Verformung der intermetallischen Verbindung MgZn2, Kristal. Techn. 7 (11) (1972) 1249–1264.
[8] D. Hinz, P. Paufler, G. Schulze, Temperature change experiments during secondary creep of the intermetallic compound MgZn2, Phys. Status Solidi (b) 36 (2) (1969) 609–615.
[9] T. Müller, P. Paufler, Yield strength of the monocrystalline intermetallic compound MgZn2, Phys. Status Solidi (a) 40 (2) (1977) 471–477.
[10] U. Krämer, G. Schulze, Gittergeometrische Betrachtung der plastischen Verformung von Lavesphasen, Kristal. Techn. 3 (3) (1968) 417–430.
[11] A. Von Keitz, G. Sauthoff, Laves phases for high temperatures—Part II: stability and mechanical properties, Intermetallics 10 (5) (2002) 497–510.
[12] M. Freund, et al., Plasticity of the C15-CaAl2 Laves phase at room temperature, Mater. Des. 225 (2023) 111504.
[13] P. Paufler, G. Schulze, Gleitsysteme innermetallischer Verbindungen, Kristal. Techn. 2 (4) (1967) K11–K14.
[14] J.B. Moran, Mechanical Behavior of MgCu2 Single Crystals, Trans. Metall. Soc. AIME 233 (8) (1965), p. 1473-&.
[15] D.P. Pope, F. Chu, Deformation of a C15 Laves phase: twinning and synchroshear, Struct. Intermetal. (1993).
[16] W.-Y. Kim, D.E. Luzzi, D.P. Pope, Room temperature deformation behavior of the Hf–V–Ta C15 Laves phase, Intermetallics 11 (3) (2003) 257–267.
[17] A. Kazantzis, M. Aindow, I. Jones, Deformation behaviour of the C15 Laves phase Cr2Nb, Mater. Sci. Eng.: A 233 (1–2) (1997) 44–49.
[18] A. Kazantzis, et al., The mechanical properties and the deformation microstructures of the C15 Laves phase Cr2Nb at high temperatures, Acta Mater. 55 (6) (2007) 1873–1884.
[19] A. Kazantzis, M. Aindow, I. Jones, Stacking-fault energy in the C15 Laves phase Cr2Nb, Philos. Mag. Lett. 74 (3) (1996) 129–136.
[20] Y. Ohba, N. Sakuma, High temperature-room temperature deformation behavior of MgCu2 Laves phase intermetallic compound, Acta Metall. 37 (9) (1989) 2377–2384.
[21] R. Lowrie, Mechanical properties of intermetallic compounds at elevated temperatures, JOM 4 (10) (1952) 1093–1100.
[22] S. Korte, W.J. Clegg, Studying plasticity in hard and soft Nb–Co intermetallics, Adv. Eng. Mater. 14 (11) (2012) 991–997.
[23] W. Luo, et al., Composition dependence of hardness and elastic modulus of the cubic and hexagonal NbCo2 Laves phase polytypes studied by nanoindentation, J. Mater. Res. 35 (2) (2020) 185–195.
[24] W. Luo, et al., Crystal structure and composition dependence of mechanical properties of single-crystalline NbCo2 Laves phase, Acta Mater. 184 (2020) 151–163.
[25] S. Korte-Kerzel, Microcompression of brittle and anisotropic crystals: recent advances and current challenges in studying plasticity in hard materials, MRS Commun. 7 (2) (2017) 109–120.
[26] Y. Xue, et al., Critical resolved shear stress of activated slips measured by micropillar compression tests for single-crystals of Cr-based Laves phases, Mater. Sci. Eng.: A 806 (2021) 140861.
[27] J. Guénolé, et al., Basal slip in Laves phases: the synchroshear dislocation, Scr. Mater. 166 (2019) 134–138.
[28] Z. Xie, et al., Thermally activated nature of synchro-Shockley dislocations in Laves phases, Scr. Mater. 235 (2023) 115588.
[29] Z. Xie, et al., Unveiling the mechanisms of motion of synchro-Shockley dislocations in Laves phases, Phys. Rev. Mater. 7 (5) (2023) 053605.
[30] P. Hazzledine, et al., Synchroshear of laves phases, MRS Online Proc. Lib. (OPL) 288 (1992).
[31] P. Hazzledine, P. Pirouz, Synchroshear transformations in Laves phases, Scrip. Metall. Mater. 28 (10) (1993) 1277–1282.
[32] F. Stein, M. Palm, G. Sauthoff, Structure and stability of Laves phases. Part I. Critical assessment of factors controlling Laves phase stability, Intermetallics 12 (7–9) (2004) 713–720.
[33] S. Amerioun, S.I. Simak, U. Häussermann, Laves-Phase Structural Changes in the System CaAl2-x Mg x, Inorg. Chem. 42 (5) (2003) 1467–1474.
[34] M. Fujita, Y. Kaneno, T. Takasugi, Phase field and room-temperature mechanical properties of C15 Laves phase in Nb–Hf–Cr and Nb–Ta–Cr alloy systems, J. Alloys. Compd. 424 (1–2) (2006) 283–288.
[35] K.C. Chen, S.M. Allen, J.D. Livingston, Factors affecting the room-temperature mechanical properties of TiCr2-base Laves phase alloys, Mater. Sci. Eng.: A 242 (1–2) (1998) 162–173.
[36] K.C. Chen, E.J. Peterson, D.J. Thoma, HfCo2 Laves phase intermetallics—Part I: solubility limits and defect mechanisms, Intermetallics 9 (9) (2001) 771–783.
[37] K.C. Chen, et al., HfCo2 Laves phase intermetallics—Part II: elastic and mechanical properties as a function of composition, Intermetallics 9 (9) (2001) 785–798.
[38] M. Yoshida, T. Takasugi, The alloying effect on the high temperature deformation of Laves phase NbCr2 intermetallic compound, Mater. Sci. Eng.: A 234 (1997) 873–876.
[39] T. Takasugi, M. Yoshida, S. Hanada, Deformability improvement in C15 NbCr2 intermetallics by addition of ternary elements, Acta Mater. 44 (2) (1996) 669–674.
[40] P. Kotula, et al., Defects and site occupancies in Nb-Cr-Ti C15 Laves phase alloys, Scr. Mater. 39 (4–5) (1998) 619–623.
[41] D. Thoma, et al., Elastic and mechanical properties of Nb (Cr, V) 2 C15 Laves phases, Mater. Sci. Eng.: A 239 (1997) 251–259.
[42] F. Chu, et al., Phase stability and defect structure of the C15 Laves phase Nb (Cr, V) 2, Acta Mater. 46 (5) (1998) 1759–1769.
[43] T. Shields, J. Mayers, I. Harris, Vacancy induced anomalies in the Laves phase CeNi2. Anomalous Rare Earths and Actinides, Elsevier, 1987, pp. 587–590.
[44] R. Mansey, G. Raynor, I. Harris, Rare-earth intermediate phases VI. Pseudo-binary systems between cubic laves phases formed by rare-earth metals with iron, cobalt, nickel, aluminium and rhodium, J. Less Common Metals 14 (3) (1968) 337–347.

[45] I. Harris, R. Mansey, G. Raynor, Rare earth intermediate phases: III. The cubic laves phases formed with aluminium and cobalt, J. Less Common Metals 9 (4) (1965) 270–280.

[46] K.A Gschneidner Jr, Systematics of the intra-rare-earth binary alloy systems, J. Less Common Metals 114 (1) (1985) 29–42.

[47] J. Gschneidner, A. Karl, V.K. Pecharsky, Binary rare earth Laves phases—An overview, Z. Kristall.-Crystall. Mater. 221 (5–7) (2006) 375–381.

[48] V. Paul-Boncour, et al., Homogeneity range and order–disorder transitions in R1−xNi2 Laves phase compounds, Intermetallics 14 (5) (2006) 483–490.

[49] K. Eichler, et al., Änderung von Verformungseigenschaften der intermetallischen Verbindung MgZn2 im Homogenitätsbereich, Kristal Techn 11 (11) (1976) 1185–1188.

[50] U. Krämer, K. Eichler, Transmissionselektronenmikroskopische Untersuchung der Defektstruktur der intermetallischen Verbindung MgZn2, Kristal Techn 10 (8) (1975) 813–820.

[51] H. Kubsch, P. Paufler, G.E. Schulze, The mobility of grown-in dislocations in the intermetallic compound MgZn2 during prismatic slip, Phys. Status Solidi (a) 25 (1) (1974) 269–275.

[52] L. Shao, et al., First-principles study of point defects in C14 MgZn2 Laves phase, J. Alloys. Compd. 654 (2016) 475–481.

[53] Y. Komura, Y. Kitano, Long-period stacking variants and their electron-concentration dependence in the mg-base friauf–laves phases, Acta Crystallogr. Sect. B: Struct. Crystallogr. Crys. Chem. 33 (8) (1977) 2496–2501.

[54] Y. Komura, K. Tokunaga, Structural studies of stacking variants in Mg-base Friauf–Laves phases, Acta Crystallogr. Sec. B: Struct. Crystallogr. Cryst. Chem. 36 (7) (1980) 1548–1554.

[55] S. Korte-Kerzel, et al., Defect phases–thermodynamics and impact on material properties, Inter. Mater. Rev. 67 (1) (2022) 89–117.

[56] S. Allen, Slip, twinning, and Transformation in Laves phases, Massachusetts Inst. of Technology (MIT), Cambridge, MA (United States), 1998.

[57] Y. Liu, J.D. Livingston, S.M. Allen, Room-temperature deformation and stress-induced phase transformation of laves phases in Fe-10 at.% Zr alloy, Metall. Trans. A 23 (1992) 3303–3308.

[58] T. Takasugi, M. Yoshida, The effect of ternary addition on structure and stability of NbCr2 Laves phases, J. Mater. Res. 13 (9) (1998) 2505–2513.

[59] N. Takata, et al., Nanoindentation study on solid solution softening of Fe-rich Fe2Nb Laves phase by Ni in Fe–Nb–Ni ternary alloys, Intermetallics 70 (2016) 7–16.

[60] F. Chu, D.P. Pope, *Deformation twinning in intermetallic compounds—The dilemma of shears* vs. *shuffles*, Mater. Sci. Eng.: A 170 (1–2) (1993) 39–47.

[61] F. Chu, D. Pope, Deformation of C15 Laves phase alloys, MRS Online Proc. Library (OPL) 364 (1994) 1197.

[62] W.C. Oliver, G.M. Pharr, An improved technique for determining hardness and elastic modulus using load and displacement sensing indentation experiments, J. Mater. Res. 7 (6) (1992) 1564–1583.

[63] W.C. Oliver, G.M. Pharr, Measurement of hardness and elastic modulus by instrumented indentation: advances in understanding and refinements to methodology, J. Mater. Res. 19 (1) (2004) 3–20.

[64] A.P. Thompson, et al., LAMMPS-a flexible simulation tool for particle-based materials modeling at the atomic, meso, and continuum scales, Comput. Phys. Commun. 271 (2022) 108171.

[65] E.V. Podryabinkin, A.V. Shapeev, Active learning of linearly parametrized interatomic potentials, Comput. Mater. Sci. 140 (2017) 171–180.

[66] A.V. Shapeev, Moment tensor potentials: a class of systematically improvable interatomic potentials, Multiscale Model. Simul. 14 (3) (2016) 1153–1173.

[67] M. Poul, et al., Systematic atomic structure datasets for machine learning potentials: application to defects in magnesium, Phys. Rev. B 107 (10) (2023) 104103.

[68] H.-S. Jang, D. Seol, B.-J. Lee, Modified embedded-atom method interatomic potentials for Mg–Al–Ca and Mg–Al–Zn ternary systems, J. Magnes. Alloys 9 (1) (2021) 317–335.

[69] P. Hirel, Atomsk: a tool for manipulating and converting atomic data files, Comput. Phys. Commun. 197 (2015) 212–219.

[70] J. Guénolé, et al., Assessment and optimization of the fast inertial relaxation engine (fire) for energy minimization in atomistic simulations and its implementation in lammps, Comput. Mater. Sci. 175 (2020) 109584.

[71] E. Bitzek, et al., Structural relaxation made simple, Phys. Rev. Lett. 97 (17) (2006) 170201.

[72] G. Henkelman, B.P. Uberuaga, H. Jónsson, A climbing image nudged elastic band method for finding saddle points and minimum energy paths, J. Chem. Phys. 113 (22) (2000) 9901–9904.

[73] G. Henkelman, H. Jónsson, Improved tangent estimate in the nudged elastic band method for finding minimum energy paths and saddle points, J. Chem. Phys. 113 (22) (2000) 9978–9985.

[74] D. Sheppard, R. Terrell, G. Henkelman, Optimization methods for finding minimum energy paths, J. Chem. Phys. 128 (13) (2008) 134106.

[75] J.S.-L Gibson, et al., Finding and characterising active slip systems: a short review and tutorial with automation tools, Materials (Basel) 14 (2) (2021) 407.

[76] S. Schröders, et al., Room temperature deformation in the Fe7Mo6 μ-Phase, Int. J. Plasticity 108 (2018) 125–143.

[77] M. Freund, et al., Plastic deformation of the CaMg2 C14-Laves phase from 50 to 250 °C, Materialia 20 (2021) 101237.

[78] K. Momma, F. Izumi, VESTA 3 for three-dimensional visualization of crystal, volumetric and morphology data, J. Appl. Crystallogr. 44 (6) (2011) 1272–1276.

[79] S.I. Ranganathan, M. Ostoja-Starzewski, Universal elastic anisotropy index, Phys. Rev. Lett. 101 (5) (2008) 055504.

[80] R. Schiltz Jr, J. Smith, Elastic constants of some MAl2 single crystals, J. Appl. Phys. 45 (11) (1974) 4681–4685.

[81] A. Tehranchi, et al., Phase stability and defect studies of Mg-based Laves phases using defect phase diagrams. arXiv preprint arXiv:2303.09576, 2023.

[82] B. Hallstedt, M. Noori, Hybrid calphad DFT modelling of the Mg–Al–Ca system, CALPHAD 82 (2023) 102577.

[83] M. Zubair, et al., Laves phases in Mg-Al-Ca alloys and their effect on mechanical properties, Mater. Des. 225 (2023) 111470.

[84] R.G. Forbes, The prediction of zero-barrier evaporation field: datasheet from Condensed Matter. Volume 45B: “Physics of Solid Surfaces” G. Chiarotti and P. Chiaradia, Editors., Springer-Verlag GmbH Germany.

[85] W. Luo, et al., Influence of composition and crystal structure on the fracture toughness of NbCo2 Laves phase studied by micro-cantilever bending tests, Mater. Des. 145 (2018) 116–121.

[86] X. Tian, et al., First-principles investigation of point defect and atomic diffusion in Al2Ca, J. Phys. Chem. Solids 103 (2017) 6–12.

[87] C. Zehnder, et al., Plastic deformation of single crystalline C14 Mg2Ca Laves phase at room temperature, Mater. Sci. Eng.: A 759 (2019) 754–761.

[88] F. Kroupa, Dislocation dipoles and dislocation loops, Le J. Phys. Colloq. 27 (C3) (1966). C3-154-C3-167.

[89] D. Dickel, et al., Dipole formation and yielding in a two-dimensional continuum dislocation model, Phys. Rev. B 90 (9) (2014) 094118.

[90] K. Li, et al., Microstructure characterization and mechanical properties of a Laves-phase alloy based on Cr2Nb, Int. J. Refract. Metals Hard Mater. 36 (2013) 154–161.

[91] K.C. Chen, S.M. Allen, J.D. Livingston, Stoichiometry and alloying effects on the phase stability and mechanical properties of TiCr2-base Laves phase alloys, MRS Online Proc. Lib. (OPL) (1994) 364.

[92] H. Huang, et al., Micromechanism in fracture toughness of NbCr2 laves phase improved by nickel alloying: first-principles calculation, J. Alloys. Compd. 857 (2021) 158040.

[93] X.-W. Nie, et al., Fabrication and toughening of NbCr2 matrix composites alloyed with Ni obtained by powder metallurgy, Mater. Sci. Eng.: A 502 (1–2) (2009) 85–90.

8. Publication 4

Metallographic preparation methods for the Mg based system Mg-Al-Ca and its Laves phases

D. Andre [a], M. Freund [a], U. Rehman [b], W. Delis [a], M. Felten [c], J. Nowak, C. Tian [b], M. Zubair [a,d], L. Tanure [b,e], L. Abdellaoui [b], H. Springer [b,e], J.P. Best [b], D. Zander [c], G. Dehm [b], S. Sandlöbes-Haut [a], S. Korte-Kerzel [a]

[a] Institute for Physical Metallurgy and Materials Physics, RWTH Aachen University, Aachen, Germany

[b] Max-Planck-Institut für Eisenforschung GmbH, Max-Planck-Straße 1, Düsseldorf, Germany

[c] Chair of Corrosion and Corrosion Protection, RWTH Aachen University, Aachen, Germany

[d] Department of Metallurgical and Materials Engineering, UET, Lahore, Pakistan

[e] Institute of Metal Forming, RWTH Aachen University, Aachen, Germany

Materials Characterization, Volume 192, 2022, 112187, **reproduced with permission of Elsevier.**

https://doi.org/10.1016/j.matchar.2022.112187

Short Summary

The Mg-Al-Ca system has been shown to be a promising alloy system since it combines the low density of Mg with a high creep resistance at high alloying contents and a high ductility for dilute alloys, while simultaneously avoiding the requirement of alloying with costly rare earth elements. Nevertheless, the adequate preparation of the alloy system for subsequent microstructural, mechanical, electrochemical and defect analysis is challenging. Therefore, within this publication, we present and apply methods for the structural, mechanical, electrochemical and defect analysis with a focus on the corresponding required metallographic preparation methods in order to support research on the alloy system.

U. Rehman (with J.P. Best) and **M. Freund** develop the idea of the manuscript and both contributed to the characterizations of the Mg-Al-Ca intermetallics and the writing – reviewing. D. Andre lead the manuscript (Conceptualization), rewrite and edit it. M. Felten, J. Nowak, D. Zander and W. Delis analysed the microstructures of Mg-Al-Ca solid solutions. M. Zubair analysed the microstructures of Mg-Al-Ca with dual phase structures. L. Tanure and H. Springer synthesised the samples. S. Sandlöbes-Haut and S. Korte-Kerzel provided feedback and suggestions to improve the experiments. All authors contributed to discussion of the results and reviewed the manuscript.

Materials Characterization 192 (2022) 112187

Contents lists available at ScienceDirect

Materials Characterization

journal homepage: www.elsevier.com/locate/matchar

Metallographic preparation methods for the Mg based system Mg-Al-Ca and its Laves phases

D. Andre [a,*], M. Freund [a], U. Rehman [b], W. Delis [a], M. Felten [c], J. Nowak [c], C. Tian [b,1], M. Zubair [a,d], L. Tanure [b,e], L. Abdellaoui [b], H. Springer [b,e], J.P. Best [b], D. Zander [c], G. Dehm [b], S. Sandlöbes-Haut [a], S. Korte-Kerzel [a]

[a] *Institute for Physical Metallurgy and Materials Physics, RWTH Aachen University, Aachen, Germany*
[b] *Max-Planck-Institut für Eisenforschung GmbH, Max-Planck-Straße 1, Düsseldorf, Germany*
[c] *Chair of Corrosion and Corrosion Protection, RWTH Aachen University, Aachen, Germany*
[d] *Department of Metallurgical and Materials Engineering, UET, Lahore, Pakistan*
[e] *Institute of Metal Forming, RWTH Aachen University, Aachen, Germany*

ARTICLE INFO

Keywords:
Mg-Al-Ca alloys
Solid solution Mg-Al-Ca
Laves phases
Metallography
EBSD
Micromechanical testing
Corrosion testing

ABSTRACT

The Mg-Al-Ca system has been shown to be a promising alloy system since it combines the low density of Mg with a high creep resistance at high alloying contents and a high ductility for dilute alloys, while simultaneously avoiding the requirement of alloying with costly rare earth elements. Nevertheless, the adequate preparation of the alloy system for subsequent microstructural, mechanical, electrochemical and defect analysis is challenging. Therefore, within this publication, we present and apply methods for the structural, mechanical, electrochemical and defect analysis with a focus on the corresponding required metallographic preparation methods in order to support research on the alloy system.

1. Introduction

The increasing requirement to improve fuel efficiency in automotive and aerospace applications leads to a shift in used materials towards light-weight alloys. A suitable candidate for light-weight applications is Mg, which is frequently alloyed with Al. However, there are several shortcomings of these alloys: the wrought alloys with low alloying content suffer from low formability due to the prevalence of basal slip and many successful alloying concepts are still based on additional rare earth elements; the cast alloys, which may contain higher alloying contents to include reinforcing intermetallic phases are still limited in their application at higher temperatures as their strength and creep resistance are reduced at elevated temperatures ($T > 150\ ^\circ\mathrm{C}$) due to the instability of the commonly precipitated $Mg_{17}Al_{12}$ phase [1,2].

A recent approach in both types of alloys to overcome these difficulties is the addition of small amounts of Ca to the Mg-Al alloys. This leads to an increase in ductility in the solid solution Mg-Al-Ca alloys and the formation of an intermetallic skeleton within the Mg matrix of alloys with Al and Ca above the solubility limit. Such in-situ composites of metallic matrix and intermetallic reinforcement are reported to possess improved creep properties [1,3–5].

If the Mg-matrix is alloyed with only small amounts of Ca and Al (e.g. 1 wt.-% Al and 0.1 wt.-% Ca), the strength and formability of the Mg-solid solution is increased. These improved mechanical properties are reported to stem from the activation of <c + a> slip compared to the basal slip and tensile deformation twinning as activated in pure Mg [6]. According to a correlative transmission electron microscopy and atom probe tomography study by Bian et al. [7], the Al and Ca atoms were found to segregate to basal <a> dislocations and were consequently hindering them in their free motion. Also, in a study by Cihova et al. [8], clusters of Al and Ca atoms have been observed in Mg-Al-Ca-Mn alloys by APT (atom probe tomography) analysis. However, the authors could not assign these clusters to certain defects. Despite recent efforts to gain a deeper understanding of the mechanisms enhancing plasticity in the Mg-Ca-Al and Mg-Ca-Zn solid solutions, much remains unknown such as the effects of solutes on the nucleation of defects, the competition

---

[*] Corresponding author.
E-mail address: andre@imm.rwth-aachen.de (D. Andre).

[1] Current address: Laboratory for Mechanics of Materials and Nanostructures, EMPA – Swiss Federal Institute for Materials Science and Technology, 3603, Thun, Switzerland.

https://doi.org/10.1016/j.matchar.2022.112187
Received 6 April 2022; Received in revised form 28 July 2022; Accepted 31 July 2022

between the different slip systems and twinning and the underlying interactions of the solutes with partial dislocations and the enclosed stacking faults or the effect of the solutes on the cross-slip behaviour from the basal plane as well as the mobility of grain boundaries during recrystallization and grain growth [9–11].

Higher alloying contents lead to the precipitation of an intermetallic skeleton consisting of different Laves phases, namely the C14 $CaMg_2$, C15 $CaAl_2$ and C36 $Ca(Mg,Al)_2$, which can be adjusted in their volume fraction, morphology and type by an adjustment of the Ca/Al ratio and the solidification rate [12–16]. In principle, a continuous intermetallic skeleton improves creep resistance but limits ductility. In tensile and creep tests at 170 °C, several co-deformation and damage mechanisms have been observed, including cracking of the Laves phases, local plastic co-deformation via dislocation slip and interfacial sliding [17]. Although recent work proposes a possible mechanism of co-deformation between the α-Mg matrix and the $Ca(Mg,Al)_2$ Laves phase in Mg-Al-Ca alloys [18], there are still further open questions, such as the effect of different orientation relationships, type of Laves phases and temperature on the mechanisms of co-deformation. Recently, Guénolé et al. [17] showed by means of atomistic simulations that the orientation relationship and temperature significantly influences the transfer of plasticity across α-Mg/$CaMg_2$ Laves phases. However, so far, these results remain only partially experimentally validated [18]. Furthermore, Mg-Al-Ca alloys have already been studied extensively regarding improved corrosion properties. Especially, secondary phases lead to micro galvanic coupling and the formation of an interconnected network at high alloy content [19–23]. However, there is still a lack in understanding the influence of small alloying contents such as in solid solutions and the interdependency of additional alloying elements with respect to the corrosion mechanism [24]. Due to their two-phase structure with intrinsically different mechanical and corrosion properties, the metallographic preparation of these alloys often proves challenging, but is a necessary pre-requisite for studying deformation and also corrosion mechanisms in these two-phase alloys. Here, we therefore describe successful preparation methods in detail.

In addition to the deformation and corrosion behaviour of the above-mentioned Mg-Al-Ca solid solutions and composites, the mechanisms of plasticity and selective dealloying during corrosion [25] of the Laves phases themselves also remain to be unravelled. These phases form a class of intermetallic compounds combining an AB_2 stoichiometry with a topologically close-packed structure. They exist in different structural types, namely, the hexagonal C14 type, which is represented by e.g. the above-mentioned $CaMg_2$, the cubic C15 structure in e.g. $CaAl_2$ and the hexagonal $Ca(Mg,Al)_2$ C36 structure [26]. Since Laves phases generally combine a high hardness with a high brittleness, the metallographic preparation of these phases differs from that of the much softer alloys and comes with its own challenges. Therefore, a further focus of this study lies on the metallographic preparation of the Laves phases.

In summary, the ternary system Mg-Al-Ca is of high relevance for future applications as the basis of promising alloy systems. However, research on the resulting alloys is often impeded by the need to prepare the materials for detailed characterisation, which is not always straightforward and varies depending on the intended analysis to be performed. The successful preparation of Mg-based alloys remains challenging not only due to its high softness and quick oxidation, but also, in case of the composites due to the mechanical contrast and different response to electrolytes of the constituent phases.

Here, we therefore present different metallographic preparation methods which can be used across the ternary system from solid solution Mg-Al-Ca alloys over metallic-intermetallic composites to bulk intermetallic Laves phases $Ca(Mg,Al)_2$.

There are three main purposes for which we compare and apply these methods, namely (1) structural analysis including phase imaging and electron backscatter diffraction (EBSD), which requires a particularly high surface quality, (2) mechanical testing with often similar target surfaces as EBSD but the need for a flat surface, and (3) electrochemical investigations to assess corrosion mechanisms including their relation to specific microstructural elements, such as precipitates, grain or phase boundaries. We hope that the methods and discussions of pitfalls and achievable results will support research efforts in other groups starting out on these materials or transitioning to different methods of their analysis.

2. Experimental

The materials metallographically prepared and investigated are all from the Mg-Al-Ca system, namely a solid solution Mg-Al-Ca alloy, a Mg composite consisting of a Mg matrix and an intra- and intergranular eutectic intermetallic skeleton and the $CaMg_2$ and $CaAl_2$ - $CaAl_4$ intermetallic phases. The following sections are subdivided into these different material groups in order to describe their preparation routines in detail and discuss potential experimental applications. The solid solution, as well as the composite Mg-Al-Ca alloys were synthesised by induction melting charges of about 800 g of raw elements in a steel crucible under an Argon atmosphere of 10 bar in order to limit oxidation and evaporation. The alloys were cast into rectangular copper moulds with an internal cross section of 30×60 mm^2. The composite material was investigated in the as-cast state [12] whereas the solid solution material was heated to 450 °C for 30 min and subsequently hot rolled to about 50% reduction in thickness (reduction per pass about 10%, reheating between each pass, reheating and water quenching after the final pass). The rolling temperature for the solid solution alloys was chosen due to preliminary work, where the temperature was found to result in superior mechanical properties as well as a homogeneous microstructure [6].

Synthesis of the intermetallic phases is detailed elsewhere [27,28], only the $CaAl_2$ material was additionally annealed at 600 °C for 24 h under Argon atmosphere to improve chemical homogeneity and reduce residual stresses (cooled within the furnace to room temperature).

2.1. Solid solution Mg-Al-Ca alloys

In the following, two preparation methods for solid solution Mg-Al-Ca specimens will be described and applied to a Mg-1Al-0.1Ca alloy. Both methods allow successful preparation of the soft specimens which are prone to scratches while simultaneously avoiding the formation of twins. However, in order to avoid any chemical modification of the specimen surface, no electropolishing step was performed if the specimens were analysed for corrosion properties.

In method I, which is particularly suitable for subsequent EBSD measurements and slip trace analyses (Fig. 1), the specimen was manually ground and polished. Grinding was performed using SiC abrasive paper with a grit size of #2000 and #4000 in conjunction with ethanol as a lubricant in order to reduce surface oxidation. The corresponding grinding times are given in Fig. 1. The polishing procedure of method I was further performed with 6 μm diamond paste on MD-DAC cloth by Struers GmbH for 20 min, while rotating the sample concentrically against the rotation direction of the cloth. The subsequent 3 μm, 1 μm and 0.25 μm steps were performed on MD-DUR cloth by Struers GmbH in the same manner as on MD-DAC, again for approximately 20 min. The lubricant for all polishing steps consisted of a mixture of 94% isopropanol and 6% polyethylene glycol in order to minimize oxidation. Furthermore, ultrasonic cleaning in ethanol was repeated after each polishing step.

In a last step, the electrolyte AC2 by Struers GmbH was cooled down to −20 to −30 °C. As the electrolyte decomposes quickly, first a beaker with ethanol was cooled down with dry ice to −30 °C. Then the beaker with freshly mixed AC2 was placed in the ethanol to be cooled down quickly. For the electropolishing procedure, the specimen was placed in the AC2 solution and the electropolishing was started immediately for 30 s. After the process, the sample was removed from the electrolyte and cleaned with ethanol. Insufficiently slow handling of the sample might

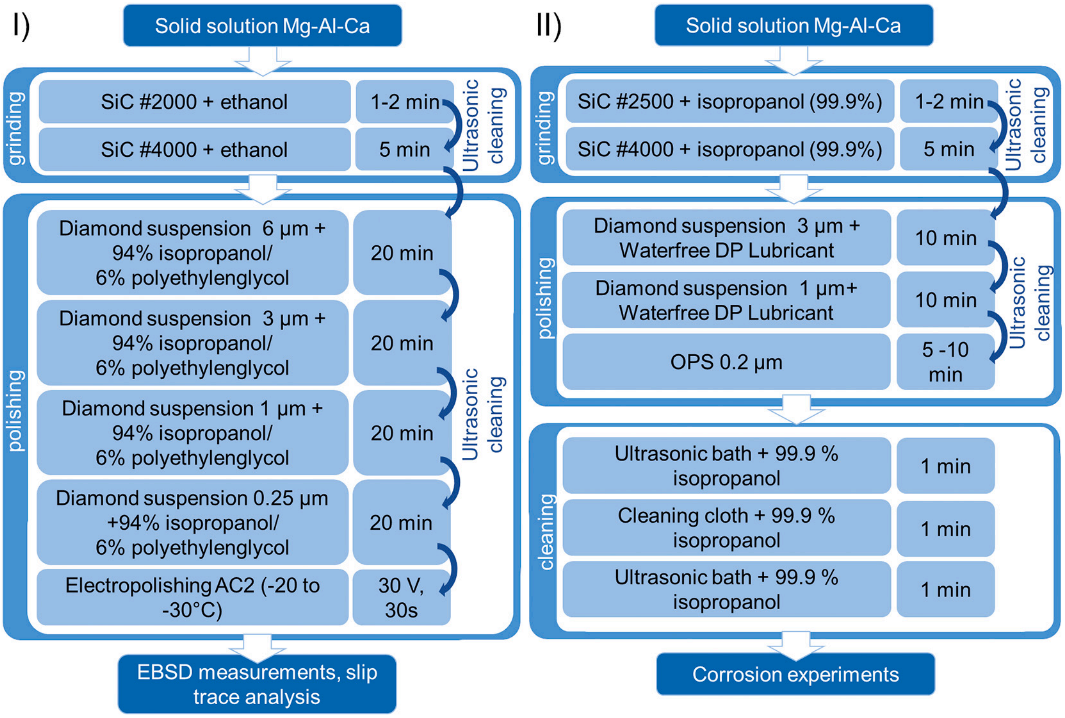

Fig. 1. Metallographic preparation procedure for the solid solution Mg-Al-Ca alloys: I) EBSD measurements and slip trace analysis, II) corrosion experiments.

result in an inhomogeneous surface quality of the sample or the start of etching, which can negatively affect further analyses. The electropolishing parameters fitting for the Mg-Al-Ca alloy was found to be 30 V for 30 s. Thereafter, the specimen surface was almost scratch free and planar.

The usage of electropolishing in method I has the advantage of a better indexing rate for EBSD measurements also post deformation. However, if the specimen will be subjected to corrosion experiments, electropolishing is not the method of choice since it might lead to potential chemical modifications of the surface. Therefore, for corrosion experiments, preparation procedure II was applied.

In preparation procedure II (Fig. 1), a steel sample holder was used to ensure plane parallelism without embedding of the sample (Fig. 2). The holder applied a constant load of 0.015 MPa on the sample. During the grinding processes, SiC abrasive paper with a grit size of #2500 and #4000 was used together with isopropanol (99.9%) as a lubricant. The corresponding grinding times are again given in Fig. 1. Between all grinding steps, the specimen was cleaned in an ultrasonic bath in 99.9% isopropanol for approximately one minute.

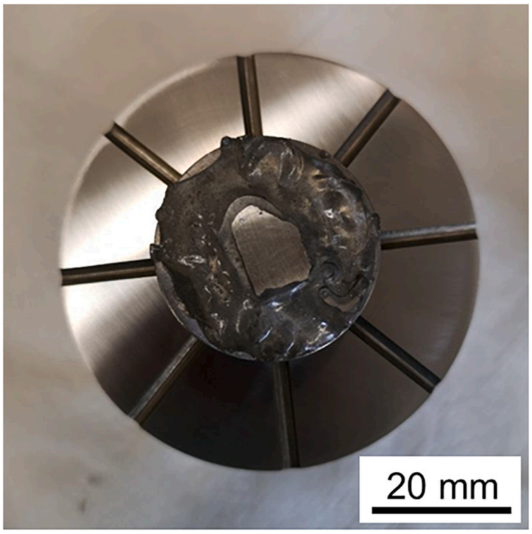

Fig. 2. Specimen attached to a steel sample holder using Crystalbond adhesive.

After the last grinding step, the sample was directly polished with 3 µm and 1 µm diamond slurry on MD-DUR cloths rotating the sample concentrically against the rotation direction of the cloth. Additionally, the waterfree DP Lubricant Blue by Struers GmbH was used as a coolant. The final polishing step used water free 0.2 µm fused silica suspension on MD-CHEM cloth by Struers GmbH. For this, approximately 5 mL of the OP-S suspension was spread on the polishing plate and distributed on the cloth with the holder. The specimen was then rotated concentrically against the rotation direction of the cloth for two minutes. Immediately after polishing, the specimen was cleaned with isopropanol and a further cleaning step in ultrasonic bath in isopropanol for one minute was performed. The last cleaning step consisted of polishing the specimen on a MD-CHEM cloth wetted with isopropanol suspension followed by an ultrasonic bath in isopropanol for one minute.

2.2. *Mg-Al-Ca composites*

The specimen preparation methods given below are suitable for nearly all different compositions of Mg-Al-Ca alloys at least till the point where the total alloying elements (Al + Ca wt.-%.) content stays below 8 wt.-%. The preparation might also work for higher alloying contents, but has not been evaluated by the authors yet. Here, a Mg-Al-Ca-alloy in the as-cast condition with the nominal chemical composition listed in Table 1 was selected in order to exemplify a suitable preparation routine for Mg-composite alloys.

Table 1
Chemical composition of the investigated magnesium composite.

Al [wt.-%]	Ca [wt.-%]	Ca/Al	Mg [wt.-%]	Sec. Phases
5.5	1.7	0.3	92.8	$Ca(Mg,Al)_2$

For the metallographic preparation of this alloy, a square shaped sample with a surface area of approximately 1 cm^2 was wet cut using a corundum blade. In the following, two metallographic preparation methods will be introduced (Fig. 3). Method III is well suited for EBSD measurements and is therefore suited for a surface/slip line analysis after macro- and micromechanical testing whereas method IV allows to perform corrosion experiments (e.g. potentiodynamic polarization, linear polarization and electrochemical impedance spectroscopy). Similar to the preparation of the solid solution Mg-Al-Ca sample, electropolishing should be avoided for the magnesium composites if corrosion experiments were to be conducted after preparation due to potential chemical modifications induced in the specimen.

For method III, the grinding process involved manual grinding on SiC abrasive paper with a grit size #2000 and #4000 using ethanol as a lubricant. The following polishing procedure was performed using a diamond suspension of 3 μm and 1 μm together with 99% ethanol and 1% PEG 400 for ten minutes each. In order to further improve the surface quality, electropolishing with AC2 at ∼ − 20 °C was performed at 15 V for 60 s followed by polishing using an OP-U suspension by Struers GmbH (colloidal suspension of SiO_2 of 0.04 μm) for one minute. Afterwards, the specimen was cleaned on a polishing cloth with isopropanol for three minutes and a last cleaning step in isopropanol in an ultrasonic bath for two minutes.

For method IV, the specimen was hand ground using a SiC abrasive paper with a grit size of #500 and #1000 and water as a lubricant for 1–2 min. During the next grinding step at a grit size of #4000, the lubricant was changed to 99.9% isopropanol. In a further step, the specimen was hand-polished with waterfree diamond suspension of 3 μm and 1 μm using a waterfree DP Lubricant Blue by Struers GmbH on a MD-Dur cloth. The final polishing step was conducted using a waterfree fumed silica suspension of 0.2 μm on a MD-Chem cloth by Struers GmbH. Each polishing step was carried out for approximately five minutes. The specimen was further subjected to a cleaning process with 99.9% isopropanol in an ultrasonic bath for two minutes after each polishing step. The specimen was then cleaned for approximately four minutes on the rotating and cleaned polishing cloth combined with a frequent wetting using isopropanol which was followed by two minutes in isopropanol in an ultrasonic bath.

2.3. Laves phases of Mg-Al-Ca alloys

Specimens of the intermetallic C14-$CaMg_2$ and the C15-$CaAl_2$ Laves phase were analysed in the as-cast condition. Both samples were cut into small pieces using electric discharge machining and attached to a sample holder using CrystalbondTM adhesive, as it was also performed for the solid solution Mg-Al-Ca alloys (Fig. 2). Mechanical grinding for both specimens was performed using a grid size of #800, #1000, #2400 and #4000 on a SiC abrasive paper with water as a lubricant. Each grinding step was finished once the grinding grooves of the former grinding step disappeared. The approximate grinding times are given in Fig. 4. For the polishing procedure, 3 μm diamond DP-Suspension, 1 μm diamond DP-Suspension and 0.25 μm DP-Suspension by Struers GmbH were used with ethanol as lubricant agent for the $CaMg_2$ phase, whereas for the $CaAl_2$ phase, the above-mentioned suspensions were used alongside the diamond solution as a lubricating agent. Similar results could be obtained by using another solution containing 96% ethanol and 4% polyethylene glycol. A further deviation in the polishing procedure occurred for the $CaMg_2$ phase, which was electropolished. Electropolishing was avoided for the $CaAl_2$ phase due to an undesired resulting topography but could be successfully applied to the $CaMg_2$ phase. Here, electropolishing was performed using AC2 for 20 s at 5 V followed by a cleaning step of 5 s, whereas the $CaAl_2$ specimen was polished using an OP-U 0.04 μm colloidal silica suspension. This last polishing step was subdivided in a 20 s polishing step with OP-U suspension on a DUR cloth and an immediately following polishing step with water and dishwashing liquid.

The entire metallographic preparation procedure pursued for the intermetallics is given in Fig. 4. The specimens were afterwards suitable for EBSD measurements as well as for micromechanical testing and electron channelling contrast imaging (ECCI) measurements.

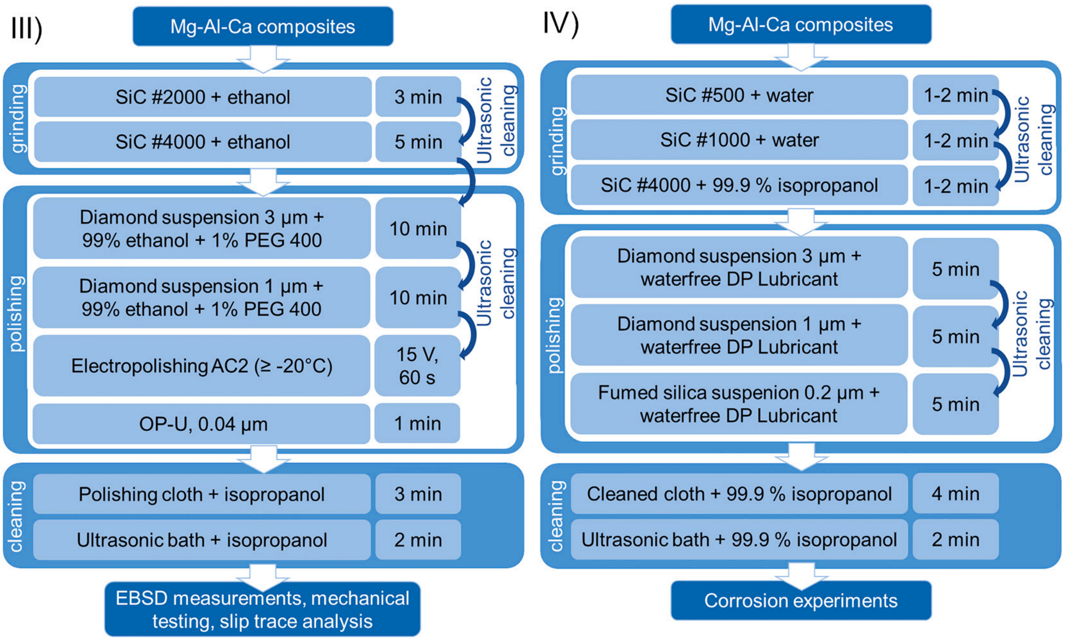

Fig. 3. Metallographic preparation procedure for the Mg-Al-Ca composites: III) this method is well suited for EBSD measurements, macro- and micromechanical testing and slip trace analysis, whereas method IV) is well suited for corrosion experiments.

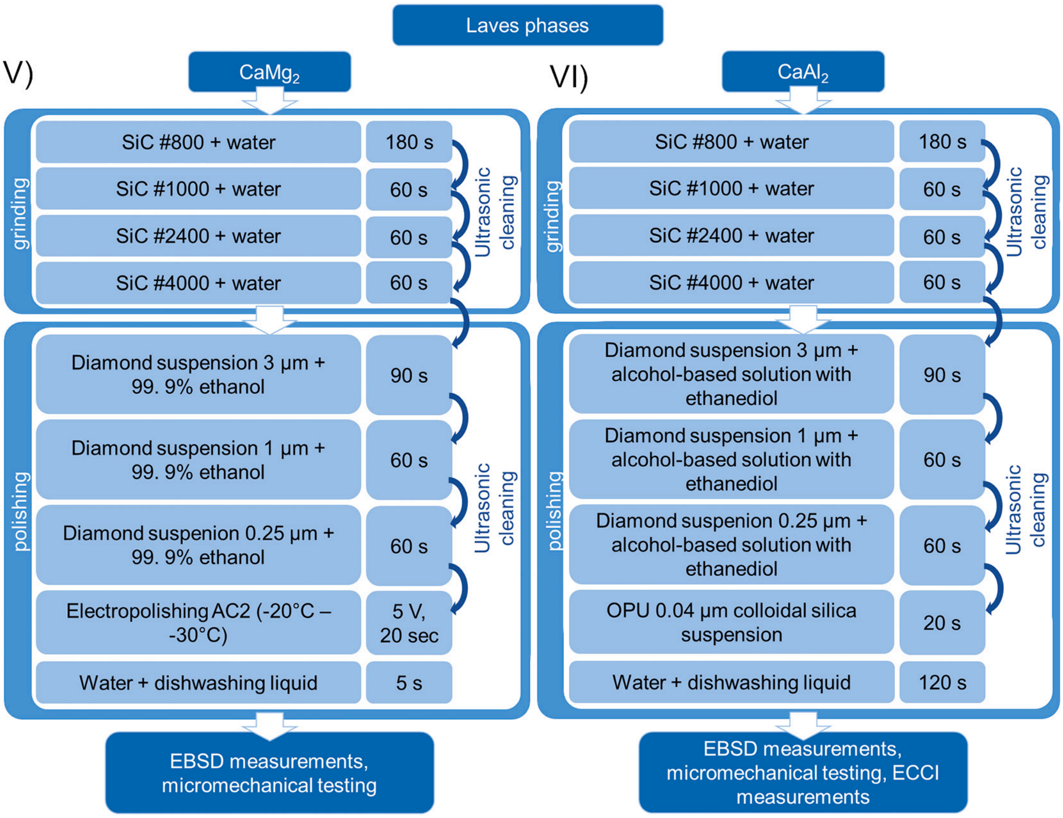

Fig. 4. Metallographic preparation procedure for Laves phases: V: the $CaMg_2$ phase and VI: the $CaAl_2$ intermetallics.

3. Results and discussion

3.1. Solid solution Mg-Al-Ca alloys

The first preparation method described for the solid solution Mg-Al-Ca alloys, which underwent a rolling procedure after casting to break the cast structure and reach a homogeneous microstructure, is well suited for EBSD measurements and following surface analysis such as slip traces after plastic deformation and leads to a high indexing rate which can still be achieved after several months when stored in vacuum, whereas the second method is well suited for corrosion experiments due to the missing electropolishing step preventing from strong surface-near dealloying effects.

The image quality (IQ) map (Fig. 5 a)), which provides a measure of the pattern quality and, thus, can be used to qualitatively estimate the strain distribution within the material gives further insights on the preparation quality. As evident from Fig. 5 a), the IQ map of the Mg-1Al-0.1Ca alloy prepared using method I reveals a homogenous contrast for all grains, representing a homogeneous pattern quality and therefore also a homogeneous strain distribution and topography within the grains [29]. The dark spots in Fig. 5 a) correspond to oxides. The corresponding confidence index (CI) map reveals an average indexing rate above 0.1 (Fig. 5 b)). The high indexing rate corresponds to a correct indexing of 95% of the Kikuchi pattern [30], which is also due to the high signal-to-noise ratio within the measured Kikuchi patterns (Fig. 5 c)). The high indexing rate did not significantly deteriorate approximately half a year after the preparation if stored in a desiccator under vacuum. These factors all indicate the suitability of the performed preparation routine for the given alloy system. All given EBSD maps within this publication correspond to raw data and did not undergo any clean-up procedure.

The specimen was further subjected to macroscopic compression tests (Zwick testing machine) at a strain rate of 10^{-3} s^{-1} until a maximum strain of ~3% at ambient temperature and afterwards imaged

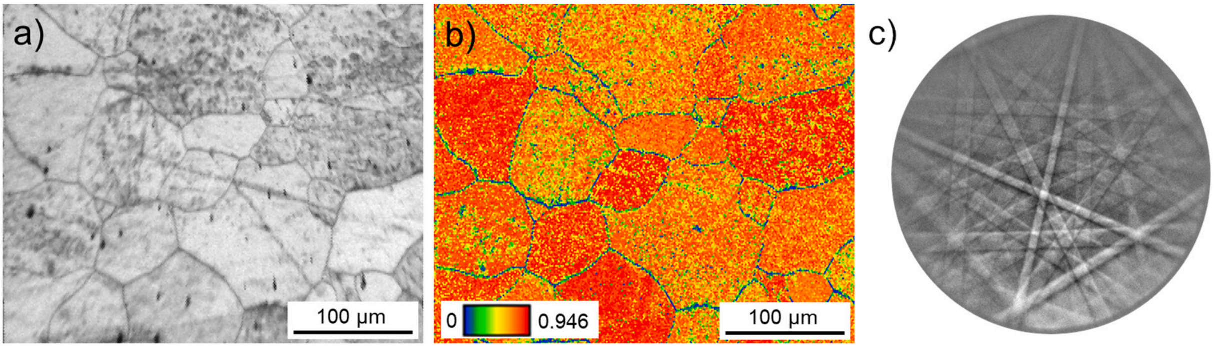

Fig. 5. a) IQ map of the as-cast Mg-1Al-0.1Ca solid solution sample, b) the CI map generated from EBSD data on the same microstructural region and c) representative Kikuchi pattern. (For interpretation of the references to colour in this figure legend, the reader is referred to the web version of this article.)

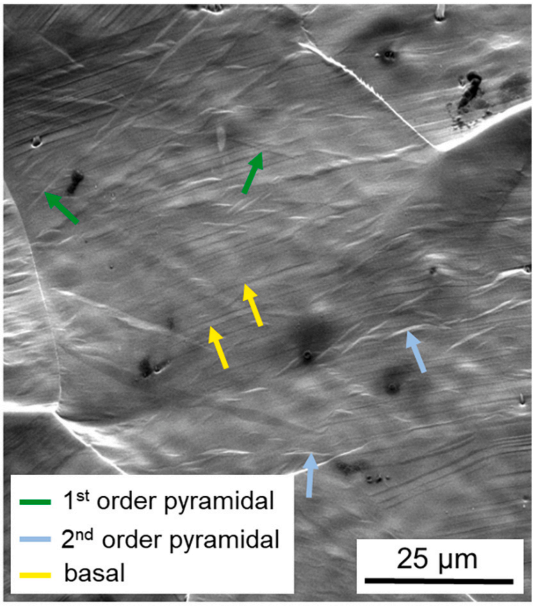

Fig. 6. SE-image of the compressed Mg-1Al-0.1Ca alloy revealing distinct slip traces on the specimen surface. (For interpretation of the references to colour in this figure legend, the reader is referred to the web version of this article.)

in a scanning electron microscope (SEM) (Helios Nanolab 600i, FEI) using an acceleration voltage of 15 kV. The subsequent surface analysis allowed a correlation between the visible slip traces on the specimen surface and possible slip planes using EBSD orientation data. In the image given in Fig. 6, the slip traces marked in yellow correspond to basal traces and can be distinguished from 1st order pyramidal (marked in green) and 2nd order pyramidal slip planes (marked in blue).

Secondary electron (SE) images taken at an acceleration voltage of 10 kV using a Supra 55VP, Carl Zeiss AG of the specimen surface of the Mg-1Al-0.1 alloy after metallographic preparation according to method II and subsequent surface corrosion in pH = 8.0 \pm 0.1 for 30 min are given in Fig. 7 a-b). An increase in OPS polishing time from a) 3 min to b) 5–10 min reduced the density of residual artefacts and led to a more uniform dissolution but did not affect the appearance of corrosion groves. These (Fig. 7 a-b)) are not related to polishing artefacts but rather correlate to material inherent defects, such as grain boundaries.

The above-described preparation methods are suitable for the investigated material system since slip traces on the specimen surface are successfully identified and the applied preparation method exhibits straightforward results on studying the influence of corrosion on, e.g. selective dissolution at grain boundaries.

3.2. *Mg-Al-Ca composites*

The Mg-4.55Al-2.91Ca alloy, which was metallographically prepared according to preparation routine III underwent an EBSD measurement (FEI Helios Nanolab 600i) at an accelerating voltage of 15 kV and a step size of 0.2 μm. The resulting inverse pole figure (IPF) map, Kikuchi patterns, IQ map and CI map are given in Fig. 8. The IPF map (Fig. 8 a)) visualises the crystallographic orientation of the α-Mg matrix. However, care should be taken in determining the orientation relationship existing between the α-Mg matrix and the C36-Ca(Mg,Al)$_2$ Laves phase. A sufficiently good Kikuchi pattern for the C36-Ca(Mg,Al)$_2$ Laves phase (Fig. 8 b)) is observable only from a small fraction of the total intermetallic phases. The IQ map has a homogeneous grayscale distribution within each α-Mg grain indicating a good pattern quality, while a darker colour along the phase boundaries indicates a rather poor pattern quality of the C36-Ca(Mg,Al)$_2$ Laves phase. This observation is based on the low indexed C36-Ca(Mg,Al)$_2$ Laves phase struts in the Mg-Al-Ca ternary alloys due to their small sizes ($\sim \leq 1$ μm). The C36 Laves phase patterns overlap with the pattern from the α-Mg matrix, thus leading to a significant difficulty in their indexing. This is further evident from the CI map (Fig. 8 d)), where the intermetallic skeleton reaches a small confidence index and is thus represented by blue. All other microstructural regions exhibit a CI of above 0.1, which represents the threshold of a 95% correct indexing of the Kikuchi bands [30]. Nevertheless, one single intra- or intermetallic C36-Ca(Mg,Al)$_2$ Laves phase strut appears to be one grain of the C36-Ca(Mg,Al)$_2$ Laves phase, as indicated by the white arrows in Fig. 8 a). Therefore, the used preparation routine is suitable for obtaining good quality diffraction patterns for this material system.

The SE-images of an indent made in a Mg-3.7Al-3.8Ca alloy up to a load of 500 mN at ambient temperature highlight the advantages of the metallography scheme III with regard to the visibility of surface features, see Fig. 9 a-b). These images were taken at an accelerating voltage of 10 kV using a Zeiss LEO1530 SEM. As can be seen in Fig. 9, the

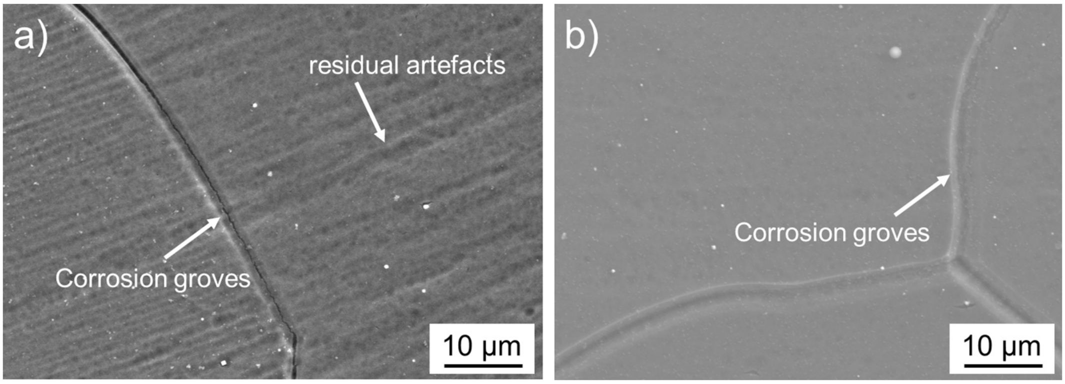

Fig. 7. SE-images of the Mg-1Al-0.1 alloy after metallographic preparation according to method II reveal varying amounts of selective dissolution (residual artefacts) depending on the applied OPS polishing time: a) 3 min and b) 5–10 min. The corrosion groves are independent of the preparation.

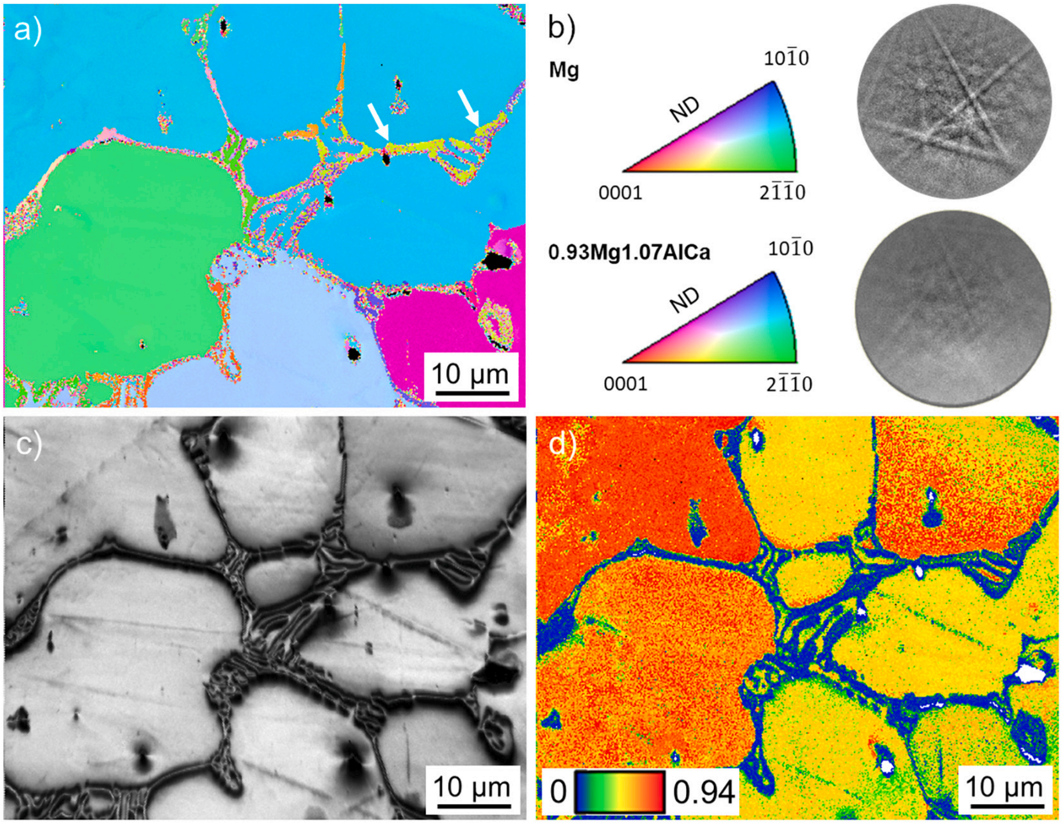

Fig. 8. a) IPF map of the α-Mg and C36 (0.93Mg1.07AlCa) Laves phase in an as-cast Mg-4.55Al-2.91Ca alloy, with struts of the C36 phase having the same orientation, as indicated by white arrows, b) IPF legends and Kikuchi patterns for α-Mg and C36 Laves phase, c) IQ map of the same region and d) CI map generated from EBSD data on the same microstructural region. (For interpretation of the references to colour in this figure legend, the reader is referred to the web version of this article.)

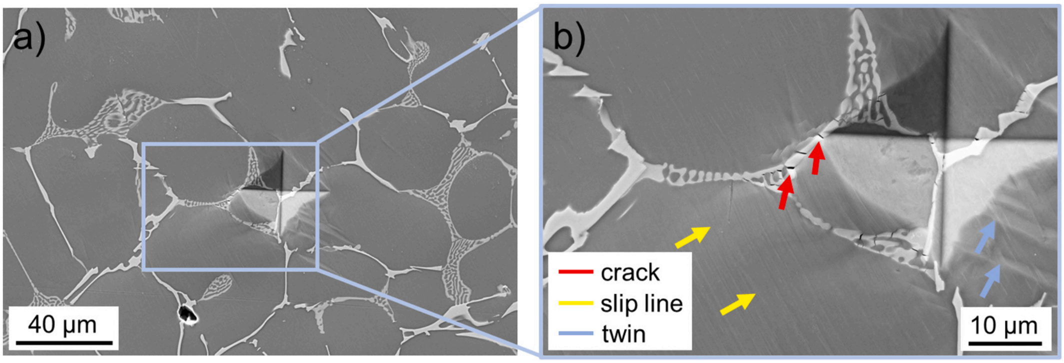

Fig. 9. a) SE-image of the indent performed at room temperature on as-cast Mg-3.7Al-3.8Ca alloy and b) magnified image of the region bounded by blue rectangle in (a). (For interpretation of the references to colour in this figure legend, the reader is referred to the web version of this article.)

deformed area around the indent reveals deformation features in the vicinity of the indent. In this case, the deformation features represent cracks in the Laves phase (highlighted in red) as well as basal slip traces (highlighted in yellow) and twins in the Mg phase (highlighted in blue). Therefore, this polishing scheme is also suitable to analyse deformation mechanisms on the specimen surface.

After preparation procedure IV, the Mg composite specimen was free from scratches and exhibited no corrosive pre-damage, as evident from the SE-image in Fig. 10 a). The specimen topography was further analysed using atomic force microscopy (AFM) (Dimension Icon XR, Bruker Corporation, Massachusetts, USA) in the tapping mode equipped with a PFQNE-silicon nitride tip (Bruker Corporation, Massachusetts, USA). The resulting topography scan in Fig. 10 b) reveals, that the comparatively softer Mg matrix was subjected to higher material removal during the preparation routine compared to the hard Laves phase. The height difference was <50 nm, but it might be relevant for any subsequent material analysis and evaluation methods.

The specimen further underwent an electrochemical measurement on the free corrosion potential for an immersion time of 30 min in a sodium borate buffer (pH = 8 \pm 0.1). The corresponding backscattered electron (BSE) image of the specimen surface after the electrochemical measurement is given in Fig. 11.

The Mg-matrix, at a distance of 1–2 µm from the interface to the secondary phases, exhibits homogeneously distributed corrosion, which is assumed to arise as a consequence of a uniform corrosion process of the Mg-matrix under the immersion conditions. Therefore, the local

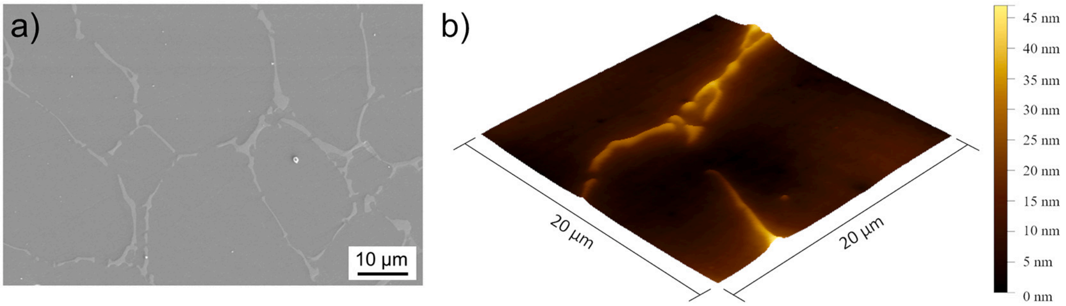

Fig. 10. a) SE-image of the metallographically prepared specimen surface of the Mg-composite at an acceleration voltage of 3 kV of and b) AFM topography scan of Mg-composite revealing a height difference of <50 nm between the intermetallic skeleton. (For interpretation of the references to colour in this figure legend, the reader is referred to the web version of this article.)

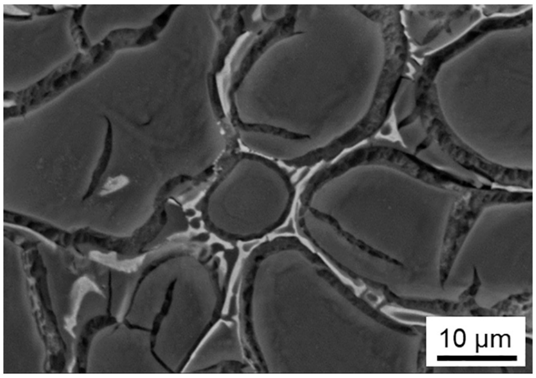

Fig. 11. BSE-image at an acceleration voltage of 10 kV of the Mg-composite specimen surface after electrochemical measurement at the free corrosion potential for 30 *minutes* in a borate buffer electrolyte.

corrosion reactions seem to be unaffected by preparation-related artefacts and represents the material's inherent electrochemical corrosion properties. The different morphology of the corrosion products near the interface between the Mg-matrix and the secondary phases, might arise due to the formation of microgalvanic elements.

3.3. Laves phases of Mg-Al-Ca alloys

The C14-$CaMg_2$ Laves phase studied consists of 68.7 ± 0.5 at.-% Mg, corresponding to a deviation of 2 at.-% from the ideal stoichiometric composition according to energy dispersive X-Ray (EDX) analysis. Nanomechanical testing could be conducted on the metallographically prepared specimen surface (method V) and allowed to perform micropillar compression experiments [28]. The example shown in Fig. 12 a) corresponds to an SE-image taken at an acceleration voltage of 10 kV.

Nanomechanical tests could also be conducted after the metallographic preparation of the C15-$CaAl_2$ phase according to method VI. These allowed to identify e.g. slip traces in the vicinity of the indent (Fig. 12 b)), which are taken at an acceleration voltage of 5 kV.

The C15-$CaAl_2$ phase was analysed for its chemical composition using electron probe microanalysis (EPMA) and EDX measurements on the metallographically prepared specimen. The EPMA analysis was performed at an acceleration voltage of 10 kV and the resulting chemical composition was averaged over 12 areas of interest per phase. The analysis reveals the existence of the $CaAl_2$ phase as well as the $CaAl_4$ phase in the microstructure (Table 2).

The subsequent EDX analysis, which was performed at an acceleration voltage of 10 kV, revealed a dual-phase structure consisting of a $CaAl_2$ matrix and a $CaAl_4$ skeleton, Fig. 13.

The phase distribution is also evident from the BSE-image in Fig. 14, taken at 5 kV. Here, the heavier $CaAl_2$ matrix phase appears brighter, whereas the lighter $CaAl_4$ phase appears in darker grey in the grain boundary regions.

EBSD measurements were conducted in a Zeiss Auriga SEM at 20 kV and a step size of 0.3 μm and resulted in a scratch free surface with no

Table 2
EPMA analysis $CaAl_2$-$CaAl_4$ sample composition after annealing of the intermetallic.

Phases	Al [at.-%]	Ca [at.-%]
$CaAl_2$	65.86 ± 0.15	34.14 ± 0.15
$CaAl_4$	79.03 ± 0.35	20.97 ± 0.35

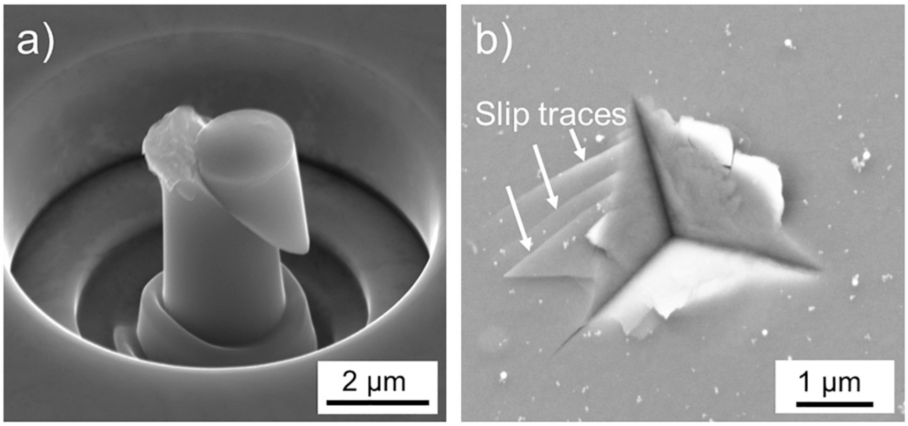

Fig. 12. SE-image of a) a plastically deformed micropillar of the $CaMg_2$ C14 phase and b) a nanoindent with slip traces in its vicinity of the $CaAl_2$ C15 phase.

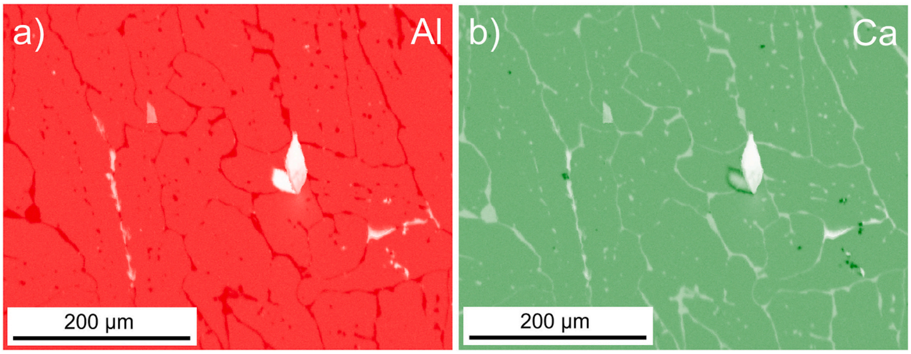

Fig. 13. SEM-EDX mapping of the intermetallic specimen with a) an elemental map of Al and b) an elemental map of Ca. Both maps reveal a skeleton structure consisting of $CaAl_2$ and a $CaAl_4$ skeleton.

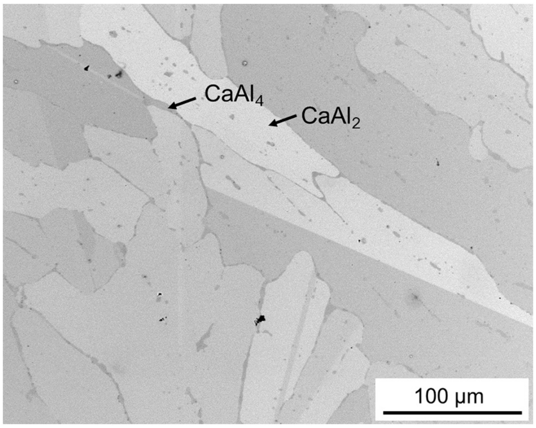

Fig. 14. BSE-image of the dual-phase $CaAl_2$-$CaAl_4$ intermetallic specimen, with the darker phase being the $CaAl_4$ phase and the brighter phase being the $CaAl_2$ phase.

strain inhomogeneities, as evident from the IQ map in Fig. 15 a). The CI map (Fig. 15 b)) reveals a high CI of above 0.1 for the entire microstructural region, except for the intermetallic $CaAl_4$ phase, which is represented in blue. The high CI of the C15 $CaAl_2$ phase stems from the good recognition of the band structure in the Kikuchi pattern, as given in Fig. 15 c). Due to a small deviation of the crystal structure of the $CaAl_4$ phase from its ideal structure in conjunction with its small volume fraction, resulting in a pattern overlap, it was not possible to refine its crystal structure. Consequently, only low CI values were obtained for the $CaAl_4$ phase.

The high surface quality of the specimen using the described preparation route VI, further allowed electron channelling contrast imaging (ECCI) measurements. Using ECCI, the underlying defects in the microstructure close to the surface of the bulk specimen could be investigated by a slight tilting of the specimen so that a specific grain fulfilled Bragg's Law. Since lattice defects such as dislocations disturb the electron channelling, a brighter contrast is obtained as in the image [31–33]. An example of the gained dislocation substructure close to a second phase particle is given in Fig. 16 and taken at 30 kV and a probe current of 2 nA.

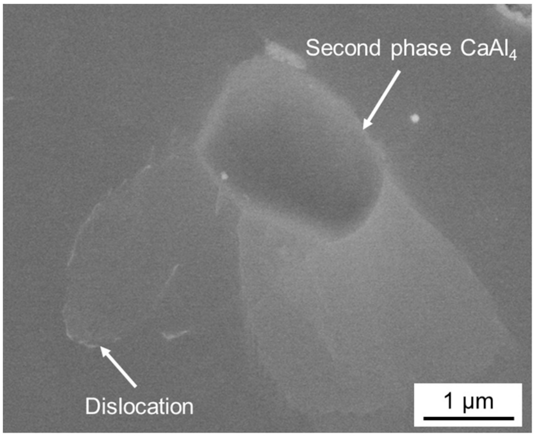

Fig. 16. ECC image of the dislocations underneath the specimen surface close to the second phase in the C15-$CaAl_2$ phase.

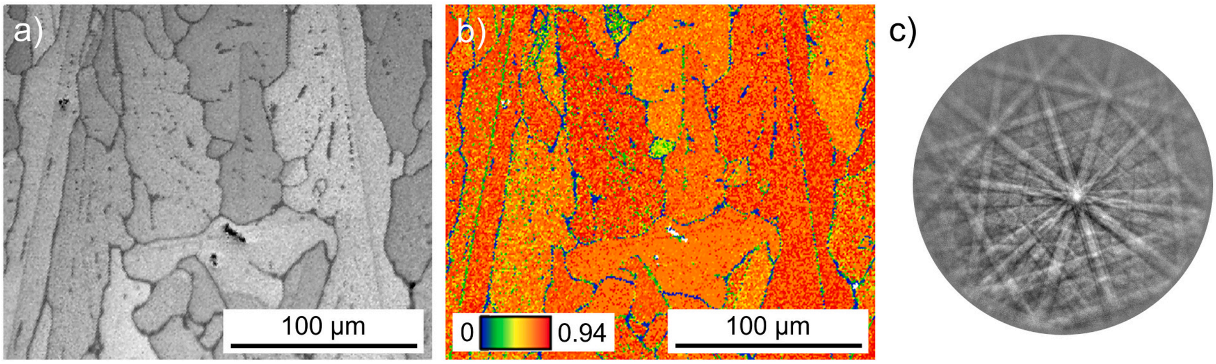

Fig. 15. a) IQ map of the as-cast $CaAl_2$-$CaAl_4$ intermetallic, b) CI map of the same microstructural region, generated from EBSD data and c) Kikuchi pattern obtained from the $CaAl_2$ phase. (For interpretation of the references to colour in this figure legend, the reader is referred to the web version of this article.)

4. Conclusion

Several methods for the metallographic preparation of the Mg-Al-Ca alloy system have been presented and can be applied on solid solution Mg-Al-Ca alloys, Mg-Al-Ca composites and intermetallic Laves phases of the Mg-Al-Ca system. The described preparation procedures are suitable for the following characterisation methods: Corrosion experiments, EBSD measurements, macro- and micromechanical testing including a subsequent slip trace analysis and ECCI. For the solid solution Mg-Al-Ca alloy and the Mg-Al-Ca composites, the metallographic preparation included an electropolishing step if EBSD measurements, a slip trace analysis or micromechanical tests were performed afterwards since electropolishing did not only improve the indexing rate for EBSD measurements even after deformation, but also allowed EBSD measurements after longer storage times. However, if corrosion testing followed the preparation, no electropolishing was applied to avoid potential selective dealloying of the surface. In case of the intermetallic phases, the use of electropolishing has to be considered on an individual basis. While electropolishing was successfully applied for $CaMg_2$ for subsequent EBSD measurements and micromechanical testing, the same routine induced an undesired topography if applied to $CaAl_2$.

Declaration of Competing Interest

The authors declare that they have no known competing financial interests or personal relationships that could have appeared to influence the work reported in this paper.

Data availability

Data will be made available on request.

Acknowledgement

The authors gratefully acknowledge the financial support of the Deutsche Forschungsgemeinschaft (DFG) within projects A01, A05, B01, B05, B06, C01, C02, C03 of the Collaborative Research Center (SFB) 1394 “Structural and Chemical Atomic Complexity - from defect phase diagrams to material properties” – project number 409476157 and INST 256/455-1 FUGG. We would like to further acknowledge Patrick Grünewald from the Department of Material Science and Technology at the Saarland University in Saarbrücken (Germany) for the technical support during the AFM measurements. H. Springer wishes to acknowledge financial support from the Heisenberg Program of the Deutsche Forschungsgemeinschaft (SP1666/1).

References

[1] B. Kondori, R. Mahmudi, Effect of Ca additions on the microstructure and creep properties of a cast Mg–Al–Mn magnesium alloy, Mater. Sci. Eng. A 700 (2017) 438–447, https://doi.org/10.1016/j.msea.2017.06.007.

[2] M.O. Pekguleryuz, A.A. Kaya, Creep resistant magnesium alloys for powertrain applications, Adv. Eng. Mater. 5 (12) (2003) 866–878, https://doi.org/10.1002/adem.200300403.

[3] D. Amberger, P. Eisenlohr, M. Göken, Microstructural evolution during creep of Ca-containing AZ91, Mater. Sci. Eng. A 510 (2009) 398–402, https://doi.org/10.1016/j.msea.2008.04.115.

[4] A.A. Luo, B.R. Powell, M.P. Balogh, Creep and microstructure of magnesium-aluminum-calcium based alloys, Metall. Mater. Trans. A 33 (3) (2002) 567–574, https://doi.org/10.1007/s11661-002-0118-1.

[5] Y. Terada, et al., A thousandfold creep strengthening by Ca addition in die-cast AM50 magnesium alloy, Metall. Mater. Trans. A 35 (9) (2004) 3029–3032, https://doi.org/10.1007/s11661-004-0046-3.

[6] S. Sandlöbes, et al., A rare-earth free magnesium alloy with improved intrinsic ductility, Sci. Rep. 7 (1) (2017) 1–8, https://doi.org/10.1038/s41598-017-10384-0.

[7] M. Bian, et al., Bake-hardenable Mg–Al–Zn–Mn–Ca sheet alloy processed by twin-roll casting, Acta Mater. 158 (2018) 278–288, https://doi.org/10.1016/j.actamat.2018.07.057.

[8] M. Cihova, et al., Rational design of a lean magnesium-based alloy with high age-hardening response, Acta Mater. 158 (2018) 214–229, https://doi.org/10.1016/j.actamat.2018.07.054.

[9] I. Basu, et al., Stacking-fault mediated plasticity and strengthening in lean, rare-earth free magnesium alloys, Acta Mater. 211 (2021), 116877, https://doi.org/10.1016/j.actamat.2021.116877.

[10] I. Basu, et al., Segregation-driven exceptional twin-boundary strengthening in lean Mg–Zn–Ca alloys, Acta Mater. (2022), 117746, https://doi.org/10.1016/j.actamat.2022.117746.

[11] H.-S. Jang, D. Seol, B.-J. Lee, A comparative study on grain boundary segregation and solute clustering in Mg-Al-Zn and Mg-Zn-Ca alloys, J. Alloys Compd. 894 (2022), 162539, https://doi.org/10.1016/j.jallcom.2021.162539.

[12] M. Zubair, et al., On the role of laves phases on the mechanical properties of Mg-Al-Ca alloys, Mater. Sci. Eng. A 756 (2019) 272–283, https://doi.org/10.1016/j.msea.2019.04.048.

[13] M. Zubair, et al., Strain heterogeneity and micro-damage nucleation under tensile stresses in an Mg–5Al–3Ca alloy with an intermetallic skeleton, Mater. Sci. Eng. A 767 (2019), 138414, https://doi.org/10.1016/j.msea.2019.138414.

[14] D. Amberger, P. Eisenlohr, M. Göken, On the importance of a connected hard-phase skeleton for the creep resistance of Mg alloys, Acta Mater. 60 (5) (2012) 2277–2289, https://doi.org/10.1016/j.actamat.2012.01.017.

[15] Y. Chai, et al., Role of Al content on the microstructure, texture and mechanical properties of Mg-3.5 Ca based alloys, Mater. Sci. Eng. A 730 (2018) 303–316, https://doi.org/10.1016/j.msea.2018.06.011.

[16] H.A. Elamami, et al., Phase selection and mechanical properties of permanent-mold cast Mg-Al-Ca-Mn alloys and the role of Ca/Al ratio, J. Alloys Compd. 764 (2018) 216–225, https://doi.org/10.1016/j.jallcom.2018.05.309.

[17] J. Guénolé, et al., Exploring the transfer of plasticity across laves phase interfaces in a dual phase magnesium alloy, Mater. Des. 202 (2021), 109572, https://doi.org/10.1016/j.matdes.2021.109572.

[18] M. Zubair, et al., Co-deformation between the metallic matrix and intermetallic phases in a creep-resistant Mg-3.68 Al-3.8 Ca alloy, Mater. Des. 210 (2021), 110113, https://doi.org/10.1016/j.matdes.2021.110113.

[19] S. Manivannan, et al., Corrosion Analysis of AZ61 Alloy with Different Level of Ca Addition and Aging, in: Applied Mechanics and Materials, Trans tech Publ., 2014, https://doi.org/10.4028/www.scientific.net/AMM.592-594.821.

[20] E. Dabah, et al., The influence of Ca on the corrosion behavior of new die cast Mg–Al-based alloys for elevated temperature applications, J. Mater. Sci. 45 (11) (2010) 3007–3015, https://doi.org/10.1007/s10853-010-4302-1.

[21] J. Yang, et al., Effect of Ca addition on the corrosion behavior of Mg–Al–Mn alloy, Appl. Surf. Sci. 369 (2016) 92–100, https://doi.org/10.1016/j.apsusc.2016.01.283.

[22] U.M. Chaudry, et al., Corrosion behavior of AZ31 magnesium alloy with calcium addition, Corros. Sci. (2022), 110205, https://doi.org/10.1016/j.corsci.2022.110205.

[23] D. Zander, C. Schnatterer, C. Kuhnt, Influence of heat treatments and Ca additions on the passivation behaviour of high-pressure die cast AM50, Mater. Corros. 66 (12) (2015) 1519–1528, https://doi.org/10.1002/maco.201508273.

[24] M. Deng, et al., Approaching “stainless magnesium” by Ca micro-alloying, Materials Horizons 8 (2) (2021) 589–596, https://doi.org/10.1039/D0MH01380C.

[25] M. Cihova, et al., Biocorrosion zoomed in: Evidence for dealloying of nanometric intermetallic particles in magnesium alloys, Adv. Mater. 31 (42) (2019) 1903080, https://doi.org/10.1002/adma.201903080.

[26] G.E. Schulze, Zur Kristallchemie der intermetallischen AB2-Verbindungen (Laves-Phasen), Z. Elektrochem. Angew. Phys. Chem. 45 (12) (1939) 849–865, https://doi.org/10.1002/bbpc.19390451202.

[27] C. Zehnder, et al., Plastic deformation of single crystalline C14 Mg_2Ca Laves phase at room temperature, Mater. Sci. Eng. A 759 (2019) 754–761, https://doi.org/10.1016/j.msea.2019.05.092.

[28] M. Freund, et al., Plastic deformation of the $CaMg_2$ C14-Laves phase from 50-250° C, Materialia 20 (2021), 101237, https://doi.org/10.1016/j.mtla.2021.101237.

[29] S.I. Wright, M.M. Nowell, EBSD image quality mapping, Microsc. Microanal. 12 (1) (2006) 72–84, https://doi.org/10.1017/S1431927606060090.

[30] D.P. Field, Recent advances in the application of orientation imaging, Ultramicroscopy 67 (1–4) (1997) 1–9, https://doi.org/10.1016/S0304-3991(96)00104-0.

[31] I. Gutierrez-Urrutia, S. Zaefferer, D. Raabe, Coupling of electron channeling with EBSD: toward the quantitative characterization of deformation structures in the SEM, Jom 65 (9) (2013) 1229–1236, https://doi.org/10.1007/s11837-013-0678-0.

[32] H. Kriaa, A. Guitton, N. Maloufi, Fundamental and experimental aspects of diffraction for characterizing dislocations by electron channeling contrast imaging in scanning electron microscope, Sci. Rep. 7 (1) (2017) 1–8, https://doi.org/10.1038/s41598-017-09756-3.

[33] S. Zaefferer, N.-N. Elhami, Theory and application of electron channelling contrast imaging under controlled diffraction conditions, Acta Mater. 75 (2014) 20–50, https://doi.org/10.1016/j.actamat.2014.04.018.

9. Publication 5

Temperature-driven nanoscale brittle-to-ductile transition of the *C*15 $CaAl_2$ Laves phase

Anwesha Kanjilal [a], Ali Ahmadian [a], Martina Freund [b], Pei-Ling Sun [b], Sandra Korte-Kerzel [b], Gerhard Dehm [a], James P. Best [a]

[a] Max-Planck-Institut für Eisenforschung GmbH, 40237 Düsseldorf, Germany

[b] Institute for Physical Metallurgy and Materials Physics, RWTH Aachen University, Aachen, Germany

Materials & Design, Volume 225, 2023, 111504, **reproduced with permission of Elsevier.**

https://doi.org/10.1016/j.matdes.2024.113206

Short Summary

The influence of temperature on the deformation behaviour of the *C*15 CaAl2 Laves phase, a key constituent for enhancing the mechanical properties of Mg alloys up to service temperatures of 200 °C, remains largely unexplored. This study presents, for the first time, the nanoscale brittle-to-ductile transition (BDT) of this intermetallic phase through in situ testing including nanoindentation, scratch testing, and micropillar splitting conducted at elevated temperatures. By correlating observations from these techniques, changes in deformation of $CaAl_2$ were identified in relation to temperature.

High-temperature nanoindentation quantitatively determined the temperature range for the BDT, and revealed that $CaAl_2$ undergoes a BDT at ~0.55T*m*, exhibiting an intermediate region of microplasticity. A noticeable decrease in nanoindentation hardness was observed at ~450-500 °C, accompanied by an increase in residual indent size, while indentation cracking was not observed above 300 °C. Results from high-temperature micropillar splitting revealed cracking and brittle pillar splitting up to 300 °C, with an increase in apparent fracture toughness from 0.9 ± 0.1 MPa·$m^{-1/2}$ to 2.8 ± 0.3 MPa·$m^{-1/2}$, and subsequent crack-free plastic deformation from 400 °C. Transmission electron microscopy analysis of the deformed material from nanoindentation revealed that the BDT of CaAl2 may be attributed to enhanced dislocation plasticity with increasing temperature.

Anwesha Kanjilal: Writing – review & editing, Writing – original draft, Visualization, Methodology, Investigation, Formal analysis, Data curation, Conceptualization. Ali Ahmadian: Writing – review & editing, Visualization, Methodology, Investigation. **Martina Freund**: Writing – review & editing, Methodology, Investigation. Pei-Ling Sun: Writing – review & editing, Methodology, Investigation. Sandra Korte-Kerzel: Writing – review & editing, Supervision, Funding acquisition. Gerhard Dehm: Writing – review & editing, Supervision, Project administration, Funding acquisition, Conceptualization. James P. Best: Writing – review & editing, Supervision, Project administration, Methodology, Formal analysis, Conceptualization.

Materials & Design 244 (2024) 113206

Contents lists available at ScienceDirect

Materials & Design

journal homepage: www.elsevier.com/locate/matdes

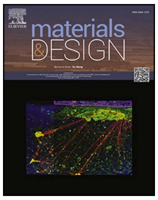

Temperature-driven nanoscale brittle-to-ductile transition of the C15 $CaAl_2$ Laves phase

Anwesha Kanjilal[a], Ali Ahmadian[a,1], Martina Freund[b], Pei-Ling Sun[b], Sandra Korte-Kerzel[b], Gerhard Dehm[a,*], James P. Best[a,*]

[a] Max-Planck-Institut für Eisenforschung GmbH, 40237 Düsseldorf, Germany
[b] Institut für Metallkunde und Materialphysik, RWTH Aachen University, 52056 Aachen, Germany

A R T I C L E I N F O

Keywords:
Brittle-to-ductile transition
High-temperature nanomechanics
Nanoindentation
Micropillar splitting
Intermetallics

A B S T R A C T

The influence of temperature on the deformation behaviour of the C15 $CaAl_2$ Laves phase, a key constituent for enhancing the mechanical properties of Mg alloys up to service temperatures of 200 °C, remains largely unexplored. This study presents, for the first time, the nanoscale brittle-to-ductile transition (BDT) of this intermetallic phase through *in situ* testing including nanoindentation and micropillar splitting conducted at elevated temperatures. By correlating observations from these techniques, changes in deformation of $CaAl_2$ were identified in relation to temperature. High-temperature nanoindentation quantitatively determined the BDT temperature range, and revealed that $CaAl_2$ undergoes a BDT at ~0.55 T_m, exhibiting an intermediate region of micro-plasticity. A noticeable decrease in nanoindentation hardness was observed at ~450–500 °C, while indentation cracking was not observed above 300 °C. Results from high-temperature micropillar splitting revealed cracking and brittle pillar splitting up to 300 °C, with an increase in apparent fracture toughness from 0.9 ± 0.1 MPa·$\sqrt{m}$ to 2.8 ± 0.3 MPa·$\sqrt{m}$, and subsequent crack-free plastic deformation from 400 °C. Transmission electron microscopy analysis of the deformed material from nanoindentation revealed that the BDT of $CaAl_2$ may be attributed to enhanced dislocation plasticity with increasing temperature.

1. Introduction

Laves phases constitute one of the largest class of intermetallic compounds and are usually present as fine precipitates in various engineering alloys such as Mg alloys, steels, Ni-based superalloys, etc. [1–3]. They have been found to be important for improving the strength and high-temperature creep resistance of structural materials [1]. Laves phases are categorised into three polytypes depending on their crystal structure – cubic C15, hexagonal C14, and dihexagonal C36 type [1,4]. These crystals have topologically close packed structures with very high space filling, and therefore possess a high barrier to plastic deformation by dislocation motion at room temperature [1,5–7]. Hence, Laves phases are generally brittle under ambient conditions [1,5]. Additionally, and similar to other intermetallics [8,9], Laves phases can undergo a brittle-to-ductile transition (BDT) accompanied by a decrease in strength as the temperature increases [4]. A precise knowledge of the BDT temperature (BDTT) is important for Laves phase-strengthened alloys, in order to predict their high-temperature mechanical response for design purposes.

A common intermetallic precipitate present in binary Mg-Al alloys is $Mg_{17}Al_{12}$ (T_m = 458 °C [10], where T_m is the melting temperature), which undergoes a marked decrease in hardness from ~3.5 GPa to ~0.7 GPa at 150 °C [11]; a much lower temperature than the desired service temperature of 175–200 °C for Mg alloys [12]. The C15 $CaAl_2$ Laves phase is commonly found in Mg-rich ternary alloys containing Al and Ca. It has garnered interest for its potential to withstand higher service temperatures compared to other intermetallics in Mg-Al alloys, such as $Mg_{17}Al_{12}$, attributed to its high melting point of 1079 °C [13,14]. Tuning the Al-Ca ratio in ternary Mg-Al-Ca alloys can therefore favour the formation of higher melting point intermetallics such as the C14 $CaMg_2$ and C15 $CaAl_2$ Laves phases [15–17], leading to improved high-temperature mechanical properties. Nevertheless, the $CaMg_2$ phase has been noted for its inadequate creep properties attributed to its hexagonal structure [14]. This underscores the need for a detailed investigation of the high-temperature deformation behaviour of the C15 $CaAl_2$ Laves phase.

---

[*] Corresponding authors.
E-mail addresses: dehm@mpie.de (G. Dehm), j.best@mpie.de (J.P. Best).
[1] Present address: Karlsruhe Institute of Technology, Institute of Nanotechnology, 76433 Eggenstein-Leopoldshafen, Germany.

https://doi.org/10.1016/j.matdes.2024.113206
Received 21 March 2024; Received in revised form 11 July 2024; Accepted 25 July 2024

Recent nano- and micromechanical studies have shown that $C15$ $CaAl_2$ possesses high hardness and strength [18], but a low fracture toughness at room temperature [19], typical of Laves phases. *In situ* microcantilever fracture tests on single-phase cast specimens of $C15$ $CaAl_2$ revealed a fracture toughness of ~2 MPa·$\sqrt{m}$, with {1 1 0} and {1 1 2} as preferential cleavage planes [19]. Freund *et al.* performed nanoindentation and micropillar compression of the same cast $CaAl_2$ material, and reported a room temperature hardness of ~4.8 GPa and yield stress ~2–3 GPa [18]. In that study, it was possible to introduce plasticity in the brittle $CaAl_2$ during microcompression at room temperature due to the small length-scales involved, which favours dislocation plasticity over crack initiation as commonly observed for brittle materials [20–22]. While there is some understanding of the micromechanical properties of $CaAl_2$ at room temperature, knowledge regarding its elevated temperature deformation and fracture behaviour, and potential BDT is currently limited. In the sole study to the authors' knowledge investigating the high-temperature deformation of $CaAl_2$, Rokhlin *et al.* reported from microhardness tests that $CaAl_2$ was the hardest among the intermetallics in the ternary Mg-Al-Ca system, where the microhardness was observed to decrease ~20 % between 20 and 300 °C [14]. However, detailed insights into temperature-induced deformation changes, such as cracking and slip activity, or a possible BDT, were not discussed. Furthermore, the microhardness measurements in Ref. [14] were conducted on $CaAl_2$ precipitates embedded within the Mg alloy, where the compliance of the surrounding matrix could also influence the obtained results.

High-temperature deformation and the BDT, however, have been extensively investigated in high melting-point transition metal Laves phases such as $NbCo_2$, $FeCo_2$, $NbCr_2$, or $TaCo_2$ using hardness testing [23] or macroscale compression testing [4,24,25]. These studies revealed that while the intermetallics exhibited brittleness at room temperature, they experienced a decrease in hardness or significant reduction in yield strength (at 0.2 % strain), accompanied by an increase in creep deformation above the BDTT of ~0.65 T_m. Additionally, the presence of pre-existing defects in the cast specimens, such as microcracks and pores, was found to limit ductility and adversely affect plasticity and fracture behaviour during macroscale testing, thereby impeding the accurate determination of the BDTT. Small-scale testing methods may offer a viable alternative to overcome this limitation for determining the BDTT of Laves phases.

Advances in nano- and micromechanical testing have opened up new possibilities to investigate small-scale mechanical properties across a wide range of temperatures. This allows for examination without the material being influenced by fabrication defects such as pre-existing flaws which affect fracture measurement [26]. Notched microcantilever bending and micropillar splitting techniques [27] have been used to determine the temperature-dependent fracture toughness of ceramic coatings [28,29] and BDT behaviour at small length-scales for Si [30,31] and W [32]. Nanoindentation has been widely used to study the elevated temperature mechanical properties for a variety of brittle materials and monitor plasticity changes with temperature [26]. Complementary to indentation testing, scratch testing has also been employed to probe the plasticity and cracking behaviour at small length-scales [33,34], and to determine orientation dependent changes in brittle and ductile deformation at room temperature due to changes in crack formation and scratch depth with crystal orientation [35,36]. In the context of Laves phases, indentation-based testing has been employed to examine the high-temperature mechanical properties of $C14$ $CaMg_2$ [37], where the indentation hardness decreased above 0.59 T_m. High-temperature nanoindentation and micropillar compression were also used to determine the temperature-dependent hardness and critical resolved shear stress (CRSS) of the activated slip systems in $C14$ $CaMg_2$ between 25–250 °C (0.53 T_m) [38], where no change in the mechanical properties was observed within the temperature range. These studies suggest the versatility of small-scale testing methods to obtain meaningful fracture and plasticity properties of brittle materials over a wide range of temperatures, without the limitation of premature fracture induced by pre-existing flaws in the material.

In this context, the present study aims to determine the elevated temperature deformation behaviour and BDT of a cast single-phase $C15$ $CaAl_2$ Laves phase intermetallic specimen using a nano- and micromechanical testing approach. For this, high-temperature testing using a commercial *in situ* nanoindenter is employed for precise quantitative determination of the BDTT from changes in hardness and fracture toughness using high-temperature nanoindentation and micropillar splitting, respectively. The mechanical properties measured at various temperatures are then correlated with their corresponding structural changes concerning crack formation and slip activity through subsequent examination of the deformed specimens using scanning and transmission electron microscopy (SEM and TEM, respectively).

2. Materials and methods

2.1. Sample fabrication and microstructural characterisation

Bulk single-phase specimens of the $C15$ $CaAl_2$ Laves phase were prepared by casting individual high purity elements of Al (99.999 % purity, HMV Hauner GmbH & Co. KG, Germany) and Ca (98.8 % purity, Alfa Aesar, Germany) in a cylindrical mould. The cast sample was then annealed at 600 °C for 24 h in an Argon atmosphere to homogenise the microstructure and relieve any residual stresses from the casting process. Small pieces of the specimen were machined using electric discharge machining and metallographically polished from 4000 grit SiC paper down to 40 nm colloidal silica to obtain a good surface finish. Further details of the sample preparation procedure can be found in Ref. [39]. Composition analysis of the same $CaAl_2$ Laves phase material was performed using electron probe microanalysis in Ref [19]. Fig. S1 in the Supplementary Information shows the representative microstructure of the annealed $C15$ $CaAl_2$ Laves phase where the grains had the $CaAl_2$ phase with the desired target composition of 67 at.% Al and 33 at.% Ca, with a skeleton network of $CaAl_4$ phase formed along the grain boundaries (chemical analysis of the respective phases from electron probe microanalysis is detailed in Ref. [19]). The grain orientation was characterised using electron backscattered diffraction (EBSD) performed with an EDAX system equipped with Hikari CCD camera mounted inside Zeiss Auriga dual beam focused ion beam/scanning electron microscope (FIB/SEM) and data collection was done using TSL OIM v7 software.

2.2. High-temperature mechanical testing

The effect of temperature on the deformation of $CaAl_2$ Laves phase was investigated using *in situ* high-temperature nano- and micromechanical testing. Measurements of BDT and high-temperature fracture behaviour of $CaAl_2$ was obtained from *in situ* nanoindentation and micropillar splitting. All *in situ* mechanical tests were performed inside a Zeiss Gemini 500 SEM under high vacuum conditions ($<5 \times 10^{-6}$ mbar) using a Hysitron PI-88 (Bruker, USA) testing system equipped with high-temperature module. Active heating of both the indenter tip and sample was used to ensure temperature matching and minimise thermal drift. The tip holder was affixed to a small ceramic sleeve to minimise heat loss and improve thermal insulation. For each type of test, the $CaAl_2$ specimen was positioned on the sample heating stage and fixed using three Mo pins. The sample and indenter tip temperatures were measured independently using two separate thermocouples, in close contact with the tip and sample heater for all tests.

2.2.1. High-temperature nanoindentation

High-temperature nanoindentation was performed within a single grain of the $CaAl_2$ intermetallic with ~(5 3 6) surface plane, determined *a priori* using EBSD. Grain orientations close to ~(1 1 1) in $CaAl_2$ have shown a propensity for indentation cracking at room temperature [38], and were thus chosen to monitor changes in cracking behaviour with temperature. A high temperature diamond cube corner tip (Synton-MDP AG, Switzerland) was used in order to facilitate investigation into crack formation as a function of temperature. Prior to testing, the tip area function calibration was carried out on fused quartz. The nanoindentation tests were performed at eight different temperatures from 25 to 580 °C, with an average of 7 to 8 indents at each temperature. This was followed by another set of indentations made at 25 °C after cooling the sample down from the maximum temperature to check for repeatability before and after the heating excursion. Both the sample and indenter were heated during the indentation experiments. Care was taken to ensure that the indents were made inside the grain, away from grain boundaries, and the spacing between the indents was maintained at greater than three times the lateral dimension of the indents to avoid the influence of overlapping plastic zones between adjacent indents [40]. The tests were performed in load-controlled mode, wherein the load was ramped up to a maximum value of $P_{\max} = 9$ mN followed by holding at the peak load for 10 s (and 30 s at temperatures higher than 450 °C to minimise transient plasticity effects during initial unloading). A drift correction segment of 30 s was introduced during unloading at 10 % of $P_{\max}$. The drift correction load was sufficiently low to ensure linear drift without time-dependent plasticity. The thermal drift rate was calculated from the drift correction segment for every indentation test at each temperature and the drift corrected load–displacement curves were subsequently obtained. The indentation hardness H was calculated for each case as [41]:

$$H = \frac{P_{max}}{A} \tag{1}$$

where the contact area A depends on the contact depth of penetration according to the calibrated area function of the cube corner indenter tip. Post-nanoindentation, the residual indent impressions were observed in the SEM in secondary electron mode to visualise changes in the indent size and microstructural features such as cracks and slip lines around indents at different temperatures.

2.2.2. *High-temperature micropillar splitting*

Micropillar splitting was performed to determine the effect of temperature on the fracture toughness of $CaAl_2$ Laves phase. In total, 17 cylindrical micropillars were fabricated by FIB milling in a Zeiss FIB-SEM. It is to be noted that as a sufficiently large grain with (1 1 1) orientation to accommodate a full set of pillars was not found, the micropillars were fabricated in a grain with surface orientation ~(5 3 13). The final milling was performed at 30 kV, 3 nA Ga^+ ion beam current down to a final pillar diameter of 10 μm and aspect ratio ~1.4. The dimensions of the pillars (*i.e.* the pillar diameter and height) were measured after FIB milling. An overview image of the micropillar and the surface orientation of the grain are given later in Section 3.3. Recently, Lauener *et al.* [30] reported that for pillars with diameter greater than 10 μm, ion beam damage has limited influence on the pillar splitting fracture toughness [28,29]. The effect of ion beam and pillar size on the room temperature fracture toughness of $CaAl_2$ has also been investigated by the authors [19], where no observable differences between the apparent fracture toughness of 10 μm diameter pillars milled with either Ga^+ or Xe^+ ions were observed. Furthermore, in the same study, $CaAl_2$ micropillars of 5 and 10 μm diameter fabricated by Ga^+ FIB were found to have similar toughness values [19]. Hence, the pillar size and fabrication procedure used in this study will not lead to ion beam induced damage effects on toughness measurement. To facilitate fracture of the micropillars and also maintain consistency with the nanoindentation tests, the pillar splitting tests were also performed using a high temperature diamond cube corner indenter (Synton-MDP AG, Switzerland) at 25, 150, 300, 400 and 500 °C. Pillar splitting tests were conducted in pseudo-displacement-controlled mode at 20 nm/s. The tests were terminated once either a load drop occurred or pillar splitting was visually observed during testing. The load–displacement behaviour was recorded and the maximum load at which splitting occurred was identified to calculate the pillar splitting fracture toughness. Since drift correction cannot be conducted during the pillar splitting tests, separate nanoindentation tests with a drift hold segment were performed immediately before and after the pillar splitting tests at each temperature to ensure temperature matching between the tip and sample and to minimize thermal drift rates. However, it is also important to note that for displacement-controlled testing thermal drift will mainly cause error in displacement measurements and not the load values [30]. During pillar splitting it is the critical load which is required for fracture toughness calculation, and hence thermal drift is not a critical factor here unlike in nanoindentation. *Post-mortem* microscopic examination was performed in a Zeiss Gemini500 SEM to observe the fractured pillars.

2.3. *TEM investigation*

To characterise the deformation structure underneath the indents using TEM, cross-sectional specimens were prepared from the nanoindents using a Thermo Fisher Scientific Scios 2 FIB equipped with a Ga^+ ion source. To understand the effect of temperature on deformation, TEM specimens were extracted from an indent made at room temperature (after cooling down from 580 °C) and an indent made at 450 °C, for which the indentation testing was stopped at this temperature without exposing the deformed microstructure to higher temperatures. TEM imaging and selected area electron diffraction (SAED) were performed on a JEOL JEM 2100+ operated at 200 kV and a C_s image-corrected Thermo Fisher Scientific Titan Themis 60-300 equipped with the Ceta CMOS camera operated at 300 kV. To identify Burgers vectors of dislocations, TEM imaging was carried out in JEOL JEM F200 at 200 kV under different two-beam conditions followed by $g{\cdot}b$ extinction analysis (where g is the diffraction vector and b the Burgers vector).

3. Results

3.1. *Effect of temperature on nanoindentation hardness*

Hardness variation with temperature was determined through nanoindentation tests to enhance understanding of how deformation behaviour changes with temperature in the $C15$ $CaAl_2$ phase. Fig. 1a shows the EBSD IPF map of the region where nanoindentation was performed, and the surface orientation of the tested grain has been marked. Fig. 1b shows the representative thermal drift-corrected load–displacement curves at temperatures from 25 to 580 °C. The load–displacement behaviour at 25 and 300 °C is also shown separately in the inset of Fig. 1b. With increasing temperature, clear differences are observed in the load–displacement behaviour in terms of: (i) progressive increase in indentation depth at the beginning of load-hold segment at the peak load from 500 °C; (ii) higher time-dependent displacement and maximum depth of indentation at the peak load from 450 °C. Both effects suggest that plastic deformability of $CaAl_2$ increases from ~450 °C, and is in broad agreement with the deformation changes observed from our preliminary scratch testing analysis of $CaAl_2$ (refer to the Supplementary Information). This implies that nanoindentation hardness of the material varies with temperature, as observed in Fig. 2. The hardness at room temperature was ~4.5 GPa, similar to that recently reported for $CaAl_2$ [18]. The hardness remained constant at ~4.5 GPa up to 400 °C, and dropped by 22 % at 450 °C to 3.5 GPa. This was followed by a more pronounced decrease at 500 °C to ~1 GPa. Subsequently, the hardness further reduced and was nearly constant at ~0.6 GPa between 550 to 580 °C. Thus, the temperature range between 450 to 500 °C marks the region where a significant enhancement in plastic deformation of $CaAl_2$ occurs in the cube corner nanoindentation tests. The elastic modulus (determined from the unloading segment of the load–displacement curves) was constant between 25 and 400 °C with an average value ~140 ± 6 GPa, while at higher temperatures the modulus values were

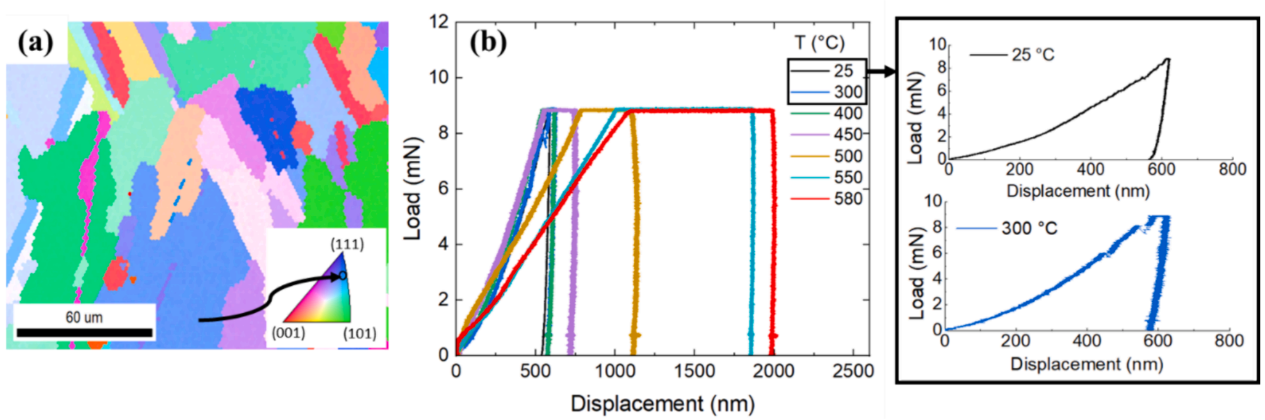

Fig. 1. High-temperature nanoindentation of $CaAl_2$. (a) Orientation map of $CaAl_2$ obtained from EBSD showing the grain orientation where nanoindentation tests were conducted. (b) Representative load–displacement curves at different temperatures obtained from nanoindentation; the inset in (b) shows separately the zoomed in version of load–displacement curves at 25 and 300 °C. In (b) the data for 25 to 500 °C correspond to 10 s hold at P_{max}, while those at 550 and 580 °C correspond to 30 s hold at P_{max}.

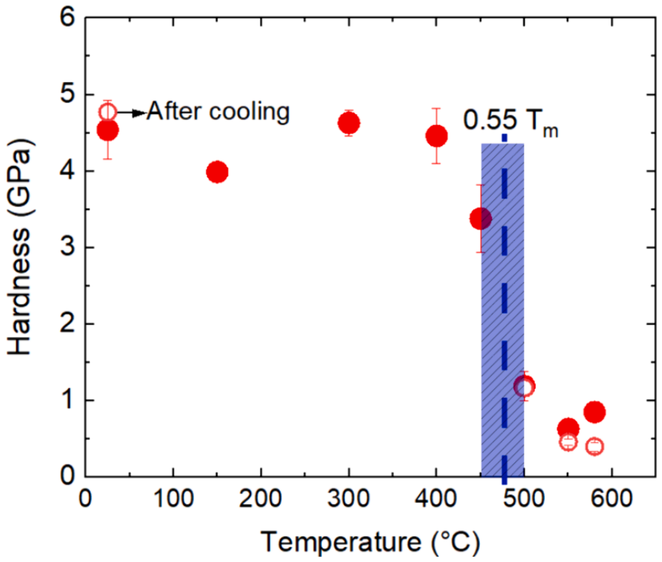

Fig. 2. Variation of nanoindentation hardness with temperature for the *C*15 $CaAl_2$ Laves phase. The filled circles denote the data for 10 s hold time and open circles are for 30 s hold time at peak load. Error bars indicate the standard deviation of hardness values at each temperature and for cases where it is invisible the error bar was smaller than the symbol size. The blue shaded region represents the transition temperature range where the hardness values decrease significantly from the upper plateau region before saturating to lower values.

affected by increasing transient deformation and could not be reliably interpreted. The observed time-dependent displacement during the hold segment (Fig. 1b) is attributed to creep deformation, influenced by high temperature and pressure in the centre of the plastic zone, as well as stress gradients from the cube corner geometry. This is distinguished from thermal drift, where displacement would vary linearly with time (discussed in Section 4.2). Comparison of hardness at different hold times (Fig. 2) reveals no significant difference at 500 °C. Longer hold times in the high-temperature regime slightly reduce hardness without altering the overall trend of saturation to lower values. A slight but consistent drop in hardness of ~12 % is observed at 150 °C with enhanced pile-up around the residual indent (Fig. 3b), although the reason for this is unclear.

Increased plastic deformation with temperature was also observed from the *post-mortem* SEM analysis of the residual indents. Fig. 3 shows representative secondary electron images of the indents performed at various temperatures. The size of the residual indent impression is similar below 450 °C and then increases from 450 °C and above. A larger size of indent impression for fixed maximum load is consistent with the lower hardness at higher temperatures shown in Fig. 2. Notable changes in deformation features around the indent can also be observed with temperature. Slip steps and material pile-up are visible in the low temperature indents, along with cracks (indicated by white arrows) extending from the corners of the indents. No slip lines or cracks are visible in the transition and high temperature regime above 300 °C. Pile-up diminishes noticeably at 450 °C and is not observed at ~500 °C. Surface features appear less defined in post-cooling images due to surface oxidation at elevated temperatures. It must be emphasised that even with high vacuum level (5×10^{-6} mbar) in the SEM, surface oxidation of $CaAl_2$ cannot be avoided (see presumed oxide scale of ~60 nm thickness observed from the TEM cross-section of an indent made at RT after exposure to 580 °C in Fig. 7a). These changes in deformation features with temperature, in conjunction with the significant decrease in hardness, suggests that the deformation behaviour of the $CaAl_2$ Laves phase changes at ~450 °C and is facilitated by higher plastic deformability with the absence of cracking. To further correlate the changes in hardness with changes in fracture behaviour across this transition zone, high-temperature micropillar splitting tests were conducted.

3.2. *Effect of temperature on the pillar splitting fracture toughness*

Fig. 4a shows an overview of micropillars fabricated on a single $CaAl_2$ grain, whose surface orientation is marked in the inset IPF. A representative high-magnification image of a micropillar is also shown in the inset in Fig. 4a. Fig. 4b shows a micrograph of the *in situ* configuration with cube corner indenter prior to testing, while Fig. 4c shows the representative load–displacement response of the pillar splitting tests at various temperatures. The load–displacement curves maintain a consistent shape up to 300 °C, showing minimal variation in slope and indicating negligible effects from indenter positioning and thermal drift. The maximum load at which pillar splitting occurs (identified by a sharp load drop) increases only slightly from 25 to 150 °C, and then increases significantly at 300 °C. A transition is observed at 400 °C, wherein the peak load increases slightly, but pillar splitting does not occur. Above 400 °C, the peak load at the pre-set maximum indentation depth decreased, signifying that the $CaAl_2$ intermetallic becomes more plastically deformable. Due to lack of pillar splitting at 400 and 500 °C, a load drop was not observed up to the maximum set displacement value of 2.5 μm, where the tests were terminated. Hence, the apparent fracture toughness was determined only up to 300 °C. The critical stress intensity factor for splitting was evaluated using Eq. (2) [27]:

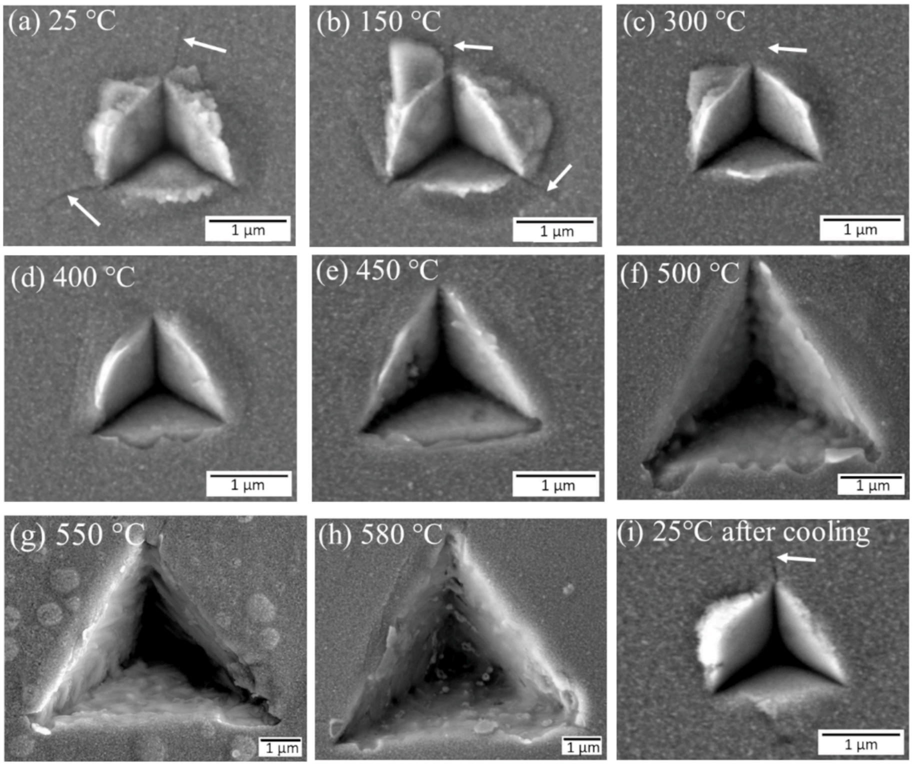

Fig. 3. Secondary electron *post-mortem* images of nanoindents made at various temperatures showing changes in slip lines and crack formation (marked with white arrows) around indents. From 25 to 450 °C all images were taken at the same magnification, whereas from 500 to 580 °C a lower magnification was used to capture the larger indents.

$$K_c = \gamma \frac{P_c}{R^{1.5}} \tag{2}$$

which assumes an isotropic material volume. K_c is the apparent fracture toughness, P_c is the critical load at which pillars split, R is the radius of the pillar, and γ is a factor which depends on the geometry of the indenter and E/H ratio of the material. A constant elastic modulus E of 140 ± 6 GPa was used between 25 and 400 °C, based on modulus values obtained from unloading segment of the nanoindentation experiments. It is to be noted that no positive displacement due to creep occurred during unloading up to 400 °C. Using the hardness values at each temperature obtained from nanoindentation measurements in Section 3.1, the E/H ratio was obtained within the constant γ range for a cube corner indenter geometry reported from Ref. [42] (*i.e.* ~31), and therefore $\gamma \approx 0.85$ was applied over the studied temperature range of 25 to 300 °C. Fig. 4d shows the variation of apparent fracture toughness from pillar splitting as a function of temperature along with the maximum load $P_{\max}$ for all temperatures. $P_{\max}$ corresponds to P_c for the case where pillar splitting occurred from 25 to 300 °C, whereas at 400 and 500 °C it was the maximum load till the displacement set-point was reached. The K_c calculated from Eq. (2) was 0.94 ± 0.05 $\text{MPa}\cdot\sqrt{\text{m}}$ at 25 °C, and increased slightly to 1.2 $\text{MPa}\cdot\sqrt{\text{m}}$ at 150 °C, whereas at 300 °C it increased significantly to 2.76 ± 0.26 $\text{MPa}\cdot\sqrt{\text{m}}$ with a commensurate increase in the critical load for splitting. Pillar splitting was observed again after cooling back to 25 °C with K_c ~0.9 ± 0.1 $\text{MPa}\cdot\sqrt{\text{m}}$, implying that exposure to high temperature did not induce any major structural changes in the material to influence the toughness, and that surface oxidation did not severely impact the toughness measurement, similar to the nanoindentation results in Section 3.1.

Fig. 5 shows *post-mortem* images of the pillars after the splitting tests at different temperatures. From 25 to 300 °C straight cracks predominately extend from the corner of the indents, leading to 3-way splitting of the pillars. In few cases, due to inaccuracy in indenter positioning, an ideal 3-way splitting did not occur wherein two of the cracks extending from the indenter corner reached the edge of the pillar while the third did not. At 400 and 500 °C no critical crack initiation for pillar splitting was observed, although some isolated tortuous cracks are present on the surface of the deformed pillars. Such surface cracks could be due to stresses arising from accommodation of the larger plastic zone below the indent, or cracking of the surface oxide layer. However, these surface cracks do not lead to pillar splitting. Crack formation was not observed during nanoindentation at similar temperatures due to the hydrostatic constraint from the surrounding material, which is reduced in the case of a micropillar volume. For the lower temperatures where pillar splitting did occur, the crack planes were indexed using the method used for surface trace analysis discussed in Ref. [18]. Some of the crack planes have been marked in Fig. 5 and belong to low index planes. However, it is not possible to discern any possible change in crack plane with temperature in this case, as cracking would primarily be driven by the cleavage planes which are aligned with the sharp corners of the indenter. In our earlier study [19], the fracture toughness values of different low index cleavage planes in $C15$ CaAl_2 were found to be similar. Hence the grain orientation and alignment of the cleavage planes with indenter diagonal will likely not significantly impact the pillar splitting fracture toughness value of $C15$ CaAl_2.

4. Discussion

4.1. BDTT of C15 CaAl_2 Laves phase: Comparison of test methods

The results presented in Section 3 highlight a clear change in the deformation behaviour of $C15$ CaAl_2 Laves phase with increasing temperature, and is supported by three distinct changes: (i) significant drop in nanoindentation hardness at 450–500 °C; (ii) absence of cracking at the corners of indents at 300 °C and above; (iii) brittle pillar splitting between 25 to 300 °C, followed by no splitting from 400 °C. These changes imply an overall transition from brittle to a more ductile

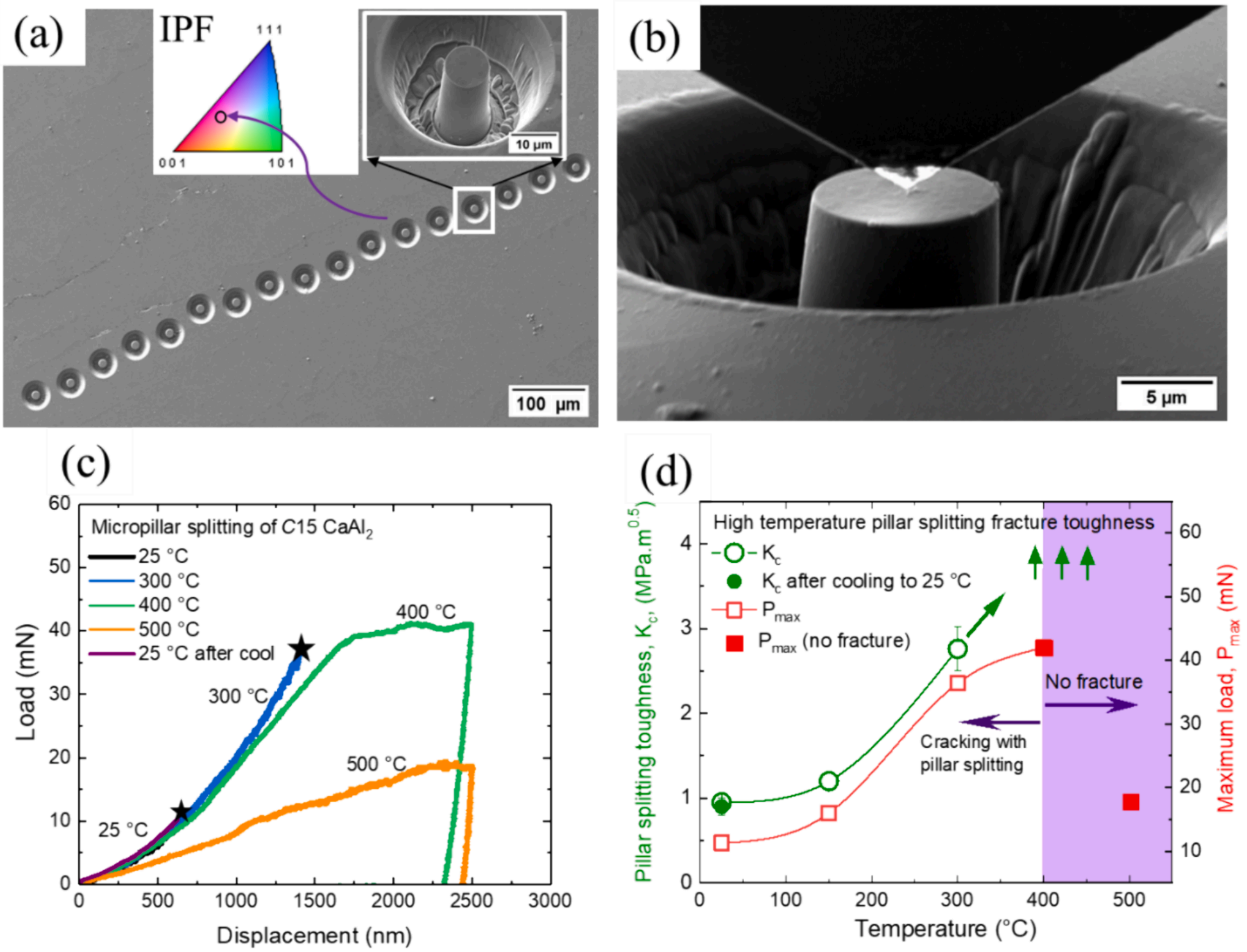

Fig. 4. (a) Secondary electron overview image of micropillars fabricated in a single grain whose surface orientation is indicated in the IPF (inset) together with a high magnification tilt-corrected image of a single micropillar at 45° tilt angle; (b) Micropillar loaded with a cube corner indenter prior to testing at 300 °C; (c) Representative load–displacement curves for pillar-splitting at various temperatures; (d) Variation of pillar-splitting fracture toughness and maximum load P_{max} with temperature. The filled red squares in (d) indicate the maximum load for the cases where no splitting occurred. The green arrows in (d) indicate that apparent fracture toughness would increase with temperature above 300 °C.

behaviour of $CaAl_2$, accompanied by a higher contribution of plasticity to fracture. Disappearance of cracks at ~300 °C during cube corner nanoindentation suggest that crack tip shielding due to local dislocation activity is already operative at these lower temperatures, which together with the hydrostatic constraint from the surrounding material may limit crack extension. This is consistent with the increase in pillar splitting fracture toughness at 300 °C. During micropillar splitting, unstable crack initiation and extension occurs at the critical load for instability. Enhanced dislocation activity under the indenter tip at higher temperatures can better accommodate local stress thereby affecting the critical load for crack initiation during the splitting process. However, brittle splitting fracture of the micropillars is still observed at 300 °C, implying that $CaAl_2$ remains brittle at this temperature.

The influence of local plasticity is more evident as temperature increases to 400 °C, where the maximum load reaches a peak value (see Fig. 4), however no splitting occurs, indicating that $CaAl_2$ becomes less brittle at this temperature. Ast *et al.* [43] reported that for crack nucleation and pillar splitting to occur within a micropillar volume size which can be typically achieved by FIB milling, the K_c/H ratio should be less than 0.8 for a cube corner indenter. For our system at 300 °C the ratio is 0.61, whereas at 400 °C it would increase to 0.88 if one assumes that the K_c increases with temperature following a linear extrapolation beyond 300 °C (see green arrow in Fig. 4d). Since pillar splitting is limited to materials which fail in a brittle manner, it is unsuitable for obtaining a high-temperature toughness for which alternate elastic–-plastic fracture mechanics approaches are required. Interestingly, while local dislocation activity can blunt the crack tip, increase fracture toughness and even prevent pillar splitting at 400 °C, no decrease in indentation hardness or increase of the residual indent size was observed (see Figs. 2, 3). Only at and above ~450 °C does the hardness drop and dislocation plasticity becomes more dominant (see TEM analysis discussed in Section 4.2). The transition zones between brittle and ductile behaviour of $CaAl_2$ are shown in Fig. 6, where both the temperature-dependent variation of hardness and pillar splitting toughness have been compared. Up to 300 °C, $CaAl_2$ exhibits brittle behaviour with constant hardness and brittle failure due to cracking. Between 300 and 400 °C a microplasticity zone is present where although the hardness does not change, cracks at indenter edges are not observed during nanoindentation, while significant local dislocation activity at the indenter apex and possible crack tip shielding effects increase the toughness to an extent that a critical fracture initiation could not be determined from micropillar splitting tests. The microplastic region above 300 °C compares well with the morphological changes in wear tracks from high-temperature nano-scratch testing of $CaAl_2$ (refer to Supplementary Information). At approximately 450 °C and above, $CaAl_2$ exhibits enhanced plasticity due to dislocation activity, as evident from the significant drop in hardness together with absence of pillar splitting, thereby transitioning into a more ductile behaviour. The close

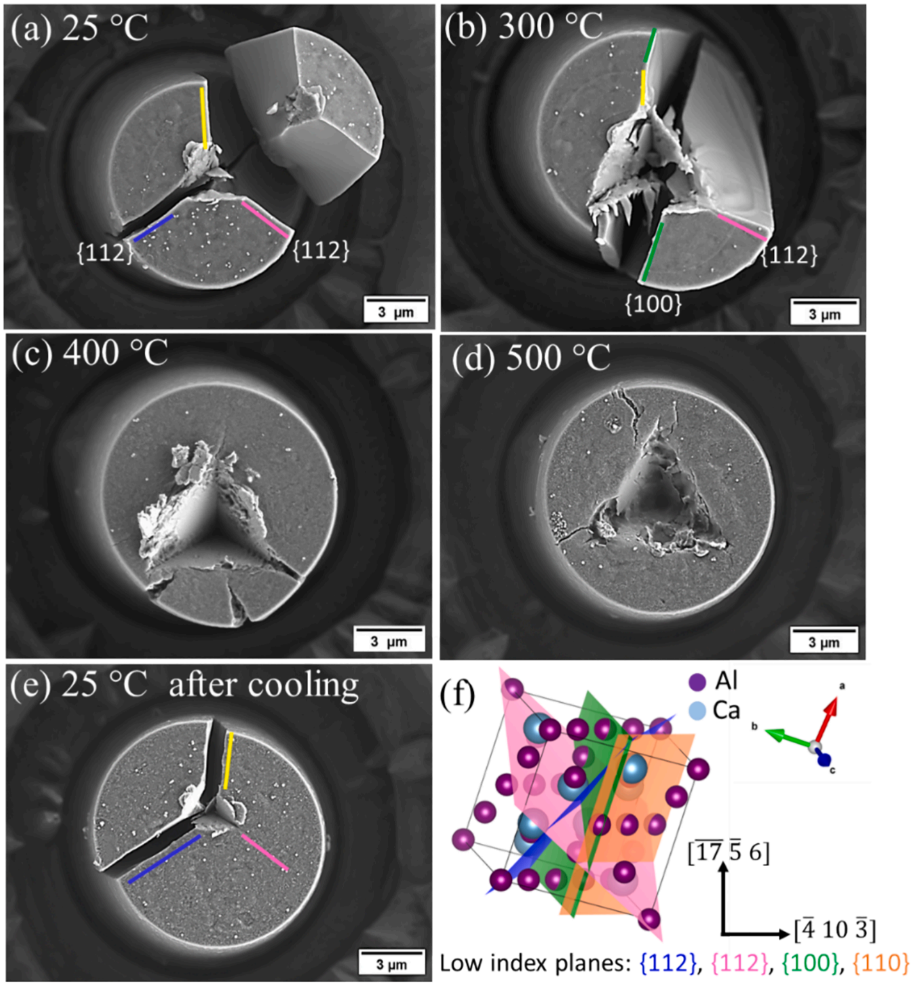

Fig. 5. *Post-mortem* secondary electron micrographs, showing the top view after pillar splitting tests at (a) 25 °C, (b) 300 °C, (c) 400 °C, (d) 500 °C and (e) after cooling back to 25 °C. (f) Crystal orientation of the grain showing potential low-index planes for cracking; the in-plane orientations of pillars in (a-e) are indicated in (f). The yellow lines in (a), (b) and (e) indicate crack planes for which two possible solutions were obtained and hence could not be assigned unambiguously.

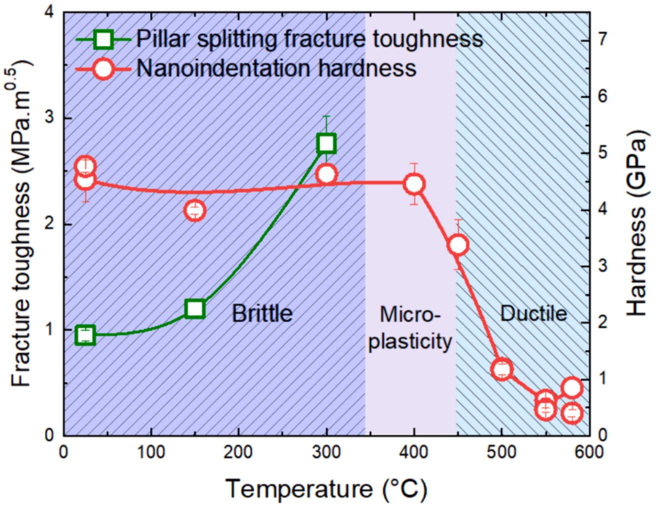

Fig. 6. Comparison of nanoindentation hardness and pillar splitting fracture toughness with temperature, highlighting brittle and ductile deformation zones.

correspondence in the temperatures where plasticity prevents the brittle failure of pillars (~400 °C) and decreases nanoindentation hardness (~450 °C) suggests that a prominent change over into the ductile regime will occur from 450 °C (~0.55 T_m).

The nanoscale BDTT (~0.55 T_m) of *C*15 $CaAl_2$ determined here is lower than the macroscale BDTT of ~0.65 T_m typically reported for other *C*15 Laves phases via macro-compression testing [4], where BDTT was defined as the temperature at which a compressive strain of 1–2 % could be achieved without specimen fracture. However, from Vickers indentation of *C*15 $NbCr_2$ a BDTT of ~0.55 T_m was obtained [44], equal to that obtained for *C*15 $CaAl_2$ in this study. Further, to contextualise the BDT behaviour of $CaAl_2$ determined here using small-scale testing methods in relation to macroscale testing, the microplasticity zone at small length-scales suggests a wider temperature range for complete transition into the ductile regime. In comparison, during macroscale tests a more abrupt BDTT could occur for intermetallic compounds [9,45,46].

Method and length-scale-dependent BDTT differences are evident in other literature examples, where various testing methods were employed. The toughness reported from Si micropillar splitting increased at ~175 °C due to local crack tip shielding possibly facilitated by dissociation of dislocations into partials [30,47], whereas the microhardness decreased at higher temperatures of 500 °C due to enhanced dislocation activity [48]. Additionally, high-temperature microcantilever fracture tests on Si demonstrated a progressive increase in mode I fracture toughness from ~300 °C to 600 °C [31]. On the other hand, macroscale testing using pre-cleaved Si single crystals revealed a sharp increase in fracture toughness at 705 °C [49]. This supports our observation that small-scale toughness increases at lower temperatures when compared to the indentation hardness. Similar length-scale effects have been observed for tungsten [32], where the BDTT obtained from macroscale testing of three- and four-point bending specimen geometries was ~150 to 200 °C [50,51], while microcantilever fracture tests revealed a BDTT of ~0 to 75 °C [32], with a gradual increase in fracture toughness and change from brittle-cleavage to micro-cleavage fracture due to increasing dislocation activity. These studies suggest that the onset of BDTT, facilitated by dislocation activity enhancing fracture toughness and promoting ductile behaviour, may occur at lower temperatures on small length scales. Differences based on the testing method, evident in case of CaAl$_2$, can also arise.

Regarding surface oxidation challenges for CaAl$_2$ at high temperatures, if small-scale techniques sensitive to surface deformation are used, as for nano-scratching, the formation of an oxide scale can obscure slip trace observation near the wear track and quantitative insights into elastic and plastic wear depth or friction coefficient with temperature may become unreliable [36]. Additionally, it must be noted that due to the observed oxidation, BDTT determination using notched micro-cantilever tests is not possible due to the changing stress/chemistry at the notch root, which can strongly affect the measured fracture toughness [52]. Moreover, the plastic zone size r_p ahead of the crack tip of notched microcantilevers can increase with temperature and exceed the cantilever dimensions, leading to size effects on cantilever fracture toughness. As such, microcantilever fracture tests were not performed here, and our nano-scratch tests (in the Supplementary Information) were interpreted with a degree of caution.

4.2. Mechanistic insights into the thermally-activated deformation

The deformed microstructure beneath the indents made at RT, and at the BDTT, were analysed to examine the effect of temperature on dislocation structure. Site-specific lamellae were extracted from below two representative indents made at 25 °C after cooling, and 450 °C, and examined by TEM. Both indents were not exposed to higher temperatures than the temperature of indentation. A schematic representation of the orientation in which the TEM lamella was extracted from indents has been given in Fig. S3 of the Supplementary Information. Fig. 7a,b show the bright-field TEM (BF-TEM) and BF-scanning TEM (BF-STEM) images of the deformed region underneath the indent at 25 °C, respectively. Straight parallel slip bands are visible, as indicated by the solid red arrows, along with dislocation entanglement in the plastic zone of the indent at 25 °C (refer to Fig. S4 for TEM images obtained from weak beam imaging by tilting to different two beam conditions). Similar slip bands in the deformed microstructure below nanoindents in the same $C15$ CaAl$_2$ sample were observed by Freund *et al.* [18] for Berkovich indents at RT. Furthermore, a crack is visible at the bottom of the indent (indicated by a dashed yellow arrow), which is consistent with SEM observation of surface cracks around the RT indent shown in Fig. 3. Fig. 7c shows the BF-TEM image of the plastic zone below a nanoindent at 450 °C. In contrast to the RT indent, no straight slip lines or cracks are observed. Rather, a high density of homogenously distributed dislocations, forming a network of curved dislocation lines, is present in the vicinity of the indent, with some isolated dislocations extending to farther regions. The absence of slip lines and cracks supports the SEM observations of homogeneous deformation without formation of slip traces on the indent surface at 450 °C in Fig. 3d, and the lower hardness due to more uniform dislocation activity. It is noted that due to the load-controlled nanoindentation tests performed here, the deformation zone of the indents at 25 and 450 °C were not of equivalent maximum depth. It is reported for the same $C15$ CaAl$_2$ sample used in this study that $a/2\langle 1\,1\,0\rangle$ (where a is the crystal lattice parameter) type perfect dislocations, as well as stacking faults on $\{1\,1\,1\}$ planes are present within the slip bands at RT [18]. The latter were thought to stem from the motion of $a/6\langle 1\,1\,2\rangle$ dislocations. The TEM images of Fig. 8 show that in case of the high temperature (*i.e.* 450 °C) indent lamella (of Fig. 7c), tilting to different zone axes and two-beam conditions also revealed similar $a/$

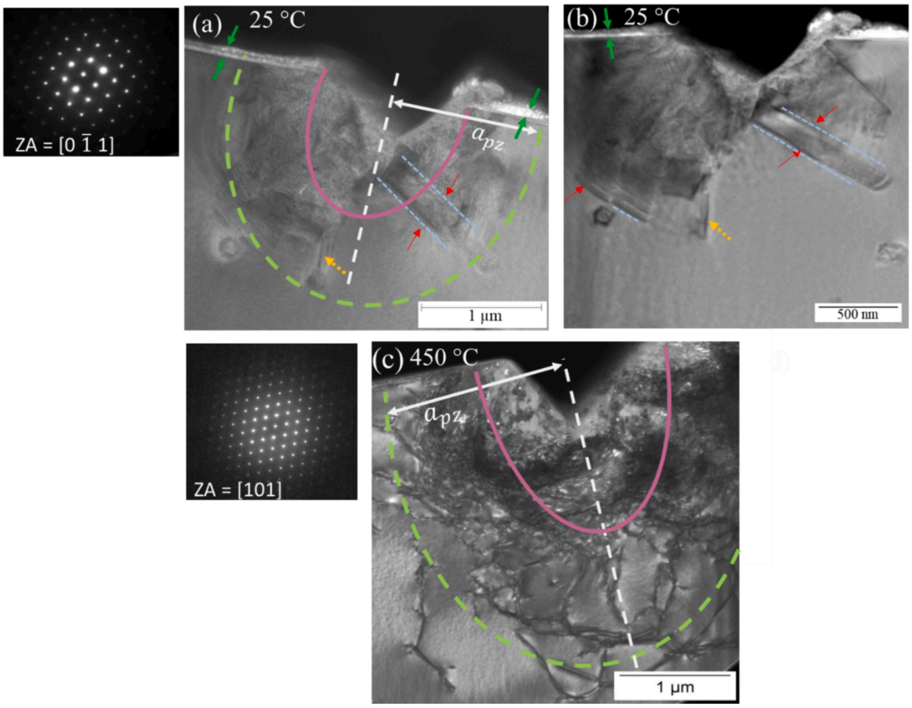

Fig. 7. TEM images showing the cross-section of the deformed region under nanoindents performed at different temperatures. (a) BF-TEM and (b) BF-STEM images of indent at 25 °C taken in the $[0\,\bar{1}\,1]$ zone axis. The orientation of the specimen is seen by the SAED pattern shown. The red arrows in (a) and (b) show the activated slip planes and the yellow arrows mark the crack observed at 25 °C; the green arrows in (a) and (b) indicate presumed oxide layer formed on the surface of indent after exposure to 580 °C. (c) The BF-TEM image of indent at 450 °C shows no slip plane activation or crack formation and the SAED pattern shows that the BF-TEM image was acquired at the $[101]$ zone axis. In (a) and (c) the theoretically computed plastic zone has been shown by the solid magenta curve for $f = 1$ and green dashed curve for $f = 2.4$ (see main text for more details). The dark region above the indented surface in (a-c) is the Pt layer.

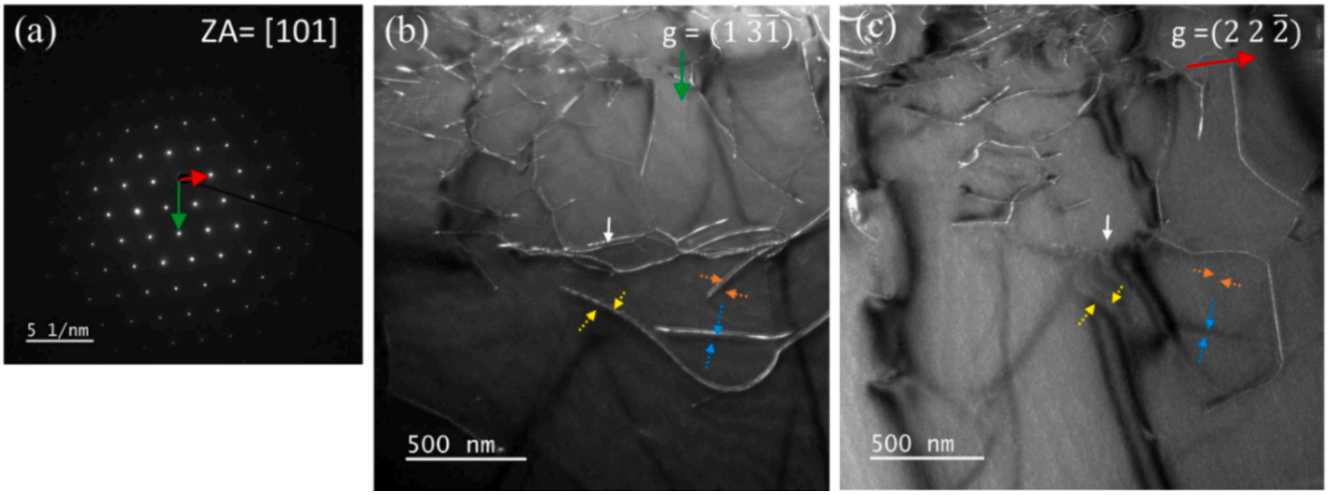

Fig. 8. Dislocation structure under different two-beam conditions underneath the nanoindent at 450 °C. (a) Diffraction pattern of [1 0 1] zone axis, and weak-beam dark field images under (b) g = $(1\overline{3}\overline{1})$where the dislocations are visible and (c) g = $(22\overline{2})$where the dislocations are invisible. Solid white arrows indicate perfect dislocation whereas dashed arrows of same colours denote partial dislocations identified from the $g{\cdot}b$ analysis.

$2\langle 1\,1\,0\rangle$ perfect dislocations (indicated with solid white arrows) and partial dislocations of $a/6\langle 1\,1\,2\rangle$ type (indicated with dashed arrows). These dislocations were identified by performing a $g{\cdot}b$ analysis on visible/invisible dislocation sets obtained from different two-beam conditions. A set of visible dislocations for zone axis [1 0 1] (in Fig. 8a) and $g = (1\overline{3}\overline{1})$ are shown in Fig. 8b, while the dislocations become invisible with $g = (22\overline{2})$as shown in Fig. 8c. Refer to Fig. S5 in the Supplementary Information for further TEM images of dislocation structure below this indent for other two beam conditions. Although resolving the partial dislocations in the RT sample may simply be impeded by the overlapping strain fields where they are concentrated in planes of high defect density, the observation of partial dislocations at elevated temperature is consistent with synchroshear requiring substantial thermal activation to operate [53] and previous TEM investigations on the structurally related Nb-Co μ-phase, which also exhibits a transition from full to partial dislocation slip [54] within the Laves phase building block of its larger unit cell, also associated with a change in slip plane that cannot be resolved by conventional TEM [55].

Fig. 7 highlights that the microstructural features within the deformed region changes with temperature, accompanied by an increase in plastic zone size. To compare between the observed plastically deformed region below the indents with the theoretical prediction, the plastic zone size a_{pz} was calculated according to the modified Nix-Gao model [56,57], where $a_{pz} = f{\cdot}a_c$, (where $a_c = h/\tan\theta$, and θ is the angle between surface and indenter and h is the indentation depth). The factor f (equal to 1 in the original Nix-Gao model [58], and greater than 1 in the modified one [56,57]), relates the contact radius to the plastic zone size, and depends on the material and its crystallographic orientation. From finite element simulations of cube corner indentation of *f.c.c.* Cu in Ref. [57], $f = 2.4$ was estimated. The theoretically predicted plastic zone regions, according to $a_{pz} = f{\cdot}a_c$, are indicated for both temperatures in Fig. 7a,c, for both $f = 1$ and $f = 2.4$ and with $\theta = 47.7^\circ$ for the cube corner indenter. It is observed that for $f = 2.4$ (where $a_{pz} =$ 1280 nm at 25 °C and 1580 nm at 450 °C), the theoretically predicted plastic zone size matches reasonably with the deformed zones observed from TEM, although it appears slightly larger for the indent at 25 °C. It is to be noted that some differences can occur due to slight misalignment of the lamella with respect to the indent centre, the effect of stresses at the corner of the indent and also due to the tendency of the intermetallic phase to highly concentrate deformation onto individual planes at ambient temperature. This increase in the plastic zone size with depth of indentation of $CaAl_2$ Laves phase, equivalent to the behaviour of *f.c.c.* metals, confirms that the observed decrease in hardness and the BDT of $CaAl_2$ intermetallic is controlled by enhanced dislocation mediated plasticity at elevated temperatures which can blunt the cracks and restrict brittle failure.

The limited plasticity of Laves phases below the BDTT is generally attributed to restricted dislocation activity within their complex close-packed structures. Initially, synchroshear was proposed as the sole dislocation mechanism [59–61]. A high lattice friction for dislocation glide has also been considered to hinder dislocation activity at RT for Laves phases [62,63]. From the room temperature activation volume of $C15$ $CaAl_2$ ($\sim 3.75b^3$, where b is the Burgers vector) [18], it was not possible to definitively determine if the deformation was governed by overcoming Peierls resistance. Here, the RT lattice friction stress of $CaAl_2$ intermetallic was estimated from the nanoindentation hardness data in Section 3.1 by following the method proposed by Qui *et al.* [64], as outlined in the Supplementary Information. Considering a perfect $a/2\langle 1\,1\,0\rangle$ dislocation with $b = 0.5656$ nm for this analysis in $CaAl_2$, the friction stress is estimated as 580 MPa, which lies in the range of values of friction stress (0.4 to 5.6 GPa) reported for other $C15$ Laves phases [65].

The enhancement of plasticity above the BDTT for many transition metal $C15$ Laves phases has been attributed to increased dislocation motion due to thermally activated processes such as creep deformation [4], while for some Laves phases it has been attributed to a Peierls mechanism due to high strain rate dependence and low activation volume [25,66]. The BDTT of the $CaAl_2$ Laves phase ($\sim 0.55\ T_m$) in the present case as well as other transition metal $C15$ Laves phases [4], is above a homologous temperature of $0.5\ T_m$ consistent with temperatures required for thermally-activated creep process. Noticeable creep deformation in $CaAl_2$ can be observed in Fig. 1b from the increased time-dependent displacement during the constant load hold segment in the nanoindentation tests at high temperatures (450 °C and above). The indentation creep behaviour of $CaAl_2$ was analysed for the highest temperatures (*i.e.* 550 °C and 580 °C with the longest holding times) from the corresponding indentation strain rate and hardness from nanoindentation results, and is presented in Fig. S6 of the Supplementary Information. The time-dependent increase in displacement and decrease in hardness during the constant load hold segment at 550 °C and 580 °C resembles typical creep behaviour (see Fig. S6a). The indentation strain rate was computed at these temperatures as the ratio of indentation velocity dh/dt to the indentation depth h [67]. After an initial rapid decrease, the strain rate varied almost linearly with hardness (see Fig. S6b), proportional to the contact stress. Interestingly, the indentation stress exponent (*i.e.* the slope of the indentation strain rate versus hardness curve in Fig. S6b) obtained for $CaAl_2$ of ~3 to 3.2 is similar to the creep stress exponent of approximately 3.5 reported from compression creep tests of other *C*15 Laves phases [4], and is indicative of dislocation creep [68]. Decoupling additional effects of temperature-dependent critical resolved shear stress and effect on high temperature plasticity would require further studies using micropillar compression. Overall, the high BDTT of 450–500 °C obtained for $CaAl_2$ suggests that this intermetallic will not undergo a loss in its strength due to enhanced plasticity at the elevated temperatures of ~200 °C desired for Mg-rich alloys [12], thereby maintaining the overall alloy strength.

5. Conclusions

- Indentation-based testing using nanoindentation and micropillar splitting were used to estimate the nanoscale BDTT of the *C*15 $CaAl_2$ Laves phase and provide quantitative insights into the high-temperature deformation behaviour of this material.
- A significant decrease in nanoindentation hardness occurred at ~450–500 °C, with distinct changes in the deformation features around the indents due to increase in size of the residual impression at and above 450 °C and disappearance of surface cracks around 300 °C. This implies a change in the deformation behaviour with temperature for the $CaAl_2$ Laves phase.
- Elevated temperature micropillar splitting revealed brittle pillar splitting up to 300 °C, with straight crack propagation from the centre to the edge of the pillar. The apparent fracture toughness remained nearly constant up to 150 °C, followed by a sharp increase at 300 °C. No pillar splitting occurred at 400 °C and above due to considerable plastic deformation.
- A comparison of the nanoindentation and micropillar splitting results indicate that $CaAl_2$ remains brittle up to 300 °C, followed by increasing microplasticity between 300–400 °C which can cause crack tip shielding but not affect the nanoindentation hardness. Finally, at ~450 °C and above a transition to a more ductile behaviour occurs with a pronounced decrease in hardness due to a more uniform dislocation activity and the absence of brittle pillar splitting.
- TEM examination of the deformed microstructure below the indents revealed slip bands and small cracks in the deformed zone under an indent made at 25 °C. At 450 °C, the deformation zone extends ~25 % further and reveals a more uniformly distributed entanglement of dislocations.
- Nanoindentation hold segments reveal creep above the BDTT with creep stress exponents indicative of dislocation creep at the highest test temperatures, suggesting that the BDT of $CaAl_2$ can be driven by thermally-activated effects on dislocation motion leading to creep.

Declaration of Generative AI and AI-assisted technologies in the writing process

During the preparation of this work the author(s) used ChatGPT (OpenAI) in order to improve the readability of some text sections. After using this tool/service, the author(s) reviewed and edited the content as needed and take(s) full responsibility for the content of the publication.

CRediT authorship contribution statement

Anwesha Kanjilal: Writing – review & editing, Writing – original draft, Visualization, Methodology, Investigation, Formal analysis, Data curation, Conceptualization. **Ali Ahmadian:** Writing – review & editing, Visualization, Methodology, Investigation. **Martina Freund:** Writing – review & editing, Methodology, Investigation. **Pei-Ling Sun:** Writing – review & editing, Methodology, Investigation. **Sandra Korte-Kerzel:** Writing – review & editing, Supervision, Funding acquisition. **Gerhard Dehm:** Writing – review & editing, Supervision, Project administration, Funding acquisition, Conceptualization. **James P. Best:** Writing – review & editing, Supervision, Project administration, Methodology, Formal analysis, Conceptualization.

Declaration of competing interest

The authors declare that they have no known competing financial interests or personal relationships that could have appeared to influence the work reported in this paper.

Data availability

Underlying data for this publication is available at DOI: 10.5281/zenodo.13139961.

Acknowledgements

The authors gratefully acknowledge the financial assistance from Deutsche Forschungsgemeinschaft (DFG) within projects B06, A05 and Z of Collaborative Research Center (SFB) 1394 “Structural and Chemical Atomic Complexity - from defect phase diagrams to material properties”, project number 409476157. Authors thank Uzair Rehman for facilitating the high temperature scratch experiments, and Leon Christiansen and Dr. Sebastian Schädler (Carl Zeiss Microscopy Customer Center, Europe) for assistance in micropillar fabrication. The authors also thank Dr. Frank Stein for meaningful scientific discussions.

Appendix A. Supplementary data

Supplementary data to this article can be found online at https://doi.org/10.1016/j.matdes.2024.113206.

References

[1] F. Stein, A. Leineweber, Laves phases: a review of their functional and structural applications and an improved fundamental understanding of stability and properties, J. Mater. Sci. 56 (2021) 5321–5427, https://doi.org/10.1007/s10853-020-05509-2.
[2] R. Vincent, Precipitation around welds in the nickel-base superalloy, Inconel 718, Acta Metall. 33 (1985) 1205–1216, https://doi.org/10.1016/0001-6160(85)90231-7.
[3] Y. Hosoi, N. Wade, S. Kunimitsu, T. Urita, Precipitation behavior of laves phase and its effect on toughness of 9Cr-2Mo Ferritic-martensitic steel, J. Nucl. Mater. 141–143 (1986) 461–467, https://doi.org/10.1016/S0022-3115(86)80083-6.
[4] A. Von Keitz, G. Sauthoff, Laves phases for high temperatures—Part II: Stability and mechanical properties, Intermetallics 10 (2002) 497–510, https://doi.org/10.1016/S0966-9795(02)00025-0.
[5] J.H. Zhu, L.M. Pike, C.T. Liu, P.K. Liaw, Point defects in binary laves phase alloys, Acta Mater. 47 (1999) 2003–2018, https://doi.org/10.1016/S1359-6454(99)00090-7.
[6] F.C. Frank, J.S. Kasper, Complex alloy structures regarded as sphere packings. I. Definitions and basic principles, Acta Cryst 11 (1958) 184–190, https://doi.org/10.1107/S0365110X58000487.
[7] F.C. Frank, J.S. Kasper, Complex alloy structures regarded as sphere packings. II. Analysis and classification of representative structures, Acta Crystallogr. 12 (1959) 483–499, https://doi.org/10.1107/S0365110X59001499.
[8] S.A. Azmi, A. Michalcová, L. Senčekova, M. Palm, Microstructure and mechanical properties of Fe-Al-Nb-B alloys, MRS Adv. 2 (2017) 1353–1359, https://doi.org/10.1557/adv.2017.138.
[9] R. Krein, A. Schneider, G. Sauthoff, G. Frommeyer, Microstructure and mechanical properties of Fe3Al-based alloys with strengthening boride precipitates, Intermetallics 15 (2007) 1172–1182, https://doi.org/10.1016/j.intermet.2007.02.005.
[10] H.L. Su, M. Harmelin, P. Donnadieu, C. Baetzner, H.J. Seifert, H.L. Lukas, G. Effenberg, F. Aldinger, Experimental investigation of the Mg-Al phase diagram from 47 to 63 at.% Al, J. Alloy. Compd. 247 (1997) 57–65, https://doi.org/10.1016/S0925-8388(96)02595-9.
[11] H.N. Mathur, V. Maier-Kiener, S. Korte-Kerzel, Deformation in the γ-Mg17Al12 phase at 25–278 °C, Acta Mater. 113 (2016) 221–229, https://doi.org/10.1016/j.actamat.2016.05.001.
[12] A.A. Luo, Recent magnesium alloy development for automotive powertrain applications, MSF 419–422 (2003) 57–66, https://doi.org/10.4028/www.scientific.net/MSF.419-422.57.
[13] N.P. Lyakishev, Phase diagrams of binary metallic systems, Mashinostroenie, Moscow 1 (1996) 996.

[14] L.L. Rokhlin, T.V. Dobatkina, N.I. Nikitina, I.E. Tarytina, Calcium-alloyed magnesium alloys, Met. Sci. Heat Treat. 51 (2009) 164–169, https://doi.org/10.1007/s11041-009-9127-7.

[15] H.A. Elamami, A. Incesu, K. Korgiopoulos, M. Pekguleryuz, A. Gungor, Phase selection and mechanical properties of permanent-mold cast Mg-Al-Ca-Mn alloys and the role of Ca/Al ratio, J. Alloy. Compd. 764 (2018) 216–225, https://doi.org/10.1016/j.jallcom.2018.05.309.

[16] A. Suzuki, N.D. Saddock, J.W. Jones, T.M. Pollock, Structure and transition of eutectic (Mg, Al)2Ca Laves phase in a die-cast Mg–Al–Ca base alloy, Scr. Mater. 51 (2004) 1005–1010, https://doi.org/10.1016/j.scriptamat.2004.07.011.

[17] G. Zhu, L. Wang, J. Wang, J. Wang, J.-S. Park, X. Zeng, Highly deformable Mg–Al–Ca alloy with Al2Ca precipitates, Acta Mater. 200 (2020) 236–245, https://doi.org/10.1016/j.actamat.2020.09.006.

[18] M. Freund, D. Andre, P.L. Sun, C.F. Kusche, S. Sandlöbes-Haut, H. Springer, S. Korte-Kerzel, Plasticity of the C15-CaAl2 Laves phase at room temperature, Mater. Des. 225 (2023) 111504, https://doi.org/10.1016/j.matdes.2022.111504.

[19] J.P. Best, A. Kanjilal, A. Ghafarollahi, U. Rehman, C. Tian, H. Bishara, M.K. Bhat, L. Christiansen, E. Bitzek, F. Stein, G. Dehm, Fracture of the C15 CaAl2 Laves phase at small length scales, J. Mater. Sci. (2024), https://doi.org/10.1007/s10853-024-09887-9.

[20] S. Korte-Kerzel, Microcompression of brittle and anisotropic crystals: recent advances and current challenges in studying plasticity in hard materials, MRS Commun. 7 (2017) 109–120, https://doi.org/10.1557/mrc.2017.15.

[21] F. Östlund, K. Rzepiejewska-Malyska, K. Leifer, L.M. Hale, Y. Tang, R. Ballarini, W. W. Gerberich, J. Michler, Brittle-to-ductile transition in uniaxial compression of silicon pillars at room temperature, Adv. Funct. Mater. 19 (2009) 2439–2444, https://doi.org/10.1002/adfm.200900418.

[22] F. Östlund, P.R. Howie, R. Ghisleni, S. Korte, K. Leifer, W.J. Clegg, J. Michler, Ductile–brittle transition in micropillar compression of GaAs at room temperature, Philos. Mag. 91 (2011) 1190–1199, https://doi.org/10.1080/14786435.2010.509286.

[23] P. Paufler, Early work on Laves phases in East Germany, Intermetallics 19 (2011) 599–612, https://doi.org/10.1016/j.intermet.2010.11.032.

[24] M. Yoshida, T. Takasugi, The alloying effect on the high temperature deformation of Laves phase NbCr2 intermetallic compound, Mater. Sci. Eng. A 234–236 (1997) 873–876, https://doi.org/10.1016/S0921-5093(97)00338-9.

[25] P. Paufler, G.E.R. Schulze, Plastic deformation of the intermetallic compound MgZn$_2$, Physica Status Solidi (B) 24 (1967) 77–87, https://doi.org/10.1002/pssb.19670240107.

[26] J.M. Wheeler, D.E.J. Armstrong, W. Heinz, R. Schwaiger, High temperature nanoindentation: The state of the art and future challenges, Curr. Opin. Solid State Mater. Sci. 19 (2015) 354–366, https://doi.org/10.1016/j.cossms.2015.02.002.

[27] M. Sebastiani, K.E. Johanns, E.G. Herbert, F. Carassiti, G.M. Pharr, A novel pillar indentation splitting test for measuring fracture toughness of thin ceramic coatings, Philos. Mag. 95 (2015) 1928–1944, https://doi.org/10.1080/14786435.2014.913110.

[28] J.P. Best, J. Wehrs, M. Polyakov, M. Morstein, J. Michler, High temperature fracture toughness of ceramic coatings evaluated using micro-pillar splitting, Scr. Mater. 162 (2019) 190–194, https://doi.org/10.1016/j.scriptamat.2018.11.013.

[29] J.P. Best, J. Zechner, J.M. Wheeler, R. Schoeppner, M. Morstein, J. Michler, Small-scale fracture toughness of ceramic thin films: the effects of specimen geometry, ion beam notching and high temperature on chromium nitride toughness evaluation, Philos. Mag. 96 (2016) 3552–3569, https://doi.org/10.1080/14786435.2016.1223891.

[30] C.M. Lauener, L. Petho, M. Chen, Y. Xiao, J. Michler, J.M. Wheeler, Fracture of Silicon: Influence of rate, positioning accuracy, FIB machining, and elevated temperatures on toughness measured by pillar indentation splitting, Mater. Des. 142 (2018) 340–349, https://doi.org/10.1016/j.matdes.2018.01.015.

[31] B.N. Jaya, J.M. Wheeler, J. Wehrs, J.P. Best, R. Soler, J. Michler, C. Kirchlechner, G. Dehm, Microscale fracture behavior of single crystal silicon beams at elevated temperatures, Nano Lett. 16 (2016) 7597–7603, https://doi.org/10.1021/acs.nanolett.6b03461.

[32] J. Ast, J.J. Schwiedrzik, J. Wehrs, D. Frey, M.N. Polyakov, J. Michler, X. Maeder, The brittle-ductile transition of tungsten single crystals at the micro-scale, Mater. Des. 152 (2018) 168–180, https://doi.org/10.1016/j.matdes.2018.04.009.

[33] S. Sawamura, R. Limbach, H. Behrens, L. Wondraczek, Lateral deformation and defect resistance of compacted silica glass: Quantification of the scratching hardness of brittle glasses, J. Non Cryst. Solids 481 (2018) 503–511, https://doi.org/10.1016/j.jnoncrysol.2017.11.035.

[34] H. Tsybenko, F. Farzam, G. Dehm, S. Brinckmann, Scratch hardness at a small scale: Experimental methods and correlation to nanoindentation hardness, Tribol. Int. 163 (2021) 107168, https://doi.org/10.1016/j.triboint.2021.107168.

[35] P. Maas, Y. Mizumoto, Y. Kakinuma, S. Min, Anisotropic brittle-ductile transition of monocrystalline sapphire during orthogonal cutting and nanoindentation experiments, Nanotechnol. Precis. Eng. 1 (2018) 157–171, https://doi.org/10.1016/j.npe.2018.09.005.

[36] P. Patil, S. Lee, G. Dehm, S. Brinckmann, Influence of crystal orientation on twinning in austenitic stainless-steel during single micro-asperity tribology and nanoindentation, Wear 504–505 (2022) 204403, https://doi.org/10.1016/j.wear.2022.204403.

[37] C.H. Kirsten, P.F. Paufler and G.E.R. Schulze, Zur plastischen verformung intermetallischer verbindungen, (1963).

[38] M. Freund, D. Andre, C. Zehnder, H. Rempel, D. Gerber, M. Zubair, S. Sandlöbes-Haut, J.-S.-K.-L. Gibson, S. Korte-Kerzel, Plastic deformation of the CaMg2 C14-Laves phase from 50–250°C, Materialia 20 (2021) 101237, https://doi.org/10.1016/j.mtla.2021.101237.

[39] D. Andre, M. Freund, U. Rehman, W. Delis, M. Felten, J. Nowak, C. Tian, M. Zubair, L. Tanure, L. Abdellaoui, H. Springer, J.P. Best, D. Zander, G. Dehm, S. Sandlöbes-Haut, S. Korte-Kerzel, Metallographic preparation methods for the Mg based system Mg-Al-Ca and its Laves phases, Mater. Charact. 192 (2022) 112187, https://doi.org/10.1016/j.matchar.2022.112187.

[40] P. Sudharshan Phani, W.C. Oliver, A critical assessment of the effect of indentation spacing on the measurement of hardness and modulus using instrumented indentation testing, Mater. Design 164 (2019) 107563, https://doi.org/10.1016/j.matdes.2018.107563.

[41] W.C. Oliver, G.M. Pharr, An improved technique for determining hardness and elastic modulus using load and displacement sensing indentation experiments, J. Mater. Res. 7 (1992) 1564–1583, https://doi.org/10.1557/JMR.1992.1564.

[42] M. Ghidelli, M. Sebastiani, K.E. Johanns, G.M. Pharr, Effects of indenter angle on micro-scale fracture toughness measurement by pillar splitting, J. Am. Ceram. Soc. 100 (2017) 5731–5738, https://doi.org/10.1111/jace.15093.

[43] J. Ast, M. Ghidelli, K. Durst, M. Göken, M. Sebastiani, A.M. Korsunsky, A review of experimental approaches to fracture toughness evaluation at the micro-scale, Mater. Des. 173 (2019) 107762, https://doi.org/10.1016/j.matdes.2019.107762.

[44] D.J. Thoma, F. Chu, P. Peralta, P.G. Kotula, K.C. Chen, T.E. Mitchell, Elastic and mechanical properties of Nb(Cr, V)2 C15 Laves phases, Mater. Sci. Eng. A 239–240 (1997) 251–259, https://doi.org/10.1016/S0921-5093(97)00589-3.

[45] M. Palm, F. Stein, G. Dehm, Iron aluminides, Annu. Rev. Mat. Res. 49 (2019) 297–326, https://doi.org/10.1146/annurev-matsci-070218-125911.

[46] D. Risanti, J. Deges, L. Falat, S. Kobayashi, J. Konrad, M. Palm, B. Pöter, A. Schneider, C. Stallybrass, F. Stein, Dependence of the brittle-to-ductile transition temperature (BDTT) on the Al content of Fe–Al alloys, Intermetallics 13 (2005) 1337–1342, https://doi.org/10.1016/j.intermet.2005.02.007.

[47] S. Korte, J.S. Barnard, R.J. Stearn, W.J. Clegg, Deformation of silicon – Insights from microcompression testing at 25–500°C, Int. J. Plast 27 (2011) 1853–1866, https://doi.org/10.1016/j.ijplas.2011.05.009.

[48] T. Suzuki, T. Ohmura, Ultra-microindentation of silicon at elevated temperatures, Philos. Mag. A 74 (1996) 1073–1084, https://doi.org/10.1080/01418619608239708.

[49] C. St. John, The brittle-to-ductile transition in pre-cleaved silicon single crystals, Philos. Mag.: J. Theor. Exp. Appl. Phys. 32 (1975) 1193–1212, https://doi.org/10.1080/14786437508228099.

[50] P. Gumbsch, J. Riedle, A. Hartmaier, H.F. Fischmeister, Controlling factors for the brittle-to-ductile transition in tungsten single crystals, Science 282 (1998) 1293–1295, https://doi.org/10.1126/science.282.5392.1293.

[51] A. Giannattasio, S.G. Roberts, Strain-rate dependence of the brittle-to-ductile transition temperature in tungsten, Philos. Mag. 87 (2007) 2589–2598, https://doi.org/10.1080/14786430701253197.

[52] J.P. Best, J. Zechner, I. Shorubalko, J.V. Oboňa, J. Wehrs, M. Morstein, J. Michler, A comparison of three different notching ions for small-scale fracture toughness measurement, Scr. Mater. 112 (2016) 71–74, https://doi.org/10.1016/j.scriptamat.2015.09.014.

[53] Z. Xie, D. Chauraud, A. Atila, E. Bitzek, S. Korte-Kerzel, J. Guénolé, Thermally activated nature of synchro-Shockley dislocations in Laves phases, Scr. Mater. 235 (2023) 115588, https://doi.org/10.1016/j.scriptamat.2023.115588.

[54] W. Luo, Z. Xie, P.-L. Sun, J.-S.-K.-L. Gibson, S. Korte-Kerzel, Plasticity of the Nb-rich µ-Co7Nb6 phase at room temperature and 600°C, Acta Mater. 246 (2023) 118720, https://doi.org/10.1016/j.actamat.2023.118720.

[55] W. Luo, Z. Xie, S. Zhang, J. Guénolé, P.-L. Sun, A. Meingast, A. Alhassan, X. Zhou, F. Stein, L. Pizzagalli, B. Berkels, C. Scheu, S. Korte-Kerzel, Tailoring the plasticity of topologically close-packed phases via the crystals' fundamental building blocks, Adv. Mater. 35 (2023) 2300586, https://doi.org/10.1002/adma.202300586.

[56] K. Durst, B. Backes, M. Göken, Indentation size effect in metallic materials: Correcting for the size of the plastic zone, Scr. Mater. 52 (2005) 1093–1097, https://doi.org/10.1016/j.scriptamat.2005.02.009.

[57] K. Durst, B. Backes, O. Franke, M. Göken, Indentation size effect in metallic materials: Modeling strength from pop-in to macroscopic hardness using geometrically necessary dislocations, Acta Mater. 54 (2006) 2547–2555, https://doi.org/10.1016/j.actamat.2006.01.036.

[58] W.D. Nix, H. Gao, Size Effects in Crystalline Materials: A Law for Strain Gradient Plasticity, 46 (1998) 411–425.

[59] A.V. Kazantzis, M. Aindow, G.K. Triantafyllidis, J.T.M. De Hosson, On the self-pinning character of synchro-Shockley dislocations in a Laves phase during strain rate cyclical compressions, Scr. Mater. 59 (2008) 788–791, https://doi.org/10.1016/j.scriptamat.2008.06.024.

[60] P.M. Hazzledine, P. Pirouz, Synchroshear transformations in Laves phases, Scr. Metall. Mater. 28 (1993) 1277–1282, https://doi.org/10.1016/0956-716X(93)90468-8.

[61] M.F. Chisholm, S. Kumar, P. Hazzledine, Dislocations in complex materials, Science 307 (2005) 701–703, https://doi.org/10.1126/science.1105962.

[62] J.D. Livingston, Laves-phase superalloys, Physica Status Solidi A (Appl. Res.); (Germany) 131:2 (1992). https://doi.org/10.1002/pssa.2211310215.

[63] W. Luo, C. Kirchlechner, J. Li, G. Dehm, F. Stein, Composition dependence of hardness and elastic modulus of the cubic and hexagonal NbCo2 Laves phase polytypes studied by nanoindentation, J. Mater. Res. 35 (2020) 185–195, https://doi.org/10.1557/jmr.2019.384.

[64] X. Qiu, Y. Huang, W.D. Nix, K.C. Hwang, H. Gao, Effect of intrinsic lattice resistance in strain gradient plasticity, Acta Mater. 49 (2001) 3949–3958, https://doi.org/10.1016/S1359-6454(01)00299-3.

[65] L. Liu, P. Shen, X. Wu, R. Wang, W. Li, Q. Liu, First-principles calculations on the stacking fault energy, surface energy and dislocation properties of NbCr2 and

HfCr2, Comput. Mater. Sci 140 (2017) 334–343, https://doi.org/10.1016/j.commatsci.2017.08.030.

[66] Y. Ohba, N. Sakuma, High temperature-room temperature deformation behavior of MgCu2 laves phase intermetallic compound, Acta Metall. 37 (1989) 2377–2384, https://doi.org/10.1016/0001-6160(89)90035-7.

[67] P.S. Phani, W.C. Oliver, A direct comparison of high temperature nanoindentation creep and uniaxial creep measurements for commercial purity aluminum, Acta Mater. 111 (2016) 31–38, https://doi.org/10.1016/j.actamat.2016.03.032.

[68] M.E. Kassner, Fundamentals of Creep in Metals and Alloys, Butterworth-Heinemann, 2015.

10. Publication 6

Metallurgical synthesis methods for Mg-Al-Ca scientific model materials

W. Luo, L. Tanure, M. Felten, J. Nowak, W. Delis, M. Freund, N. Ayeb, D. Zander, C. Thomas, M. Feuerbacher, S. Sandlöbes-Haut, S. Korte-Kerzel, H. Springer

[a] RWTH Aachen University, Sustainable Ferrous Metallurgy

[b] RWTH Aachen University, Corrosion and Corrosion Protection

[c] RWTH Aachen University, Institute of Physical Metallurgy and Materials Physics

[d] Ernst Ruska-Centre for Microscopy and Spectroscopy with Electrons, Forschungszentrum Jülich GmbH

[e] Max-Planck-Institut für Eisenforschung GmbH

Metallurgical and Materials Transactions A, 2024, r**eproduced with permission of Springer Nature.**

https://doi.org/10.1007/s11661-024-07655-7

Short Summary

Mg-based alloys are industrially used for structural applications, both as solid solutions alloys and as composites containing intermetallic compounds. However, a further development in terms of mechanical properties requires the investigation of underlying causalities between synthesis, processing and microstructure to adjust the mechanical and the corrosion properties, ideally down to the near atomic scale. Such fundamental scientific investigations with high resolution characterisation techniques require model materials of exceptionally high purity and strictly controlled microstructure e.g. with respect to grain size, morphology, chemical homogeneity as well as content and size of oxide inclusions. In this context, the Mg-Al-Ca system appears exceptionally challenging from a metallurgical perspective due to the high reactivity and high vapor pressures, so that conventional industrial techniques cannot be successfully deployed. Here, we demonstrate the applicability of various scientific synthesis methods from arc melting over solution growth to diffusion couples, extending to effects and parameters for thermo-mechanical processing. Suitable pathways to overcome the specific challenges of the Mg-Al-Ca system are demonstrated, as well as the persistent limitations of the current state of the art laboratory metallurgy technology.

L. Tanure and H. Springer conceived and designed the experiments. W. Luo wrote the manuscript. M. Felten, J. Nowak, D. Zander and W. Delis analysed the microstructures of Mg-Al-Ca solid solutions. N. Ayeb performed characterizations of the Mg-Al-Ca composites. **M. Freund** contributed to the characterizations of the Mg-Al-Ca intermetallics. C. Thomas and M. Feuerbacher contributed to the synthesis of the C36-Ca(Mg,Al)$_2$ Laves phase. S. Sandlöbes-Haut and S. Korte-Kerzel provided feedback and suggestions to improve the experiments. All authors contributed to discussion of the results and reviewed the manuscript.

ORIGINAL RESEARCH ARTICLE

Metallurgical Synthesis Methods for Mg-Al-Ca Scientific Model Materials

W. LUO, L. TANURE, M. FELTEN, J. NOWAK, W. DELIS, M. FREUND, N. AYEB,
D. ZANDER, C. THOMAS, M. FEUERBACHER, S. SANDLÖBES-HAUT,
S. KORTE-KERZEL, and H. SPRINGER

Further improving the mechanical and corrosion properties of Mg-based alloys requires the investigation of underlying causalities between synthesis, processing, and microstructure, ideally down to the near atomic scale. However, such investigations with high resolution characterisation techniques require model materials of exceptionally controlled chemical composition and microstructure. In this context, the Mg-Al-Ca system, being attractive for offering significant improvement of the inherent brittleness of Mg alloys, is exceptionally challenging from a metallurgical perspective due to the inclusion of components with high reactivity and vapor pressures. Here, we demonstrate the applicability of various synthesis methods from arc-melting over solution growth to diffusion couples, extending to parameters for thermomechanical processing. Suitable pathways to overcome the specific challenges of the Mg-Al-Ca system are demonstrated, as well as the persistent limitations of the current state-of-the-art metallurgical laboratory technology. Solid solution sheet or wrought materials are ideally produced by induction melting in steel crucibles and casting under elevated pressure, with intermittent annealing steps between hot rolling passes to ensure homogenous chemical composition without excessive grain growth. Composite microstructures strongly depend on the solidification rate, and special care needs to be taken with regards to crucible reactions with increasing Al concentrations. Binary intermetallic compounds can be successfully produced in bulk by a variety of techniques, but the interplay between reactivity and evaporation of the melt when both Ca and Al are present required more complex approaches such as the Bridgman method for the synthesis of ternary compounds.

https://doi.org/10.1007/s11661-024-07655-7

I. INTRODUCTION

THE application of lightweight components in the aeronautic and automotive industry has both environmental and economic benefits.[1] Mg-based alloys are especially attractive due to their low density compared to steels, aluminium, and even some polymer-based materials. The most common industrial production method for structural Mg materials is casting[2] after electric melting (either inductive or conductive) using steel crucibles and Cl-F-based flux protection. While fast and cost effective once the required tooling is set-up, the presence of typical casting artefacts such as inhomogeneous grain size distribution and porosity is often resulting in comparatively low mechanical performance, leading to the application of Al-Zn alloyed compositions or even composite structures optimized for effective processing. Wrought alloys on the other hand,[3] often based on Mn and rare earth element additions, generally offer an improved property profile, and are typically shaped by hot extrusion techniques—sometimes coupled with additional cold-rolling and ageing treatments—into profiles and shaped slabs for further machining operations. However, most of the commercial Mg alloys typically still suffer from limited strength and low ductility inherent to the hexagonal crystal structure of Mg.[4] Recent studies show that Mg-based solid solution alloys with a small amount (typically below 1 wt pct) of

---

W. LUO, L. TANURE, and M. N. AYEB are with the RWTH Aachen University, Sustainable Ferrous Metallurgy, Intzestrasse 10, 52072 Aachen, Germany. M. FELTEN, J. NOWAK, and D. ZANDER are with the RWTH Aachen University, Corrosion and Corrosion Protection, Intzestrasse 5, 52072 Aachen, Germany. W. DELIS, M. FREUND, S. SANDLÖBES-HAUT, and S. KORTE-KERZEL are with the RWTH Aachen University, Institute of Physical Metallurgy and Materials Physics, Kopernikusstrasse 14, 52074 Aachen, Germany. C. THOMAS and M. FEUERBACHER are with the Ernst Ruska-Centre for Microscopy and Spectroscopy with Electrons, Forschungszentrum Jülich GmbH, Wilhelm-Johnen-Straße, 52428 Jülich, Germany. H. SPRINGER is with the RWTH Aachen University, Sustainable Ferrous Metallurgy and also with the Max-Planck-Institut für Eisenforschung GmbH, Max-Planck-Strasse 1, 40237 Düsseldorf, Germany. Contact e-mail: hauke.springer@iehk.rwth-aachen.de
Manuscript submitted June 7, 2024; accepted November 6, 2024.

Ca and Al exhibit improved formability and ductility due to the activation of $\langle c + a \rangle$ slip.[5] With increasing the Al and Ca content, different types of intermetallic phases precipitate in the Mg-Al-Ca alloys, resulting in a composite structure.[6] The precipitates change from $Mg_{17}Al_{12}$ to the C15-$CaAl_2$, C36-$Ca(Mg,Al)_2$ and C14-$CaMg_2$ Laves phases with increasing Ca/Al ratio.[7,8] A continuous Laves phase network reinforces the soft Mg-matrix and improve the creep resistance of the Mg-Al-Ca alloys.[9–11] However, the knowledge of the impact on mechanical[12–14] and corrosion properties[15–17] of the Laves phase is still limited, motivating further investigations based on suitable samples and model materials. However, such fundamental investigations require the application of high resolution characterisation techniques such as transmission electron microscopy, micropillar compression testing and atom probe tomography, which in turn necessitate model materials of exceptionally controlled chemical composition and microstructure, *e.g.*, with respect to the grain size, morphology, and chemical homogeneity, as well as the content and size of oxide inclusions.

The main challenges in the production and processing of Mg-Al-Ca alloys are related to the high reactivity[17] and the high vapor pressures[3,18] especially of Mg and Ca. Although the synthesis of solid solutions and Mg-Al-Ca composites on an industrial scale is feasible,[19,20], it is more challenging to prepare the Mg-Al-Ca alloys for specific scientific purposes, *i.e.*, achieving a desired chemical composition and precisely controlling the microstructure with regards to constitution, grain size and morphology of the intermetallic phases. Induction melting for example under a protective atmosphere with elevated pressure can reduce the evaporation of Mg and Ca, while steel crucibles can be utilised by exploiting the low mutual solubility and difference in melting temperature between Mg and Ca with Fe, respectively. However, this does not hold true when Al is added to the melt.[21] Ceramic crucibles, on the other hand, are typically not suitable as they are severely attacked by the highly reactive Mg and Ca. While a limited lifespan of crucibles due to chemical interactions with Mg-Al-Ca melts is not a direct problem for synthesizing scientific model materials (albeit increasing the cost of sample production substantially), it does lead to undesired contamination of the melt, for example with oxide inclusions, and additional elements affecting microstructure and properties thereafter, for example by the formation of Fe-aluminides. Furthermore, independent of the utilized melting technology and crucible material, phenomena such as grain boundary precipitation and intergranular segregation need to be addressed by subsequent thermomechanical processing for as-cast Mg-based solid solution materials. However, the reduced ductility of composites—induced by the intermetallic compounds which in parallel increase the strength—typically renders such procedures unfeasible.[22]

The underlying phenomena of plasticity as well as the co-deformation processes with the surrounding Mg-matrix illustrate the motivation for the investigation of binary and ternary[23–27] intermetallic phases of the Mg-Al-Ca system. Similar basic considerations apply as those for the synthesis of solid solution and composite materials: while induction melting using a steel crucible under Ar atmosphere is applicable to the synthesis of C14-$CaMg_2$ Laves phase, it is not suitable for the synthesis of the C15-$CaAl_2$ Laves phase due to the Al-induced contamination with Fe. On the other hand, the absence of Mg with its low boiling point now allows for considering arc-melting without an expected severe evaporation by its extreme local temperatures. However, the inherent brittleness of the Laves phases[28] needs to be considered as well for all liquid metallurgical techniques, as the stresses from solidification and further cooling might lead to their cracking up to total disintegration of the solidified ingot, even after the melting procedure itself could be performed successfully. Casting into a pre-heated alumina crucible followed by slow cooling for example was reported to reduce thermal stress during cooling.[29] However, alumina crucibles cannot be used in synthesis of the C14-$CaMg_2$ and C15-$CaAl_2$ Laves phases synthesis due to the high reactivity of Ca. It has also been reported that the $Mg_{17}Al_{12}$ intermetallic phase with a small amount of a second phase can be produced using an electrical resistance melting furnace in a graphite crucible under protective Ar atmosphere, but the potential formation of porosity and Al-carbides needs to be considered.[28] The majority of these challenges, *i.e.*, excessive crucible reactions and unwanted solidification phenomena, might be avoided using solid state synthesis techniques. Powder metallurgy, however, appears not favourable for the specific alloy system here, as the huge surface area of the Mg, Al and Ca powder particles substantially increases the risk of oxide inclusions and also poses a considerable health and safety risk by spontaneous combustion. More interesting are solid state diffusion couples, which are comparatively straightforward to fabricate for binary compounds, but appear more challenging for the most complex intermetallic compound of this system from a metallurgical perspective, namely the C36-$Ca(Mg,Al)_2$ Laves phase, due to its high Mg and Ca contents coupled with a narrow compositional and temperature range.[25,29]

Together with the published overview of respective metallographic preparation methods,[30] we explore the challenges and pitfalls in the corresponding synthesis procedures—ranging from induction melting, diffusion couples, flux-growth and Bridgman methods—of Mg-Al-Ca bulk materials in solid solution, composite and purely intermetallic configuration in the current study.

II. MATERIALS AND METHODS

The chemical compositions of the investigated materials in conjunction with the deployed synthesis techniques are summarized in Table I. The Mg-Al-Ca alloys were prepared from pure Mg (99.95 wt pct), Ca (98.8 wt pct) and Al (99.999 wt pct). The chemical analyses of the starting materials and the synthesized alloys were performed by inductively coupled plasma optical

Table I. Summary of the Metallurgical Synthesis Methods for the Mg-Al-Ca Solid Solutions, Composites and Intermetallics

Materials	Composition (Wt Pct)	Targeted Phases	Synthesis	Processing
Solid Solutions	Mg-1Al-0.5Ca Mg-1Al-0.05Ca Mg-1Al-0.1Ca Mg-1Al-0.2Ca Mg-2Al-0.05Ca Mg-2Al-0.1Ca Mg-2Al-0.2Ca	Mg	induction melting (60 kW furnace, Ar atmosphere of 0.8 and 15 bar, steel crucible) and casting (Cu moulds of 30x60 mm internal dimensions and wall thickness of 15 mm)	hot rolling at 450 °C, 5 passes with 10 pct reduction per pass, annealing at 500 °C for 24 h
Composites	Mg-6Al-2Ca Mg-5Al-3Ca Mg-4Al-4Ca	Mg + laves phase	induction melting (16 kW furnace, Ar atmosphere at 0.8 bar, steel crucible) and casting (Cu moulds of 25x65 mm internal dimensions and a wall thickness of 15 mm)	annealing (Ar atmosphere at 500 °C for 48 h, furnace cooling)
Intermetallic Compounds	Mg-45Ca	C14-CaMg$_2$	as composite materials	as-cast
	Al-42Ca	C15-CaAl$_2$	arc-melting on a water-cooled copper hearth under Ar atmosphere of 800 mbar	annealing (glass tube furnace at 600 °C for 24 h under Ar atmosphere)
	Mg-28Al-46Ca Mg-53Al-36Ca	C36-Ca(Mg,Al)$_2$ C15-CaAl$_2$	bridgman apparatus (cylindrical tantalum crucible sealed with 0.6 bar Ar, placed on a water-cooled cold finger heated to 900 °C, lowering with 5 mm/h)	as-cast

emission spectroscopy (ICP-OES). The metallographic preparation methods for characterizing the obtained Mg-Al-Ca alloys are explained in details elsewhere.[30] Selected samples were colour-etched with a picric acid-based solution for optical microscopy (OM; Leica DMR, Leica AG) observations. Microstructures of the alloys were characterized using scanning electron microscopy (SEM; Helios Nanolab 600i, FEI Inc.). The compositions of the phases in the alloys were determined by energy dispersive X-ray spectroscopy (EDS; EDAX Inc.). Phase analyses were carried out by electron backscatter diffraction (EBSD; Hikari, EDAX Inc.).

III. RESULTS AND DISCUSSION

A. *Mg-Al-Ca Solid Solutions*

The limited amount of Al within the solid solution materials (max. 2 wt pct) led to very low Fe contamination of the melt (< 0.0068 wt pct) despite the use of steel crucibles, which offered the additional benefit of being heated by the inductive field of the furnace coil, facilitating rapid heating and melting of the base materials. The elevated pressure of 15 bar was found to be beneficial for reducing the Mg evaporation by local overheating and simultaneously minimising shrinkage porosity during solidification after casting. As shown in Figure 1(a), the Mg-1Al-0.05 Ca alloy cast under high pressure Ar exhibit only a small amount of pores, which translated into a higher strength as well as ductility compared to materials prepared under conventional lower pressure (0.8 bar) conditions. A detailed analysis on the pore formation, size and dispersion—for example by X-ray tomography—as a function of atmospheric pressure during solidification of Mg alloys would be worth of future investigations. Microstructure and resulting mechanical properties of solid solution materials can be substantially improved by thermomechanical treatments (TMTs) such as hot rolling and subsequent annealing procedures, as they generally minimize porosity remaining in as-cast materials, reduce or at least homogenize the grain size, and reduce segregations by recrystallization and diffusion processes. The corresponding parameters, especially the temperature, has to be chosen based on the Mg-Al-Ca phase diagram.[25,29] On the one hand, the temperature should be as high as possible to facilitate recrystallization and diffusion processes, as well as dissolving any (here unwanted) intermetallic phases, which becomes especially for alloys close to the solubility limit of Mg. On the other hand, too high temperatures can cause grain growth, localized melting of segregated areas, and generally enhance surface oxidation when the TMT is performed in a non-protective atmosphere.

We found that a temperature of 450 °C ensured an optimum balance for the investigated alloy compositions. As with all other metallic structural materials, the other parameters such as reduction per pass, rolling diameter and speed, as well as surface preparation including the use of lubricants need to be carefully adjusted for the given geometries and targets of the

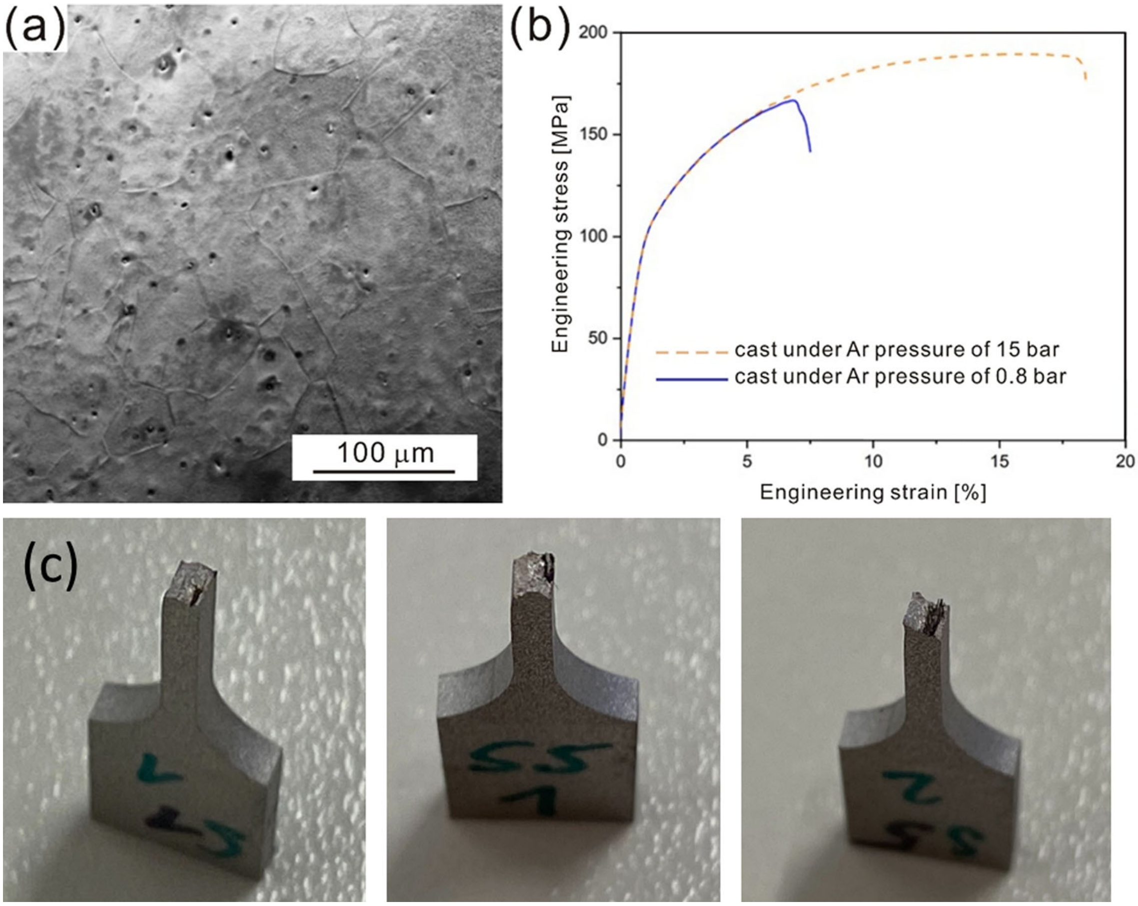

Fig. 1—(*a*) SEM overview of an Mg-1Al-0.05Ca (wt pct) alloy cast under Ar atmosphere with pressure of 15 bar. (*b*) Corresponding tensile testing results, illustrating the beneficial effects of limiting porosity by increasing the pressure within the melting and casting furnace. (*c*) Porosity in fractured tensile samples from material cast under 0.8 bar, causing the observed reduction in ductility. Parts of this Figure are being reproduced from Ref. [37] under license CC-BY-4.0.

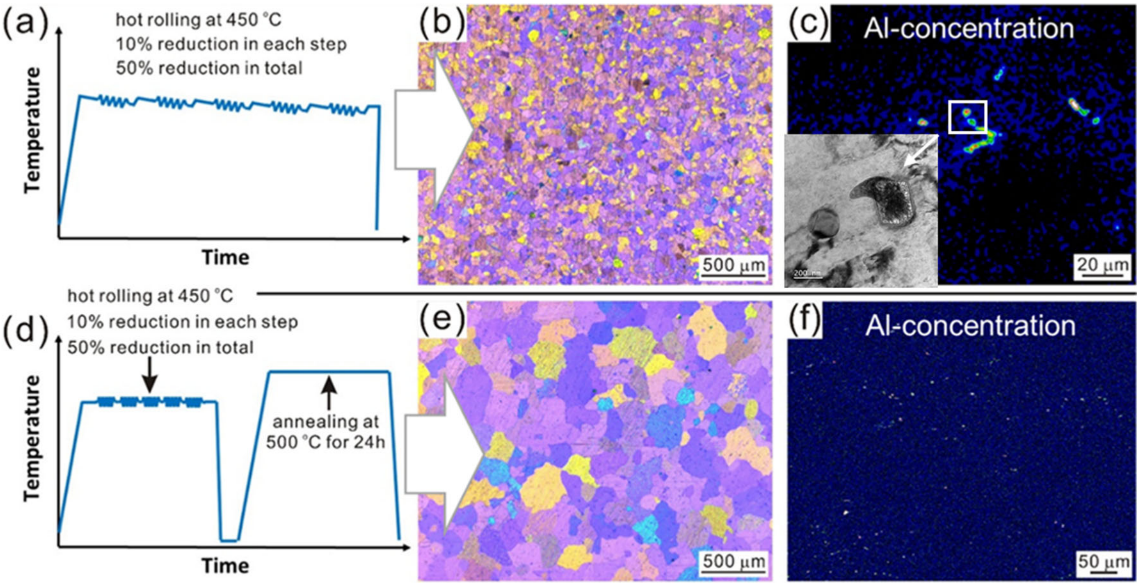

Fig. 2—Thermomechanical processing of a Mg-2Al-0.2Ca (wt pct) alloy. (*a*) hot rolling sequence and (*b*) corresponding OM overview image and (*c*) SEM-EDS map of Al (the areas in red and yellow indicate high concentrations of Al) showing traces of remaining segregations as well as Al-rich precipitates (TEM insert). After additional annealing at 500 °C for 24 h (*d*) significant grain growth can be observed (*e*) as well as successful improvement of chemical homogeneity (*f*). Parts of this Figure are being reproduced from Ref. [37] under license CC-BY-4.0.

TMT processing. Figure 2 outlines the effect of a final annealing treatment at 500 °C after hot rolling the Mg-2Al-0.2Ca (wt pct) alloy at 450 °C in five passes with 10 pct thickness reduction per pass, with reheating for 10 minutes between the individual passes. After the final pass the alloy was annealed at 450 °C for 15 minutes followed by quenching in water [Figure 2(a)]. The corresponding hot-rolled microstructure [Figure 2(b)] shows well recrystallised grains with an average size of 74 ± 6 μm, but with traces of intragranular segregations and most probably intermetallic precipitates visible in the EDS mappings [Figure 2(c)]. These detrimental phenomena—both from a mechanical as well as a corrosion perspective—could be successfully mitigated by additional annealing at 500 °C for 24 h followed by water quenching [Figures 2(d) through (f)]. However, this subsequent annealing also caused a significantly enlarged grain size. These finding suggest that a combined strategy consisting of (i) initial hot rolling to break up the as-cast microstructure, reducing the diffusion length and recrystallizing coarse dendritic structures followed by (ii) a prolonged homogenization annealing step, and (iii) final hot rolling—maybe even with additional cold-rolling beforehand—to refine the grain size would produce optimal mechanical properties. For that purpose, the initial dimensions of the cast blocks must be of sufficient size to allow for the required rolling reduction, while not getting too thin for both later testing procedures as well as too strong heat loss to the cold forming tools (rolls) during the TMT procedure.

B. *Mg-Al-Ca Composites*

Similar to the solid solution materials, Mg-Al-Ca composites consisting of a Mg solid solution matrix containing a network of Laves phases were successfully synthesized by induction melting using a steel crucible under protective Ar atmosphere. While Fe-Al intermetallic layers forming at the crucible wall can hinder the diffusion of Fe into the Al-containing melt,[31] the Fe contamination remained negligible (0.002–0.018 wt pct Fe) when the Al content was below 6 wt pct. The types of intermetallic phases formed within the composites can be modified by adjusting the alloy composition.[4–7,21]. With increasing Ca/Al in the range of 0 to 1, the intermetallic phases change from $Mg_{17}Al_{12}$ to the C15-$CaAl_2$, C36-$Ca(Mg,Al)_2$ and C14-$CaMg_2$ Laves phases.[5,6] Moreover, the precipitates become more interconnected and form a skeleton structure.[6,7] Representative images of the as-cast Mg-6Al-2Ca, Mg-5Al-3Ca and Mg-4Al-4Ca (wt pct) alloys are shown in Figures 3(a) through (c), respectively. The respective Ca/Al ratios of the Mg-6Al-2Ca, Mg-5Al-3Ca and Mg-4Al-4Ca (wt pct) alloys are 0.21, 0.41 and 0.65. It has been confirmed that their main types of intermetallic phases are C15-$CaAl_2$, C36-$Ca(Mg,Al)_2$ and C14-$CaMg_2$, respectively. After heat treatment at 500 °C for 48 h, the interconnectivity decreases and the Laves phase morphology changes to more isolated and spherical particles.[32] Interestingly, the porosity observed within the solid solution materials (Figure 1) was strongly reduced in the composite materials despite the use of sub-atmospheric pressure during melting and casting. This effect is most probably linked to the closer positioning of the alloy composition to eutectic ridges as the alloying content is increased, which reduces the solidification interval.

C. *Mg-Al-Ca Intermetallic Phases*

The Mg-Al-Ca ternary system as well as the Mg-Al, Mg-Ca and Al-Ca binary systems show various types of intermetallic phases. The ternary C36-$Ca(Mg,Al)_2$ Laves phase and the binary C14-$CaMg_2$, C15-$CaAl_2$ and $Mg_{17}Al_{12}$ intermetallic phases are in focus of the present work. In order to synthesize the C14-$CaMg_2$ Laves phase, Mg-45Ca (wt pct) alloys were successfully produced from pure Mg and pure Ca by induction melting using a steel crucible. In order to avoid increasing Fe-contaminations, the Al-42Ca (wt pct) alloys were prepared by arc-melting on a water-cooled copper hearth to synthesize the C15-$CaAl_2$ Laves phase. After arc-melting, the Al-42Ca (wt pct) alloy was heat treated in a glass tube furnace at 600 °C for 24 h under Ar protection. A Mg-Al diffusion couple was prepared from two blocks of pure Mg and Al, targeting the formation of the $Mg_{17}Al_{12}$ intermetallic phase. The two $5 \times 5 \times 5$ mm^3 blocks of Mg and Al were ground up to #4000 grit using SiC paper and polished to 1 μm using diamond paste and ethanol lubricant. The blocks were subsequently cleaned in an ultrasonic bath in acetone, dried and lightly pressed together using a molybdenum clamp. Thereafter, the clamped blocks were placed in the furnace, evacuated and purged with Ar, and then annealed at 400 °C for 1 week, followed by furnace cooling.

The obtained microstructures of the C14-$CaMg_2$ and C15-$CaAl_2$ Laves phases are shown in Figures 4(a) and (b), respectively. While a high density of pores can be observed in the C14-$CaMg_2$ Laves phase [Figure 4(a)], the C15-$CaAl_2$ Laves phases [Figure 4(b)] exhibits a more homogeneous microstructure and a comparatively coarse grain size. The synthesis of $Mg_{17}Al_{12}$ intermetallic phase using the diffusion couple technique was not successful. As shown in Figure 4(c), neither a concentration gradient indicating measurable interdiffusion nor the formation of intermetallic phases could be achieved despite numerous trials. This is most probably due to rapid re-oxidation of the polished Mg surface despite only few minutes between the last polishing step and evacuation of the furnace. This result highlights the requirement of materials preparation in an oxygen-free atmosphere (such as a glovebox) and transport of the samples in vacuum containers to the diffusion bonding furnace.

However, several other pathways remain for the synthesis of intermetallic compounds of the Mg-Al-Ca system, especially for the ternary C36-$Ca(Mg,Al)_2$ Laves phase, which combines all three elements and thus also their specific limiting factors of reactivity (Ca), vapor pressure (Mg) and solubility (Al). While it has been reported that the Mg-Al-Ca intermetallic phases can be synthesized by combinatorial sputtering, desorption of

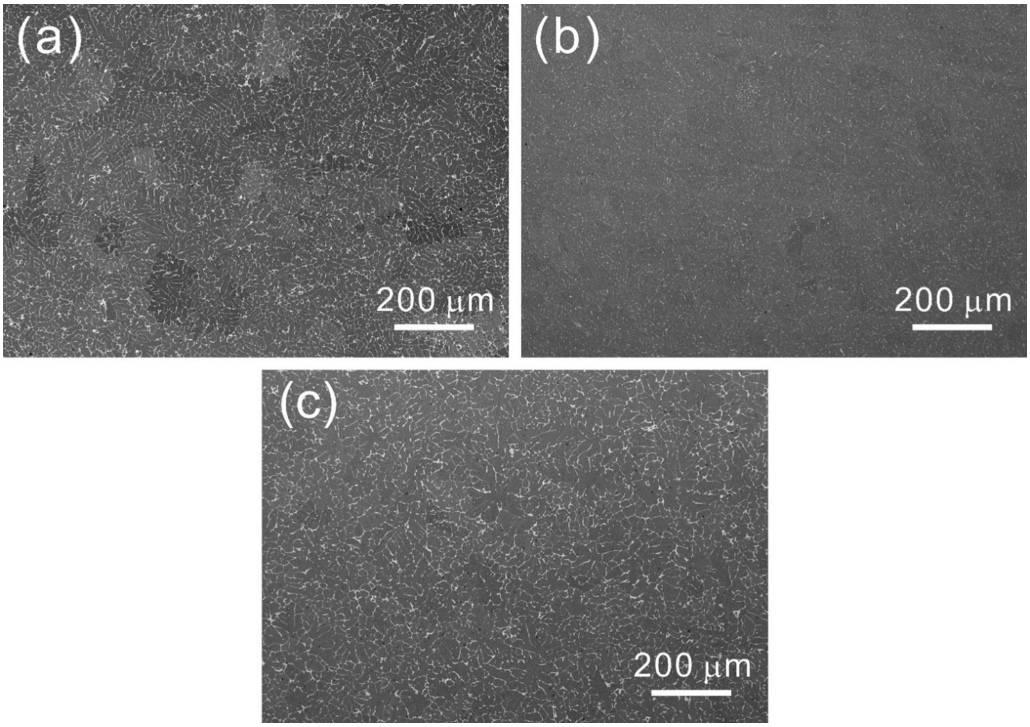

Fig. 3—Image of as-cast composite materials (*a*) Mg-6Al-2Ca, (*b*) Mg-5Al-3Ca and (*c*) Mg-4Al-4Ca (wt pct) alloys synthesized by induction melting. The corresponding intermetallic compounds were identified as C15-$CaAl_2$, C36-$Ca(Mg,Al)_2$ and C14-$CaMg_2$ Laves phases, respectively. ImageJ analysis gave the following volume fractions of the intermetallic compounds: Mg-6Al-2Ca 5.5 vol pct, Mg-5Al-3Ca 6.8 vol pct, Mg-4Al-4Ca 8.7 vol pct. This Figure is reproduced from Ref. [37] under license CC-BY-4.0.

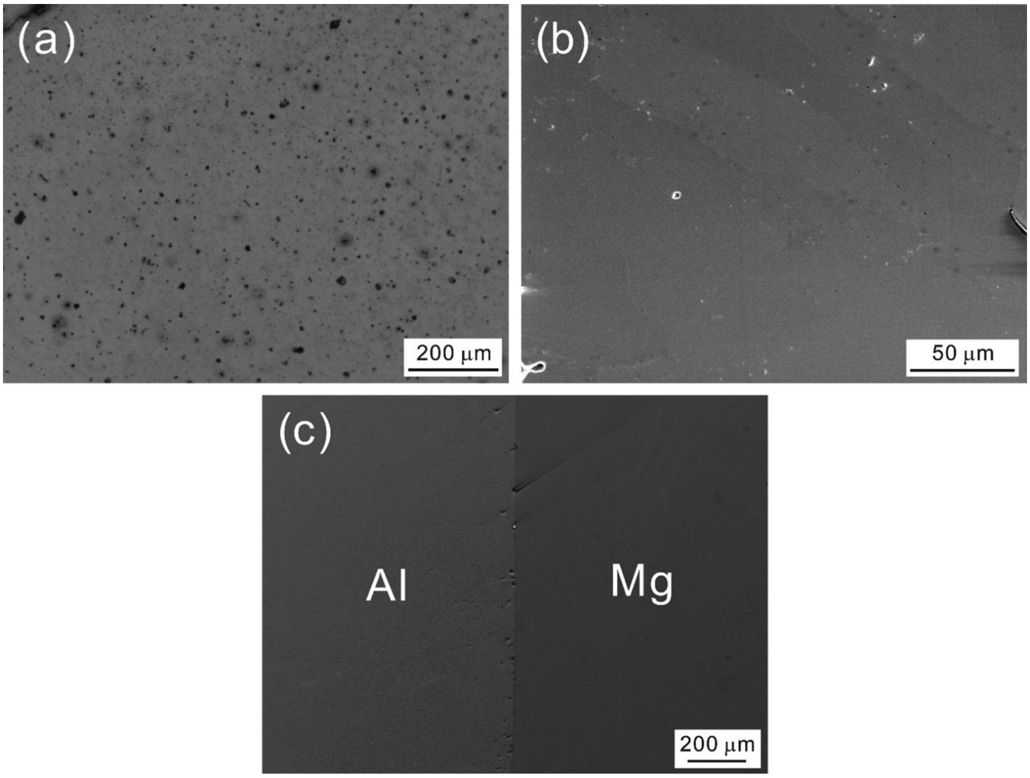

Fig. 4—Synthesis of intermetallic phases. SEM images of the (*a*) C14-$CaMg_2$ Laves phase synthesized by induction melting showing high number of porosity, (*b*) C15-$CaAl_2$ Laves phase synthesized by arc-melting, and (*c*) an unsuccessful attempt at fabricating an Mg-Al diffusion couple after heat treatment at 400 °C for 1 week, showing no sign of interdiffusion or intermetallic phase formation. This Figure is reproduced from Ref. [37] under license CC-BY-4.0.

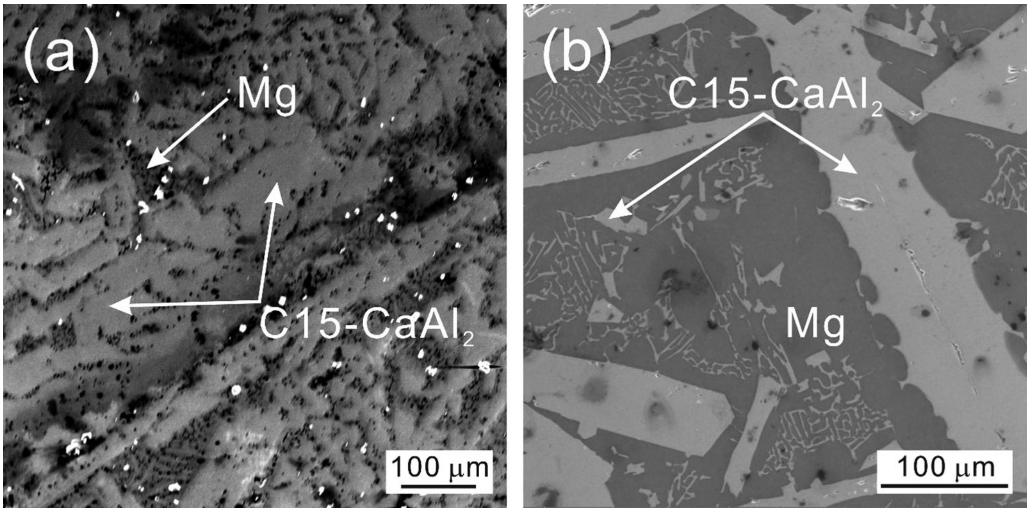

Fig. 5—SEM images of the trials for fabricating bulk C36 ternary Laves phase: (*a*) Mg-30Al-44Ca (wt pct) alloy synthesized by manual induction melting, and (*b*) reaction zone of a Mg-CaAl$_2$ liquid-solid diffusion couple. This Figure is reproduced from Ref. [37] under license CC-BY-4.0.

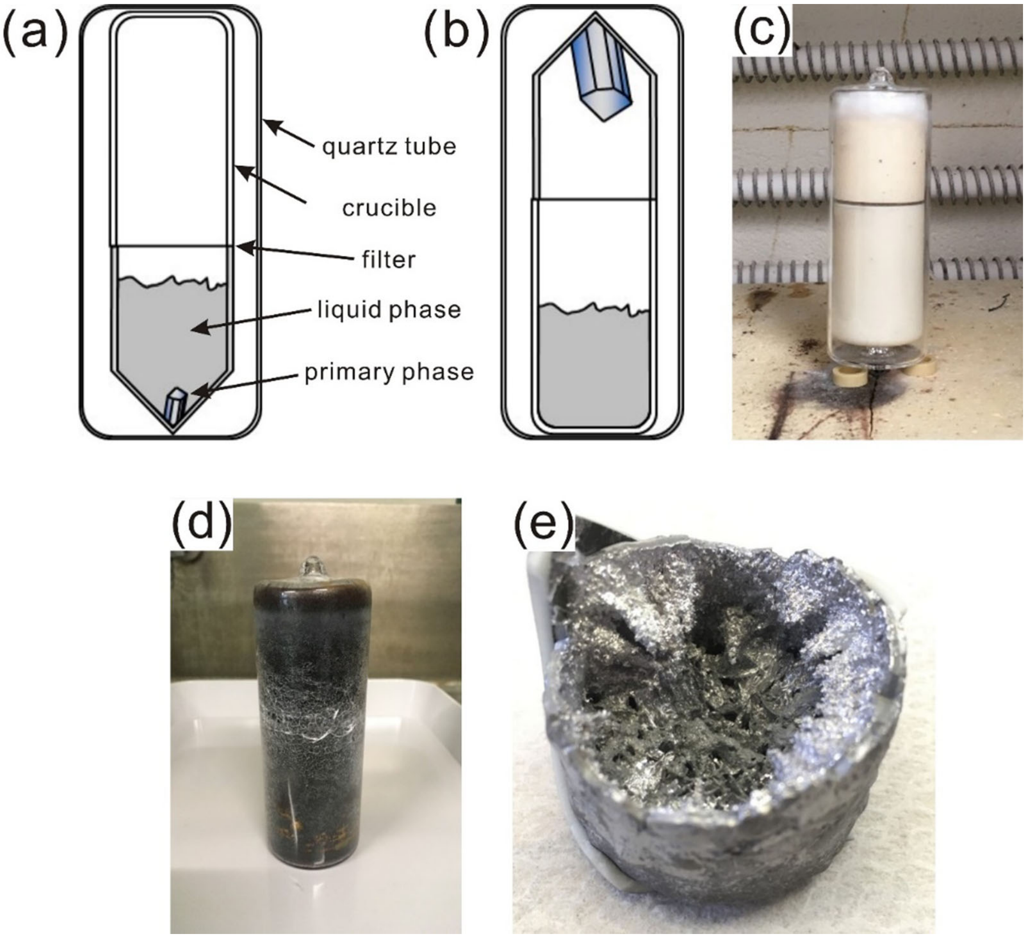

Fig. 6—(*a*) A schematic illustration of the set-up of the solution growth method. (*b*) After heat treatment, the primary phase was separated from the remaining liquid phase by centrifugation. (*c*) An alumina crucible encapsulated in a quartz tube filled with Ar. (*d*) After cooling the quartz tube was blackened on the inside and showed radial cracks. (*e*) Only one ingot was obtained in the crucible and no materials were left on the grid. This Figure is reproduced from Ref. [37] under license CC-BY-4.0.

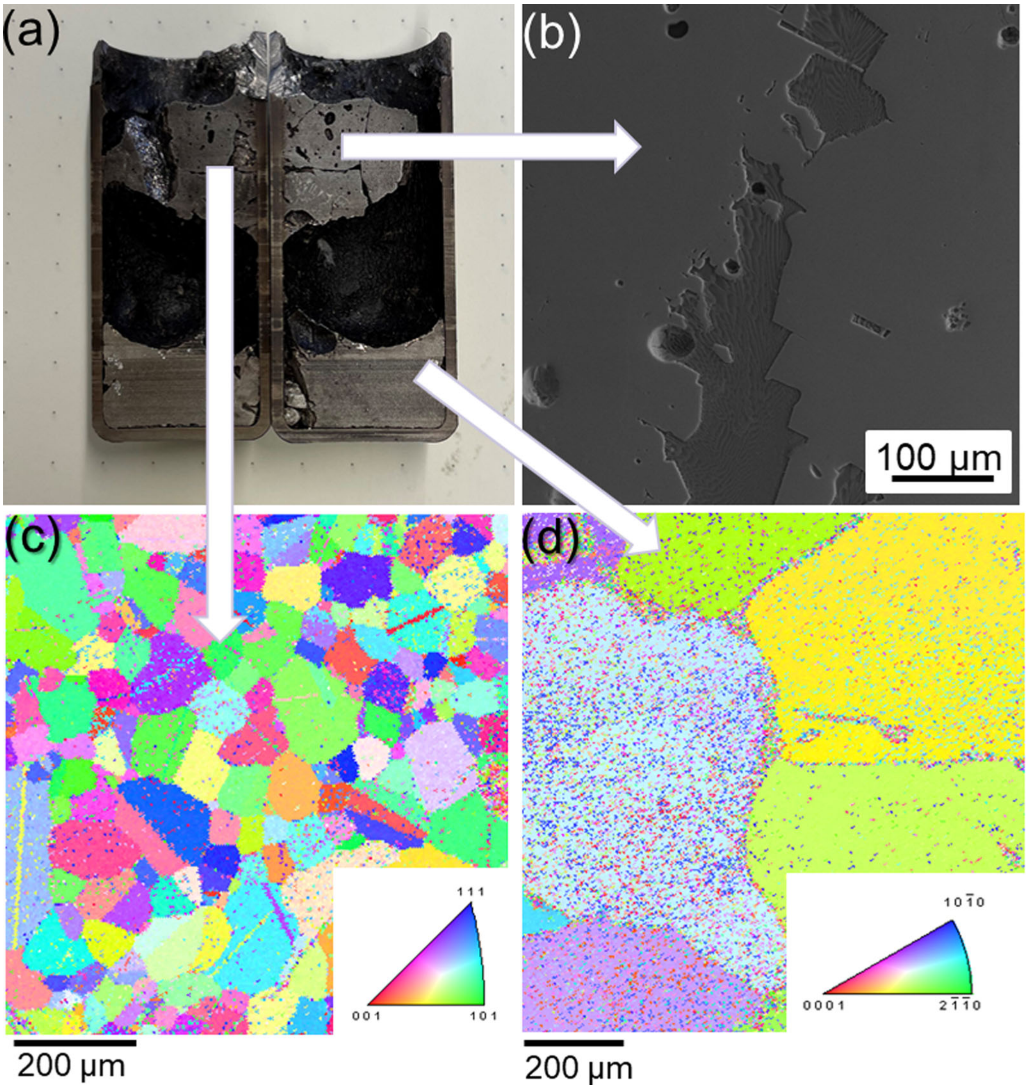

Fig. 7—Results from synthesising the C36-Ca(Mg,Al)$_2$ Laves phase using the Bridgman method. (*a*) overview of the obtained ingot with SEM images of the (*b*) top right of the sample. EBSD allowed us to identify the grain orientation of the cubic CaAl$_2$ phase (*c*) as well as the hexagonal CaMg$_2$ phase (*d*). Parts of this Figure are being reproduced from Ref. [37] under license CC-BY-4.0.

volatile film-forming species during sputtering at elevated temperatures demonstrates the challenges in this process routine for the C36-Ca(Mg,Al)$_2$ Laves phase.[33]

We therefore investigated the feasibility of alternative approaches: induction melting of a Mg-30Al-44Ca (wt pct) using a graphite crucible with boron nitride spray proved unfeasible to rapid disintegration of the crucible, while both sintered boron nitride and aluminumtitanite crucibles repeatedly fractured during heating. As it allows for more gentle heating of the base materials and does not require any additional crucible material, manual induction melting on a water-cooled Cu finger within an Ar filled quartz tube was performed ("copper boat" furnace by Edmund Bühler GmbH, 12 kW power). However, Mg evaporation could not be avoided entirely, and the resultant microstructure [Figure 5(a)] predominantly consists of the here undesired C15-CaAl$_2$ Laves phase with small amounts of Mg. Utilizing a Mg-Al-Ca diffusion multiple with a 50 μm thin Ca foil between two polished blocks of pure Mg and Al failed as the oxidation of Ca—even more rapid than that of Mg—precluded any interdiffusion in a similar manner as for the Mg-Al binary diffusion couple. Cold rolling Ca foils in between Al and Mg did not lead to a successful bond due to the vastly different rates of deformation of the three materials involved. Another approach relied on positioning a block of Mg on top of a C15-CaAl$_2$ Laves phase alloy, placing the stack in an Ar filled annealing furnace and bringing it to 700 °C (above the melting point of Mg). Although liquid/solid interdiffusion could be achieved, the desired formation of the C36 Laves phase could not be observed [Figure 5(b)].

In view of these unsuccessful attempts, the flux solution growth method[34] was used to synthesize the targeted C36-Ca(Mg,Al)$_2$ Laves phase. Figures 6(a) and (b) show a schematic illustration of the utilized setup. The starting materials of a Mg-28.4Al-43.2Ca (wt pct) alloy were mixed and placed in an alumina crucible with a mesh fixed at a position above the alloy for decanting the melt at the end of crystal growth. The entire crucible was encapsulated in a Quartz tube filled with Ar [Figure 6(c)]. The quartz tube was heated up to 870 °C and annealed for 2 h to melt the starting materials. After melting, the quartz tube was cooled down to 850 °C at 10 oC/h and then slowly cooled down to 750 °C at 1°/h, followed by centrifugation to separate the remaining liquid phase from the solidified material. According to the phase diagram,[25,29,35], at the used composition the C36-Ca(Mg,Al)$_2$ Laves phase is in equilibrium with the liquid phase at 750 °C. Therefore, after removing the liquid phase, the crystal of the C36-Ca(Mg,Al)$_2$ Laves phase should be obtained.

However, after cooling the quartz tube was blackened on the inside and showed radial cracking at the position where the crucibles met [Figure 6(d)]. After opening the tube one ingot was found in the crucible and no material was left on the grid [Figure 6(e)]. This suggests that the entire melt solidified above 750 °C, with no liquid left to be centrifuged into the upper crucible. The fact that no liquid phase was present at 750 °C could either hint at inconsistency with the existing phase diagram, be linked to a significant change in melt composition due to evaporation losses, or caused by a temperature offset between the thermocouple and the actual temperature in the crucible. Lastly, the feasibility of synthesizing the C36-Ca(Mg,Al)$_2$ Laves phase by the Bridgman method was investigated. Pure elements were positioned in a cylindrical Ta crucible of 14 mm in diameter and 70 mm in length. The crucible was sealed containing an Ar atmosphere of 0.6 bar, and placed on a water-cooled cold finger in a Bridgman apparatus After temperature equilibration at 900 °C, the growth was carried out by lowering the crucible out of the hot zone at a velocity of 5 mm/h. As shown in Figure 7(a), the obtained alloy contained two parts and a large void of yet unknown origin in the center. The microstructures of the top and the bottom parts of the sample are shown in Figures 7(b) through (d), with average compositions (at. pct) of Mg-45.37Al-38.63Ca and Mg-2.27Al-39.40Ca, respectively. At least three phases are present in both top and bottom regions. EBSD analyses showed that the right top regions consists predominantly of the targeted C36-Ca(Mg,Al)$_2$ phase [Figure 7(b)], but with inclusions of eutectic regions containing the C15-CaAl$_2$ Laves together with Mg solid solution. On the left top, the main region revealed the C15-CaAl$_2$ Laves phase and small eutectic regions [Figure 7(c)]. The bottom is mainly consisting of the C14-CaMg$_2$ phase, with traces of other components of the compositions of Mg-53Al-36Ca (at. pct) as indicated by the white arrow in Figure 7(d). While the resultant size of the C36-Ca(Mg,Al)$_2$ domains in the right top of the ingot are not large enough for bulk mechanical testing, they allow for micromechanical testing such as micropillar compression or nanoindentation testing after f.e. focussed ion beam preparations. While surely representing substantially increased effort compared to other laboratory scale synthesis methods, the Bridgeman technique thereby offers at last the possibility to probe the mechanical properties of the C36 Laves phase, thereby elucidating its contribution to Mg-Al-Ca composite materials. Another potential strategy to overcome the outlined difficulties would be to follow a powder metallurgical route, blending either elemental or pre-alloyed binary powders and sintering them—preferably under isostatic pressure—at elevated temperature in the solid state into a bulk specimen. However, close attention would have to paid to the formation of oxide inclusions potentially originating from the large surface area of the powder particles. Larger samples with surface areas in the order of 100 mm^2 to facilitate corrosion studies are as of yet not feasible with current metallurgical laboratory techniques.

IV. CONCLUSIONS

Due to the high reactivity and high vapor pressures of Mg and Ca, and the mutual solubility of Al with Fe, the synthesis of bulk materials of Mg-Al-Ca solid solutions, composites and intermetallic phases is a complex metallurgical challenge. Different bulk metallurgical methods were investigated, demonstrating their specific challenges and pitfalls, and the following conclusions can be drawn:

(1) Solid solutions can be synthesized by induction melting using a steel crucible under Ar atmosphere. Elevated pressure was found to minimize evaporation and porosity within the solidified sample. Intermetallic precipitations and intragranular segregation can be significantly reduced by subsequent hot rolling and homogenization annealing, with careful selection of temperatures and processing sequence to minimise grain growth.

(2) Composites can also be synthesized by induction melting under Ar atmosphere, ideally using Mg-Ca master alloys instead of pure elements to minimize evaporation and oxidation. When the Al content is low (≤ 6 wt pct), the Fe contamination in the Mg-Al-Ca composites is negligible, and thus steel crucibles can be used. Porosity formation and thus the need for high pressure solidification seems to be less pronounced than for solid solution materials.

(3) The intermetallic C14-CaMg$_2$ Laves phase can be readily synthesized by induction melting, while the C15-CaAl$_2$ Laves phase can be prepared by arc-melting. The Bridgman method was identified as the most promising pathway for synthesizing of the C36-Ca(Mg,Al)$_2$ Laves phase, albeit in small amounts only suitable for micromechanical testing.

(4) Solid state diffusion couples require extreme care to avoid oxidation of Mg and especially Ca, which otherwise inhibits interdiffusion and interfacial phase formation.

ACKNOWLEDGMENTS

We thank Mr. Jürgen Wichert and Mr. Michael Kulse for their technical supports in alloy synthesis. This work was supported by the German research foundation (DFG) within the Collaborative Research Centre SFB 1394 "Structural and Chemical Atomic Complexity—From Defect Phase Diagrams to Materials Properties" (Project ID 409476157). H. Springer wishes to acknowledge funding through the Heisenberg-program of the Deutsche Forschungsgemeinschaft (Project ID 416498847).

AUTHOR CONTRIBUTIONS

L. Tanure and H. Springer conceived and designed the experiments. W. Luo wrote the manuscript. M. Felten, J. Nowak, D. Zander and W. Delis analysed the microstructures of Mg-Al-Ca solid solutions. N. Ayeb performed characterizations of the Mg-Al-Ca composites. M. Freund contributed to the characterizations of the Mg-Al-Ca intermetallics. C. Thomas and M. Feuerbacher contributed to the synthesis of the C36-Ca(Mg,Al)$_2$ Laves phase. S. Sandlöbes-Haut and S. Korte-Kerzel provided feedback and suggestions to improve the experiments. All authors contributed to discussion of the results and reviewed the manuscript.

FUNDING

Open Access funding enabled and organized by Projekt DEAL.

CONFLICTS OF INTEREST

The authors declare no conflict of interest.

OPEN ACCESS

REFERENCES

1. M.K. Kulekci: *Int. J. Adv. Manuf. Technol.*, 2008, vol. 39, pp. 851–65.
2. A. Kumar, S. Kumar, and N.K. Mukhopadhyay: *J. Magnes. Alloy.*, 2018, vol. 6, pp. 245–54.
3. S. You, Y. Huang, K.U. Kainer, and N. Hort: *J. Magnesium Alloys*, 2017, vol. 5, pp. 239–53.
4. S. Jayasathyakawin, M. Ravichandran, N. Baskar, C. Anand Chairman, and R. Balasundaram: *Mater. Today: Proc.*, 2020, vol. 27, pp. 909–13.
5. S. Sandlöbes, M. Friák, S. Korte-Kerzel, Z. Pei, J. Neugebauer, and D. Raabe: *Sci. Rep.*, 2017, vol. 7, p. 10458.
6. A. Suzuki, N.D. Saddock, J.W. Jones, and T.M. Pollock: *Acta Mater.*, 2005, vol. 53, pp. 2823–34.
7. L. Zhang, K.-K. Deng, K.-B. Nie, F.-J. Xu, K. Su, and W. Liang: *Mater. Sci. Eng. A*, 2015, vol. 636, pp. 279–88.
8. S. Sanyal, M. Paliwal, T.K. Bandyopadhyay, and S. Mandal: *Mater. Sci. Eng. A*, 2021, vol. 800, p. 140322.
9. M. Zubair, S. Sandlöbes, M.A. Wollenweber, C.F. Kusche, W. Hildebrandt, C. Broeckmann, and S. Korte-Kerzel: *Mater. Sci. Eng. A*, 2019, vol. 756, pp. 272–83.
10. D. Amberger, P. Eisenlohr, and M. Göken: *Mater. Sci. Eng. A*, 2009, vol. 510–511, pp. 398–402.
11. A.A. Luo, B.R. Powell, and M.P. Balogh: *Mater. Sci. Eng. A*, 2002, vol. 33, pp. 567–74.
12. M.F. Chisholm, S. Kumar, and P. Hazzledine: *Science*, 2005, vol. 307, pp. 701–03.
13. P.M. Hazzledine and P. Pirouz: *Scr. Metall. Mater.*, 1993, vol. 28, pp. 1277–82.
14. P. Paufler: *Intermetallics*, 2011, vol. 19, pp. 599–612.
15. M. Felten, J. Nowak, P. Grünewald, F. Schäfer, C. Motz, and D. Zander: The role of native oxides on the corrosion mechanism of laves phases in Mg-Al-Ca Composites, in *Proceedings of the magnesium*. Springer, Cham, 2021, pp. 217–25.
16. M. Felten, J. Nowak, O. Beyss, P. Grünewald, C. Motz, and D. Zander: *Corros. Sci.*, 2023, vol. 212, p. 110925. https://doi.org/10.1016/j.corsci.2022.110925.
17. M. Hasegawa: Chapter 3.3—Ellingham Diagram, in *Treatise on Process Metallurgy*. S. Seetharaman, ed., Boston, Elsevier, 2014, pp. 507–16.
18. R.E. Honig: *RCA Rev.*, 1957, vol. 18, pp. 195–204.
19. N. Xiong, S. Friedrich, S.R. Mohamed, I. Kirillov, X. Ye, Y. Tian, and B. Friedrich: *J. Sustain. Metall.*, 2022, vol. 8, pp. 1561–72.
20. A.A. Luo: *J. Magnes. Alloy.*, 2013, vol. 1, p. 2.
21. O. Ikeda, I. Ohnuma, R. Kainuma, and K. Ishida: *Intermetallics*, 2001, vol. 9, pp. 755–61.
22. M. Hradilová, D. Vojtěch, J. Kubásek, J. Čapek, and M. Vlach: *Mater. Sci. Eng. A*, 2013, vol. 586, pp. 284–91.
23. H. Okamoto: *J. Ph. Equilibria Diffus.*, 1998, vol. 19, p. 490.
24. H. Okamoto: *J. Ph. Equilibria Diffus.*, 1998, vol. 19, p. 598.
25. H. Okamoto: *J. Ph. Equilibria Diffus.*, 2003, vol. 24, pp. 91-1.
26. D. Kevorkov, M. Medraj, J. Li, E. Essadiqi, and P. Chartrand: *Intermetallics*, 2010, vol. 18, pp. 1498–506.
27. F. Stein and A. Leineweber: *J. Mater. Sci.*, 2021, vol. 56, pp. 5321–427.
28. S. Voß, F. Stein, M. Palm, and D. Raabe: *Mater. Sci. Eng. A*, 2010, vol. 527, pp. 7848–53.
29. A. Zolriasatein and A. Shokuhfar: *Mater. Des.*, 2015, vol. 75, pp. 17–23.
30. H. Cao, C. Zhang, J. Zhu, G. Cao, S. Kou, R. Schmid-Fetzer, and Y.A. Chang: *Acta Mater.*, 2008, vol. 56, pp. 5245–54.
31. D. Andre, M. Freund, U. Rehman, W. Delis, M. Felten, J. Nowak, C. Tian, M. Zubair, L. Tanure, L. Abdellaoui, et al.: *Mater Charact*, 2022, vol. 192, p. 112187.
32. Z.T. Li, X.D. Zhang, M.Y. Zheng, X.G. Qiao, K. Wu, C. Xu, and S. Kamado: *Mater. Sci. Eng. A*, 2017, vol. 682, pp. 423–32.
33. M. Zubair, M. Felten, B. Hallstedt, M. Vega Paredes, L. Abdellaoui, R. Bueno Villoro, M. Lipinska-Chwalek, N. Ayeb, H. Springer, J. Mayer, et al.: *Mater. Des.*, 2023, vol. 225, p. 111470.
34. P. Keuter, S. KarimiAghda, D. Music, P. Kümmerl, and J.M. Schneider: *Materials*, 2019, vol. 12, p. 3026.
35. A.-P. Tsai and C. Cui: 26—Crystal growth of quasicrystals, in *Handbook of Crystal Growth*, 2nd ed., T. Nishinaga, ed., Boston, Elsevier, 2015, pp. 1113–56.

36. A. Janz, J. Gröbner, H. Cao, J. Zhu, Y.A. Chang, and R. Schmid-Fetzer: *Acta Mater.*, 2009, vol. 57, pp. 682–94.
37. Luo, W., Tanure, L., Felten, M., Nowak, J., Delis, W., Freund, M., Ayeb, N., Zander, D., Thomas, C., Feuerbacher, M., Sandlöbes-Haut, S., Korte-Kerzel, S., Springer, H. Metallurgical synthesis methods for Mg-Al-Ca scientific model materials. arXiv: 2303.08523.